Hippocampal network and inhibitory neuron dysfunction in age and disease

Dissertation zur Erlangung
des Doktorgrades (Dr. rer. nat.)
der Mathematisch-Naturwissenschaftlichen Fakultät
der Rheinischen Friedrich-Wilhelms-Universität Bonn

Vorgelegt von

Eleonora Ambrad Giovannetti

aus Cartagena (Kolumbien)

Bonn, 2021

Angefertigt mit Genehmigung der Mathematisch-Naturwissenschaftlichen Fakultät der Rheinischen Friedrich-Wilhelms-Universität Bonn

1. Gutachter: Prof. Dr. Martin Fuhrmann

2. Gutachter: Prof. Dr. Michael Hofmann

Erscheinungsjahr: 2021

Tag der Promotion: 17.06.2021

Summary

Aging and Alzheimer's disease (AD) are two highly intertwined pathological processes. Indeed, one of the highest risk factors for developing AD is age. Mechanistically, it has been suggested that remodeling of inhibitory neuron function causes the disruption of the homeostatic excitatory/inhibitory balance that is at the basis for effective information processing in the central nervous system. In the hippocampus proper and medial entorhinal cortex (MEC), a plethora of inhibitory neurons is tailored to orchestrate input/output conversion in excitatory neurons, thereby supporting hippocampal-dependent cognitive processes, like episodic memory and navigation. Furthermore, altered inhibitory function is a major contributor to aberrant oscillatory activity recorded by means of electroencephalograms and local field potentials (LFP) in the hippocampal system of both aged and AD brains. Hence, therapeutic approaches devoted to the restoration of inhibitory tone, with the aim of normalizing oscillatory correlates of cognitive processes, have emerged as a strategy to counteract the deleterious effects of aging and AD. In particular, theta and gamma oscillations have been the preferred target of investigation and manipulation. Nonetheless, more evidence is required to understand how age and AD impact oscillatory activity in the hippocampus and MEC, and whether inhibitory-neurons driven rhythmogenesis is a viable strategy to alleviate the cognitive burden associated with both conditions.

Here, I probed the hippocampal network of aged PV-Cre::WT mice and their APPswe/PS1dE9 (PV-Cre::APP/PS1) transgenic littermates, used as model of familial AD. To do so, I employed LFP recordings, and LFP recordings coupled with optogenetic stimulation of local parvalbumin-positive (PV^+) interneurons in the CA1 compartment of the hippocampus of awake, freely moving animals. I showed that theta oscillations linearly decrease with age in PV-Cre::WT animals, but not in PV-Cre::APP/PS1 mice, which is indicative of inhibitory neuron dysfunction. Interestingly, theta-gamma coupling measured as a modulation index (MI) in the *stratum lacunosum moleculare* (SLM) was reduced in PV-Cre::APP/PS1 animals, showing that feedback communication between the hippocampus and the MEC is altered. Besides, I detected an age-dependent linear increase in the MI of PV-Cre::WT animals, but not in PV-Cre::APP/PS1 animals, indicating that age-related network remodeling differs between healthy and AD conditions. Next, I investigated the effects of optogenetically stimulating hippocampal PV^+ neurons of aged PV-Cre::WT and PV-Cre::APP/PS1 mice during memory tasks probing recognition-, working- and spatial memory. Here, optogenetic stimulation of PV^+ interneurons in aged PV-Cre::WT and PV-Cre::APP/PS1 animals was sufficient to rescue

cognitive deficits of APP/PS1 animals, but not WT animals, in a spatial memory task. Furthermore, I showed that somatostatin-positive (SOM^+) long-range inhibitory projections between the hippocampus and the MEC, a poorly described neuronal population, are impaired in SST-Cre::APP/PS1 mice. This was concomitant with a reduction of local SOM-immunoreactivity in the MEC. Potentially, the structural and functional alterations of local and long-range projecting SOM^+ neurons underlie the alterations of theta-gamma coupling observed in APP/PS1 animals.

The results presented in this thesis thus contribute to the existing knowledge about oscillatory aberrations in health and disease. In addition, these results provide new perspectives on the mechanisms that cause network dysfunction and cognitive deficits in healthy and AD-like conditions.

Table of contents

Summary ..... **iii**

Table of contents ..... **v**

1 Introduction **1**

1.1 Generation and functional relevance of neural oscillations 2

1.1.1 Oscillations at the macro-, meso- and microscopic scale 2

1.1.2 Generation of local and global oscillatory synchrony 6

1.1.3 Relevance of mesoscopic neural oscillations for learning and memory 7

1.2 Functional anatomy of the rodent hippocampal system 10

1.2.1 Hippocampus proper and entorhinal cortices 12

1.2.2 Local and long-range inhibitory neurons 16

1.2.3 Hippocampal oscillations and their relation to episodic memory 18

1.3 Alzheimer's disease 26

1.3.1 Molecular and cellular mechanisms behind Aβ deposition 27

1.3.2 Evidence for network dysfunction 30

1.3.3 Inhibitory neuron dysfunction 33

1.4 Aim of study 36

2 Materials and Methods **37**

2.1 Mouse lines 37

2.1.1 APPswe/PS1dE9 (APP/PS1) 37

2.1.2 PV-Cre::APP/PS1 37

2.1.3 SST-Cre::APP/PS1 37

2.1.4 Thy1-GCaMP6f-GP5.5::APP/PS1 38

2.2 Surgical procedures 38

2.2.1 Anesthesia and analgesia 38

2.2.2 Stereotactic viral injections 39

2.2.3 Procedures for cranial window, light fiber and silicone probe implantation 39

2.3 Anterograde tracings in SST-Cre::APP/PS1 mice 40

2.4 Combined optogenetics and LFP recordings 40

2.4.1 Adeno-associated viral constructs 40

2.4.2 Single wire electrodes and amplifier system 40

2.4.3 Fiber-optic cannulas' and LFP electrodes' implantation 41

2.4.4 Data acquisition and stimulation protocols 41

2.5 Behavioral tests 43

2.5.1 Local field potentials in the open field 43
2.5.2 Novel object recognition and location 43
2.5.3 Y-Maze 44
2.6 Combined laminar probe LFP recordings and two-photon calcium imaging 44
2.6.1 Silicon probes and amplifier system 44
2.6.2 Hippocampal window and laminar probe implantation 45
2.6 Two-photon microscopy 46
2.6.1 Image acquisition 46
2.6.2 Linear treadmill and head-fixation procedures 46
2.7 Immunohistochemistry 47
2.7.1 Perfusion and vibratome sectioning 47
2.7.2 Fluorescent immunohistochemistry 47
2.7.3 Confocal microscopy 48
2.8 Data analyses 49
2.8.1 Baseline recordings in the open field 49
2.8.2 Optogenetic sitmulation in the open field 49
2.8.3 Theta-gamma modulation index 49
2.8.4 Freely moving behavior 50
2.8.5 Two-photon in vivo calcium imaging 50
2.8.6 Histological quantifications 51
2.9 Statistical analyses 52

3 Results 53

3.1 Theta oscillations and locomotor activity of PV-Cre::WT and PV-Cre::APP/PS1 mice 53
3.2 Peak frequency of theta oscillations is inversely correlated to age in PV-Cre::WT animals 57
3.3 Reduced theta-gamma modulation index in PV-Cre::APP/PS1 animals 61
3.4 Entrainment of theta oscillations via optogenetic stimulation of PV^+ interneurons 63
3.5 Closed-loop feedback optogenetic stimulation protocol 67
3.6 Arrhythmic optogenetic stimulation of hippocampal PV^+ interneurons during the NOR test 69
3.7 Rhythmic optogenetic stimulation of hippocampal PV^+ interneurons during the Y-Maze test 73
3.8 Rhythmic optogenetic stimulation of hippocampal PV^+ interneurons during the NOL test.. 75
3.9 Simultaneous two-photon calcium imaging and laminar LFP recordings 80
3.10 Layer-specific analysis of Aβ deposition in the MEC of APP/PS1 mice 82
3.11 Reduced SOM-immunoreactivity in the MEC of APP/PS1 mice 84
3.12 Dysfunction of hippocampal SOM^+ long-range inhibitory projections 88

3.13 Two-photon calcium imaging in the EC 91

4 Discussion 93

Peak frequency of theta oscillations decreases with age 93

Altered theta-gamma phase-amplitude coupling in PV-Cre::WT and PV-Cre::APP/PS1 animals 96

Entrainment of theta oscillations via optogenetic stimulation of PV^+ interneurons 98

Increasing inhibitory tone is not sufficient to restore recognition memory 101

Rhythmic optogenetic stimulation of hippocampal PV^+ interneurons during the Y-Maze test 104

Rhythmic optogenetic stimulation of hippocampal PV^+ interneurons during the NOL test 106

Aβ plaques show a layer-specific deposition in the MEC of APP/PS1 mice 110

Reduction of SOM-immunoreactivity in the MEC of APP/PS1 mice 112

Dysfunction of hippocampal SOM^+ LRIPs in SST-Cre::APP/PS1 mice 114

5 Conclusions and future directions 118

6 Appendix 121

6.1 Abbreviations 121

6.2 Consumables 124

6.2.1 Anesthesia and medication 124

6.2.2 Commons for surgical procedures 124

6.2.3 Adeno-associated viruses used for stereotactic injections 125

6.2.4 Local field potential recordings 126

6.2.5 Immunohistochemistry 126

6.3 Equipment 127

6.3.1 Surgery equipment 127

6.3.2 Local field potential recordings 128

6.3.3 Behavior and optogenetics 128

6.3.4 Two-photon microscopy 128

6.3.5 Immunohistochemistry 129

6.4 Software 129

6.5 Statistical tests 129

7 References 135

8 Contributions 154

List of figures 155

Acknowledgements 156

List of publications 158

1 Introduction

Ever since electron microscopy was applied to investigate neural tissue, researchers in the field of Neurosciences have been confronted with a completely new chapter and set of questions. The dismissal of the reticular view of the nervous system in favor of the "neuron doctrine" lead to the realization that, albeit being physically separated unities, no neuron in our central and peripheral nervous systems behaves as a discrete entity, and that connectivity between them relies on events taking place at the synaptic compartment. Hence, in addition to the molecular and cellular machinery that sustains each individual cell's functionality, a further layer of complexity is required to ultimately generate not only our whole organism's vital functions, but also our response to external stimuli: the instatement and maintenance of a network within the nervous system.

The manifestation of context-appropriate actions and reactions in presence or absence of a stimulus, i.e. an organism's behavior, is at the basis for its evolution as an individual and as part of a species. Understanding the computations required to produce any type of behavior is possibly one of the biggest challenges of science. However, the incredible technological advancements of the past decades have enabled researchers to increasingly shift their attention from the properties of the single elements within the nervous tissue, to how these act as a global entity to produce higher functions that are intrinsic to animal behavior, such as memory and cognition. In parallel, accumulating evidence suggests that disturbances of the network underlie the cognitive dysfunctions typically observed not only in healthy aging, but also in dementia linked to neurodegenerative disorders such as Alzheimer's disease (AD).

Maintenance of the network's homeostasis requires finely tuned communication within and between brain areas that are sometimes anatomically distant and that therefore need to be "connected" via non-physical means. Neuronal oscillations within the mammalian brain have been proposed as a candidate mechanism to orchestrate neuronal ensembles that participate in the generation and maintenance of specific brain functions and behavior. In turn, disruption of the neuronal oscillatory activity has been appointed as a potential cause for the development of neuropsychiatric disorders. The excitatory/inhibitory balance between excitatory and inhibitory neurons is a key feature behind the production and propagation of neuronal oscillatory activity. Interestingly, inhibitory neurons are particularly affected by both healthy aging and by the AD pathology. Therefore, manipulating inhibitory neurons at an early stage, with the aim of rescuing neuronal network function and possibly prevent the deleterious cognitive deficits that

occur with it, has emerged as a promising therapeutic strategy to battle cognitive dysfunction associated with age and disease.

1.1 Generation and functional relevance of neural oscillations

1.1.1 Oscillations at the macro-, meso- and microscopic scale

Brain oscillations from the single cell to the population level are the product of the electrochemical movement of ions (Na^+, Ca^{2+}, K^+ and Cl^-) across the cellular membrane of neurons and/or glial cells (Buzsaki, Anastassiou, & Koch, 2012), which represents the process at the basis of signaling and information processing in the nervous system. Because of the cellular membrane's chemical composition and capacitive properties, electric charges separate and accumulate in the intracellular and extracellular compartments, thus generating an electric potential. The difference in electric potential between two sites is defined as voltage. Voltage changes over time, due to transmembrane ionic currents, reflect the excitability of the single cell or of the brain region where the measurement is taking place. Brain-wide (macroscopic) and single-cell (microscopic) oscillations differ in biophysical properties and information content (Buzsaki, 2002, 2004; Buzsaki & Draguhn, 2004). Indeed, it has been proposed that the combination of rate- (i.e. firing frequency of single neurons) and phase- (i.e. the way single neurons oscillate with respect to the rest of the extracellular field) coding strategies, and in turn their modulation by the underlying macroscopic oscillations of the extracellular field, is an energy efficient way to guarantee synchronicity and efficient information transmission between neurons of the same functional network. It is therefore highly relevant to investigate the relationship between macro and microscopic oscillations by, for example, measuring the effect of the manipulation of one on the other. This can only be achieved by recording oscillatory activity at an intermediate, "mesoscopic" level, at which both levels of activity can be recorded (Buzsaki, 2010; Einevoll, Kayser, Logothetis, & Panzeri, 2013; Zanos, Zanos, Marmarelis, Ojemann, & Fetz, 2012).

The discovery that the nervous tissue has the potential to produce electric signals can be dated back to the first bioelectrical experiments on the frog's muscle tissue carried out by Galvani in the late 1700s. Following the footsteps of his predecessor, Richard Caton was the first to position a galvanometer on the brain of several animals at his reach, in 1875. He was followed by Nevinsky and finally by Hans Berger, who placed electrodes on the scalp of his patients in 1929, and is therefore considered the pioneer of the electroencephalogram (EEG) technique (Haas, 2003; Verkhratsky & Parpura, 2014). It was maybe due to Berger's lack of understanding of physics that his discoveries were first received with abundant criticism and

skepticism, and only after independent replications of his experiment clinicians started to identify the "Berger rhythm" as indeed deriving from the electrical activity produced by the brain, during a specific brain state, and not as an artifact of muscle twitching (Adrian & Matthews, 1934). Nowadays, recording cortical macroscopic oscillations in the extracellular space with an EEG is a widespread and well established methodology that finds its relevance in basic research and clinical settings (Uhlhaas & Singer, 2012). Due to the biophysical properties of the extracellular medium, which functions as a low-pass filter, and to the damming properties of the skull, scalp-EEG measurements mainly reflect smoothed voltage changes in the superficial layers of the brain, especially those occurring in the cortices (Biasucci, 2019). Even though there are multiple standardized ways to place the recording electrodes on the skull, depending on the research question, EEG measurements always reflect the summation of potentials occurring in a relatively large portion of the cortical tissue (approximately $10cm^2$) in relation to another one (differential measurement of field potentials) and they do not yield any measurement of single neuron activity (Bedard, Gomes, Bal, & Destexhe, 2017). To record voltage changes in single neurons, either from the extracellular space in their direct vicinity or from their intracellular compartment, it is necessary to insert the recording electrode inside the neural tissue.

Oscillatory events in single neurons are widely varied: they assume various waveforms and their anatomical localization along the neuron determines their function. Typically, oscillations at the single neuron level are arise upon the generation and/or the integration of an action potential in the pre- and post-synaptic neuron, which generates excitatory and inhibitory synaptic potentials (EPSPs and IPSPs). Nonetheless, special classes of spontaneously oscillating neurons can generate subthreshold oscillations and/or spiking activity in absence of pre-synaptic activation (Lee, Urbano, & Garcia-Rill, 2018). Historically, extracellular recordings of single nerve's action potentials were carried out for the first time already in the early 1800s. After several decades and multiple experiments, Cole and Curtis conducted extracellular recordings on the giant squid axon preparation (Cole & Hodgkin, 1939), thereby paving the way for the development of intracellular recording techniques (voltage clamp) and, ultimately, for the formalization of the ionic theory of membrane excitability by Hodgkin and Huxley (Hodgkin, 1937, 1939). The foundations of this theory would be confirmed by several independent observations (Mueller & Rudin, 1963) and ultimately the patch clamp measurements several decades later (Neher & Sakmann, 1992; Neher, Sakmann, & Steinbach, 1978). Hence, establishment of intracellular recordings was crucial and pivotal for the development of a unified theory on axon conduction and for the further understanding of how

intracellular and extracellular currents relate to each other. Most importantly, the patch clamp technique also enabled to unveil how intrinsic rhythmicity (i.e. the manifestation of oscillatory activity in single neurons in absence of an artificial stimulation) is a property of both subcortical (Llinas & Yarom, 1986) and cortical neurons (Alonso & Llinas, 1989). Until today, intrinsic membrane oscillations have been described in neurons throughout the rodent brain (Lee et al., 2018), and it is postulated that they are a crucial element for the generation of network-wide rhythmic oscillations.

In spite of the establishment of both micro- and macroscopic electrophysiological recording techniques, there was a seemingly unsurmountable bridge between the manifestation of epi-cortical rhythms of the EEG and those produced by single cells (Caspers, Speckmann, & Lehmenkuhler, 1980; Petsche, Pockberger, & Rappelsberger, 1984). This was the reason behind the development of the "micro EEG" technique, which was based on the implantation of one or multiple intracranial electrodes in more confined portions of the tissue. Recording voltage changes that are generated from a smaller neuronal sample only partially solves the problem of interpreting oscillatory signals, but the spatial resolution of an intracranial recording is significantly higher compared to that of a scalp recording. Nowadays, the term "micro-EEG" was substituted with the term local field potential recordings (LFP) (Buzsaki et al., 2012), and these are often referred to as "mesoscopic oscillations". Depending on the materials, dimensions of the recording electrode and voltage amplifier settings, the information content of the LFP varies. Indeed, frequencies up to 40 kHz can be measured in a typical LFP. Conventionally, though, the term refers to the "slow-frequency" component of a neural oscillatory signal (<500-700 Hz) (Einevoll et al., 2013; Linden et al., 2011). The spiking component of the LFP (>700 Hz), which represents the output of the neural circuit producing the slow wave component of the LFP ("population spike"), was typically filtered out and often regarded as a "contamination" that confounds the information content of the LFP (Zanos et al., 2012). Recently, though, new methods were developed to extract information about the temporal sequence of the population spike, hence reviving the interest for the high frequency component of the LFP (Waldert, Lemon, & Kraskov, 2013).

Similar to the EEG, the slower wave component of the LFP reflects the summation of all ionic processes taking place around the electrode; the higher the distance of the recording electrode from the source of the current, the less information about that source in the LFP (Linden et al., 2011). Additionally, like EEG recordings, LFPs are differential/referential measurements: voltage fluctuations in the LFP reflect the difference in potential between the recording electrode and a second electrode placed either within (referential recording) or outside

(differential recording) the region of interest (Meyer, Carponcy, Salin, & Comte, 2018). In physiological situations, the content of the LFP mainly reflects the net effect of voltage changes caused by multiple synaptic currents that are slow enough to summate over time and space, such as EPSPs and IPSPs generated by gamma-ammino-butyrric acid (GABA) receptor *type a* mediated inward currents of Cl^-, which can generate strong currents when the neurons are actively spiking (Buzsaki et al., 2012). Generally, influx of positive charges (Na^+ and Ca^{2+}) from the extracellular to the intracellular space of neurons creates a so called "sink" in the extracellular space. Sinks are instead typically coupled to the outward movement of ions from the intracellular to the extracellular membrane (K^+), which generates a "source" in the extracellular space. Importantly, LFPs provide and indirect readout of neuronal activity by reflecting, mostly, current flow in the brain region of interest, which is generated by afferent input in the area; thus, spectral changes observed in LFPs upon stimulus presentation or change in behavior are the result of combined upstream activity and locally generated computing (Fernandez-Ruiz & Herreras, 2013; Herreras, 2016). For example, among the extra-synaptic events that contribute to the LFP, Ca^{2+} spikes generated by back-propagating action potentials can substantially contribute to the extracellular field, and distinguishing them from EPSPs can be complicated. This can generate erroneous interpretations about input activation at dendritic compartments, and should be considered when analyzing the LFP (Buzsaki et al., 2012).

To generate measurable mesoscopic oscillations, not one, but a population of neurons needs to receive synchronized (i.e. temporally organized) excitatory and inhibitory input (Buzsaki & Draguhn, 2004). The amplitude of the LFP, in fact, scales with the amount of cells contributing to the potential (Linden et al., 2011). This, in turn, is highly dependent on the geometrical arrangement of the neurons (Buzsaki et al., 2012). Regions where neural cell bodies and dendrites are highly organized in a laminar fashion are the optimal generators of electric fields and neural oscillations, because if a spatially limited compartment is composed by highly similar structures (e.g. dendritic spines), their coherent recuitment upon input activation will generate a stronger ionic current in the extracellular space (Buzsaki et al., 2012).

In the past decade, in spite of the difficulties that arise when trying to interpret the complexity of LFP dynamics, these have gained a resurgence of interest given newly developed recording and manipulation techniques, new analysis tools and the increase in computational power that enables the continuous streaming of data from multiple recording sites (Kriener, Helias, Rotter, Diesmann, & Einevoll, 2013; Mazzoni et al., 2015). Hence, the content and nature of the LFP has increasingly gained relevance as diagnostic tool and as proxy for cognitive function. Within the LFP, in fact, distinct frequency bands can be extrapolated.

1.1.2 Generation of local and global oscillatory synchrony

In mammalian cortical and subcortical networks, oscillations patterns, or frequency bands, range from <1 Hz (ultra slow oscillations) to 500 Hz (ultrafast rhythms) (Buzsaki & Draguhn, 2004). In spite of the approximately 17,000 fold variability in brain volume across species, the hierarchical organization of frequency bands is partially conserved in both EEG and LFP measurements (Buzsaki, Logothetis, & Singer, 2013). Frequency bands can be separated as there is a constant ratio between neighboring frequencies, which are distributed on a logarithmic scale (Buzsaki & Draguhn, 2004). In addition, oscillatory patterns can sometimes compete with each other, as they are associated to different brain states (Buzsaki & Draguhn, 2004). As a general rule, the period of the oscillation is inversely proportional to the dimension of the neuronal circuit which is participating to the generation of the oscillation (slow oscillations being the result of the coordinated, synchronous firing of widely distributed brain networks and fast oscillations usually resulting from local computations (Buzsaki & Wang, 2012)). Similarly, the amplitude or power of the oscillation is inversely proportional to its period, with faster oscillations displaying a smaller amplitude, or power, than slower ones (Buzsaki et al., 2013). Due to axonal conduction and synaptic delays, the generation of faster oscillations is only possible within smaller portions of the tissue (Buzsaki & Draguhn, 2004). In the situation of a stimulus presentation, for example, the different brain regions that process the input will transiently dissociate themselves from the global rhythm and oscillate at faster frequencies, reflecting the higher degree of computation taking place in those areas (Palop, Chin, & Mucke, 2006; Palop & Mucke, 2010). Hence, faster rhythms are correlated to wakefulness states, and the participating neurons are depolarized, closed to firing threshold; inversely, slower rhythms in the EEG and LFP are associated to states of sleep, low responsiveness and higher depolarization thresholds (Tukker, Beed, Schmitz, Larkum, & Sachdev, 2020). Another conserved observation across mammalian species is that the phase of slow oscillations modulates power and rhythm of fast frequency bands (*phase amplitude-* and *cross-frequency coupling*). Phase separation of different fast frequency bands, which are nested on slow waves, may serve as a mechanism to route converging information from distinct brain regions into the same target cells, at different synaptic sites (Buzsaki & Freeman, 2015).

Of particular importance in the context of rhythm and power generation of each frequency band in cortical networks is the contribution of the mono- and polysynaptic connectivity from different distal structures, both cortical and subcortical. The origin and biophysical properties of each frequency band are in fact the result of brain-region specific local and distal computations, which is also reflected in their correlation to distinct behavioral states (Buzsaki

& Draguhn, 2004). Large- and small-scale connectivity is however not sufficient to explain the mechanisms behind the emergence of network oscillations, which are indeed influenced by several other factors including the typical channel constellation and biophysical properties of each neuronal type, the geometry in which their dendritic and axonal compartments are arranged within the tissue, and the conductivity of the extracellular space (Buzsaki et al., 2012). Nevertheless, despite their different ontogeny within the brain, we know today that all cortical and subcortical oscillations arise from the interplay between excitatory, modulatory and inhibitory inputs, a process being in turn majorly influenced by the intrinsic membrane oscillatory mechanisms of the recruited neurons. Thanks to these voltage fluctuations, neurons resonate (i.e. have a preferred frequency for maximal response) and oscillate at specific frequencies, which results in the presence of proper "excitability windows". Finally, the organization of specific cell ensembles into mesoscopic and macroscopic oscillatory frameworks by means of a wide variety of inhibitory neuron "clocking networks" (Buzsaki & Chrobak, 1995; Isaacson & Scanziani, 2011; Roux & Buzsaki, 2015) could serve as a mechanism to promote their concerted and optimally timed input/output conversion, a phenomenon known as *cell ensemble binding*. This phenomenon also guarantees that synchrony between neuronal ensembles is achieved also in absence of strong synaptic connections, provided that the phase of the oscillations is aligned. This theory is strengthened by the observation that, within the cycle of an oscillation, the sequence of inhibitory and excitatory spikes is conserved across behavioral states (Klausberger et al., 2003; Klausberger & Somogyi, 2008; Varga, Golshani, & Soltesz, 2012). Phase- and rate coding of excitatory and inhibitory neurons along the cycle may vary between frequency bands and brain regions, possibly depending on the anatomical connections that compose the microcircuit (English et al., 2017). Different classes of inhibitory neurons, whether local or long range projecting, are structurally and functionally tailored to gate and modulate synaptic integration or spike generation in a precisely timed fashion, during slow and/or fast oscillatory events. Of particular interest are long-range inhibitory projections (LRIPs), which have been described between multiple regions. By anatomically reducing distances between brain regions within the same network, these neurons may serve as potent actuators of associative processes by fast synchronization of distal oscillatory ensembles (Caputi, Melzer, Michael, & Monyer, 2013; Letzkus, Wolff, & Luthi, 2015; Melzer et al., 2012).

1.1.3 Relevance of mesoscopic neural oscillations for learning and memory

Since the development of EEG and following the technological advancements of intracranial recording techniques, numerous studies have investigated the causal relationship between

neural oscillations, the organization of neuronal firing within them, and the emergence of cognitive functions, in particular mnemonic processes. Mechanistically, neural oscillations may support crucial aspects of animal memory such as associative processes and stimulus persistence (for more details see chapter 1.2.3) by influencing various properties of local and global, cortical and subcortical circuits like synaptic plasticity and the E/I balance itself (Zhou & Yu, 2018).

Noteworthy, studies of neural oscillations in rodents and humans were performed in parallel. This has resulted in the lack of a congruent systematic definition of frequency bands between rodents and primates, which means the width and functional relevance of each frequency band is disputed among researchers. As a consequence, evidence supporting the contribution of each frequency band to learning and memory processes is sometimes contradictory and highly confounding, especially when trying to extrapolate and translate findings from one species to another. Additionally, the limited applicability of invasive recording techniques in humans introduced another degree of variability (de la Prida, 2019; Herweg, Solomon, & Kahana, 2020). One perfect example for this is the highly debated role of theta oscillations for human memory. As a matter of fact, the rodent theta band in the hippocampus (4-12 Hz; see chapter 1.2.3) encompasses both human theta (4-8 Hz) and alpha rhythms (8-12 Hz, originally the Berger rhythm). Human theta band spans the 4-8 Hz spectrum and occurs in very short bouts (similar to bats), in contrast to the continuous epochs of rodent theta. Further layers of complexity are introduced by, for example, the strong anatomical influence (i.e. location of the recording along the dorsoventral/anteroposterior axis of the hippocampus) on the prominent theta rhythmicity measured in both humans and rodents. Besides, human cognitive tasks dependent on the hippocampus are lateralized; in humans, right and left hemispheres process navigational information and episodic memories, respectively (de la Prida, 2019), a phenomenon partially observed in rodents too (Miller et al., 2018). Nevertheless, while it was at first difficult to identify a theta homologue in humans, it is now possible to reconcile the apparent discrepancies and confirm the role of human theta oscillations for the formation of episodic memories (de la Prida, 2019; Goyal et al., 2020; Herweg et al., 2020; Miller et al., 2018).

Ample evidence originating from observational, lesion, and manipulation studies in rodents and humans, indicates that both the MTL and the prefrontal cortex (PFC) are key regulators of distinct types (e.g. working, semantic and episodic memory) and stages of memory (e.g. encoding, consolidation and retrieval) (Eichenbaum, 2017a; Johnson et al., 2018). Oscillatory correlates of mnemonic processes are observed in three frequency bands in the MTL and PFC:

the theta band (4-12 Hz in rodents and 4-7 Hz in humans), the gamma band (30-80 Hz, slow gamma, and 90-140 Hz, fast gamma) and the so called ripples (ca. 150-200 Hz). However, not only the power of the single frequency bands, but also their co-occurrence within (*phase coupling*) and across (*phase synchronization*) brain regions have been thoroughly investigated as correlates of learning and memory processes (Lisman & Jensen, 2013; Nyhus & Curran, 2010). Interestingly, during memory encoding and retrieval, the PFC and the temporal lobe, specifically the hippocampus, become coupled via oscillatory synchrony, possibly thanks to the influence of thalamic inputs (Eichenbaum, 2017a).

In fact, theta and gamma oscillations and their phase-coupling are thought to not only participate in the encoding of object and context memories, but also to coordinate the communication between the brain structures involved in the process by promoting their oscillatory synchrony (Duzel, Penny, & Burgess, 2010). For example, it has been shown that the degree of theta-gamma coupling in humans (measured by a modulation index) positively correlates to successful item memorization during working memory tasks in the PFC (Alekseichuk, Diers, Paulus, & Antal, 2016). Applying transcranial alternating current stimulation (tACS) at continuous theta and repetitive gamma pulses on the PFC improves spatial working memory in humans (Alekseichuk, Diers, et al., 2016). Similarly, the degree of theta-gamma coupling increases in rats during the performance of context-item associations (Tort, Komorowski, Manns, Kopell, & Eichenbaum, 2009), and it was shown that the phase of hippocampal theta rhythm modulates locally emerging gamma oscillations in the PFC (Sirota et al., 2008). Furthermore, Rheinhart et al. (Reinhart & Nguyen, 2019) have demonstrated that age-related decline in working memory can be ameliorated by application of tACS at theta pulses, thereby restoring the lost synchronicity between the temporal and frontal cortices.

Oscillatory activity measured during different sleep stages, such as slow wave sleep and sleep spindles, is thought to also substantially contribute to memory consolidation (Binder et al., 2019). Interestingly, theta oscillations are strongly present during periods of “paradoxical sleep” (rapid eye movement, REM phase (Leung, 1984)). In cortical structures, states of high reactivity and unresponsiveness are represented by the dominance of faster and slower frequency bands in the EEG, respectively termed “UP” and “DOWN” states, and their interchange is believed to support memory formation and (Tukker et al., 2020). Finally, there is evidence in both humans and rodents that “ripples” play a role in memory consolidation and retrieval during periods of alert immobility and sleep (Colgin, 2016). Ripples are discrete fast oscillatory events that are presumed to originate in the hippocampus and broadcasted to the rest of the neocortex. During human and rodent ripples, the phenomenon known as “replay” occurs,

in which the sequential firing of cells in the MTL, occurring repeatedly during memory encoding, is replayed at a much faster scale during successful memory retrieval (Khodagholy, Gelinas, & Buzsaki, 2017; Vaz, Wittig, Inati, & Zaghloul, 2020). Similar to theta and gamma patterns, increased frequency of cortical and hippocampal ripples correlates to learning (Khodagholy et al., 2017).

In rodents and humans, the hippocampal formation is a preferred site for investigating oscillatory correlates of learning and memory. Therefore, the next section will focus on the functional anatomy supporting the emergence of its prominent oscillatory activity.

1.2 Functional anatomy of the rodent hippocampal system

In the mammalian brain, the hippocampal system supports two distinct higher cognitive functions: the formation of episodic and spatial memories and spatial navigation (Buzsaki & Moser, 2013). Episodic memories are associative memories that are immersed in a personal, subjective context in both space and time, and are often imbued with emotional salience. In contrast, the ability to orient and navigate in an environment relies on neuronal circuits and computations in which subjective, emotional salience does not necessarily play a role. It is therefore not surprising that extensive research has been conducted to decipher how the hippocampus supports these processes that appear to be very different at first glance. Historically, the relevance of the hippocampal system for processing emotionally salient information was demonstrated first, as the Papez circuit hypothesis appointed the hippocampus as the emotional center within the limbic system already in 1937 (Korotkova et al., 2018). Further independent studies in various species, the enlightening case of the patient H.M. in 1954, whose surgical removal of both hippocampi resulted in severe anterograde amnesia (Scoville & Milner, 2000), and the discovery of long term potentiation (LTP, (Andersen, Holmqvist, & Voorhoeve, 1966; R. Morris, 1984)) underscored the profound relevance of the hippocampal formation for the formation of long-term memories (R. G. Morris, Garrud, Rawlins, & O'Keefe, 1982; Squire & Wixted, 2011; Strange, Witter, Lein, & Moser, 2014; Zola-Morgan, Squire, & Amaral, 1986). Ultimately, upon the discovery of place cells, O Keefe et al (O'Keefe & Dostrovsky, 1971) proposed that the hippocampus functions as a “cognitive map” (a concept already introduced by Tolman in 1948), a model merging the gap between subjective experiences, salience and navigation. With the further description of spatially modulated cells in the hippocampal and parahippocampal areas (i.e. grid cells, border cells and head direction cells), the concept of the cognitive map gained further strength (Buzsaki &

Moser, 2013; Fyhn, Molden, Witter, Moser, & Moser, 2004; Hafting, Fyhn, Molden, Moser, & Moser, 2005).

Today, one of the prevailing theories is that hippocampal cells integrate converging emotional, spatial, and temporal information that are previously processed in parallel by upstream cortical and subcortical regions (Zemla & Basu, 2017). Even though physical objects, space, and time are encoded by distinct cortical and subcortical networks, as revealed for example by increase in power of different EEG bands upon the performance of a temporal or spatial memory task, these anatomically and functionally separate streams are unified in a contextual framework (in a space-time matrix) in the hippocampus (Eichenbaum, 2017b), where dedicated cell ensembles encode distinct features of an episode (Sasaki, Leutgeb, & Leutgeb, 2015). Indeed, the hippocampus is thought to not only form an invariant representation of an episode in which the unique identities and properties of its single elements are preserved, but, most importantly, also the spatial and temporal relations between objects and events in time (Moscovitch, Cabeza, Winocur, & Nadel, 2016). These two functions are supported by, on the one hand, the activity of spatially tuned cells in the hippocampal formation (place, grid, head-direction and border cells), and on the other by the so called "episodic cells" (also called "time cells"), which fire sequentially and independently from environmental stimuli (Zemla & Basu, 2017). According to this hypothesis, then, navigating through one's own memories ("mental time travel") would be analogous to actually navigating through a physical environment (Buzsaki & Moser, 2013); the strategies used for recalling subjective, episodic memories would correspond to an "egocentric" approach to navigation, while recalling semantic memory (concepts that are objectively shared by the social framework they exist in) would correspond to using an "allocentric" approach to navigation. Finally, further corroboration of the "cognitive map" hypothesis is provided by evidence that the hippocampus is required for the retrieval of memories in which the spatio-temporal component of the experience is highly relevant.

Numerous studies have investigated the strongly present "hippocampal electrical activity" of the LFP in relation to navigation in space (navigation) and time (memory). To better understand how the hippocampal system sustains the association of convergent information streams, and to what extent neural oscillations support this mechanism, it is important to describe its functional anatomy (i.e. the target regions of the relevant afferent and efferent axonal projections) in more detail. For the sake of time and space, I will focus on the hippocampal formation of the mouse.

1.2.1 Hippocampus proper and entorhinal cortices

The hippocampal system comprises several anatomically interconnected brain regions which are the relay station of primary sensory information arriving to somatosensory cortices, and of proprioceptive stimuli processed by subcortical and dedicated cortical regions (van Strien, Cappaert, & Witter, 2009).Traditionally, the predominant assumption is that medial and lateral entorhinal cortices within the hippocampal formation (MEC and LEC, respectively) convey two parallel streams of information to the hippocampus, as they both receive top-down information from different upstream cortical regions. Neural activity in the frontal, insular, piriform and temporal regions is believed to encode local landmarks that are present in the cognitive map (i.e. reference points, objects within a map), and to reach the lateral portions of the entorhinal cortices via the perirhinal cortices **(Fig.1.1, a)**. In dorsolateral portions of the LEC, in fact, cells encode not only physical properties of objects, but also the temporal aspects of object sequences within an experience (Doan, Lagartos-Donate, Nilssen, Ohara, & Witter, 2019). The other stream of information is thought to feed the hippocampus with global features of the environment (i.e. the spatial relations between the objects in a space) via parahippocampal regions, known as postrhinal regions in the rodent, which then project onto the medial entorhinal cortices; this information is preprocessed by parietal, occipital cingular and portions of the temporal cortices (Bird & Burgess, 2008; Julian, Keinath, Marchette, & Epstein, 2018) **(Fig.1.1, a)**. Dorsal portions of the hippocampus are strongly connected to the LEC and MEC, whereas ventral portions of the hippocampus are anatomically and functionally linked to brain regions that process affective and emotional stimuli like the amygdala, the lateral septum, and the hypothalamus (Strange et al., 2014). This strict separation between the lateral "what" and medial "where" (MEC) streams (Eichenbaum, Yonelinas, & Ranganath, 2007) has recently been questioned by newly discovered abundant anatomical connections between postrhinal cortices and LEC in rats (Doan et al., 2019). Besides, in the past years, increasing numbers of subdivisions in both the dorso-ventral and the septo-temporal axes within these pathways have emerged (Valero & de la Prida, 2018). However, basic connectivity principles can be described as follows.

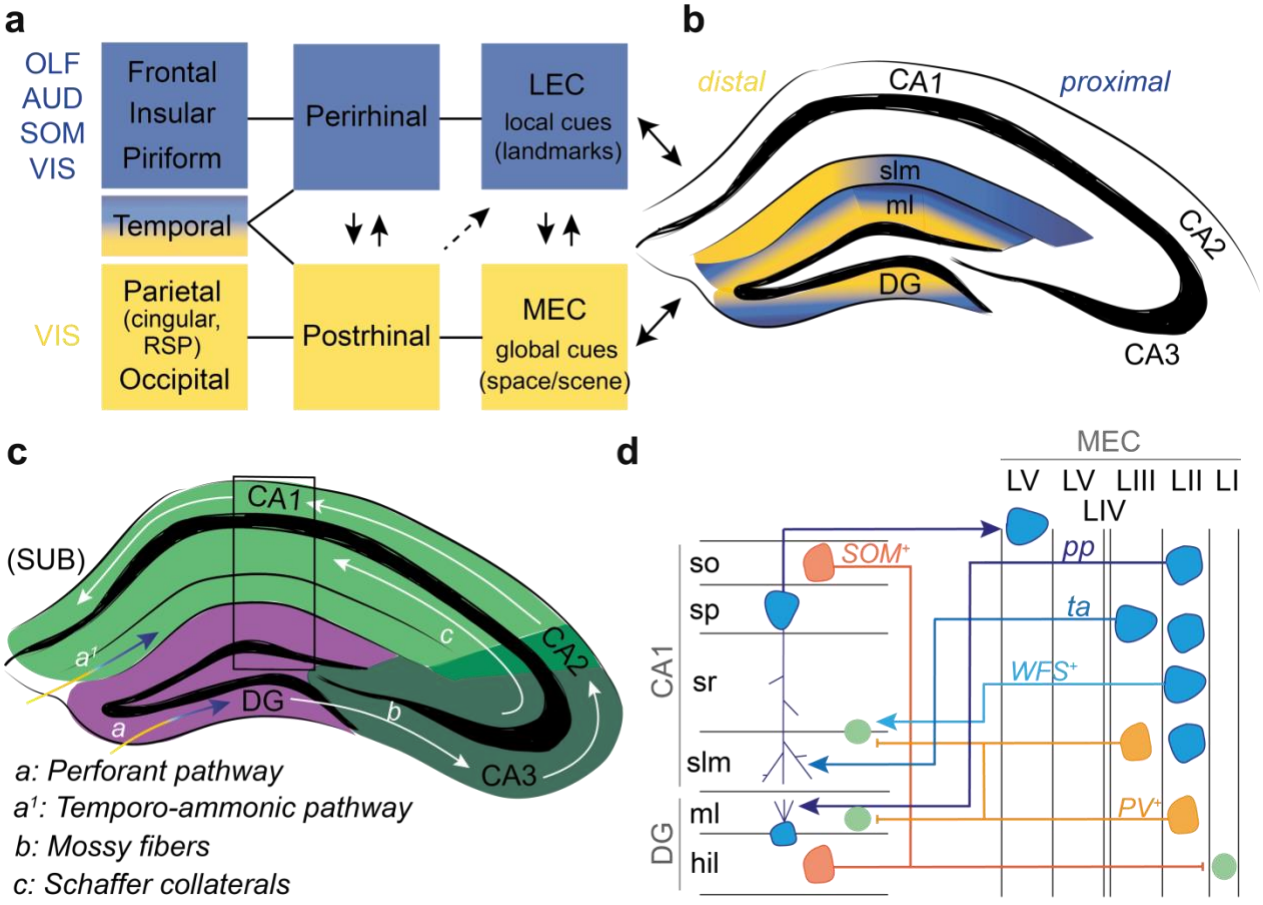

Figure 1.1 Cortical afferents into the dorsal hippocampus and hippocampal microcircuit. a) Two parallel streams of information are conveyed to the hippocampus from different cortical areas. The frontal, insular, piriform and part of the temporal cortices receive information from olfactory (OLF), auditory (AUD), tactile (SOM) and visual (VIS) cues and convey it to the hippocampus via perirhinal and lateral entorhinal cortices (LEC). Neurons in dorsal LEC encode information about local cues of an environment. In parallel, visual cues are strongly encoded in parietal cortices, in particular in cingular and retrosplenial cortices (RSP), and occipital cortices. This information is conveyed to the hippocampus via postrhinal cortices and medial entorhinal cortices (MEC). Neurons in the dorsal MEC are strongly spatially tuned, and they encode global information about the space or scene where the experience is taking place. Arrows indicate anatomical connectivity between the different regions, dashed lines represent a proven but less investigated connection. **b)** LEC and MEC monosynaptic projections to different compartments of the dentate gyrus (DG) and CA1. LEC projections (blue shading) occupy the first third of the molecular layer (ml) of DG, MEC axons occupy the second two thirds (yellow shading). In CA1, LEC projections occupy proximal portions of the *stratum lacunosum moleculare* (slm), MEC projections occupy distal portions of the SLM instead. **c)** Entorhinal projections to DG constitute the *perforant pathway (a)*, and those to CA1 form the *temporo-ammonic pathway (a')*. DG afferents to CA3 are termed *Mossy fibers (b)*, and those from CA3 to CA1 *Schaffer collaterals (c)*. CA1 pyramidal cells project to subicular neurons (SUB) and also send feedback to LEC and MEC. **d)** Reciprocal connectivity of excitatory and inhibitory neurons between CA1, DG and MEC is highly layer specific. Excitatory connections are indicated by blue arrows, inhibitory connections by red and orange arrows. **HPC→MEC:** pyramidal neurons in CA1 predominantly project to MEC layer 5 (LV). Somatostatin positive (SOM^+) inhibitory neurons in stratum oriens (SO) of CA1 and in the hilus (HIL) of DG project onto local inhibitory neurons (light green) in layer 1 (LI) of the MEC. **MEC→HPC**: the perforant pathway (*pp*) to DG-ML is constituted by axons of neurons residing in layer 2 (II), which target the dendritic compartment of DG granule cells. The temporo-ammonic pathway (*ta*) is formed by

axons of neurons in layer 3 (LIII), which target apical dendrites of pyramidal neurons in SLM. Wolframin1-syndrome-positive ($WFS1^+$) neurons in LII send projections to CA1-SLM, parallel to the *ta* pathway, where they target local inhibitory neurons. Similarly, parvalbumin-positive (PV^+) inhibitory neurons in LII-III project to local inhibitory neurons in CA1-SLM and DG-ML.

Within the hippocampo-entorhinal circuit, diverse cell types originating in layers II and III of the ECs project mono-and poly-synaptically to all compartments of the hippocampus proper **(Fig. 1.1 b)**. The hippocampus proper consists of four main compartments: the dentate gyrus (DG), the *cornu ammonis* area 3 (CA3), CA2, CA1 and the subiculum **(Fig.1.1 c;** (Witter, Wouterlood, Naber, & Van Haeften, 2000). The excitatory polysynaptic loop that converges at first into the molecular layer of the DG (first synapse), whose granule cells then send a monosynaptic input into pyramidal cells of CA3 via the *Mossy fibers* (second synapse), is the *perforant pathway,* and its axons are supposedly those of the so called "ocean cells" in EC layer II. The third synapse in the circuit, which is indeed called the "*tri-synaptic loop*", is formed by pre synaptic input of pyramidal CA3 onto inhibitory and excitatory neurons in CA2 and CA1 via the *Schaffer collaterals* (Witter et al., 2000).

Monosynaptic connections from medial entorhinal cortex (MEC) onto CA3 and CA1 have also been extensively described. The parallel stream of information that reaches CA1 from MEC layers II and III constitutes the *temporo-ammonic pathway*, and it is considered a subdivision of the *perforant pathway*. Researchers have focused on the excitatory component of this pathway **(Fig.1.1 c)**. However, a recent study revived the interest into the long range inhibitory projections (LRIPs) originating in layers II and III of the MEC, targeting local interneurons in the CA1 area (Basu et al., 2016; Melzer et al., 2012). The same interneurons are targeted by excitatory "island cells" of EC layer II, which are positive for the marker Wolframin syndrome 1 (*$WFS1^+$*, **Fig.1.1 d** (Kitamura et al., 2015)**)**. Efferent axonal projections from the hippocampus proper onto the EC are both excitatory and inhibitory. A major output is formed by subicular pyramidal cells, which receive input from CA1 pyramidal cells. CA1 pyramidal cells also send axonal projections independently to layers V and VI of both ECs. A less studied output, which was only recently discovered, is formed by LRIPs residing in DG and CA1. These projections, differently than those of excitatory cells, reach superficial layers of the ECs (layers I and II) (Melzer et al., 2012). A molecular characterization of the respective pathways has revealed that the majority of MEC→HPC LRIPs is parvalbumin (*PV*) positive, while the majority of HPC→MEC LRIPs is somatostatin (*SOM*) positive. These populations share however an important role; they mediate disinhibition in both their target areas by forming functional synapses with local inhibitory neurons.

Excitatory cells within the MEC are characterized by three principal molecular markers in distinct combinations: reelin (*RE*), calbindin (*CB*) and *WFS1*$^{+}$. Morphologically, these cells are defined as "stellate cells", pyramidal cells, intermediate pyramidal and intermediate stellate cells (Fuchs et al., 2016) these cells express the aforementioned molecular markers in a variable extent. In particular, the pyramidal cells forming MECII islands are *CB*$^{+}$ and *WFS1*$^{+}$. These islands have a homologue in the human MEC, whose surface was initially described as presenting some "bumps", scientifically termed "verrucae" (Augustinack et al., 2012). Island cells are "immersed" in the more represented population of stellate cells, which are therefore termed by some researchers "Ocean cells" (Kitamura et al., 2015). It has been postulated that the projections from the Ocean cells form the perforant pathway to DG-CA3.

Crucially, the hippocampal formation also receives abundant monosynaptic input from subcortical GABAergic, glutamatergic and cholinergic neurons from the septal nuclei (lateral and medial septum) in the forebrain, and to a lesser degree from the dopaminergic neurons in the VTA and locus coeruleus, located in the midbrain and hindbrain, respectively (O'Mara & Aggleton, 2019). GABAergic and cholinergic input from the medial septum (MS) is crucial for the generation of hippocampal oscillatory activity, as will be described in the following section.

The multitude of afferent projections into the hippocampus proper is anatomically segregated within its structures. Indeed, axonal projections originating from different source regions target specific sets of synapses along the dorso-ventral axis of the dendritic tree of pyramidal cells in the CA compartments, granule cells in the DG, and local inhibitory neurons, thus forming well-defined information streams. This, in turn, results in the generation of ionic movements at different synaptic compartments along the neuronal somata upon activation of different pathways. Input segregation is also made possible by the geometrical arrangement of excitatory pyramidal neurons in the CA3, CA2 and CA1 areas, which are arranged in a laminar way along the antero-posterior axis of the dorsal and ventral hippocampus. The cell bodies of pyramidal neurons form a single, highly compact layer (*stratum pyramidale,* SP), while their dendrites are disposed in a parallel fashion both above (basal dendrites) and beyond (apical dendrites) the SP. Spiny basal dendrites extend within the *stratum oriens* (SO) and apical dendrites extend in the *stratum radiatum* (SR). At the bottom of the apical dendrites, distal dendrites branch out in the *stratum lacunosum moleculare* (SLM). Pyramidal cell dendrites hence populate and define layers characterized by the absence of excitatory neurons, which can be further subdivided according to the origin of their pre-synaptic inputs. Indeed, the majority of input from the MS forms synapses in SO and SR, while inputs from the EC form synapses in the SLM.

Whether intermingled in the pyramidal layer, or distributed within SO and SR, or located at the border between SR and SLM, a plethora of inhibitory neuron types is displayed in the hippocampus proper (Freund & Buzsaki, 1996; Kullmann, 2011; Nilsson, 2018; Pelkey et al., 2017). Interestingly, the function of distinct inhibitory neuron classes can be partially inferred by their widely diversified morphology and anatomical localization. Similar local inhibitory neurons are present in both ECs.

1.2.2 Local and long-range inhibitory neurons

In the early days of neuroscience, as Santiago Ramón y Cajal and Camillo Golgi were investigating neural tissue, inhibitory neurons were broadly categorized as "non pyramidal" cells, and little was known about their function or relevance. Further investigations lead to the definition of inhibitory neurons as cells that possess short axons that form local "symmetric" synapses onto excitatory neurons and are positive for the neurotransmitter gamma-ammino-butyrric acid (GABA). Today, however, we know that this classification is misleading and simplistic.

Already in 1934, Lorene de Nò elucidated the morphological diversity in hippocampal "non pyramidal" cells and attempted to predict their function based on their dendritic and axonal arborization (Freund & Buzsaki, 1996). Freund and Buzsaki (Freund & Buzsaki, 1996) published a seminal review on the matter, identifying at least 20 types of inhibitory neurons based on their morphology and immunohistochemical reactivity to calcium binding proteins or neuropeptides. Specifically, the authors made a clear distinction between local inhibitory neurons targeting dendrites of principal cells, which can inhibit specific pathways onto hippocampal pyramidal cells, those innervating their somas or axons (perisomatic inhibition or axo-axonic inhibition), which strongly inhibit cell firing, and local inhibitory neurons specialized in targeting other inhibitory cells, hence promoting disinhibition. Today we know that inhibitory neurons constitute approximately 11% of the whole hippocampal cell population (Pelkey et al., 2017). However, not only their total numbers (i.e. the percentage of a specific inhibitory neuron type compared to another), but also their relative distribution among hippocampal compartments and layer is highly diverse. For example, SOM^+ inhibitory neurons are densely present in the SO of all CA compartments and in the hilus of the DG, whereas PV^+ inhibitory neurons are highly prevalent in SP of all CA compartments and the GCL of the DG. Another distinctive characteristic is the presence of dendritic spines on SOM^+ interneurons located in SO. These are referred to as "O-LM" interneurons, as their axons extends to the SLM, and their dendrites extend horizontally and are rich in spines that receive inhibitory, excitatory,

and neuromodulatory inputs. Instead, the dendrites of PV^+ "basket cells", "bistratified", and "axo-axonic" interneuronal types are typically aspiny (they lack dendritic spines); interestingly, their inhibitory tone is enhanced compared to that of O-LM interneurons (Maccaferri, Roberts, Szucs, Cottingham, & Somogyi, 2000). By providing strong perisomatic inhibition to pyramidal cells, PV^+ interneurons are potent regulators of spike timing of excitatory and inhibitory cells (Freund & Katona, 2007). Furthermore, one single PV^+ neuron connects to approximately 1500 other pyramidal cells (Buhl, Halasy, & Somogyi, 1994), and also forms electrical synapses with other PV^+ interneurons (Galarreta & Hestrin, 2002), hence amplifying the effect of one single action potential.

Subsequent studies elucidated how local inhibitory neurons are further distinguished by their embryological origin and intrinsic electrophysiological features. Most importantly, it was revealed that inhibitory neurons can be distinguished by their task- and time- dependent firing (Klausberger et al., 2003; Klausberger & Somogyi, 2008; Somogyi & Klausberger, 2005). In particular, it is possible to correlate the firing rate of distinct classes of inhibitory neurons to distinct phases of oscillatory activity in the extracellular field, in both anesthetized and awake behaving rodents (Klausberger & Somogyi, 2008). Therefore, local inhibitory neurons are thought to provide a spatio-temporal framework of innervation to pyramidal cells in the hippocampus, inhibiting different domains along their cell bodies and thus a) controlling the timing of their input integration, and b) guaranteeing maximal pyramidal cell excitability at recurring time windows over the course of an oscillation (Roux & Buzsaki, 2015). An instructive example is provided by the phase-dependent firing of three major inhibitory neuron classes in the CA1 area: the PV^+ "basket cells" (PVBCs), innervating the perisomatic region of pyramidal cells (somata and proximal dendrites), and the SOM^+ "O-LM" interneurons, which target the apical dendrites of pyramidal cells and inhibit dendritic integration of EC inputs. PVBCs fire preferentially on the peak and descending phase of theta oscillations (recorded from the pyramidal layer) which corresponds in fact to the point in time when pyramidal cells fire with the lowest probability, hence the "source", or peak, of the LFP. In contrast, O-LM interneurons fire preferentially at the descending phase/trough of a pyramidal theta phase oscillation (Klausberger & Somogyi, 2008). In fact, O-LM interneurons silence EC inputs at the time when pyramidal cell firing is the highest (during the "sink" of the LFP caused by depolarization of neurons), which results in the enhancement -of CA3 and MS inputs in the CA1-SO (M. Lovett-Barron et al., 2014). Besides, PVBCs and not O-LM interneurons are recruited during ripple oscillations (Klausberger & Somogyi, 2008). Finally, another class of cells positive for the molecular marker cholecystochinine (*CCK*) is located at the border

between SR and SLM, and is therefore termed “perforant path associated”; these interneurons discharge typically at the peak of theta oscillations, hence when pyramidal cells are mostly inhibited, but are silent during ripple events (Klausberger et al., 2003). This class of neurons promotes depolarization induced suppression of inhibition in pyramidal cells (Dudman, Tsay, & Siegelbaum, 2007), and is the target of PV^+ LRIPs originating from the MEC. Local microcircuit computations would therefore result in the disinhibition of pyramidal cells upon CCK^+ neuron firing, which is consistent with their phase preference (Klausberger & Somogyi, 2008). Indeed, next to inhibitory neurons whose axons do not abandon the compartment where their soma is located (typical interneurons) some of them also send collaterals to distal brain areas, sometimes spanning millimeters in distance. In addition to establishing reciprocal LRIPs between each other, LRIPs originating in both dorsal hippocampus and the superficial layers of MEC establish functional synapses with neurons in extra-hippocampal regions like the striatum, the MS, the fimbria and the diagonal band (Caputi et al., 2013; Melzer et al., 2012)

The relevance of inhibitory neurons for cognitive functions such as learning and memory is nowadays widely accepted. In the prefrontal cortex and hippocampus, for example, PV^+ interneurons are key regulators of working and spatial (Murray et al., 2011; Ognjanovski et al., 2017; Xia et al., 2017), and inactivation of SOM^+ O-LM interneurons in dorsal CA1 has resulted in the impaired recollection of fear memory (M. Lovett-Barron et al., 2014; Schmid et al., 2016). The supporting role of inhibitory neurons for memory is tightly linked to their role in the generation and maintenance of oscillatory activity. Hence, I will briefly describe how oscillatory activity in the hippocampus supports cognitive functions, and what the role of inhibitory neurons in this context.

1.2.3 Hippocampal oscillations and their relation to episodic memory

As briefly mentioned in chapter 1.2.1, the geometrical arrangement and organization of cell bodies within the hippocampus and its richness in highly spatially segregated input/output streams result in the prominent rhythmicity of its extracellular field (Buzsaki et al., 2013; Stark et al., 2013). The question as to whether and how oscillatory patterns may promote learning and memory mechanism within this region has been addressed by an extensive number of studies, seeking to link synaptic mechanisms to global micro- and macro-circuit phenomena.

Theta oscillations

Theta rhythmicity (4-12 Hz) in the dorsal hippocampus is present in immobile awake alertness states, during REM sleep, and during exploration or voluntary locomotion (Buzsaki, 2002, 2005; Colgin, 2016). Historically, it was thought that rhythmically bursting cholinergic

afferents from the MS are the sole responsible for theta generation in the hippocampus. Initially, in fact, studies were performed in immobile or urethane-anesthetized animals, and it was found that application of the cholinergic blocker atropine lead to complete abolishment of theta oscillations (Kramis, Vanderwolf, & Bland, 1975). However, later investigations of theta rhythmogenesis in moving animals revealed more complex underlying mechanisms behind its generation, as application of atropine was not sufficient to abolish the rhythm (Buzsaki, Czopf, Kondakor, & Kellenyi, 1986; Kramis et al., 1975). Today, the most supported view is that the frequency of theta oscillations in the dorsal hippocampus of behaving rodents is predominantly entrained by rhythmic inhibitory bursts onto local GABAergic neurons by medial septal neurons that fire at a high rhythmicity (Freund & Antal, 1988; Joshi, Salib, Viney, Dupret, & Somogyi, 2017; Unal et al., 2018; Unal, Joshi, Viney, Kis, & Somogyi, 2015). Long-range projecting inhibitory neurons from the MS have not only temporally staggered firing properties, but they also promote disinhibition of distinct compartments of pyramidal cells (i.e. distal dendrites or perisomatic regions), thus "constricting" the maximum excitability window of hippocampal neurons at precise phases of the theta cycle (Melzer et al., 2017). GABAergic, cholinergic and glutamatergic neurons in the MS, in turn, integrate converging inputs from various subcortical nuclei like the thalamus and supramammillary nucleus ((Buzsaki, 2002); **Fig.1.2)**. Nevertheless, MS cooling (Petersen & Buzsaki, 2020) or blockade by pharmacological agents in awake animals results in only partial disruption of theta rhythm in CA1 (Bolding, Ferbinteanu, Fox, & Muller, 2020; Koenig, Linder, Leutgeb, & Leutgeb, 2011). Furthermore, hippocampal preparations devoid of distal inputs are able to generate intrinsic oscillations in this range (Amilhon et al., 2015). This is possibly driven by so called "internal rhythm generators", like the CA3 afferents (Lopez-Madrona et al., 2020), and also by intrinsic oscillatory properties of local CA1 inhibitory neurons, especially PVBCs. In CA1, PVBCs support theta rhythmicity by theta-paced release of GABA at fast frequencies (in the gamma range), thus generating regularly timed IPSPs in both other inhibitory neurons and pyramidal cells (Gulyas et al., 2010), and subsequent release of inhibition results in post-inhibitory rebound spiking of pyramidal neurons. While theta frequency shows a positive correlation with GABAergic function, theta amplitude has been shown to positively correlate with septal glutamatergic function in behaving animals (Fuhrmann et al., 2015). Aside the MS and the internal rhythm generators, the strongest contributors to theta oscillation amplitude are the excitatory inputs from the EC **(Fig.1.2)** (Z. Gu, Alexander, Dudek, & Yakel, 2017; Z. Gu & Yakel, 2017). The relevance of the EC inputs is reflected by how theta oscillations change across the CA1 compartment. Here, the SO displays the smallest theta oscillatory amplitude

and SLM the highest. Additionally, theta phase shifts gradually towards the left compared to superficial layers (i.e. the trough of the oscillation's cycle in SP corresponds to the peak of the cycle in SLM (Buzsaki, 2002)). The phase/amplitude shift across layers is partially explained by the existence of two current generators (MS and EC): upon septal activation, the IPSPs produced by the perisomatic region of pyramidal cells (in *stratum pyramidale*, SP) are paralleled by EPSPs produced at the distal dendrites that occurs when perforant path EC inputs are firing, therefore causing the peak of the oscillation at the SP to align with the trough of the oscillation at the SLM (Buzsaki, 2002; Deshmukh, Yoganarasimha, Voicu, & Knierim, 2010; Mizuseki, Sirota, Pastalkova, & Buzsaki, 2009). Besides, EC afferents in SLM are strong current generators, as they activate a high number of synapses simultaneously (Buzsaki, 2002). Moreover, the SLM exhibits a larger proportion of perforated synapses, which tend to express high density of AMPA receptors, indicative of strong synaptic currents (Bragin, Jando, Nadasdy, van Landeghem, & Buzsaki, 1995; Buzsaki et al., 1986; Sheremet et al., 2019), hence amplifying the amplitude of the theta oscillation recorded at this site.

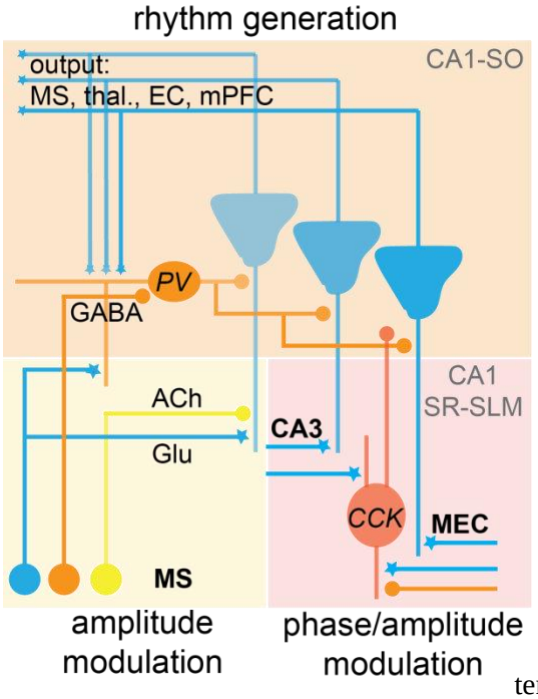

Figure 1.2 Theta generation in CA1. Theta rhythmicity in CA1 is generated by rhythmic disinhibition of pyramidal neurons, which emerges as the result of rhythmic inhibition of local PV^+ interneurons by long-range projecting medial septal (MS) PV^+ inhibitory neurons (GABA secreting). Local and distal feedback connectivity between CA1 and "rhythm generator" regions like the MS, thalamus and EC sustains the oscillatory activity. Theta amplitude is influenced by MS-cholinergic (Ach) and glutamatergic (Glu) afferents, and by glutamatergic MEC and CA3 afferents in SR and SLM. Input-timing of CA3 and MEC afferents at pyramidal apical dendrites and onto local cholecystochynin-positive interneurons (*CCK*) influences the phase of the oscillation. Note that the role of MEC-LRIPs in theta rhythm/amplitude and phase modulation is not yet investigated. Star shaped terminations indicate excitatory synapses, circles indicate inhibitory (GABA, in orange), and neuromodulatory synapses (Ach).

The theta range can be divided into type I theta (8-12 Hz) and type II theta (4-7 Hz), which correlate, respectively, with locomotor activity and other brain states, especially anxiety related (Korotkova et al., 2018). The frequency and amplitude of type I theta are positively correlated to the animal's running speed; hundreds of milliseconds before locomotion onset, amplitude of theta oscillations increases in the hippocampus, and theta activity persists as long as movement is sustained (Bender et al., 2015; Fuhrmann et al., 2015; Green & Arduini, 1954; Vanderwolf,

1969) **(Fig. 1.3)**. Additionally, frequency and power of theta oscillations are positively correlated to running speed (Bender et al., 2015; Cayzac et al., 2015; Fuhrmann et al., 2015; McFarland, Teitelbaum, & Hedges, 1975; Richard et al., 2013). These observations lead researchers to believe that theta oscillations represent the "online state" of the hippocampus (Buzsaki, 2002), and they suggest that theta plays a key role in adjusting hippocampal firing to the pace of external stimuli, with the intent of forming a first memory trace (Itskov, Pastalkova, Mizuseki, Buzsaki, & Harris, 2008; Pastalkova, Itskov, Amarasingham, & Buzsaki, 2008). This hypothesis is corroborated by the fact that firing rate of pyramidal cells and certain classes of inhibitory neurons is positively correlated to theta rhythm, although cells that are putatively linked to memory processing fire faster than the underlying field oscillation (Pastalkova et al., 2008; Petersen & Buzsaki, 2020). Interestingly, stimulation of PV^+ long range inhibitory neurons of the septum resulted in entrainment of hippocampal theta, but not in increase in locomotor activity (Bender et al., 2015). In contrast, stimulation of glutamatergic projections in the septum was sufficient to initiate frequency dependent running (Fuhrmann et al., 2015). Cholinergic septal neurons are instead thought to enhance theta oscillations in the hippocampus by negatively modulating peri-theta frequency bands in freely behaving animals (Vandecasteele et al., 2014).

A mechanistic insight of how hippocampal theta oscillations could directly influence spatial orientation, exploration, and memory of a previously encoded context was first provided by John O' Keefe at (O'Keefe, 1976; O'Keefe & Dostrovsky, 1971). Hippocampal "place cells" are cells whose firing fields are centered at a particular location in an arena. These cells not only fire rhythmically at various theta frequencies (rate coding), but their firing with respect to the phase of the field oscillation is modulated by time and experience (phase coding) (Huxter, Burgess, & O'Keefe, 2003). Shift of action potential firing of place cells along the theta cycle is a phenomenon known as "theta phase precession", and it consists in the shift of action potential bursts of place cell sequences to earlier phases of the theta cycle as the animal is crossing the place cells' firing field. Remarkably, initial place cell burst firing occurs near the peak of the theta oscillations measured in *stratum pyramidale*, thus when the global population of pyramidal cells is inhibited (O'Keefe & Recce, 1993). As the animal crosses the place field of the neurons, and as theta oscillations are sustained by running speed, the burst firing of place cells occurs at the trough of the theta cycle. This in fact corresponds to a) the time when inhibition is the least along the theta cycle, and b) the point in time when firing of adjacent place cells is minimal. In fact, within one theta cycle, various place cells fire at relatively lower or higher rates, according to the position of the animal in the arena. It has been postulated that

theta phase precession of place cells within a sequence promotes synaptic plasticity such as rate coding- and spike-timing dependent plasticity (STDP) between place cells that have partially overlapping place fields (Melamed, Gerstner, Maass, Tsodyks, & Markram, 2004), thus enabling subsequent memory retrieval. Remarkably, place cell sequences are replayed at faster speed "offline" during sleep within ripple events, and also during awake immobility (Drieu, Todorova, & Zugaro, 2018), and theta phase precession may promote the generation of these sequences, or ensembles, that occur in absence of the contextual stimulus. Interestingly, abolishing these "fast" theta-dependent sequences, while preserving slower, stimulus-driven place cell sequences that appeared while rats were passively being transported along a track resulted in impaired memory consolidation (Drieu et al., 2018). It was also recently shown that cooling off the medial septum, an approach that guarantees gradual slowing down of neural activity in absence of lesion, causes not only reduction of frequency and power of theta oscillations, but also results in place cell sequences within one cycle to fire at larger time intervals (Petersen & Buzsaki, 2020). This was correlated with increased number of errors in a spatial memory task, indicating that the medial septum sustains theta phase coordination of cell assemblies in the hippocampus and therefore supports learning and memory processes (Mitchell, Rawlins, Steward, & Olton, 1982; Petersen & Buzsaki, 2020).

Another key mechanism that is possibly dependent on theta oscillations is a form of plasticity peculiar to the hippocampal circuit, named input timing dependent plasticity (ITDP). According to this rule, excitatory post synaptic potentials of pyramidal cells in CA1 are potentiated when inputs from the MEC (via the performant pathway) and from CA3 (via the Schaffer collaterals) trigger synaptic activation at their basal dendrites at exactly 20ms distance from each other (Basu et al., 2013; Basu et al., 2016; Dudman et al., 2007). Interestingly, this time interval corresponds to the delay at which the temporo-ammonic and performant pathway action potentials arrive at the CA1 dendrites, and it also corresponds to the theta-coupled increase in slow and mid gamma along the theta phase (Schomburg et al., 2014; Shim, Philippides, Staras, & Husbands, 2016) This type of heterosynaptic plasticity requires precisely timed disinhibition of local CCK^+ inhibitory neurons in CA1, and this is provided by LRIPs from the EC (Basu et al., 2016). Timing of this input may rely on strictly regulating the window for post-synaptic potential integration in both source and target area, a phenomenon which is possibly dependent on theta and theta-gamma modulation, but this has not been proven yet. The presence of ITDP, and the necessity for an extremely precise disinhibition window, integrates well in the theory proposed by Hasselmo et al. (Hasselmo, 2005b), according to which consolidation and retrieval of hippocampal memories occur during the same theta cycle, but at different times within it

(theta phase separation theory). In fact, they propose that encoding takes place when GABAergic inhibition is at its maximum in the CA3 region, while, simultaneously, input from the entorhinal cortex is able to excite CA1 pyramidal cells. Retrieval of previously encoded information is possible when the recurrent networks within the CA3 are disinhibited in the following phase of the theta cycle. During memory retrieval, the CA1 area then serves as a "mismatch detector" between information that is currently being broadcasted by the entorhinal streams, and information that was previously encoded and is stored in the CA3 recurrent networks (Hasselmo, 2005a, 2005b; Hasselmo & Eichenbaum, 2005).

To summarize, theta oscillations are the result of the complex interplay between local and global rhythm generators. Most importantly, they reflect the synchronization between internally generated neural activity that possibly supports memory storage and retrieval, and the stream of neural activity that supports encoding of external stimuli occurring when the animal is actively exploring (Lopez-Madrona et al., 2020). The correlation of theta oscillatory activity with cognitive processes is paralleled by growing evidence about the synaptic and cellular mechanisms that may support these functions. Next to theta oscillations, gamma oscillations are thought to contribute to overlapping and specific cognitive functions.

Gamma oscillations

Oscillations in the hippocampal gamma frequency band are divided into sub-bands. Typically, Gamma oscillations are divided into slow gamma (30-60 Hz), mid gamma (60 or 80/90 Hz) and fast gamma (90-120/130 Hz). This indeed reflects the high heterogeneity behind gamma rhythmogenesis in the hippocampus (Colgin, 2016). Regardless of the particular sub-band, gamma oscillations are tightly linked to the function of inhibitory neurons and to the interplay between excitatory and inhibitory neurons (Belluscio, Mizuseki, Schmidt, Kempter, & Buzsaki, 2012; Buzsaki & Watson, 2012; Colgin, 2016; Lasztoczi & Klausberger, 2014) and, generally, gamma oscillations in the LFP reflect increased spiking in the network (Roux & Buzsaki, 2015). In SP, gamma oscillations are predominantly the product of reciprocal perisomatic inhibition provided by PVBCs, and their inhibition onto pyramidal cells (Butler, Mendonca, Robinson, & Paulsen, 2016; Schomburg et al., 2014). In SR, gamma oscillations are thought to be generated by CA3-driven feedforward inhibition (Fernandez-Ruiz et al., 2017). Finally, in SLM, gamma oscillations are thought to reflect synaptic activity that occurs in response to distal input provided by the entorhinal cortex, where local inhibitory mechanisms give rise to gamma oscillations (Fernandez-Ruiz et al., 2017; Mizuseki et al., 2009).

It is hypothesized that simultaneously active neurons within one gamma cycle constitute one transient ensemble, hence the postulated relevance of gamma oscillations in local network computations (Buzsaki, 2010; Buzsaki & Watson, 2012; Lisman & Jensen, 2013). Furthermore, by forming spiking neuronal ensembles that are segregated into distinct gamma sub-bands, the receiving neurons at the post-synaptic sites will preferentially tune in to one of the multiple input streams according to their preferred excitability states, thus making gamma oscillations a way for coupling distal networks in a dynamic and flexible way (Akam & Kullmann, 2014; Roux & Buzsaki, 2015). Nonetheless, gamma oscillations are shorter lived compared to slower scale oscillations like theta oscillations. For this reason, gamma coherency between distal regions is hard to achieve unless a short axonal connection is present between input and output regions. Therefore, theta oscillations are thought to be the underlying rhythm in support of long-distance transmission of gamma-modulated neural ensemble activity. Indeed, gamma oscillations emerge when there is high energy in the circuit, once neurons have begun to oscillate at theta frequencies, a phenomenon known as theta-gamma phase-amplitude coupling (Tort, Komorowski, Eichenbaum, & Kopell, 2010; Tort et al., 2009)

Theta-gamma coupling

Amplitude and frequency of gamma oscillations are modulated by the underlying phase of theta (**Fig.1.3**). Theta-gamma coupling is highest in SR and SLM when rodents are travelling at a velocity higher than 3 cm per second (Sheremet et al., 2019), and the degree of modulation is dependent on speed. The EC is thought to be responsible for the generation of mid and fast gamma oscillations in the CA1-SLM (Fernandez-Ruiz et al., 2017; Mizuseki et al., 2009). In turn, slow gamma rhythms show the highest coherence between CA3 and CA1-SR (Fernandez-Ruiz et al., 2017). Furthermore, there is evidence that theta-gamma coupling in SP is mediated by PV^+ interneurons in the hippocampus (Wulff et al., 2009).

Functionally, coupling of mid and fast gamma oscillations onto hippocampal theta is thought to support integration of sensory stimuli via MEC input, a crucial step in the process of memory encoding, although strong evidence for this hypothesis is still lacking (Colgin, 2015). Furthermore, the degree of theta-gamma coupling was shown to correlate with correct choices in a working memory task in humans, and to be less pronounced in subjects with AD and MCI (Goodman et al., 2018). In the CA3 area of rats, coupling of theta and slow gamma increased linearly with the learning of context-items association (Tort et al., 2009). Finally, it has been shown that place cells sequences in the hippocampus, in the CA3 area, can perform prospective coding of future locations (Bieri, Bobbitt, & Colgin, 2014; Pfeiffer & Foster, 2013), which may

serve as a decision making mechanism. This process has also been linked to theta-gamma coupling, as place cells sequences would switch between current and future locations within the theta cycle, in a gamma-frequency band dependent way (Amemiya & Redish, 2018). Whichever the role of entorhinal-driven fast gamma oscillations, their phase-locking onto underlying theta oscillations has been appointed as an important mechanism behind memory processing in the hippocampo-entorhinal circuit (Canolty & Knight, 2010; Colgin, 2015; Lisman & Jensen, 2013).

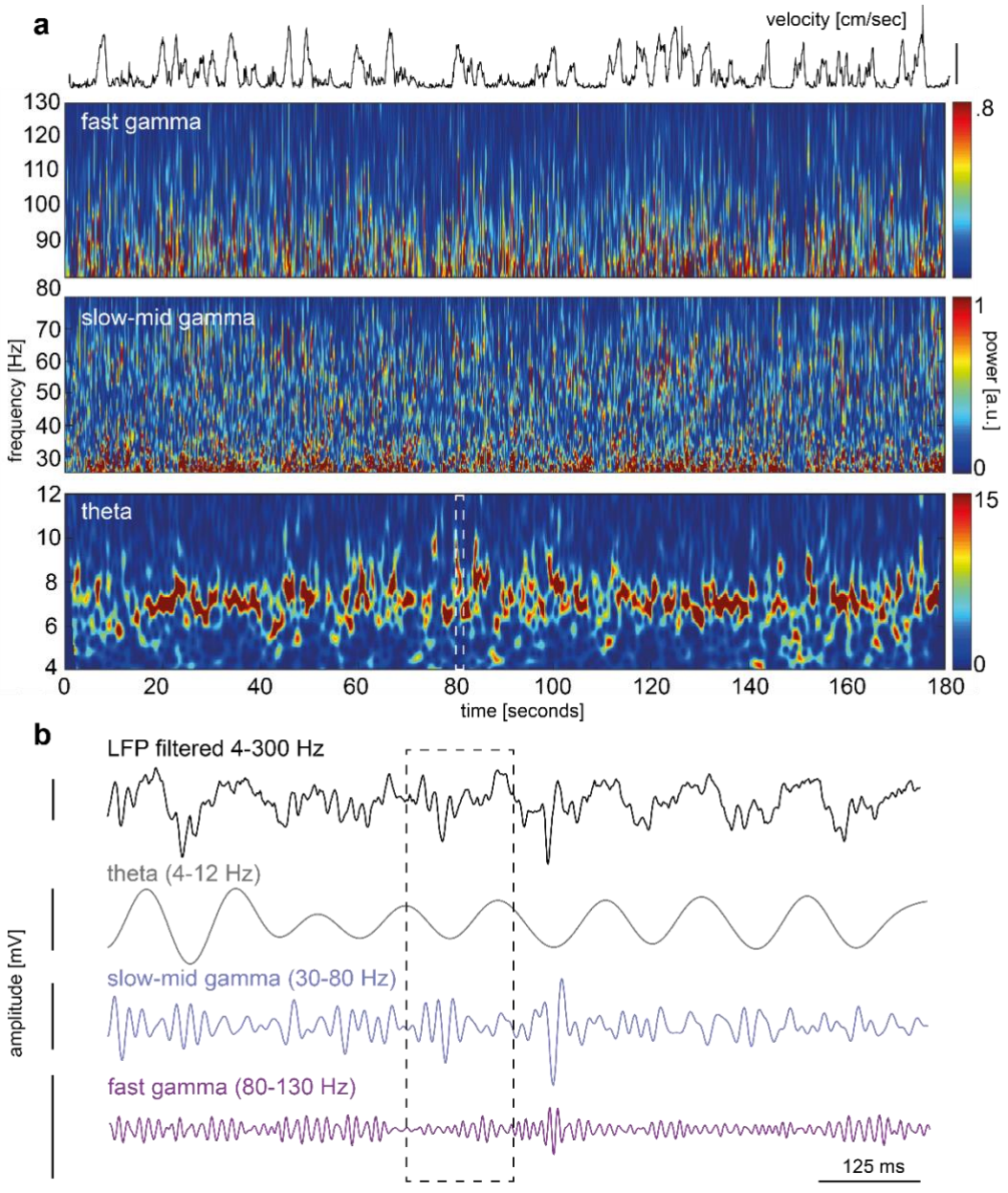

Figure 1.3 Exemplary recording of hippocampal local field potentials during active exploration in CA1-SLM. a) Velocity trace of the mouse. Scale bar: 20 cm/sec. b) Spectrograms showing power (amplitude) of the fast gamma (80-130 Hz), slow-mid gamma (30-80 Hz) and theta (4-12 Hz) range over the course of the exploration. Note that intervals of movement (high velocity) correspond to intervals of increased power in the theta and gamma range. Dashed box corresponds to the epoch of the recording shown in **b)** Local field potential (LFP) trace (1 second) bandpass filtered at different

frequencies. Note that the phase of theta oscillations modulates the amplitude of slow-mid and fast gamma (dashed box); at the trough of the theta cycle, gamma amplitude is highest. Left scale bar: 0.5 mV.

Ripples

Ripples are discrete oscillatory events occurring in the range of 100 to 250 Hz (Buzsaki, 2015; Ylinen et al., 1995). In the hippocampus, ripples are most evident in SP, and are concurrent with a characteristic deflection in the LFP of the SR termed sharp wave (SW). Hence, ripples are often investigated as SWR complexes. The occurrence of ripples is associated to sleep spindles in the cortex. It has also been observed that hippocampal and cortical ripples are correlated (Khodagholy et al., 2017). Ripples are thought to be a mechanism with which neurons in the hippocampus transfer consolidated information to neurons in the cortex at moments of quiet wakefulness or slow wave sleep (in so called "offline states"). During a ripple, the activity of place cells active in sequence is repeated at faster speed (compressed information) (Buzsaki, 2015). Forward replay refers to the replay of the sequence in the order that it previously occurred as the animal crossed a linear track; inverted replay happens when this sequence is repeated in an inverse order with respect to the experience (Diba & Buzsaki, 2007).

1.3 Alzheimer's disease

Alzheimer's disease, today's most common form of dementia, is nowadays considered a "synaptopathy" – a disease that is characterized by synaptic dysfunction (Palop & Mucke, 2010; Selkoe, 2002) – together with other neurodegenerative and neurodevelopmental disorders such as schizophrenia and autism (Lepeta_2016). Indeed, the growing focus on the synaptic compartment in disease conditions only reflects the paradigm shift that research on neuropsychiatric disorders has undergone in the past decade. Diseases that were previously thought to be caused solely by the selective vulnerability of a specific cell type, or brain region, are now being revaluated in light of the complex systemic alterations due to upstream and downstream effects of the "local" pathology on the "global" network's homeostasis (Sitaram et al., 2017). Network alterations are manifested not only at the level of synaptic wiring defects. In fact, aberrant oscillatory activity and neural dysrhythmias are a commonly observed phenotype in many neuropsychiatric disorders (Uhlhaas & Singer, 2015). Because synaptic defects and network alterations are highly interdependent, it is difficult to elucidate the causal relationship between these two pathological phenomena. Nonetheless, researchers agree that oscillatory dysrhythmias reflect an imbalance in the local excitation/inhibition ratio and also a potential dysfunction in long-range connectivity between brain regions participating in the same

functional network, possibly caused by synaptic dysfunction. Most importantly, neural network dysfunction is observed in both familial and sporadic forms of AD.

1.3.1 Molecular and cellular mechanisms behind Aβ deposition

Individuals affected by AD will display overt cognitive symptoms like loss of episodic memory and spatial orientation. As the pathology progresses, these alterations become progressively more severe, until the patients' personality is completely altered and they become incapable of performing daily tasks. Nonetheless, to differentially diagnose AD from other types of dementia, a behavioral assessment is insufficient, as a definite diagnosis can only be performed upon detection of beta-amyloid plaques (Aβ plaques, also called "neuritic" or "senile" plaques) and intracellular neurofibrillary tangles in post-mortem neural tissue. These hallmarks are paralleled by enlarged ventricles, resulting from the massive atrophy of neural tissue (Dubois et al., 2007). β-Amyloid plaques are fibrillary aggregates of misfolded proteins exhibiting a β-sheet secondary structure that are released from the transmembrane compartment into the extracellular space. The generation of the fragments that aggregate and become larger over the course of the disease is caused by the cleavage of the transmembrane protein amyloid precursor protein (APP) (Weidemann et al., 1989). Under non-amyloidogenic conditions, APP is subsequently cleaved by two enzymatic complexes, the α- and γ-secretases. APP is successively cleaved into the soluble extracellular domain sAPPα and the amyloid precursor intracellular domain (AICD). The amyloidogenic pathway, in contrast, involves the processing of APP by the β- and γ-secretase. The membrane-bound product of the cleavage by the beta secretases (BACE1 and BACE2) is named CTFβ, and it is cleaved at various sites by the presenilin 1 and presenilin 2 complexes (PS1 and PS2) (Vassar et al., 1999). Various species of Aβ monomers are produced as a result of APP cleavage: Aβ40 (ca. 90%) and Aβ42 (ca.10%) represent the most abundantly secreted species, and their names derive from the cleavage site along CTFβ. Aβ42 monomers are the less soluble and more lipophilic species, so they tend to accumulate with higher probability in the extracellular space, forming oligomers and fibrils, and ultimately amyloid plaques (Haass & Selkoe, 2007; Walter et al., 1996). Different types of plaques are present in the extracellular space when AD is advanced: dense core plaques, surrounded by inflammatory cells like astrocytes and microglia, and diffuse plaques (Rak, Del Bigio, Mai, Westaway, & Gough, 2007). Dense core plaques are composed by a mixture of degraded neuritic material surrounded by beta amyloid load (Serrano-Pozo, Frosch, Masliah, & Hyman, 2011). Aβ is mostly degraded by two enzymes, neprilysin and insulysin (Iwata et al., 2000; Numata & Kaplan, 2010). Additionally, Aβ oligomers can be excreted into the blood flow through the blood brain barrier via the low-density lipoprotein receptor-related protein (LRP)

and its re-uptake is mediated by the receptor for advanced glycation end products (RAGE) (G. F. Chen et al., 2017). RAGE receptors are also expressed on microglia, where they contribute to Aβ-mediated microglial activation. This in turns initiates a pro-inflammatory response that can exacerbate the progression of Alzheimer's disease if dysregulated (Heneka, O'Banion, Terwel, & Kummer, 2010; Tejera & Heneka, 2016). Aβ oligomers coexist in various tertiary conformations and their relative toxicity is thought to change accordingly **(Fig. 1.4)**.

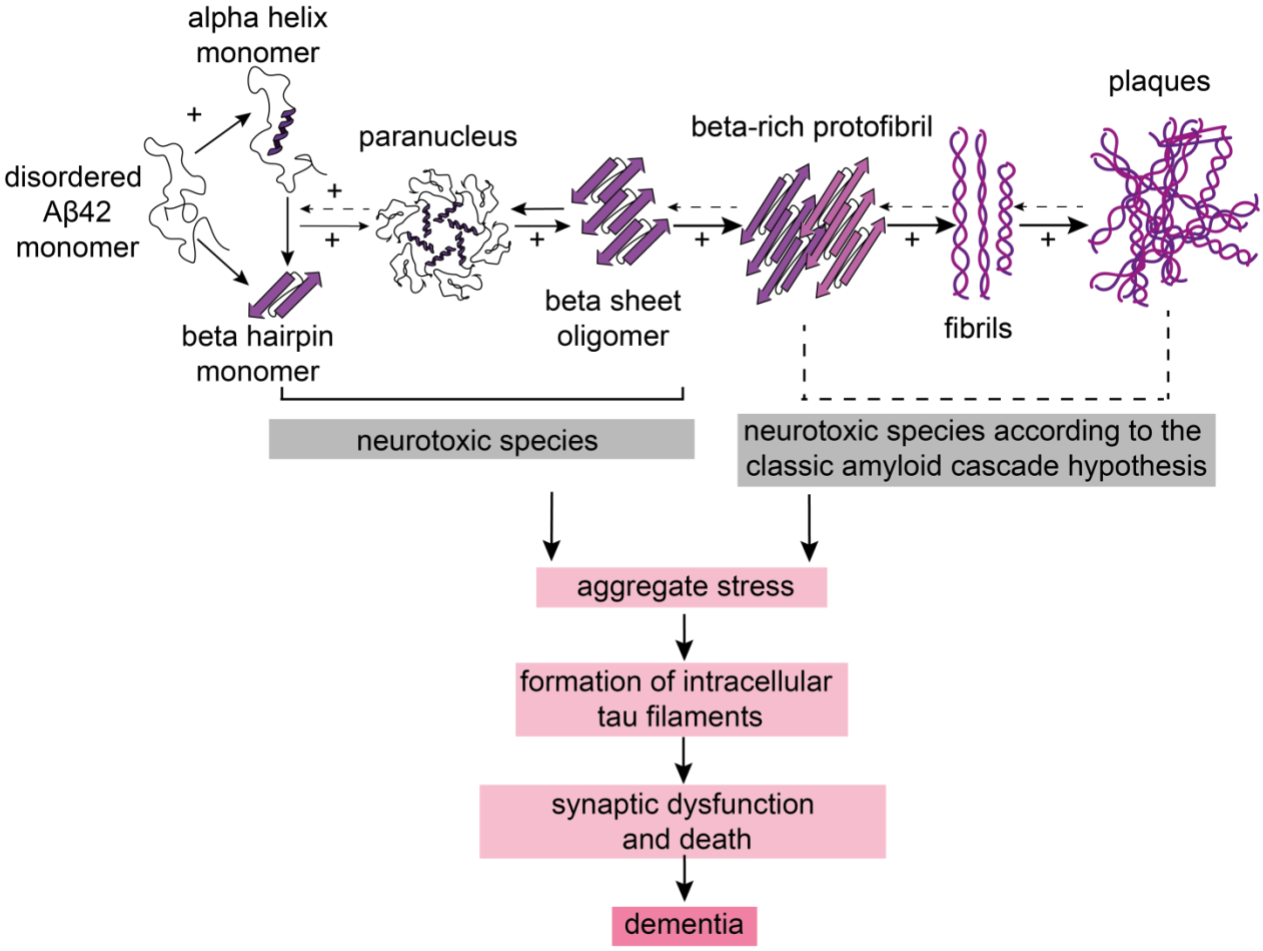

Figure 1.4 Generation of Aβ plaques and amyloid cascade hypothesis. Aβ monomers exist in both "ordered" and "disordered" states. Secondary structures can assume both alpha-helical conformation and β-sheet conformations. Both secondary structures have the potential to aggregate and form toxic oligomeric species with variable degrees of toxicity. The further aggregation of oligomers and paranuclei into protofibrils (tertiary structures) is the rate limiting step for the final nucleation of fibrils, which then further elongate and accumulate into amyloid plaques. The higher the proportion of β sheet structures, the easier the formation of protofibrils and fibrils. The classical amyloid cascade hypothesis postulates that insoluble aggregates (plaques and fibrils) are the cause of cytotoxic stress, lead to aggregation of tau filaments, which in turn aggravates synaptic failure and neurodegeneration ultimately leading to dementia. This hypothesis has been disregarded; currently, soluble forms of Aβ (monomers and oligomers) are presumed to have a higher toxicity and to affect brain function more severely and from much earlier on in the progression of the disease.

The amyloid cascade hypothesis posits that Aβ plaques are the cause for the biochemical and cognitive alterations observed in late stage AD patients. Recent evidence has led researchers to revisit this hypothesis, as there is little to no correlation between cognitive decline and neuritic plaque deposition (Erten-Lyons et al., 2009; Herrup, 2015). The focus has shifted towards more soluble oligomers, which appear at earlier stages of the pathology and then nucleate to create the larger insoluble deposits. It has been speculated that these may trigger a cascade of events that is then independent from the presence of the neuritic plaques. Indeed, there is strong evidence that oligomers affect calcium homeostasis, synaptic transmission and overall cellular excitability by acting on receptors and causing oxidative stress (Kayed & Lasagna-Reeves, 2013). Besides, oligomers alone were sufficient to cause cognitive deficits in the absence of plaques (Gandy, 2010).

AD is considered a polygenic, irreversible and progressive neurodegenerative disease, and only a small fraction of AD cases is inherited in an autosomal dominant manner. The incidence of hereditary AD cases is in fact approximately 1% compared to the total number of individuals affected by AD. These are caused by mutations in either the PS1 and PS2 enzymes (in ca. 40% of the cases), or in the APP itself. This form of AD is termed “familial AD”, and symptoms typically appear before the age of 65 (Hardy, 1997). One of the best characterized mutations is the so called “Swedish mutation”, which is a double point mutation on the APP site adjacent to the beta secretase cleavage and has a penetrance of about 85%. Mutations in the APP, PS1 and PS2 genes cause overproduction of Aβ42 fragments, as the result of the hyperactivation of the amyloidogenic pathway over the non-amyloidogenic one. Interestingly, though, 90% of all AD cases are termed “sporadic”, as they occur in absence of mutations in these genes. Individuals affected by sporadic AD start showing cognitive symptoms later than the age of 65 (Small & Duff, 2008). Even though the greatest known risk factor for AD is ageing, given the fact that genetic AD accounts only for a small percentage of cases, there are several genes that are linked to an increase in the risk of developing late-onset sporadic AD (Bellenguez, Grenier-Boley, & Lambert, 2020). One of the most characterized are the polymorphisms in the gene encoding for the apolipoprotein E (*APOE*), which lead to the production of the APOE4 protein (Corder et al., 1993; Liu, Liu, Kanekiyo, Xu, & Bu, 2013).

Aβ deposition follows a hierarchical course as the disease progresses, and the first plaques are observed in the neocortex. Subsequently, plaques spread to the temporal lobe and to subcortical regions (Jucker & Walker, 2011). Diverse mouse models of AD have been developed to recapitulate molecular and cognitive progression of AD. In each model, not only plaque burden over time, but also topological distribution of plaques and NFTs differs, according to which

genes were subjected to mutations (Hall & Roberson, 2012). Similarly, cognitive defects are observed at different stages, sometimes as early as 15 weeks of age (Hijazi, Heistek, Scheltens, et al., 2020) as it is the case for the APPswe/PS1dE9 mouse model employed in this study. In the same mouse model, behavioral deficits were observed in working memory tasks, hippocampal-dependent spatial memory tasks, and recognition memory (Webster, Bachstetter, Nelson, Schmitt, & Van Eldik, 2014), and these deficits are often detectable at the age of at least 10 months. This plethora of models enables the study of independent aspects of the pathology, with the aim of dissecting the effect of each of the multiple pathophysiological processes that occur in AD. Nonetheless, even though extensive research has been conducted on multiple rodent models and humans, it is not yet fully disclosed whether the production of toxic species is the direct cause of cognitive deficits, or whether these are only a byproduct of cellular and systemic alterations that would inevitably lead to degenerative processes observed in the AD pathology. Multiple hypotheses, next to the amyloid cascade hypothesis, have been advanced in the last years. In the next section, the so called "network dysfunction hypothesis" will be described in more detail.

1.3.2 Evidence for network dysfunction

Alzheimer's disease course can divided into three stages, according to symptomatology: 1) preclinical AD, when molecular changes start to occur and can be detected in the brain, blood and cerebrospinal fluid; 2) mild cognitive impairment, when the first cognitive lapses start to occur, especially episodes of profound disorientation in familiar environments and loss of declarative memories; 3) dementia due to AD, when the individual's daily life is severely affected by cognitive impairments due to the profound loss of neural tissue . Across all stages of human and rodent AD, not only an increasing amount of circuits is affected, but the way that each of them is altered progresses with the pathology. Interestingly, aberrant oscillatory activity and impairments in synaptic turnover and connectivity precede the drastic neurodegeneration that is the ultimate cause of death of AD patients (Palop et al., 2006; Palop & Mucke, 2010, 2016).

Among the most striking changes observed in MCI and demented patients is the loss of structural and functional connectivity between brain areas that support memory processes (Palop & Mucke, 2016; Zott, Busche, Sperling, & Konnerth, 2018), especially in the MTL (Stoub et al., 2006). Functional alterations are manifested by the significantly higher activity of the hippocampus in MCI patients, and a simultaneous an unsuccessful deactivation of the default mode network (DMN) in fMRI studies (D. T. Jones et al., 2017; Palop & Mucke, 2016).

The DMN is a network of brain regions that is particularly active in moments of rest or lack of memory task performance. Activation of the DMN correlates with increased power of slow waves (delta 1-4 Hz, and theta 4-7 Hz) in the EEG recorded during awakefulness, and reflects high synchrony between brain regions. Higher computations, as previously mentioned, correlate with faster oscillating fields. Thus, hyperactivity of the DMN, and "slowing" of the EEG upon task performance indicate that the network is in a state of "hyper-synchrony" and the single brain regions cannot function properly or independently (Palop & Mucke, 2016). Coherent with the "hyper-synchrony" hypothesis, EEG recordings of AD patients displayed intervals of subclinical epileptiform activity in the pre-symptomatic stages of the pathology, during intervals of REM sleep (Vossel et al., 2016). Furthermore, the incidence of EEG dysrhythmias correlated with the increase in cognitive decline observed at later time points (Vossel et al., 2016). With the progression of the disease, the incidence of overt seizures (either convulsive or partial complex) increases and it is 6 to 10 fold higher in sporadic AD patients than in healthy aged controls (Pandis & Scarmeas, 2012). Interestingly, mouse models of AD display a similar pathophysiological phenotype. For example, in the hAPP J20 mouse model, which overproduces human Aβ, epileptiform activity was detected in mice aged 4-7 months. Reversing this phenotype by restoring inhibitory neuron function was beneficial for the cognitive performance of the animals in a spatial memory task (Martinez-Losa et al., 2018; Verret et al., 2012). Similarly, treatment of mice with the antiepileptic drug Levetiracetam was able to rescue abnormal spiking activity in the cortex and hippocampus of the same mouse model (Sanchez et al., 2012). When the drug was applied chronically for 28 days, the authors reported rescued cognitive function in a novel object recognition task, as well as synaptic protein function and LTP at mossy fibers in the hippocampus (Sanchez et al., 2012). Not only epileptiform activity, but also aberrations in the slow frequency component of the EEG and /or LFP have been recapitulated in a plethora of mouse models. We and others have observed that APPswe/PS1dE9 mice showed a slightly but significantly decreased hippocampal theta frequency upon exploration of an open field arena, while displaying an increased running velocity (Ambrad Giovannetti, 2018; Cayzac et al., 2015). Interestingly, alterations of theta oscillations were observed in two other mouse models, namely the 5xFAD (Wang et al., 2020) and the TgCNRD8 (Goutagny et al., 2013) at pre-plaque stage in organotypic hippocampal preparations. Wang et al. (Wang et al., 2020) were able to rescue spatial memory deficits in this mouse model by applying transcranial magnetic stimulation (TMS), which resulted in the normalization of the reduced theta power observed in transgenic animals at the age of 2 months, a stage in which plaque deposition is only starting in this model. This indicates that the toxicity

of the Aβ oligomers is sufficient to induce LFP aberrations in the theta range, and that this may initiate a cascade of events that ultimately exacerbates the disrupted inhibitory/excitatory balance in the network. Mechanistically, inhibitory neuron dysfunction has been appointed as a causal factor exacerbating, and possibly driving this cascade of events (see chapter 1.3.3).

Next to disturbances of the 1-12 Hz component of the EEG spectrum, it was shown that power of slow (30-60 Hz, CA3 associated) and mid-fast (60-130 Hz, entorhinal associated) gamma oscillations is altered in both mouse models of AD (Etter et al., 2019; Mably & Colgin, 2018) and human subjects affected by the pathology, albeit in sometimes contradictory ways. For instance, Van Deursen et al. (van Deursen, Vuurman, Verhey, van Kranen-Mastenbroek, & Riedel, 2008) report increased induced gamma power in AD patients compared to the MCI group, while Iaccarino et al. (Iaccarino et al., 2016) found diminished slow gamma power during SWRs in the cortex and hippocampus of 5xFAD mice. Optogenetic stimulation of PV^+ neurons, but also the simple exposure to a 40 Hz light flicker was sufficient to reduce the β-amyloid load in the visual cortex of a 5xFAD mouse model (Iaccarino et al., 2016), and cognition of transgenic animals was improved upon combined light and auditory stimulation at 40 Hz (Martorell et al., 2019). As a mechanistic explanation to the beneficial effects of GENUS, the authors propose Aβ clearance is dependent on inhibitory-neuron driven microglial activation (Adaikkan et al., 2019; Adaikkan & Tsai, 2020; Iaccarino et al., 2016), and the increase in activity of auditory and visual cortex is able to entrain in downstream regions in the memory processing network like the hippocampus and the prefrontal cortices. Notably, this visual and auditory stimulation therapeutic protocol is currently being evaluated in a cohort of 15 AD patients (GENUS, clinical trial identifier NCT04055376). Similar interventional strategies aimed at increasing gamma power had already been applied in AD patients, although these relied on invasive or mildly invasive procedures like transcranial direct current stimulation (tDCS) and deep brain stimulation (DBS). Until today, the outcome of these studies has yielded confounding results, possibly because of the high variability in study designs and stimulation protocols employed (Chang, Lane, & Lin, 2018). Further evidence corroborating the beneficial effect of entrainment of the network at gamma frequencies via increasing PV^+ function was provided by Etter et al. (Etter et al., 2019). In this study, the authors also found that the decreased gamma power observed in the hippocampus of APPJ20 model could be restored by manipulation of long range PV^+ neurons in the septum, which in turn led to amelioration of cognitive functions. Finally, two very recent *in vitro* studies revealed how SST^+ and PV^+ inhibitory neuron manipulation at the local microcircuit level in the hippocampus are able to restore Aβ42-induced impairments in theta-gamma coupling (Chung, Park, Jang, Kohl,

& Kwag, 2020), a phenomenon also observed in humans (Goodman et al., 2018). Theta-gamma coupling was also impaired in mice deficient for APP, further stressing that disease-related alterations in synaptic transmission underlie systemic network dysfunction (X. Zhang et al., 2016).

Another crucial insight into how network-dependent oscillatory mechanisms that support cognition are altered in age and disease is provided by the prevalence of sleep disturbances in aged individuals, MCI and demented patients. As sleep and slow-wave oscillations (SWS) present during sleep support memory consolidation (via modulation of higher frequency spindles and SWR complexes), it is thought that these may be pathological mechanisms behind the inability to store new memories, a hallmark typical of AD. In fact, AD patients spend significantly less time in NREM sleep and show decreased slow wave sleep activity (Lucey et al., 2019), and disturbances of sleep rhythms are predictors for the development of AD in MCI subjects (Lloret et al., 2020). Moreover, there is a positive correlation between loss of sleep and increase in Aβ42 levels in the blood plasma of both patients and healthy subjects, indicating a link between preservation of neuronal function and proper sleep rhythms (Ooms et al., 2014).

Finally, it is important to note that not only systemic, but also excitability disturbances at the single neuron level have been described in AD mouse models. Clusters of hyperactive cortical neurons around amyloid deposits have been revealed by two-photon calcium imaging in anesthesized APP23xPS45 mice (Busche et al., 2008), while 20% of neurons not in proximity of amyloid plaques showed reduced activation. Hyperexcitability of pyramidal cells was also revealed in the hippocampus of the same mouse model, where it preceded Aβ plaque deposition, and of a rat model of AD (Sosulina, 2020). Similarly, in MCI patients, fMRI revealed increased activation of hippocampal formation, but this reverses strongly over the course of the disease (Zott et al., 2018).

The findings presented in this chapter indicate the strong link between excitatory/inhibitory balance and the emergence of cognitive dysfunction in disease conditions. Diverse hypotheses were introduced to explain this pathophysiological process, including a generalized inhibitory neuron dysfunction at the micro- and macro-circuit level.

1.3.3 Inhibitory neuron dysfunction

In the past decade, ample research showed that reduction in numbers or impairment in function of inhibitory neurons is a pathological phenomenon common to both humans and mouse models of AD. Therefore, historically dominating theories on AD, which put a strong weight on the loss of cholinergic and excitatory neurons, or on the toxicity of the amyloid plaques, have now

been flanked with the view that not only AD related dysrhythmias, but also synaptic dysfunctions, may be caused by the hyper/hypo activity of inhibitory tone at the early stages of the pathology (**Fig. 1.5;** (Ambrad G. & Fuhrmann, 2019)).

Indeed, inhibitory neurons are affected in both number and function, as revealed by multiple immunohistochemical quantifications of inhibitory neuron and GABA receptors in humans and mouse models (Xu, Zhao, Han, & Zhang, 2020). Interestingly, SOM^+ expression in cortical neurons is prominently reduced in human AD and in healthy aging (Burgos-Ramos et al., 2008; Epelbaum et al., 2009; Gahete et al., 2010; Rossor, Emson, Mountjoy, Roth, & Iversen, 1980). Hippocampal alterations are less well documented (Rossor et al., 1980). Alterations of PV^+ inhibitory neurons were also reported in humans. Recently, a study showed reduced expression of GluA4, a glutamate receptor primarily expressed on PV^+ interneurons (Xiao et al., 2017). Similarly, reduction of Nav 1.1 channels in PV^+ interneurons is a common feature of human AD and mouse models (Martinez-Losa et al., 2018).

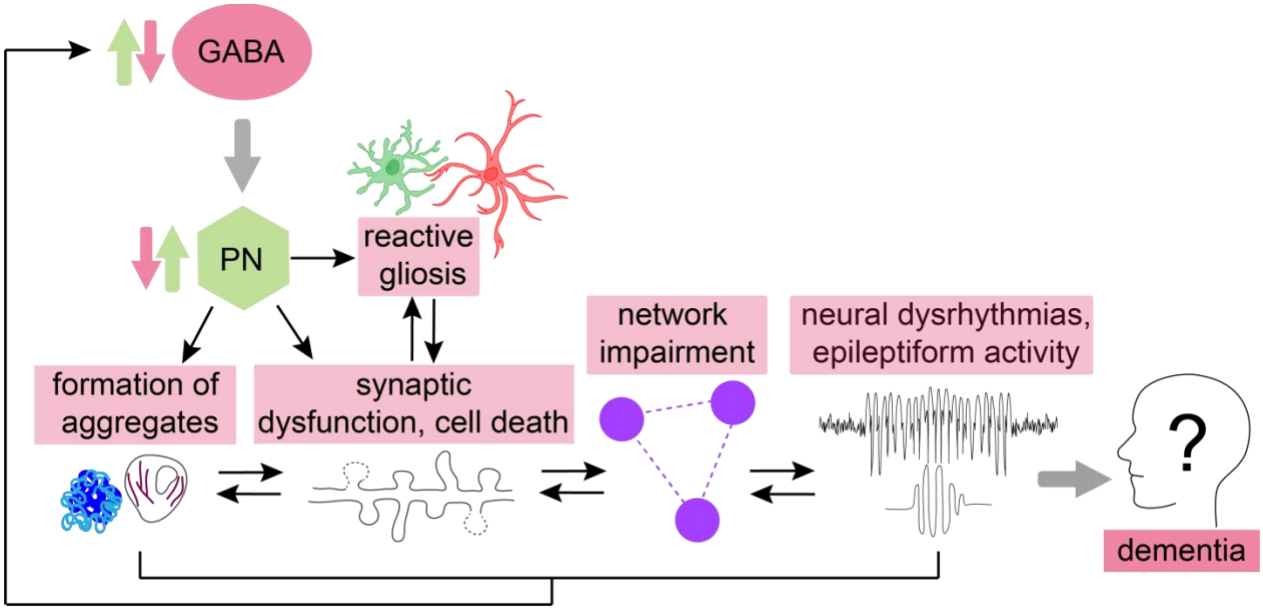

Figure 1.5 "GABAergic cascade hypothesis" of Alzheimer's disease. GABAergic transmission alterations in either direction are echoed in uncontrolled principal neuron (PN) responses. These, in turn, provoke disruptive microglial and astrocytic responses, which may lead to the production of toxic protein species like Aβ deposits and hyperphosphorylated Tau. These will cause defects in synaptic and structural plasticity such as long-term depression and synaptic loss. All these factors lead to improper network functionality and impaired neural communication within and between brain areas that are responsible for learning and memory processes. These alterations are reflected in the epileptiform discharges and other AD related dysrhythmias observed in the electroencephalograms of individuals who will develop AD dementia, but at earlier stages of the pathology, prior to neurodegeneration.

In comparison to the numerous immunohistochemical and stereological studies, direct evidence of the impact of oligomers and/or plaques on inhibitory neuron function is less frequently observed in literature. Villette et al. (Villette et al., 2010) were among the first to causally link Aβ deposition to dysfunction of PV^+ long range projecting septal neurons and concomitant reduction in power o theta oscillations in the septum. Besides, as previously mentioned, levels of Nav1.1 and Nav1.6 were reduced in PV^+ neurons (Hamm et al., 2017; Verret et al., 2012), which correlated with decreased gamma power. Cognitive deficits and oscillatory impairments were reverted by reinsertion of the Nav1.1 transgene, and also by transplantation of neurons overexpressing the construct, in relatively aged hAPP/J20 mice (Martinez-Losa et al., 2018). This approach had already resulted effective in a study by Tong et al, performed on an APOe4 overexpressing mouse model (Tong et al., 2014). In a study performed in our laboratory, we showed that hippocampal SOM^+ interneurons in aged APPswe/PS1dE9 mice model display alterations in synaptic turnover, loss of axonal segments, and reduced response to aversive stimuli (Schmid et al., 2016). Restoring SOM^+ function via pharmacological manipulation was sufficient to rescue behavioral impairments in a contextual fear conditioning task (Schmid et al., 2016). Finally, Hijazi et al. (Hijazi, Heistek, Scheltens, et al., 2020) reported Aβ related hyperexcitability of PV^+ interneurons in young APPswe/PS1dE9 mice, and chemogenetic silencing of PV^+ interneurons was sufficient to restore spatial memory deficits in a Morris water maze task. Furthermore, in a following study, the authors show that PV^+ interneuron hyperexcitability is sufficient to cause alterations in the network, leading to cognitive deficits resembling those displayed by mouse models of AD (Hijazi, Heistek, van der Loo, et al., 2020). In addition, chemogenetic activation of hippocampal PV^+ interneurons rendered the hippocampal network more sensitive to β-amyloid incubation (Hijazi, Heistek, van der Loo, et al., 2020).

In conclusion, an increasing number of studies provided evidence that manipulating oscillatory activity by targeting inhibitory neurons seems to be a promising therapeutic approach to ameliorate cognitive deficits in animal models of the disease, as the two pathophysiological mechanisms appear to be strictly intertwined.

1.4 Aim of study

Hippocampal oscillatory activity correlates with cognition and behavior, reflecting the key contribution of the hippocampal system to learning and memory processes. Alterations in power and frequency of neural oscillatory activity are a hallmark of aged individuals, patients suffering from mild cognitive impairment and from neurodegenerative disorders such as Alzheimer's disease (AD). Besides, epileptiform activity is readily detected in the EEG of AD patients, and its incidence is a predictor of the severity of the pathology before symptoms occur. Therefore, researchers have increasingly shifted their attention towards investigating whether and how restoration of hippocampal field activity is sufficient to rescue the overt cognitive deficits that emerge with age and disease, in particular AD. Nonetheless, it is not yet known whether this interventional strategy is age and task dependent. Furthermore, mechanistic evidence regarding the way that inducing oscillatory activity may promote reorganization of hippocampal neuron assemblies is missing.

The experiments described in this thesis are aimed at describing how hippocampal local field potential (LFPs) activity is impaired by age and disease. Furthermore, it is known that inhibitory neurons are affected by both age and AD, in humans and rodent models. Inhibitory neurons are pivotal generators and regulators of oscillatory activity, as they gate input integration and control output generation of both pyramidal cells and other inhibitory neurons. Thus, I tested whether stimulating hippocampal inhibitory neurons during various behavioral tasks would ameliorate the putative cognitive deficits observed with age and AD-like pathology. Hippocampal PV-positive interneurons were transfected with an excitatory opsin, and they were stimulated according to the ongoing, simultaneously recorded theta oscillations detected in LFP. Finally, it is known that hippocampal LFPs in the CA1 compartment are highly modulated by input from the medial entorhinal cortex. Thus, I investigated potential disturbances of local MEC inhibitory neurons and of hippocampo-entorhinal long range inhibitory projections under AD-like conditions.

2 Materials and Methods

2.1 Mouse lines

Animals were either single or group housed (maximum 5 mice) with their same-sex littermates in individually ventilated cages (IVCs) under specific-pathogen free conditions (SPF). Temperature (22°C), humidity (40%) and the light-dark cycle (lights on at 6:00 am and off at 6:00 pm) were kept constant. Water and food were provided *ad libitum*. The experimental procedures were in accordance with guidelines established by the DZNE and were approved by the government of North-Rhine-Westphalia.

2.1.1 APPswe/PS1dE9 (APP/PS1)

B6.Cg-Tg(APPswe,PSEN1dE9)85Dbo/Mmjax mice (referred to as "APP/PS1", MMRRC stock number 034832, The Jacksons Laboratory) are a mouse model of amyloidosis and Alzheimer's disease (Jankowsky et al., 2004). These mice express both the human "Swedish" mutation in a chimeric mouse/human amyloid precursor gene (Mo/HuAPP695 harboring the Swedish K594M/N595L mutation) under the control of the mouse prion protein promoter (PrnP) and the exon 9 deletion in the presenilin 1 gene (PS1) with a single genomic insertion site, so that both transgenes are transmitted as one locus. These mice overproduce Aβ, which aggregates progressively into amyloid deposits in an age-dependent fashion. Female mice show heavier signs of plaque deposition earlier than male mice (Jiao et al., 2016). In this thesis, only heterozygous (referred to as APP/PS1) or wild type (referred to as WT) progeny was used for experiments, due to the high severity of APP/PS1 mutation in the homozygous condition.

2.1.2 PV-Cre::APP/PS1

PV-Cre::APP/PS1 mice were generated by crossbreeding B6.129P2-Pvalb$^{tm1(cre)Arbr}$/J mice (named PV-Cre, Stock number: 008069, The Jacksons Laboratory) to the above mentioned APP/PS1 line. PV-Cre mice express a knock-in allele that encodes for Cre recombinase (IRES-Cre-pA cassette in the 3' UTR of exon 5) under the control of the Parvalbumin (Pvalb) promoter , leaving endogenous parvalbumin expression untouched. Over 90% of PV^+ neurons express Cre recombinase in this mouse line (Hippenmeyer et al., 2005).

2.1.3 SST-Cre::APP/PS1

B6N.Cg-*Sst*$^{tm2.1(cre)Zjh}$/J mice (stock number 018973, The Jackson's Laboratoy) express Cre recombinase (IRES-Cre-pA cassette) in the 3' UTR of the Somatostatin locus (Taniguchi et al., 2011). These mice were crossbred to APP/PS1 mice and only offspring heterozygous for the

C*re* transgene was used for experiments due to the partial knockout of the endogenous somatostatin protein resulting from the insertion method of the transgene.

2.1.4 Thy1-GCaMP6f-GP5.5::APP/PS1

B6-Tg(Thy1-GCaMP6f)-GP5.5Dkim/J mice were crossbred to the APP/PS1 line. These mice express a transgene encoding the ultrasensitive calcium indicator GCaMP6f under the control of the *Thy1* pan-neuronal promoter in a subset of excitatory neurons (Dana et al., 2014). We used mice that were heterozygous for the transgene, in which the expression of the calcium indicator was stable over time and enabled in-vivo imaging approaches. These mice were generated at HHMI's Janelia Farm Research Campus as part of the Genetically-Encoded Neuronal Indicator and Effector (GENIE) Project.

2.2 Surgical procedures

2.2.1 Anesthesia and analgesia

Mice were intra-peritoneally anesthetized with a mixture of ketamine (0.13 mg/g bodyweight, Ketavet® 10%, Bela Pharm GmbH&Co. KG, Vechta, Germany) and xylazine (0.01 mg/g bodyweight, Rompun® 2%, Bayer Vital GmbH, Leverkusen, Germany), dissolved in sterile sodium chloride (NaCl 0.9%, AppliChem, Germany) and given intra-peritoneally. Dexamethasone (0.2 mg/kg, Sigma Aldrich, Taufkirchen, Germany) was given subcutaneously as an anti-inflammatory drug. After 10 minutes, mice were head-fixed to a custom-built stereotactic frame with the help of a mechanical auxiliary adaptor inserted in their auditory canal (Narishige®, Tokyo, Japan). To induce complete absence of reflexes, tested with the toe-pinch method, isofluorane (Actavis, New Jersey, USA) was dispensed through a custom tubing system and its volume and flow were regulated throughout the surgery. After wiping the skin above the skull with 70% ethanol and a sterile cotton swab (EUROTUBO®), a portion of it was either incised with a disposable scalpel (for stereotactic injections, section 2.2.2) or removed with scissors (for cranial window and optic fiber implantations, sections 2.2.3 and 2.4). Sufficient eye ointment (Bepanthene®) was applied to the eyes of the mouse to prevent them from drying and the body was kept warm throughout the surgery with a heat pad (Fine Science Tools GmbH, Heidelberg, Germany) set at 37C. Surgical tools (all acquired from Fine Science Tools GmbH, Heidelberg, Germany) were regularly sterilized by means of a bead sterilizer (Steri250, Simon Keller GmbH, Burgdorf, Switzerland). Mice were administered burprenophine (0.05 mg/kg, Temgesic®, RB Pharmaceuticals Limited, Mumbai, India) sub-cutaneously and metamizol (Metapyrin® 500 mg/ml, Pharma-Partner-Vertriebs GmbH, Hamburg, Germany) in the drinking water for three days after all surgical procedures.

2.2.2 Stereotactic viral injections

Neurons can be driven to express a construct of interest through the injection of a modified adeno-associated virus (AAV) containing a synthetically cloned plasmid encoding the genetic sequence of the protein. The variety of serum types derives from the naturally occurring, or artificially engineered antigens on the AAV capsid; these can in turn influence reproduction properties of the AAV such as spread within the tissue and penetration efficacy. To precisely target the region of interest and inject a specific volume of virus in the living, anesthetized animal, the AAV suspension was loaded into a Hamilton syringe equipped with a 34-gauge needle (World Precision Instruments, Berlin, Germany). Speed of injection and volume of injections were digitally set with an Ultra Micro Pump controller (World Precision instruments, Berlin, Germany), whereas the position of the syringe was manually controlled with a motorized micromanipulator (Luigs and Neumann, Ratingen. Germany). With the micromanipulator, it was possible to control the placement of the needle in all dimensions (antero-posterior, medio-lateral and dorsoventral) relative to a reference point on the skull, in this case bregma, with micrometer precision. The different sets of stereotactic coordinates relative to bregma (antero-posterior, AP, and medio-lateral, ML) and to brain surface (dorso-ventral, DV) mentioned throughout the text were calculated with the Franklin and Paxinos Mouse Brain Atlas (The Mouse Brain in Stereotaxic Coordinates, Third Edition, Academic Press). Holes of approx. 0.5 mm in diameter were drilled through the skull at the desired coordinates with a dental drill (Dental drill, Tungsten carbide, Gebr. Brasseler GmbH & Co. KG, Lemgo, Germany). The tip of the syringe was then lowered through the holes until the surface of the brain and from here it was inserted into the brain tissue at lower speed, at the depth of interest. AAVs were injected at a speed of 100 nl/min. Afterwards the needle was left in place for about 10 minutes to minimize spillover of the liquid upon its retraction from the brain tissue. Finally, the wound on the skin was sutured with surgical wire (Vicryl, Ethicon, Norderstedt, DE).

2.2.3 Procedures for cranial window, light fiber and silicone probe implantation

Once the skin above the skull was cut away, to guarantee strong attachment of the cranial window, light fiber and electrodes, or silicone probes to the skull, the first step consisted in removing the periosteum above the exposed surface with a disposable scalpel (Swann-Morton, Sheffield, England). Afterwards, the skull's surface was roughened with Gel Etchant (OptiBond™ FL bottle kit) for ca. 20 seconds. This compound was then thoroughly rinsed away with 1x PBS, and the now porous skull was primed with a two-component dental cement, only

after being completely dried with sterile cotton swabs (Sugi®Eyespear) and lightly administered pressured air. First, the primer was evenly distributed on the skull and let air dry for 10 seconds. Second, the adhesive was rubbed in the primer with circular motion and this mixture was let dry for 30 seconds before being cured with a portable LED lamp (Schott, Mainz, Germany). During the whole procedure, the eyes of the mouse were protected with aluminum foil and Bepanthene® to prevent damage to the cornea caused by the intense light of the LED lamp. Once the procedure was complete, the elements on the skull were stabilized and further fixated with the LED curable composite (GRADIA® DIRECT Flo).

2.3 Anterograde tracings in SST-Cre::APP/PS1 mice

To investigate potential axonal segment degeneration of hippocampal SOM^+ LRIPs (Figure 3.3), SST-Cre::APPswe/PS1dE9 mice at the age of 11 months were stereotactically injected with *AAV1.CAG.DIO.tdTomato* virus at the following injection coordinates: AP -2.0 mm from bregma, ML +1.6 mm from bregma , DV +1.72 mm and +1.1 mm from brain surface. 300nl of virus were injected at each site. This way, SOM^+ neurons in both the SO of CA1 and the hilus of DG were transfected. Mice were transcardially perfused after 4 weeks of incubation with 1xPBS and the brains were post-fixed with 4%PFA in PBS for 24-48 hours.

2.4 Combined optogenetics and LFP recordings

2.4.1 Adeno-associated viral constructs

To drive the activity of PV^+ neurons, the excitatory opsin C1V1 (*AAV2/1-Ef1a-DIO-C1V1-(t/t)-TS-mCherry)* was stereotactically injected in the CA1 region of both hippocampi (see paragraph 2.4.2). C1V1 is a fast, red-shifted opsin which was excited by a 561 nm wavelength laser (OBIS 561 nm). As a control, mice were injected with either sterile PBS1x or a mixture of CamKII-Cre and the loxP-flanked fluorophore tdTomato (1:1 dilution). 1 µl of virus was injected in each hemisphere, above the CA1 area (AP: -1.8 mm from bregma, ML: ±1.5 mm from midline and DV: +1.1 mm from brain surface).

2.4.2 Single wire electrodes and amplifier system

Electrodes were custom made by soldering a coated tungsten wire (bare wire: 0.075 mm, coating thickness quadruple PTFE: 0.018 mm, 99.98% purity, ADVENT Research Materials ltd., Oxford, England) into a gold pin (Conrad Electronic SE, Hirschau, Germany) used for connection to the cables (on average 2 m long, single conductor wire LifY, 0.05 mm^2 and 0.8 mm insulation, (Conrad Electronic SE, Hirschau, Germany), which were in turn attached to the preamplifier headstage system (NPI electronic GmbH, Tamm, Germany). The preamplifier

headstages were then connected to an extracellular amplifier system (EXT-02F, NPI electronic GmbH).

2.4.3 Fiber-optic cannulas' and LFP electrodes' implantation

Implantation of light fibers and LFP electrodes was performed 2-4 weeks after viral injections. The skull of the animals was prepared according to section 2.3.3. Light to both CA1 areas was delivered through double fiber-optic cannulas (B284-3015-2.5, TFC_300/370 – 0.22-2.5 mm, TSM3_FLT, Doric Lenses, Quebec, Canada), insulated along their length to prevent ectopic excitation of cortical neurons. Prior to the implantation, one monopolar LFP electrode was glued to each of the optic fibers on the cannula; their tip was cut so that it would protrude by 250μm from the tip of the optic fibers. The custom-made cannula and LFP electrode assembly was fixated to the micromanipulator and lowered at a depth of 1 mm from the brain's surface. Ground and reference electrodes were then implanted in the cerebellum, through two newly opened holes in the skull. The fiber optic cannulas, ground and reference electrodes were first fixated on the skull with a non-hydrophobic two-component dental cement mixture (Cyano Verneer®), which dried in about 30 seconds. This was necessary due to potential leakage of CSF from the holes, which would otherwise prevent the proper attachment of the LED curable composite and therefore not enable stable chronic recordings. All the components on the skull were stabilized according to procedures described in section 2.3.1.

2.4.4 Data acquisition and stimulation protocols

The extracellular neural signal was acquired at 10 kHz and low-pass filtered at 700 Hz. 50 Hz electric noise was filtered with a humbug (Quest Scientific, Canada) and a custom-made wire mesh was used as a faraday cage around the open field arena. LFPs were digitized with an ITC-18 interface analog-to-digital board (InstruTech, New York, USA) and streamed to the PC via a USB2.0. The IgorPro software v.6.22A (Wavemetrics, Portland, USA) was used for data collection and control of the laser stimulation. LFP data was downsampled to 1 kHz for offline analysis. Laser stimulation was carried out via a 561 nm wavelength laser (Coherent Inc., Santa Clara, USA), connected to the implanted cannulas via 1.5 m long fiber-optic patch cords (patch cords). A rotary joint was used to split the laser power evenly between the two patch cords and to prevent them from tangling while the mice were freely moving in the open field (rotary joint; **Figure 2.2**). Laser power (20 mW) and width of stepped light pulses (15 ms) were kept constant for all stimulation protocols. Power output at each optic cannula was 9 ±1 mW.

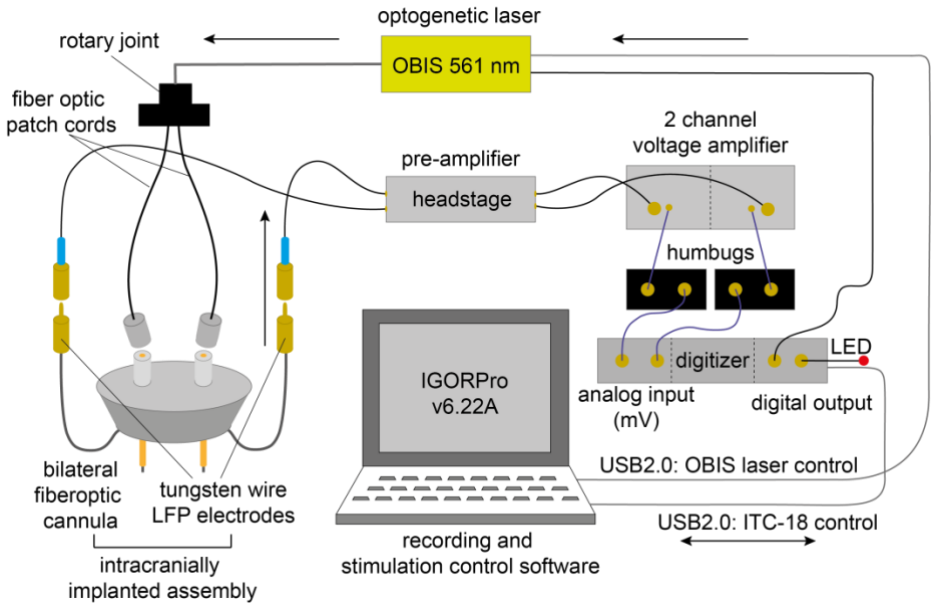

Figure 2.2 Experimental setup. Arrows indicate direction of recording/stimulation. Bilateral fiberoptic cannulas coupled to single coated tungsten wires used for LFP recordings were implanted above both hippocampi of PV-Cre::APP/PS1 and APP/PS1 animals. Hippocampal LFPs were recorded during various behavioral tests using a headstage preamplifier, in turn connected to an extracellular amplifier. 50 Hz noise was filtered using two humbugs (one per recording channel). Digitization of the LFPs was carried out using the ITC-18 board, which was also used to send transistor-transistor logic (TTL) pulses to the OBIS 561nm laser when optogenetic stimulation was required. Mice were connected to the laser via fiber-optic patch cords that were in turn attached to a rotary joint which prevented cables from twisting. Control of laser and readout of LFP recordings was controlled by the software IgorPro v6.22A.

Rhythmic closed loop feedback stimulation

Using a custom designed procedure in IgorPro, a closed-loop stimulation was established to modulate theta frequencies in the local field potential: In intervals of 500ms a Fourier transform of the past 4 s of LFP recording was calculated using a fast Fourier transformation function (FFT). A clear peak in the theta band (4-12 Hz) was defined as a ratio of the peak theta amplitude to the average theta amplitude exceeding 4 or 3. Whenever this criterion was fulfilled, a stimulation interval at the detected peak frequency plus 0.5 Hz with 15 ms pulse duration was initiated and protracted for 5.5 s. After each stimulation event, no new stimulation was initiated for at least 5 seconds to avoid detection of the induced activity.

Arrhythmic closed loop feedback stimulation

The protocol described above was modified with a random jitter that followed a uniform distribution in the interval [-30 ms, +30 ms] to shift the timing of light pulses. This caused the randomization of the pulses across the stimulation interval. Every stimulation interval produced a different randomized set of pulses. However, on average, the stimulation frequency was the detected theta frequency plus 0.5 Hz as during the rhythmic stimulation.

Optogenetic stimulation in the open field

Stimulation protocols were designed in IgorPro. A 20 second protocol was employed to test whether stimulation at 5, 8, 10 or 15 Hz would increase the amplitude of the respective stimulation frequency in the LFP. The protocol consisted of 5 seconds of baseline followed by 5 seconds of stimulation and further 10 seconds of recording in absence of stimulation.

2.5 Behavioral tests

2.5.1 Local field potentials in the open field

The open field test is used to evaluate basic exploratory behavior and potential anxiety levels of the mice, respectively described by parameters like total travelled distance and time spent in the center of the arena. This behavioral test was carried out in a 50x50 cm wooden box, with 50 cm high walls, under dim-light conditions. Mice were inserted in the open field box after having been connected to the LFP recording cables. To do so, mice had to be restrained, but this did not disrupt the exploratory capacity of the animals. To prevent visual distractions, the open field arena was surrounded by a white plastic curtain that hid both experimenter and equipment from the mouse. The arena was evenly but dimly illuminated by means of a standing lamp and ceiling illumination. The camera used to record the behavior of the mouse was fixated on a metal beam placed on top of the arena, part of the structure supporting the curtain. Mice were let freely explore the open field for a minimum of 30 minutes to a maximum of 1 hour, depending on the quality of the acquired LFP recordings. Both left and right channels were acquired, but data from one of the two electrodes only (i.e. from one hippocampus only) was analyzed. A custom-made faraday cage was placed around the open field box. Before and after inserting the mouse in the area, the floor was wiped with 70% EtOH and water and dried with a paper towel.

2.5.2 Novel object recognition and location

Both novel object recognition (NOR) and novel object location (NOL) tests were carried out in the same open field arena, in the same room and employing the same light settings as those mentioned in paragraph 2.5.1. During the “acquisition phase” of both tests, two identical objects were placed in the center of the arena (NOR) or close to one of the walls of the box (NOL). After connecting the mouse to the recording cables and the fiber-optic patch cords used to deliver light through the fiber optic cannulas, mice were inserted in the open field box. For the cohorts described in figures 3.6.1, 3.6.2, and 3.8.1, mice were introduced in the open field and let explore the objects for a total of 6 minutes. This procedure was repeated for another two

times at intervals of 20 minutes (total exploration time of 18 minutes). For the cohort described in figure 3.9, mice were introduced in the open field box once, for 12 minutes for two consecutive days. After a delay of 24 hours, on the third day, one of the two objects was either replaced with a new one (NOR) or its position was swapped to the opposite corner of the arena (NOL). Mice were connected to the amplifier system and stimulation laser and then inserted in the arena and let freely explore the objects for 10-12 minutes (testing phase). The corner of entrance was pseudorandomized across groups and either changed between acquisition and testing phase (NOR) or kept constant (NOL). The objects used for the acquisition phase of the NOR (familiar objects) and for both acquisition and testing phase of the NOL were two cell culture flasks (ca. 15 cm in height) filled with brown ground and sealed with a yellow cap. As a novel object, a cylindrical aluminum can filled with liquid was used (ca 15cm in height). After completion of the test, objects and arena were wiped with 70% EtOH and water.

2.5.3 Y-Maze

Several variants of the Y-Maze test are available, to be used according to the type of memory to be assessed. In our case, we employed a version of the Y-Maze that enables assessment of spatial working memory, a hippocampal dependent process requiring egocentric and allocentric navigational strategies. The Y-Maze consisted of three corridors disposed in the shape of a Y with an angle of 45° between each other. Black and white geometric shaped visual cues were glued at the end of each arm. Mice were placed in the center of the Y-Maze and let freely explore the maze for a total of 9 minutes.

2.6 Combined laminar probe LFP recordings and two-photon calcium imaging

2.6.1 Silicon probes and amplifier system

16-channel silicon probes for laminar LFP recordings were purchased from Neuronexus (A1x16-5mm-100-177 packed in an H16_21 mm connector, Neuronexus, Ann Arbor, Michigan, USA). Electrode sites had a dimension of 177 µm and were spaced at a distance of 50 or 100 µm along the shank of the probe, in a linear fashion. Recording sites were made with iridium and the shank had a dimension of 50 or 100 µm. To enable placement of the connector further away from the implanted shank, the probes were equipped with a 21 mm long flexible cable between the shank and the connector. A portable headstage was used to filter, amplify and digitize the recordings of neural data (RHD-16-2132-omnetics connector A7904, Intan Technologies, Los Angeles, California, USA) was connected to an ultra-thin serial peripheral interface recording cable (SPI-RHD 6ft, part #C3216, Intan Technologies). The cable was in turn connected to an OpenEphys acquisition board (Siegle JH et al., 2017), which streamed the

information via a USB2.0 to the PC. Data was sampled at 10kHz and not filtered during acquisition.

2.6.2 Hippocampal window and laminar probe implantation

To enable access to the CA1 area, a hippocampal window was implanted above the alveus of the right hemisphere of Thy1-GCaMP6f::APP/PS1 mice. The construct consisted of a stainless steel cylinder (1.5 mm high), with a circular coverslip (#1 thickness) glued at its bottom by means of LED curable glue (Norland Products, Cranbury, New Jersey). After preparing the skull according to the procedures described in section 2.3.3, a biopsy punch (3 mm ∅, PFM Medical, Cologne, Germany) was used to mark the position of the cranial window on the skull. The centre of the circular shape was at the following coordinates from bregma: AP -1.90mm and ML +2.10 mm. Afterwards the portion of the skull marked with the biopsy punch was removed with the dental drill and the dura was exposed. After incision of the dura with a sharp needle (Sterican® cannula, BL/LB, 27G), the cortical tissue above the hippocampus (ca.1 mm of cortex) was removed with an automatic pump connected to a blunt needle at the end (Sterican® cannula, blunt, 21G and 27G). The axons composing the corpus callosum were also partially lifted and moved to the side of the window, to guarantee penetration of the excitation light through the coverslip upon imaging. To prevent blood coagulation and clotting once the cortical tissue was aspirated, the exposed brain tissue was regularly perfused with 1x PBS. If necessary, excessive bleeding was stopped with an absorbable gelatine sponge (GELITA-SPON®). The hippocampal window was manually inserted in the cavity and glued to the surrounding skull, provided the absence of liquid, using instant glue (Pattex instant adhesive, Henkel, Dusseldorf, Germany). Once the window was firmly fixated on the skull, a hole was drilled on the left hemisphere (AP -2.0 mm and ML -1.65 mm from bregma) to proceed to the implantation of the silicone probe for laminar recordings of LFPs in the contralateral hemisphere. The probe was carefully mounted on a custom-made holder which, in turn, was controlled by the motorized micromanipulator (Luigs and Neumann, Ratingen, Germany). After removing the dura and positioning the probe at the above-mentioned coordinates, this one was lowered until a depth of 2.5 mm from brain surface. A drop of curable composite was applied to the hole to fix the shank of the probe to the skull of the animal. Then, the connector of the probe was glued to the left side of the skull using the LED curable composite (GRADIA® DIRECT Flo). Reference and ground electrodes, which consisted of fine and very flexible cables already equipped on the probe, were inserted in the cerebellum through two previously drilled holes in the skull. Finally, a custom-made headbar was positioned on top of the probe's connector with the help of a mechanical micromanipulator (Narishige, Tokyo, Japan) sliding

on a rail (Thorlabs, Newton, USA) on the metal breadboard where the surgery was carried on (Thorlabs).

2.6 Two-photon microscopy

2.6.1 Image acquisition

In-vivo two-photon microscopy on awake, head-fixed animals, was conducted with a custom built galvo-resonant system (Thorlabs, Newton, USA) on a two-photon microscope equipped with a titanium sapphire (Ti:Sa) 80MHz Chamaleon Ultra-II laser (Coherent, Dieburg, Germany). To excite GCaMP, the laser was tuned at 920nm, its emission was detected using a GaAsP photomultiplier (PMT, Thorlabs, Newton, USA). An additional band-pass filter (525/50, AHF, Tübingen, Germany) was placed in front of the PMT to enhance signal to noise ratio. Images were acquired through a 16x water immersion objective (NA 0.8, N16XLWD, Nikon, Düsseldorf, Germany) at a scanning frequency of 30 Hz. Pixel size was kept constant at 0.715 µm. Image acquisition parameters and laser power were controlled using the ThorImage software.

2.6.2 Linear treadmill and head-fixation procedures

A three-wheeled linear treadmill and the 2 m long belts were purchased from Luigs and Neumann (Luigs and Neumann, Ratingen, Germany). Each mouse was exposed to one belt only. The position of the mouse along the belt was recorded via an optical mouse sensing the movement of one of the wheels of the treadmill. Information was streamed to the PC via a USB2.0, processed with a custom-written Python script (Python 2.7, Python Software Foundation, Delaware, USA) and then fed into the ITC-18 digitizer board. Data was collected via the IgorPro software, together with the frame trigger signal of the two-photon microscope. Synchronization of imaging and recording of the belt's position was achieved by means of a digitizer board (National Instruments, Mopac Expwy, USA), in which the first pulse of the frame trigger served as start signal for the recording of the belt's position.

Mice were handled for three days and provided sucrose (20%, dissolved in drinking water) as reward prior to first exposure to the linear treadmill. During this time interval, mice were exposed to the experimenter's hand. On the fourth day, mice were placed on the treadmill, where they were head-fixed. Head fixation was provided with an adaptor metal plate attached via a screw to the head-bar mounted on the head of the animal. In turn, the adaptor was inserted into a three-piece jointed head-holder (Luigs and Neumann, Ratingen, Germany), attached to the same components onto which the 16x objective was screwed. Imaging of neural activity in

combination with laminar LFP recordings was carried out for 20-30 minutes per session. Mice were then returned to the homecage and given sucrose as a reward.

2.7 Immunohistochemistry

2.7.1 Perfusion and vibratome sectioning

After completion of all behavioral and imaging procedures, or after stereotactic injections for anterograde tracing, mice were sacrificed and their brains extracted for further histological characterizations. To do so, they were transcardially perfused with 1xPBS and 4%Paraformaldehyde (PFA) using an electric pump, after being given a lethal dose of anesthesia intra-peritoneally. Brains were stored in 4%PFA for 24- 48 hours at 4°C and subsequently transferred to a solution of 1xPBS and 0.01% sodium azide (NaN_3), which functions as a bactericide. Sectioning was performed with a vibratome (Leica Biosystems, Wetzlar, Germany) equipped with disposable razor blades. Brain slices varied in thickness (50 or 100 µm) and in orientation plane (coronal or sagittal), and they were stored in multi-well plates filled with 1xPBS-Nazid (0.01%) at 4°C.

2.7.2 Fluorescent immunohistochemistry

Post-mortem fluorescent immunofluorescent stainings were performed using various antibodies on free-floating sections (see table 2.7.1). However, in general, brain slices were simultaneously permeabilized, blocked and incubated with the first antibody over night at 4°C on a shaker (300 rpm) in a solution composed by 0.2%Triton-X100 (AppliChem GmbH, Darmstadt, Germany), 4% normal goat serum (NGS 10%, Thermo Fisher Scientific, Darmstadt, Germany) and 2% bovine serum albumin (BSA, Carl Roth GmbH + Co. KG, Karlsruhe, Germany). On the next day, the primary antibody solution was carefully aspirated with a disposable pipette and slices were washed for three times in 1xPBS (3 times for 5 minutes). Then, slices were incubated for 1:30 hours with the secondary antibody (300 rpm, RT), dissolved in a solution containing 3% BSA in 1xPBS. Then, brain slices were washed with 2% Triton-X100 for 5 minutes and again rinsed with 1xPBS (3x5 minutes). Following removal of the TritonX100 solution, chemical stains for either amyloid plaques or cell bodies were performed. To stain Aβ plaques, the compound Methoxy X04 (MeX04; 0.5 µg/µl MeXO4, 10% DMSO, 45% 1,2-propanediol) was pipetted in the well, incubated for 30 minutes and then washed away with 1xPBS (3x5 minutes). To stain the Nissl substance, slices were incubated with NeuroTrace®435/455 (Invitrogen, Darmstadt, Germany) for 20 min and then rinsed with 1xPBS. Slices were either stored in the multiwall plates (in 1xPBS-Nazid) or mounted on glass microscope slides (Carl Roth GmbH,

Karlsruhe, Germany) using fluorescent mounting medium (Dako, Deutschland GmbH, Hamburg, Germany) and glass coverslips (Carl Roth GmbH).

Compound	Species	Dilution	Company	Product no.
α-PV primary Ab	Rabbit α-mouse	1:1000	Swant (Marly, Switzerland)	PV25/PV27
α-mCherry primary Ab	Rat α-mouse	1:5000	ThermoScientific (Germany)	M11217
α-SOM primary Ab	Rat α-mouse	1:250	Millipore	MAB354
Alexa Fluor®488	Goat α- rabbit	1:400	Life Technologies (Carlsbard, USA)	A11008
Alexa Fluor®594	Goat α- rat	1:400	Life Technologies (Carlsbard, USA)	A11007
NeuroTrace®435/455 (Nissl stain)	-	1:400	Life Technologies (Carlsbard, USA)	N21479

Table 2.7.1 Antibodies and chemical compounds used for immunohistochemical stainings

2.7.3 Confocal microscopy

Confocal microscopy pictures were acquired using a Zeiss system (LSM700, Carl Zeiss Microscopy, Jena, Germany). Fluorescent emissions were collected using photomultipliers (PMTs) and pinhole size was set at 1 airy unit. A 488nm wavelength laser was used for excitation of Alexa Fluor 488® (Life Technologies, Carlsbard, Germany). Fluorophore emission was bandpass filtered (490-555 nm). For excitation of Alexa 594® and tdTomato, a 555 nm wavelength excitation laser was employed, and their emission was long pass filtered at 580 nm. All sections were stained with the MeXO4 dye for plaque detection. MeXO4 was excited with a 405 nm wavelength laser and emission was short pass filtered at 490nm. For detection of all three dyes, two separate PMTs were employed, (green and blue on PMT1 and red on PMT2). Images were acquired with variable resolutions. Importantly, for histological quantifications of SST-Cre::APP/PS1 axonal densities, overview images to confirm injection site were acquired on 50µm sagittal sections at a frame size of 512x512 µm in x-y direction and a pixel size of 0.781µm/pixel. Afterwards, the same area of dorsal medial entorhinal cortex (1550x300 µm) was scanned with a frame size of 1280x1280 µm and a pixel size of 0.26µm/pixel, and z-stacks for a total volume of 30 µm in depth were acquired with 18 planes per z-stack.

2.8 Data analyses

2.8.1 Baseline recordings in the open field

Peak frequency and power of LFP frequency bands were extracted from spectrograms produced with the wavelet method in MATLAB R2015b and R2016b (The MathWorks, Inc., Natick, USA**)** using the FieldTrip toolbox {Oostenveld, #1947}. Data acquisition consisted of several 3 minute long LFP recordings, performed as mice were actively exploring the open field arena. Only recordings where the mice were actively exploring the open field were included in the analysis (total travelled distance >100 cm in 3 minutes). Additionally, a velocity threshold of ≥3 cm/sec was introduced, and only those intervals of the LFP were used to compute the wavelet transform. Intervals of movement across recordings were then stitched together, and theta oscillations were detected only when smoothed peak theta amplitude (5-12 Hz) increased by a ratio of 2 (empirically set) over the mean delta band (4-5 Hz) within the previously velocity-thresholded LFP trace. For each animal, one spectrogram was produced as an average of 1-6 recordings (each 3 minutes long). Travelled distance, mean velocity and time spent in the center (defined as the squared portion of the open field being 5 cm distant from every wall of the arena) were automatically analyzed in EthoVision XT (v.11.5 and 13.5, Noldus, Wageningen, NL).

2.8.2 Optogenetic sitmulation in the open field

Fourier transformations of baseline and stimulation intervals were computed with MATLAB using the quickFFT algorithm. The peak amplitude of the frequency of interest (f_i , 5, 8, 10 or 15 Hz) was extracted for both baseline (5 seconds) and stimulation intervals (5 seconds) and imported to Microscoft Excel. Two to six stimulation protocols were applied and analyzed per mouse.

2.8.3 Theta-gamma modulation index

The theta-gamma modulation index (MI) was calculated as described in Tort et al. (2010). Briefly, the MI detects phase-amplitude coupling between theta phase and, in this case, mid-gamma oscillations (60-80 Hz). The phase modulating frequency, in this case theta (5-11 Hz) and the amplitude modulated frequency, in this case gamma are defined as f_P and f_A, respectively. First, the raw LFP signal was filtered at theta frequencies (5-11 Hz). Then, the phase and amplitude information of the theta filtered signal were extracted using a Hilbert transform algorithm. In the next step, the amplitude of the fA is plotted against the phase of fp. The MI is then calculated by measuring the deviation of the obtained distribution from a

hypothetically uniform distribution. The higher the MI, the greater the deviation of the observed distribution from a uniform distribution, indicating that the f_A signal is modulated by f_P.

2.8.4 Freely moving behavior

Behavioral analyses were conducted using the software EthoVisionXT (v. 11.5 and 13) and exported in Microsoft Excel (v. 2010 and 2016, Microsoft Corp., USA). For all tests, the center point of the animal was considered to calculate travelled distance and mean velocity. For the NOR and NOL tests, object exploration was considered any interval in which the nose point was within the area surrounding the object (manually defined, 3 cm around each side of the object). For the Y-maze, arm exploration was considered when the center point of the animal had crossed the manually defined border of the arm. Discrimination index (DI) for both NOR and NOL was calculated as: (time exploring new or displaced object/total time exploring objects)*100 Alternation percentage for the Y-maze was calculated by the Ethovision software with the following formula: [(number of alternations)/(total number of arm entries − 2)] × 100. Exploration was considered when the nose point of the animal found itself within the 3cm radius surrounding the objects in both cases. For all behavioral tests, the behavior of the animals was analyzed for a total duration of 5 minutes during the test phase. For Fig. 3.6.1 and 3.6.2 scoring started 4 minutes after mice were in the arena. For Figures 3.8.1 and 3.8.2, scoring started once mice explored either of the two objects. Fig. 3.8.2; time exploring objects was scored manually due to interference of the fiber optic patch cords with the software detection.

2.8.5 Two-photon in vivo calcium imaging

Calcium transient preprocessing

Motion correction of time-series data was performed using a combination of efficient subpixel registration and in-frame motion correction with the Lucas-Kanade method (Lucas and Kanade 1981). Alternatively, the Fiji macro TurboReg (Dr. Philippe Thévenaz, Swiss Federal Institute of Technology) was used. Only data that did not show a shift larger than 10 µm for more than 10 consecutive frames after registration was analyzed. Regions of interest (ROIs) were manually drawn around principal cell bodies in CA1 using ImageJ/Fiji software on an average intensity projection image of a 1 minute long time series during which the animal was not moving. Then, the ROI mask was applied to the full time series and the change in mean gray value over time (that is GCaMP6 fluorescence changes) for each ROI was stored as a text file.

To calculate the ΔF/F, the baseline fluorescence F0 was subtracted from the F (peak fluorescence) signal and divided by F0 (baseline fluorescence): ΔF/F= (F-F0)/F0. F0 was

calculated by averaging the smallest 20% fluorescence values of the time series. The algorithm used for calcium detection was implemented in Python (v.3.7.8).

Identification of spatially tuned cells

To identify spatially tuned cells from the identified calcium transients, analyses were performed using custom scripts written in Python (v. 2.7). Upon motion correction of the time series, performed as described, ROIs were manually drawn around cells that showed a 10% increase in_ΔF/F during intervals of active running. Running was defined as intervals of movement during which the velocity of the animals was ≥3cm/sec. Gray values of fluorescence were then extracted only during these phases, and the ΔF/F was calculated as previously described. To identify place cells (spatially tuned cells) from the Ca^{2+} activity, a procedure described in Dombeck et al 2010 was employed. Animals were running on a 2 m linear treadmill (not textured), which was divided into spatial bins of 2 cm, thus resulting in a total of 100 positions. Then, the ΔF/F of all the previously identified ROIs was calculated as a function of virtual position for each of the 100 positions on the treadmill. Putative place cells were identified as cells whose ΔF/F was contiguously higher than 25% of the difference between the peak ΔF/F value (for all 100 bins) and the baseline value (mean of lowest 25 out of 100 ΔF/F values) at the position taken into consideration. Then, place cells were further selected based on the following criteria: 1) the place filed had to be longer than 16cm (8 bins); 2) one value had to be 10% mean ΔF/F; 3) the mean ΔF/F in the place field had to be more than two times the ΔF/F outside of the field; 4) significant transients, defined as a transient that lead to 4 ΔF/F values to be larger than 2.5 times the rolling mean and SD in a 6 seconds window, had to be present at least 33% of the times that the animal crossed the field.

2.8.6 Histological quantifications

Aβ plaque burden and cell densities (SOM^+ and PV^+ neurons in the medial entorhinal cortex)

For each mouse, 3-5 images (1 image per slice) were used for analyses. Plaque burden was assessed as area covered by Aβ plaques after the raw image was binarized (semi-automatically set threshold) using Fiji. Cells were counted manually in the area acquired for each slice and the density was calculated as cell/area.

Quantification of axonal branches in the medial entorhinal cortex of SST-Cre::APP/PS1 animals.

For each mouse, 2-6 images were used for analyses (1 image per slice). Fiji's skeletonization macro was employed on the z-stacks after images were smoothed (Gaussian smoothing, radius of 1mm) and binarized using a manually set threshold.

```
open("image.tif");
run("Split Channels");
selectWindow("C1-image.tif");  #window with signal of interest
run("Smooth (3D)", "method=Gaussian sigma=1.000 use");
setAutoThreshold("Default dark");
run("Threshold...");
setThreshold(3, 255);  # change if necessary
setOption("BlackBackground", false);
run("Convert to Mask", "method=Default background=Dark");
run("Skeletonize (2D/3D)");
run("Analyze Skeleton (2D/3D)", "prune=none show");
saveAs("Results", "image.xls");  #select path manually
close();
selectWindow("Smoothed");
close();
selectWindow("C1-image.tif");
close();
selectWindow("C2-image.tif");
close();
```

2.9 Statistical analyses

All statistical analyses were performed using the GraphPad Prism 7 software (GraphPad Software Inc., La Jolla, USA). Normality of data distribution was tested using the D'Agostino Pearson normality test or Shapiro- Wilk normality test. Each graph shows individual data points and bars represent mean ±standard error of the mean (SEM) for normally distributed data or median for not normally distributed data. In the latter case, box plots represent median, 25^{th} and 75^{th} percentile and whiskers represent maximum and minimum values. In the text, not normally distributed values are indicated as median [25^{th} percentile, 75^{th} percentile]. Significances were tested using different two-tailed tests, reported in the figure legends for all individual cases. Alpha value was set at 0.05 for all tests employed. For not significant results, the annotation n.s. was used in all graphs. Graphs were exported from the GraphPad Prism software and figures were prepared with Adobe Illustrator CS5 Version 15.0.1 (Adobe, San José, USA). Results of all statistical tests are partially described in the figure legends and fully in the Appendix, section 6.5.

3 Results

3.1 Theta oscillations and locomotor activity of PV-Cre::WT and PV-Cre::APP/PS1 mice

Hippocampal oscillatory activity is the result of complex micro- and macro-circuit operations that result in the synchronous depolarization and hyperpolarization of pyramidal cells in the CA1 area. In humans and rodents, different frequency bands correlate with specific brain states and behaviors. Theta oscillations are thought to reflect the "online state" of the hippocampus. Indeed, theta oscillations correlate with states of wakefulness and alertness (Buzsaki, 2002; Korotkova et al., 2018). Most importantly, reducing the power of theta oscillations by inactivation of the medial septum causes spatial navigation deficits in rodents (Bolding et al., 2020; Brioni, Decker, Gamboa, Izquierdo, & McGaugh, 1990; Koenig et al., 2011; Petersen & Buzsaki, 2020; Winson, 1978). In addition, theta oscillations are thought to support, and constitute a framework for the neural processes underlying not only spatial navigation, but also episodic memory (Buzsaki, 2005). Previously, we had observed that PV-Cre::APP/PS1 wt/tg animals (PV-Cre::APP/PS1) showed a significantly reduced CA1 peak theta frequency compared to PV-Cre::APP/PS1 wt/wt (PV-Cre::WT) littermates aged 9.5 months on average (Ambrad Giovannetti, 2018); PV-Cre::WT: 9.2 ±3.1 months [mean ±SD], PV-Cre::APP/PS1: 10.11 ±3.4 months [mean ±SD]). Interestingly, it is known that the degradation of spatial navigation and episodic memory that occurs with both age and disease (Lester, Moffat, Wiener, Barnes, & Wolbers, 2017) is strongly linked to aberrations in neural oscillatory activity (Palop et al., 2006). Therefore, I investigated whether and how hippocampal oscillatory activity is affected at later stages in PV-Cre::WT and PV-Cre::APP/PS1 animals aged on average 15 months (PV-Cre::WT: 14.6 ±3.03 months [mean ±SD]; PV-Cre::APP/PS1: 15.2 ±3.63 months [mean ±SD]). Single tungsten wire electrodes targeting the CA1-SLM compartment were implanted in both hippocampi together with optic fibers in mice that had previously been intracranially injected with an adeno-associated viral vector encoding a Cre-dependent excitatory opsin (*rAAV.DIO.C1V1.mCherry*) or Sham-treated. After a period of recovery and handling in the experimental room, animals were introduced in an open field arena, where their exploratory activity was recorded simultaneously to their hippocampal local field potentials (LFPs; **Fig. 3.1 a-c**). Type I theta oscillations (~8 Hz) are most prominent when animals are moving or exploring an arena. Therefore, LFP analysis was restricted to bouts of movement when the animal's velocity was equal or higher than 3 cm/sec. During the open field test, peak theta frequency of PV-Cre::WT and PV-Cre::APP/PS1 mice (**Fig. 3.1 c**; PV-Cre::WT: 7.51

±0.05 Hz, n= 38 mice; PV-Cre::APP/PS1: 7.43 ±0.0.8 Hz, n= 28 mice) was not significantly different. Similarly, neither the absolute amplitude (**Fig. 3.1 d**) nor the average duration of theta oscillations (**Fig. 3.1 e,** ThetaON; PV-Cre::WT median 120.3 sec [106.5 sec, 143.5 sec]; PV-Cre::APP/PS1 median 122.5 sec [96.08 sec, 153.4 sec]) were significantly different between PV-Cre::WT and PV-Cre::APP/PS1 animals. Because theta oscillations positively correlate with locomotor activity, mean velocity and travelled distance were quantified per each genotype. This revealed that the mean velocity of PV-Cre::WT and PV-Cre::APP/PS1 mice (**Fig. 3.1. f**; PV-Cre::WT median: 9.68 cm/sec [8.53 cm/sec, 10.55 cm/sec]; PV-Cre::APP/PS1 median 9.54 cm/sec [7.86 cm/sec, 10.95 cm/sec]) was not significantly different, opposite to what we had previously observed in the younger cohort of mice. Additionally, total distance travelled in the open field (**Fig. 3.1 g**; PV-Cre::WT median: 942.8 cm [771.8 cm, 1141 cm]; PV-Cre::APP/PS1 median 977.1 cm [727.7 cm, 1234cm]) was not statistically different. Finally, the time spent in the center of the open field (**Fig. 3.1 h**; PV-Cre::WT: 19.28 ±1.59 sec; PV-Cre::APP/PS1: 14.88 ±1.57 sec), a measure of anxiety-related behavior, was not significantly different between PV-Cre::WT and PV-Cre::APP/PS1 animals.

In summary, the presented results indicate that theta oscillations recorded in the CA1-SLM of PV-Cre::WT and PV-Cre::APP/PS1 mice aged on average 15 months do not differ in peak frequency, amplitude, nor duration when mice are preforming an open field test. However, because it is known that LFP spectral properties change with age, and because we had previously observed a significant difference in peak theta oscillations between younger PV-Cre::WT and PV-Cre::APP/PS1 animals, I next investigated whether and how theta oscillations in the hippocampus progressively change with age in both PV-Cre::WT and PV-Cre::APP/PS1 animals (see **Figure 3.2**).

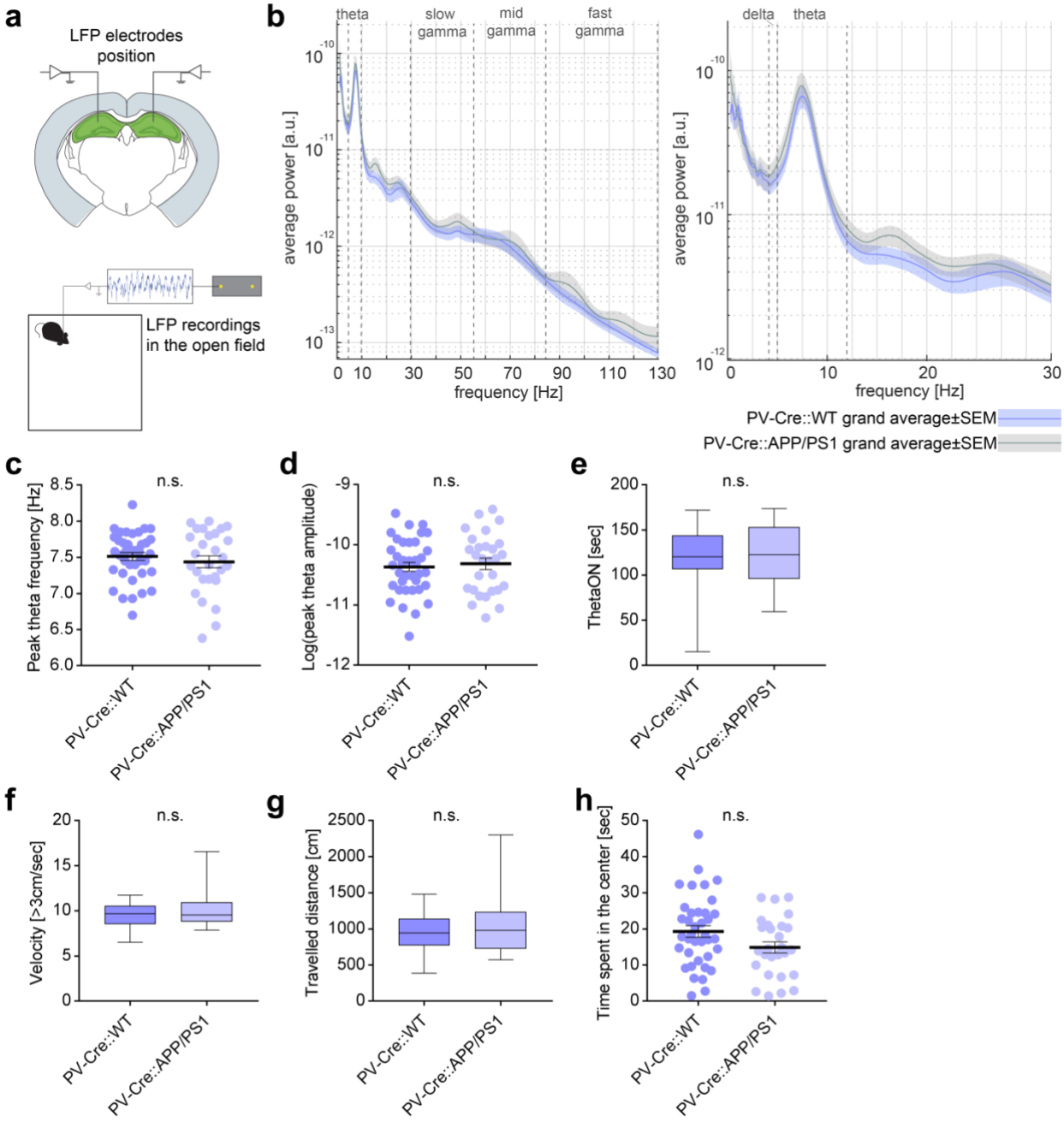

Figure 3.1 Theta oscillations and locomotor activity of 15 month old PV-Cre::WT and PV-Cre::APP/PS1 animals. a) Schematics of electrode implantation site and recording setup. Animals performed an open field test where they could freely explore the arena. **b)** Grand averaged powerspectrum of hippocampal LFPs recorded in the SLM of n= 38 PV-Cre::WT and n= 28 PV-Cre::APP/PS1 animals. **c)** Peak frequency of theta oscillations. Two-tailed unpaired student's t-test: t(64)= 0.78, p= 0.43. **d)** Logarithmically transformed peak amplitude of theta oscillations. Two-tailed unpaired student's t-test: t(64)= 0.43, p= 0.66. **e)** Average duration of theta oscillations over 3 minutes (ThetaON= theta detection time). Two-tailed Mann-Whitney test: p= 0.54. **f)** Mean velocity during movement intervals ≥3cm/sec. Two-tailed Mann-Whitney test: p= 0.52. **g)** Travelled distance. Two-tailed Mann Whitney test: p= 0.79. **h)** Time spent in the center of the open field. Two-tailed student's t-test: t(63)= 1.98, p= 0.06. Graphs show individual values (mice) and mean ±SEM (**c** ,**d**, **e**, **h**). Box plots indicate median, 25th and 75th percentiles, and whiskers represent min. and max. values (**f**, **g**). Each

individual value is an average of 2-6 recordings of 3 minutes each (max duration of recorded theta oscillations per recording 180 seconds).

3.2 Peak frequency of theta oscillations is inversely correlated to age in PV-Cre::WT animals

To further investigate whether and how theta oscillations are modulated by age or behavior within each genotype, correlations were computed between the oscillation parameters described above (peak theta frequency, amplitude and duration of theta oscillations) against age and velocity. This revealed that peak frequency of theta oscillations negatively correlate with age of PV-Cre::WT animals (**Fig. 3.2 a**; Y-intercept: 8.08 ±0.25 Hz [best fit values ±SEM], r^2= 0.12, Sy.x= 0.31, *p= 0.03). However, neither amplitude (**Fig. 3.2 b)** nor duration of theta oscillations were modulated by age in PV-Cre::WT mice **(Fig. 3.2 c**; Y-intercept= 132,1 ± 26,83 sec [best fit values ±SEM], Sy.x= 33.01, r^2= 0,007, p= 0.61). Because it is known that age can negatively modulate locomotor activity, (Bordner et al., 2011; Shoji, Takao, Hattori, & Miyakawa, 2016; Szentes, Tekus, Mohos, Borbely, & Helyes, 2019), mean velocity was correlated with age of PV-Cre::WT mice. This revealed that, as expected, mean velocity of PV-Cre::WT mice linearly decreases with age (**Fig.3.2 d**; Y-intercept: 11.76 ±1 [best fit values ± SEM], r^2= 0.12, Sy.x= 1.2, *p= 0.03). Peak frequency of hippocampal theta and its amplitude have been shown to positively correlate with the animal's speed (Bender et al., 2015; Fuhrmann et al., 2015; Richard et al., 2013). Here, though, peak frequency of theta oscillations did not correlate with mean velocity of PV-Cre::WT animals (**Fig. 3.2 e**; Y-intercept= 7.28 ±0.41 Hz [best fit values ± SEM], Sy.x= 0.33, r^2= 0.008, p= 0.57). Similarly, amplitude of theta oscillations did not positively correlate with mean velocity in the same animals (**Fig. 3.3 f**). Nonetheless, the data showed a positive linear correlation between mean velocity of movement and duration of theta oscillations (**Fig. 3.2 g**; Y-intercept= -25.01 ± 32.3 sec Sy.x= 26.52 [best fit values ±SEM], r^2= 0.35, p<0.0001). This indicates that, on average, mice that move faster also move for longer time intervals, resulting in longer intervals of theta detected by the algorithm employed for the analysis.

The findings described in PV-Cre::WT mice were only partially recapitulated in PV-Cre::APP/PS1 animals. In fact, neither peak frequency (**Fig. 3.2 h**; Y-intercept: 7.82 ±0.36 Hz [best fit values ±SEM]; r^2= 0.06; Sy.x= 0.73; p=0.18), amplitude (**Fig. 3.2 i)**, nor duration of theta oscillations **(Fig. 3.2 j**; Y-intercept= 134.7 ± 25.6 sec [best fit values ±SEM], Sy.x= 30.6, r^2= 0.006, p= 0.67) correlated with age in PV-Cre::APP/PS1 mice. Additionally, in contrast to the PV-Cre::WT group, no linear decrease of mean velocity was observed with age in PV-Cre::APP/PS1 animals (**Fig. 3.2 k**; Y-intercept: 11,79 ±1,57 cm/sec [best fit values ±SEM]; r^2= 0.04; Sy.x= 1.88, p= 0.28). As for PV-Cre::WT mice, peak frequency of theta oscillations in PV-Cre::APP/PS1 mice was not correlated with mean velocity of the animals (**Fig. 3.2 l**; Y-

intercept= 8.1 ± 0.4 [best fit values ±SEM], Hz Sy.x= 0.42, r^2= 0.09, p= 0.1) nor amplitude of theta oscillations (**Fig. 3.2 m**). Similar to the PV-Cre::WT group, duration of theta oscillations was directly proportional to the mean velocity of PV-Cre::APP/PS1 animals (**Fig. 3.2 n**; Y-intercept: 13.62 ±23.43 sec [best fit values ±SEM]; r^2=0.46; Sy.x= 22.43; p<0.0001). This indicates that theta oscillations are sustained during intervals of continuous movement in both PV-Cre::WT and PV-Cre::APP/PS1 animals, and that this ability does not deteriorate with age (**Fig. 3.2 c** and **Fig. 3.2 j**).

In summary, these results indicate that, between approximately 9 and 24 months of age, a decline in peak frequency of theta oscillations is observed in PV-Cre::WT animals, but not in PV-Cre::APP/PS1 animals. Because rhythmic disinhibition is the basis for the generation of periodic oscillatory activity in the hippocampus, subtle changes in peak frequency of theta oscillations may reflect alterations of the GABAergic excitatory/inhibitory balance of the circuit. Therefore, we investigated whether theta-gamma coupling, a phenomenon that relies on the function of inhibitory neurons, is also affected in age and /or disease.

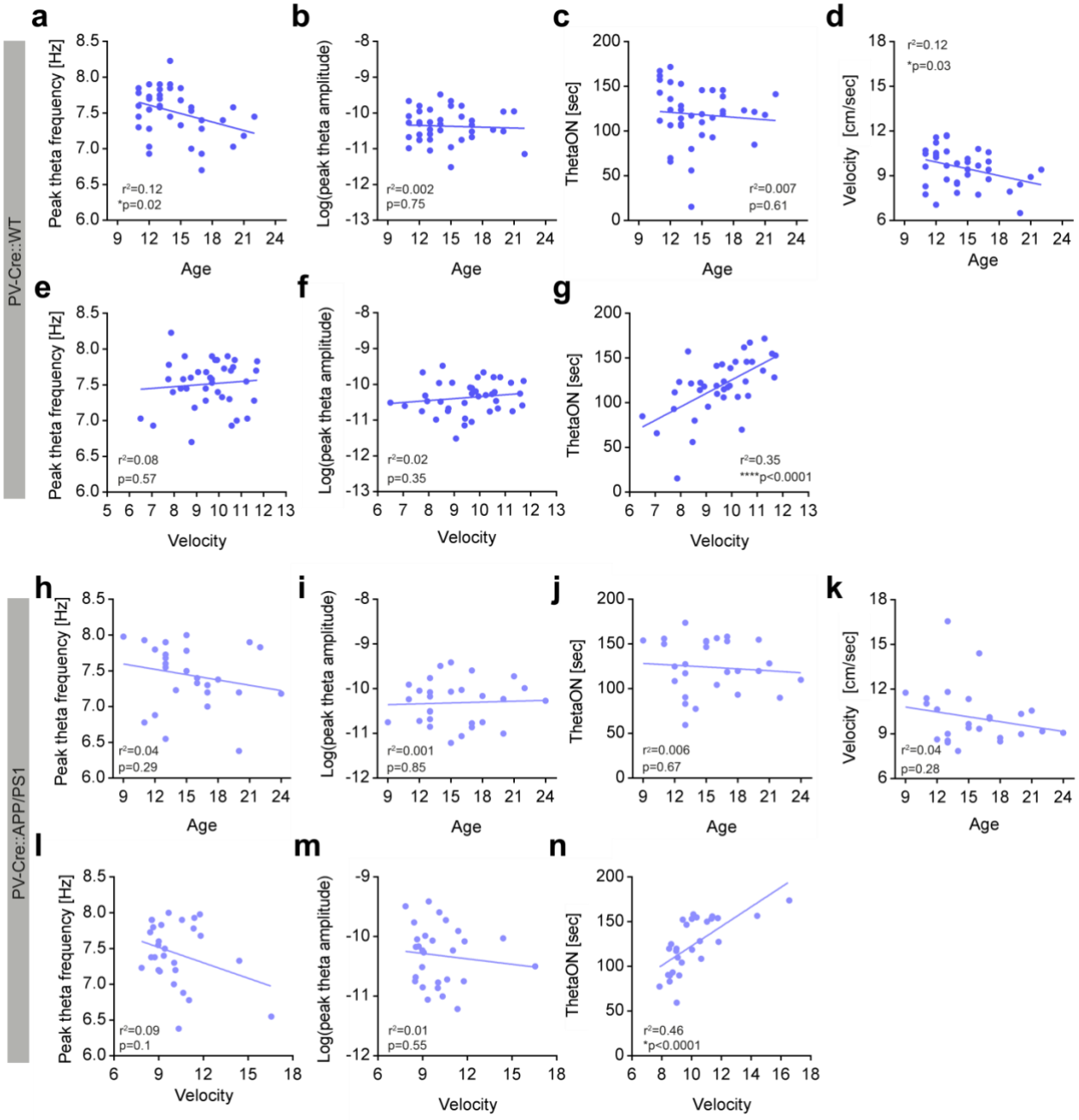

Fig. 3.2 Peak frequency, but not amplitude of theta oscillations negatively correlates with age in PV-Cre::WT mice. a-g) Data from n= 38 PV-Cre::WT animals, same as in 3.1. **a)** Peak frequency of hippocampal theta oscillations as a function of age in PV-Cre::WT animals. Linear regression analysis: r^2=0.12, *p=0.02. **b)** Peak amplitude of hippocampal theta oscillations as a function of age. Linear regression analysis; r^2= 0.002, p=0 .75. **c**) Average duration of theta oscillations in a 3 minute interval (ThetaON) during movement as a function of age. Linear regression analysis, r^2= 0.07, p= 0.61. **d)** Mean velocity during exploration of the open field as a function of age. Linear regression analysis; r^2= 0.12, *p=0.03. **e)** Peak frequency of theta oscillations as a function of mean velocity. Linear regression analysis; r^2= 0.008, p= 0.57. **f)** Peak amplitude of hippocampal theta oscillations as a function of mean velocity. Linear regression analysis; r^2=0.02, p=0.35. **g)** Average duration of theta oscillations during active exploration as a function of mean velocity. Linear regression analysis; r^2= 0.35, p<0.0001. **h-n)** Data from n=28 PV-Cre::APP/PS1 animals, same as in 3.1. **h)** Same as **a**. Linear regression analysis: r^2=0.04; p=0.29**. i)** Same as **b**. Linear regression analysis: r^2=0.001, p=0.85. **j)** Same as **c**. Linear regression analysis: r^2= 0.006, p=0.67. **k)** Same as **d**. Linear regression analysis: r^2=0.04, p=0.28. **l)**

Same as e. Linear regression analysis: r^2= 0.06, p= 0.18. **m)** Same as f. Linear regression analysis: r^2= 0.01, p= 0.55. **n)** Same as **g**. Linear regression analysis: r^2= 0.46, p<0.0001. Each individual value is an average of 2-6 recordings of 3 minutes each (max duration of recorded theta oscillations per recording 180 seconds).

3.3 Reduced theta-gamma modulation index in PV-Cre::APP/PS1 animals

In mammalian brains, high amplitude, slow oscillations modulate the amplitude and phase of faster, lower amplitude oscillations, a phenomenon known as *cross-frequency coupling* (Buzsaki & Draguhn, 2004). The locking of fast oscillations onto slower oscillations is thought to support information transfer between brain areas that oscillate coherently. In particular, hippocampal theta oscillations modulate the phase and amplitude of gamma oscillations (30-120 Hz) (Korotkova, Fuchs, Ponomarenko, von Engelhardt, & Monyer, 2010; Tort et al., 2010; Tort et al., 2009; Wulff et al., 2009). In the SLM of CA1, slow (30-50 Hz) and mid gamma (60-80 Hz) rhythms are most coherent with CA3 gamma and MEC gamma, respectively (Fernandez-Ruiz et al., 2017). Thus, it is thought that 60-80 Hz gamma oscillations in SLM reflect the interactions between the hippocampus and the MEC (Fernandez-Ruiz et al., 2017). In the SLM, mid gamma oscillations are typically locked to the trough of the theta phase (**Fig. 3.3 a**). The degree of locking of gamma onto the underlying theta is measured with a modulation index (MI); the higher the MI, the stronger the phase-amplitude coupling between theta and gamma oscillations. Strikingly, it is not yet known whether theta-gamma modulation is altered in the APP/PS1 mouse model. Furthermore, it was shown that theta-gamma modulation is altered in subjects with mild cognitive impairment and AD, indicating that aging influences this aspect of the network (Goodman et al., 2018). Thus, the theta-gamma MI (Tort et al., 2010) was calculated for PV-Cre::WT and PV-Cre::APP/PS1 animals performing the open field test. Here, PV-Cre::APP/PS1 animals showed a significantly reduced MI compared to PV-Cre::WT mice (**Fig. 3.3 b**; PV-Cre:: WT: 0.007 ±0.0006, n= 24; PV-Cre::APP/PS1: 0.0048 ±0.00049, n= 21). This result indicates that the amplitude of the gamma oscillation envelope calculated for the PV-Cre::APP/PS1 animals was uniform across all phases of theta (**Fig. 3.3 a**), thereby deviating from what is expected by a phase-modulated oscillation as observed in PV-Cre::WT animals. Moreover, an age-dependent positive correlation between age and modulation index was detected in PV-Cre::WT animals (**Fig. 3.3 c**; Y-intercept: -0.0004 ±0.002 [best fit values ±SEM], r^2= 0.24, Sy.x= 0.002, *p=0.01), but not in PV-Cre::APP/PS1 animals (**Fig. 3.3 d**; 0.004 ±0.002 [best fit values ±SEM], r^2= 0.007, Sy.x= 0.002, p= 0.71).

In conclusion, these findings indicate that theta-gamma modulation in the mid-gamma range is reduced in PV-Cre::APP/PS1 animals. Furthermore, theta-gamma coupling increased linearly with age in PV-Cre::WT but not in PV-Cre::APP/PS1 animals. This, together with the finding that peak theta frequency is reduced with age in PV-Cre::WT animals, suggest that the hippocampal-entorhinal circuit undergoes remodeling in healthy aging and that this was not detected in age-matched PV-Cre::APP/PS1 animals.

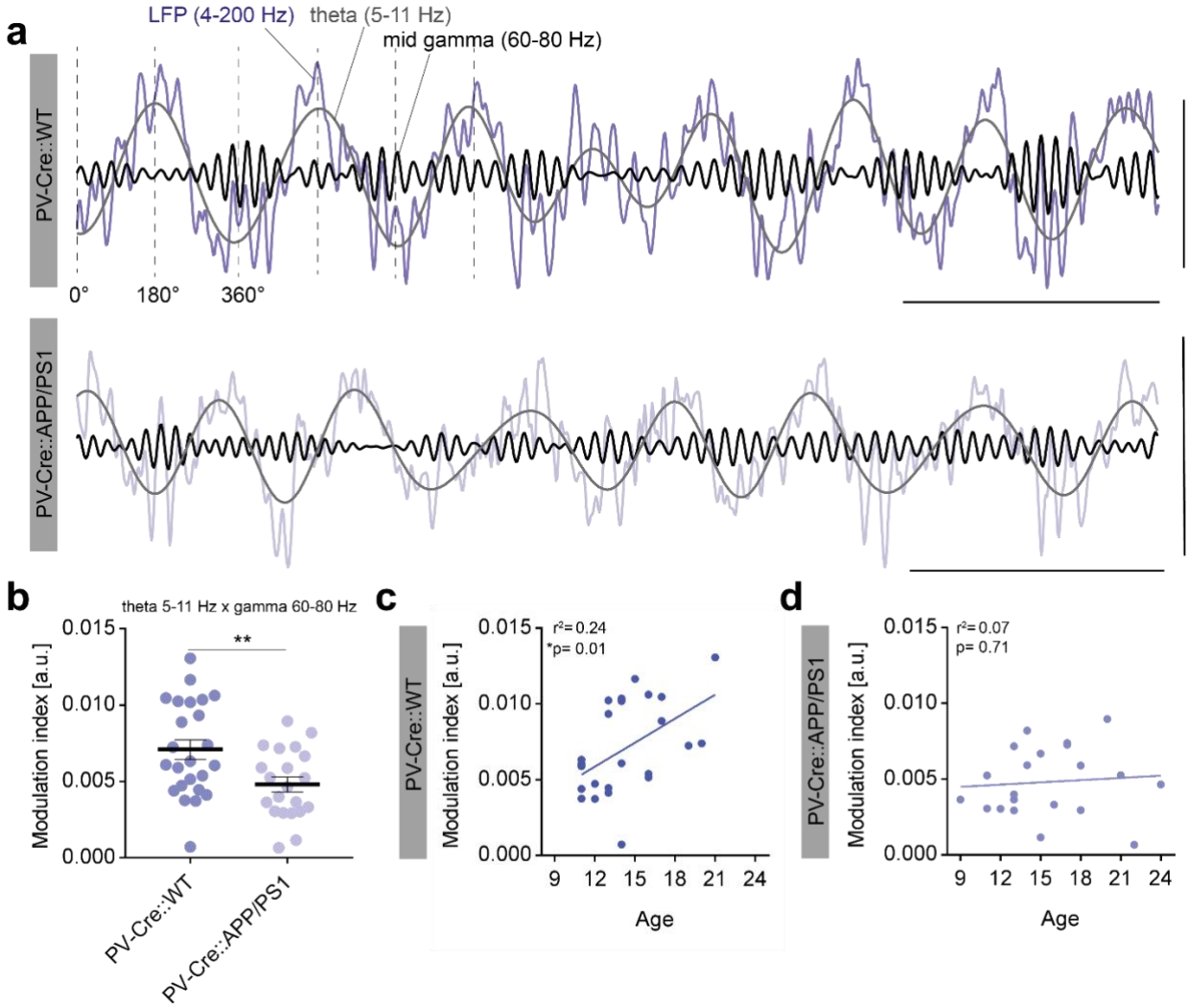

Figure 3.3 Reduced theta-gamma modulation index in PV-Cre::APP/PS1 animals. a) Exemplary LFP recordings filtered in the 4-200 Hz range, 5-11 Hz (theta range) and mid-gamma (60-80 Hz) from on PV-Cre::WT and one PV-Cre::APP/PS1 animal showing how faster frequencies in the mid-gamma range are phase locked on the trough of theta oscillations. Phase of theta cycle is described by degrees and dashed lines (0º, 180º, 360º). Note that in PV-Cre::APP/PS1 the amplitude of gamma oscillations is uniform across all phases of the theta cycle. Scale bars: 200 ms and 1 mV. **b)** Modulation index in PV-Cre::WT and PV-Cre::APP/PS1 animals. Two-tailed unpaired student's t-test: t(43)= 2.79, **p=0.0078. **c)** Modulation index as a function of age in PV-Cre::WT animals. Linear regression analysis: r^2= 0.24, *p=0.01. **d)** Modulation index as a function of age in PV-Cre::APP/PS1 mice. Linear regression analysis: r^2= 0.07, p= 0.71). PV-Cre::WT n= 24 mice, PV-Cre::APP/PS1 mice n= 21. Graphs show individual values (mice) and bars represent mean ±SEM. Each individual value is an average of 4-8 recordings of 3 minutes each.

3.4 Entrainment of theta oscillations via optogenetic stimulation of PV$^+$ interneurons

The oscillatory alterations detected in PV-Cre::WT and PV-Cre::APP/PS1 animals lead to the question whether the hippocampal network would respond to an interventional strategy aimed at rescuing the defects observed in both genotypes. Stimulating PV$^+$ inhibitory neurons represents, on the one hand, a way to restore the decreased inhibitory tone observed in aging and AD-models (Palop & Mucke, 2016; Rozycka & Liguz-Lecznar, 2017). On the other hand, it could serve as a tool to potently control pyramidal neuron action potential generation in a timely manner, hence promoting circuit-wide synchronization. Thus, PV$^+$ interneurons in PV-Cre::WT (18.45± 4.49 months [mean ±SD]) and PV-Cre::APP/PS1 mice (mean age 16.53 ±4.48 months [mean ±SD]) were optogenetically stimulated at frequencies within and outside the theta range (5, 8, 10 and 15 Hz). Delivery of 561 nm light pulses was achieved through fiber optic cannulas implanted above both hippocampi (**Fig. 3.4 a**). The animals had been intracranially injected with an AAV encoding a Cre-dependent excitatory opsin (PV-Cre::WT and PV-Cre::APP/PS1 + C1V1; **Fig. 3.4 b**) or sterile PBS as control (PV-Cre::WT and PV-Cre::APP/PS1 + Sham). Simultaneously, LFPs were recorded to detect whether the optogenetic stimulation would elicit a change in the field's activity. Because of the position of the electrode (i.e. in SLM, **Fig. 3.4 a**), recording an amplitude increase in the LFP would reflect that entorhinal inputs are recruited by the stimulation, as it is known that theta current in this compartment reflects the activity of entorhinal inputs from the temporo-ammonic and perforant-pathway (Z. Gu & Yakel, 2017). Briefly, the recording protocol consisted of 5 seconds of "baseline" LFP recording (no light stimulation), followed by 5 seconds of light stimulation at the mentioned frequencies ("stimulation" interval). Fast Fourier transforms (FFTs) of the unfiltered LFPs were computed for each interval and the peak amplitude of the frequency of interest (i.e. the stimulation frequency) was extracted for both intervals (**Fig. 3.4 c-f**). Optogenetic stimulation of PV-Cre::WT animals expressing C1V1 in PV$^+$ neurons resulted in the increase of the frequency of interest in the LFP for stimulation at 5, 10 and 15 Hz (**Fig. 3.4 g, i, j**). Surprisingly, optogenetic stimulation at 8 Hz, which is among the most prominent theta frequencies observed in a freely exploring mouse, was not sufficient to significantly increase the amplitude of this frequency above baseline (**Fig. 3.4 h**). Indeed, stimulation of PV$^+$ interneurons at 10 Hz and 15 Hz was more efficient compared to stimulation at 5 Hz and 8 Hz in eliciting a frequency matched response from the network (**Fig. 3.5 i, j**). Furthermore, as expected, optogenetic stimulation in PV-Cre::WT mice that did not express the excitatory opsin (PV-Cre::WT + Sham) never resulted in a signifiantly increased amplitude of the stimulation frequency over baseline, ruling out the possibility of inducing light artifacts in the recordings.

Interestingly, the same stimulation protocols in PV-Cre::APP/PS1 animals always resulted in a significant increase of stimulation frequency above baseline in case of C1V1-expressing animals, but not in case of the Sham-treated group (**Fig. 3.4 k-n**). Stimulation at 8 Hz also successfully elicited a network response, in contrast to what was observed in PV-Cre::WT animals. Similar to the results obtained in C1V1-expressing PV-Cre::WT animals, though, stimulation of PV^+ neurons at 10 Hz and 15 Hz strongly elicited a response of the network compared to stimulation at 5 Hz.

Overall, these results indicate that it is possible to entrain hippocampal oscillations at various frequencies in the theta range and outside of it by optogenetically stimulating local PV^+ interneurons in both PV-Cre::WT and PV-Cre::APP/PS1 animals. Optogenetic stimulation efficiently increased the amplitude of the stimulation frequency in the LFP at all frequencies except 8 Hz in PV-Cre::WT animals. Furthermore, as no significant increase in amplitude of the stimulation frequency over baseline was detected in either PV-Cre::WT nor PV-Cre::APP/PS1 mice, it was excluded that the optogenetic stimulation induced photovoltaic artifacts in the LFP.

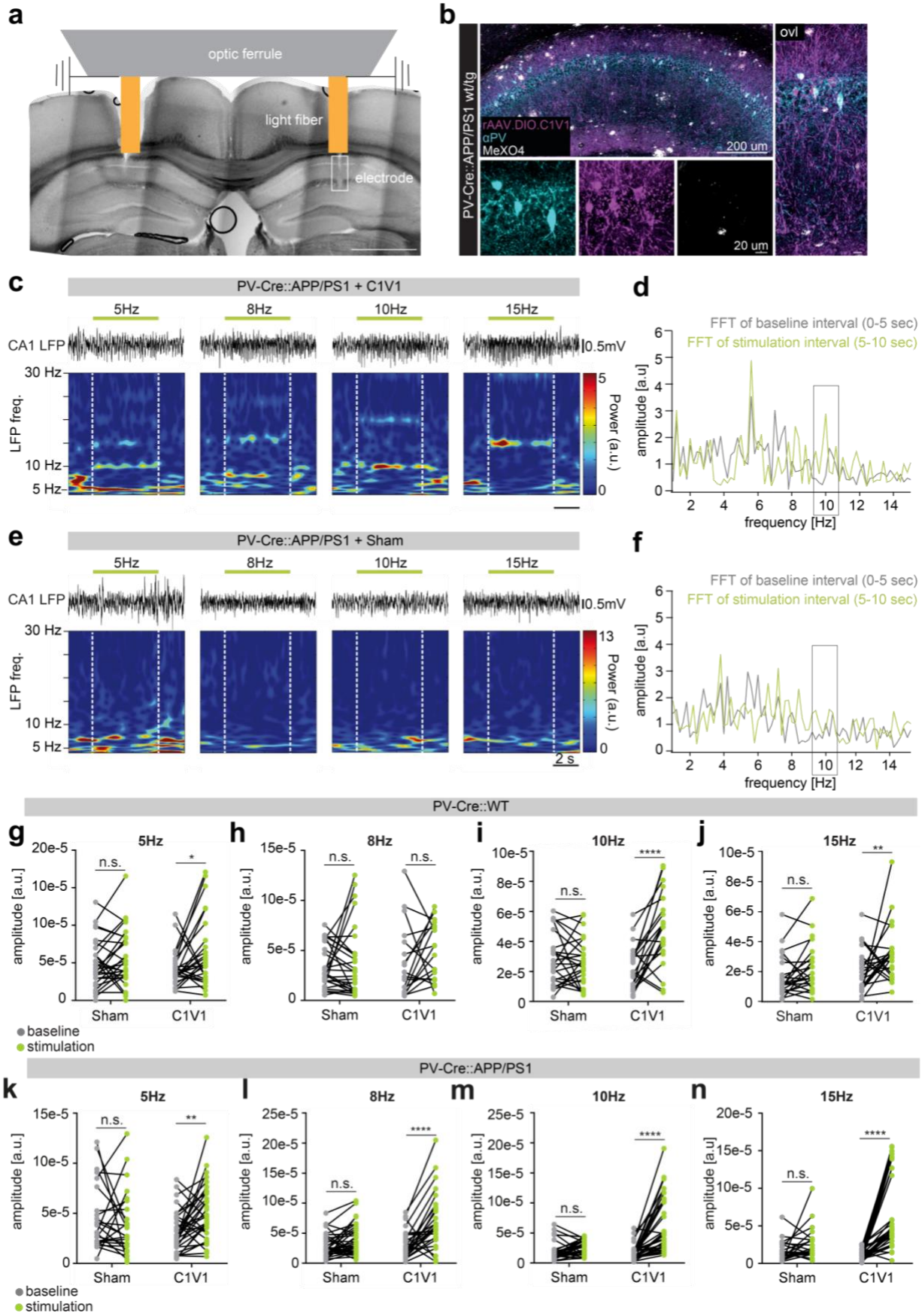

Figure 3.4 Optogenetic stimulation of hippocampal PV⁺ neurons entrains oscillatory activity in CA1. a) Exemplary histological section and schematic of optic ferrule and electrode placement site. White box indicates the tract and position of the tungsten wire (one of two) used for LFP recordings. **b)**

Exemplary histological immunostaining showing co-expression of PV^+ and mCherry, used to tag C1V1, in PV^+ interneurons in the hippocampus. **c)** Exemplary spectrograms showing that optogenetic stimulation at 5, 8, 10 and 15Hz increases the amplitude of the stimulation frequency over baseline in the LFP of a C1V1-expressing animal. **d)** FFTs of the baseline and stimulation intervals of a 10 Hz stimulation epoch in a C1V1-expressing animal. Note that during the stimulation period the amplitude of the 10 Hz component of the LFP increases over the one recorded during the baseline period. **e)** Exemplary spectrograms showing that optogenetic stimulation at 5, 8, 10 and 15 Hz does not increase the amplitude of the stimulation frequency over baseline in the LFP of a Sham-treated animal. **f)** FFTs of the baseline and stimulation intervals of a 10Hz stimulation epoch in a Sham-treated animal. Note that during the stimulation period the amplitude of the 10Hz component in the LFP does not increase in amplitude over the baseline period. **g-j)** Optogenetic stimulation at 5, 8, 10 and 15Hz in Sham-treated and C1V1-expressing PV-Cre::WT animals. **g)** Stimulation at 5 Hz. PV-Cre::WT + Sham, p=0.24; PV-Cre.:WT + C1V1, *p=0.01. **h)** Stimulation at 8 Hz. PV-Cre::WT + Sham, p= 0.53; PV-Cre::WT + C1V1, p= 0.41. **i)** Stimulation at 10 Hz. PV-Cre::WT + Sham, p= 0.62; PV-Cre::WT + C1V1, ****p<0.0001. **j)** Stimulation at 15 Hz. PV-Cre::WT + Sham, p= 0.2; PV-Cre::WT + C1V1, **p= 0.007. **k-n)** Optogenetic stimulation in PV-Cre::APP/PS1 + Sham and PV-Cre::APP/PS1 + C1V1 animals. **k)** Stimulation at 5 Hz. PV-Cre::APP/PS1 + Sham, p= 0.44; PV-Cre:: APP/PS1 + C1V1, **p= 0.005. **l)** Stimulation at 8Hz. PV-Cre:: APP/PS1 + Sham, p= 0.17; PV-Cre:: APP/PS1 + C1V1, ****p<0.0001. **m)** Stimulation at 10 Hz. PV-Cre:: APP/PS1 + Sham, p= 0.17; PV-Cre:: APP/PS1 + C1V1,****p<0.0001. **n)** Stimulation at 15Hz. PV-Cre:: APP/PS1 + Sham, p= 0.27; PV-Cre:: APP/PS1 + C1V1, baseline vs stimulation., ****p<0.0001.

Statistics: two-way repeated measures ANOVA with Holm-Sidak's correction for multiple comparisons Paired comparisons indicate baseline vs stimulation intervals. PV-Cre::WT, n= 18-30 recordings per stimulation frequency in 11 animals; PV-Cre::APP/PS1 animals: 27-40 recordings per stimulation frequency in 13 animals. Graphs show individual values (recordings) and lines show paired condition (baseline interval vs stimulation interval).

3.5 Closed-loop feedback optogenetic stimulation protocol

Previously, we had observed a beneficial effect of a feedback stimulation at theta frequencies for the recognition memory of 13 month old PV-Cre::APP/PS1, but not PV-Cre::WT animals tested in the novel object recognition test (NOR) (Ambrad Giovannetti, 2018). The feedback stimulation protocol was designed so that an increase in amplitude of theta oscillations in the hippocampal LFP above an experimentally set threshold would trigger the laser stimulation at the detected peak theta frequency (between 4 and 12 Hz) (**Fig. 3.5 a-e**). An additional 0.5 Hz were added to the endogenous peak theta frequency during the stimulation (**Fig. 3.5 a**), as this defect was detected in the average peak theta frequency of PV-Cre::APP/PS1 animals exploring an open field. The NOR test relies on the innate exploratory behavior of the mice to investigate a novel object compared to a familiar one, and it does not require prior training nor food restriction. Therefore, on day 1 of the test (**Fig.3.5 f**), mice were inserted in the open field arena from one corner for 3 times (each time for 6 min), at an interval of 20 min apart. Entry corners were pseudo-randomized between genotypes and treatments with the purpose of not introducing spatially confounding factors in the preference of one object over the other. Two identical objects were placed in the center of the open field. On day two of the test, after 24 hours (**Fig. 3.5 f**), mice were inserted in the same open field arena where one of the objects had been replaced with a different one. For this experiment, the walls of the arena were not cued. This test is designed to assess recognition memory by determining the time spent exploring the novel object in comparison to the time spent exploring both objects (total exploration time). A discrimination index (DI) higher than 50% is indicative of correct long-term recognition memory processes. In addition to the improvement in recognition memory of PV-Cre::APP/PS1 animals compared to Sham-injected controls, we have shown that, in PV-Cre::WT animals, the stimulation caused a decrease in recognition memory in C1V1-expressing animals compared to Sham-treated mice (**Fig. 3.5 g**). As expected, the stimulation resulted in an increase of amplitude of stimulated frequency in C1V1-expressing animals (see example in **Fig. 3.5 h**), but not in the Sham-treated groups, as shown by a higher r^2 value (**Fig. 3.5 i**).

These results indicate that entraining, prolonging and normalizing theta oscillations during learning and memory by means of the optogenetic feedback stimulation protocol described in this chapter was sufficient to improve the DI of 13 month old PV-Cre:APP/PS1 animals in the NOR test. In contrast, entraining theta oscillations was detrimental for the recognition memory of age matched PV-Cre::WT animals.

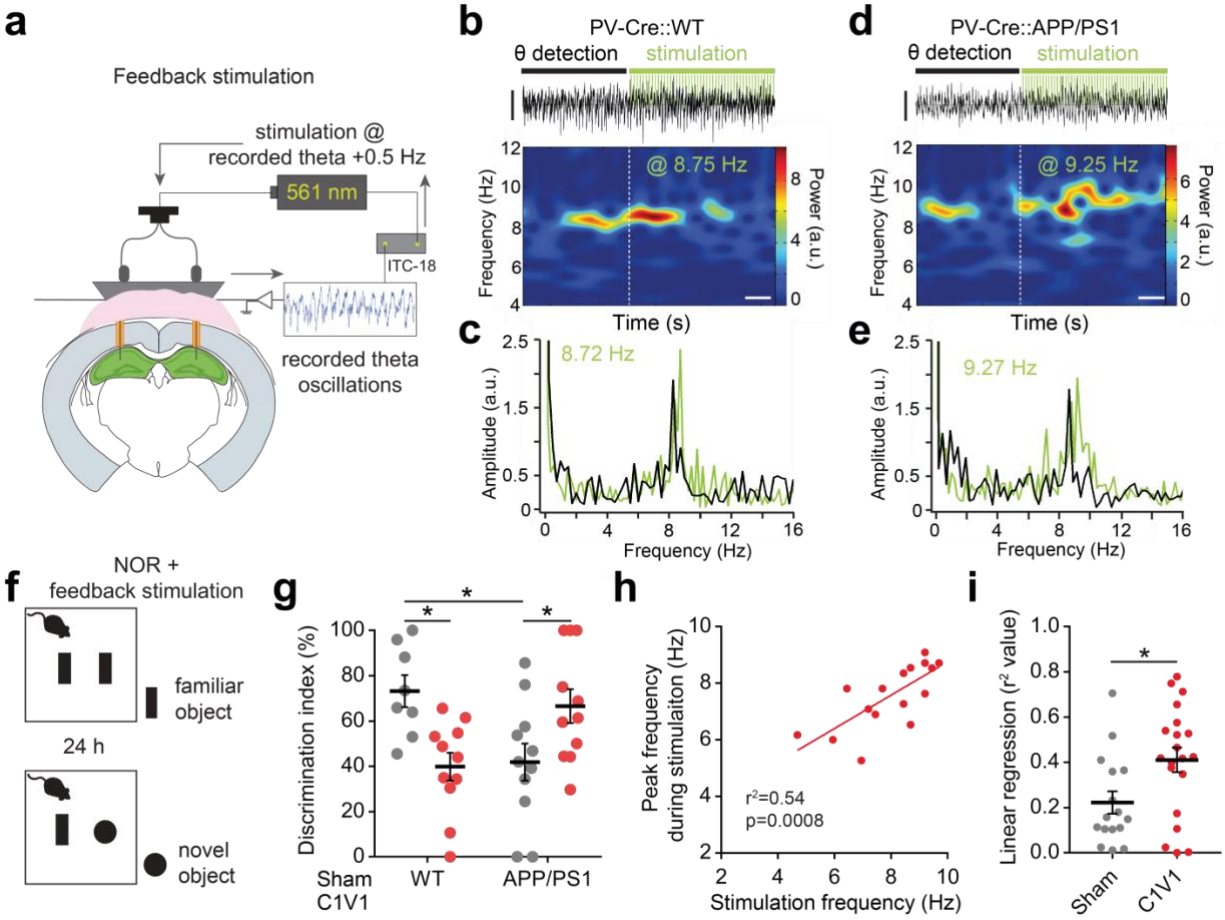

Fig. 3.5 Closed-loop rhythmic feedback optogenetic stimulation ameliorates recognition memory of 13 month old mice. *Panel **g** of this figure shows results that were not acquired during the doctorate period. Subsequent analyses were performed during the doctorate period (panels **b-e** and **h, i**)* **a)** Schematic of the feedback stimulation protocol Based on the recorded increase in amplitude of theta oscillations in the LFP (4-12 Hz), optogenetic stimulation (561 nm wavelength) was carried on for 5 seconds at the recorded frequency +0.5 Hz. **b)** Exemplary LFP epoch in a PV-Cre::WT animal expressing C1V1 in PV^+ interneurons, filtered in the 3-200 Hz range. Below, the spectrogram shows increase in power of theta oscillations (θ detection) during 4 seconds, followed by an interval of stimulation for 5.5 seconds at the detected peak amplitude +0.5 Hz. **c)** FFT of the LFP trace shown in c. Black trace: FFT of the field during the theta detection phase. Green trace: FFT of the field during stimulation phase. Note that the stimulation increased the frequency of the LFP. **d-e)** Same as b-c, in a PV-Cre::APP/PS1 animal expressing C1V1 in PV^+ interneurons. Scale bars: 1 second and 0.5 mV. **f)** Schematics of the NOR test. Closed loop feedback optogenetic stimulation was applied throughout sample and test phase of the NOR. **g)** Discrimination index. Two-way ANOVA with Holm-Sidak's correction for multiple comparisons; PV-Cre::WT + Sham vs PV-Cre::APP/PS1 + Sham, *p= 0.013; PV-Cre::WT + Sham vs PV-Cre::WT + C1V1, *p= 0.012; PV-Cre::APP/PS1 + Sham vs PV-Cre::APP/PS1 + C1V1, *p= 0.018. **h)** Exemplary correlation between stimulation frequency and peak theta frequency recorded in the LFP during intervals of stimulation in a PV-Cre::APP/PS1 + C1V1 mouse. **i)** Comparison of r^2 values from linear regression analyses of stimulation intervals. Two-tailed unpaired student's t-test: t(34)= 2.51, *p= 0.01. For **g**: PV-Cre::WT + Sham n= 8, PV-Cre::APP/PS1 + Sham n= 11, PV-Cre::WT + C1V1 n= 11, PV-Cre::APP/PS1 + C1V1 n= 11. For **i**: Sham-treated mice n= 16, C1V1-expressing n= 20. Graphs show individual values (mice) and bars represent mean ±SEM (g and i) and stimulation intervals in one mouse (h).

3.6 Arrhythmic optogenetic stimulation of hippocampal PV^+ interneurons during the NOR test

The beneficial effects of the optogenetic stimulation of PV^+ interneurons at theta frequency for the recognition memory of PV-Cre::APP/PS1 animals may have been due to, on the one hand, a sole increase of inhibition, or to both the imposition of rhythmic activity in the field and an increase in inhibitory tone. To discern this, I tested whether long-term recognition memory of PV-Cre::APP/PS1 transgenic animals would benefit from exclusively increasing the inhibitory tone without amplifying endogenous theta oscillations. For this, purpose, a feedback stimulation protocol was designed in which the laser pulses would be delivered with a jitter of ±30 ms (arrhythmic stimulation). This resulted in an increase of iPSCs in pyramidal neurons, recorded in acute brain slices, but not in an induction of membrane oscillations in the theta range (Ambrad Giovannetti, 2018). *In vivo*, the feedback stimulation was carried out during both sample and test phase of the NOR test, carried out as described in section 3.5 (**Fig. 3.6.1 a, b**). The PV-Cre::APP/PS1 mice that underwent this experiment were aged on average 14.4 ±2.27 months [mean ±SD]. As a result, employing the arrhythmic stimulation protocol did not result in an increase in DI in C1V1-expressing PV-Cre::APP/PS1 animals compared to Sham-treated controls (**Fig.3.6.1 c**; PV-Cre::APP/PS1 + Sham: 64.9 ±11.33%, n= 5; PV-Cre::APP/PS1 + C1V1: 49.48 ±13.47%, n= 5). Total object exploration time of both groups (**Fig.3.6.1 d**; PV-Cre::APP/PS1 + Sham: 14.48 ±5.77 sec; PV-Cre::APP/PS1 + C1V1: 13.18 ±7.41 sec) was not significantly different. Similarly, travelled distance (**Fig.3.6.1 e**; PV-Cre::APP/PS1 + Sham: 1173 ±246.8 cm, PV-Cre::APP/PS1 + C1V1: 1032 ± 77.02 cm) and mean velocity (**Fig.3.6.1 f**; PV-Cre::APP/PS1 + Sham: 3.91 ±0.82 cm/sec, PV-Cre::APP/PS1 + C1V1: 3.44 ±0.25 cm/sec) Sham-treated and C1V1-expressing PV-Cre::APP/PS1 mice during the test phase were not significantly different between the groups.

Overall, these results indicate that, in 14 month old PV-Cre::APP/PS1 mice, an acute increased inhibition during the NOR was not sufficient to restore long-term recognition memory compared to Sham- treated animals.

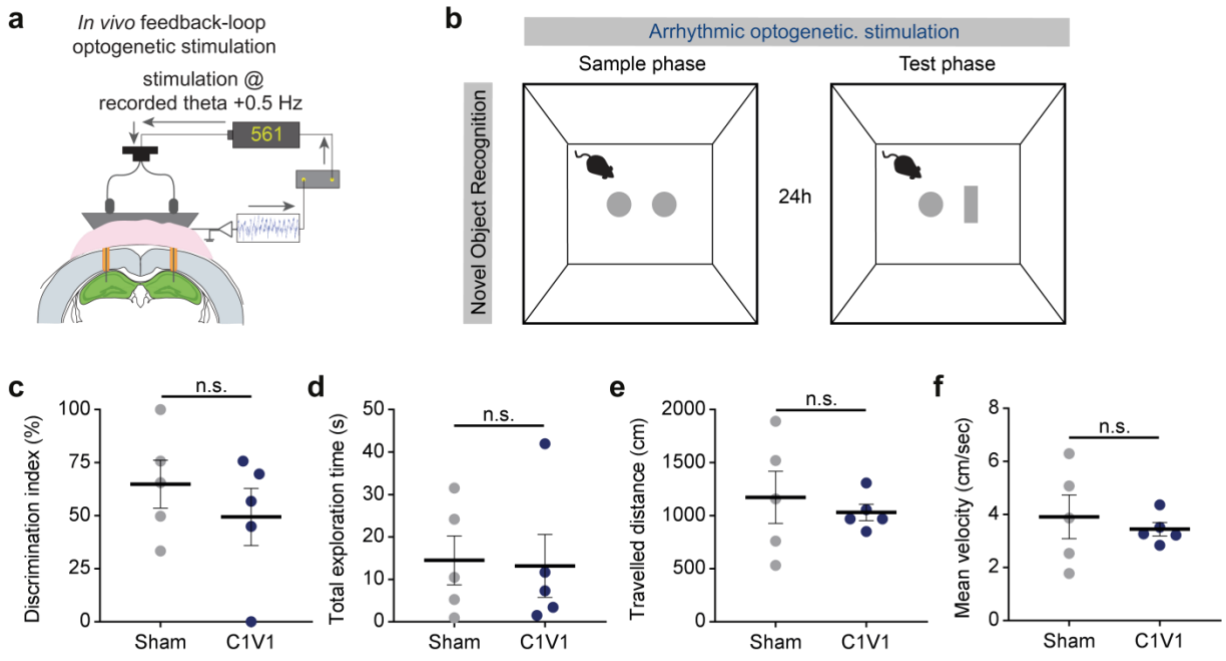

Figure 3.6.1 Closed-loop arrhythmic feedback optogenetic stimulation does not ameliorate recognition memory of 14 month old mice. a) Schematic of the feedback stimulation protocol and optic fiber implantation onto the hippocampi of PV-Cre::APP/PS1 mice. **b)** Schematics of the NOR protocol. A 24 hour interval between sample and acquisition phase was employed. **c)** Discrimination index. t(8)= 0.87, p=0.4 **d)** Total time spent exploring both novel and familiar object. t(8)= 0.13, p=0.89 **e)** Total travelled distance during the test phase (5 minutes). Two-tailed unpaired student's t-test with Welch's correction, t(4.7)= 0.54, p=0.60 **f)** Mean velocity during the test phase. Two-tailed unpaired student's t-test with Welch's corection: t(4.7)= 0.54, p=0.61.
Statistics for **c, d**: two-tailed unpaired student's t-test; for **e, f**: two-tailed unpaired student's t-test with Welch's correction. n=5 PV-Cre::APP/PS1 + Sham and n=5 PV-Cre::APP/PS1 + C1V1. Graphs represent individual values (mice), means ±SEM.

Subsequently, to test whether increasing inhibitory tone in PV-Cre::WT animals at an older age, when the decrease of peak theta oscillations is most evident, would improve recognition memory, an independent cohort of animals aged on average 20.3 ±3.5 months [mean ±SD] (referred to as 19-20 month old animals in the rest of the manuscript) was tested in the NOR. The same arrhythmic stimulation protocol described in **Fig. 3.6.1 a, b** was applied throughout sample and test phase of the NOR test. As a result, neither PV-Cre::WT + C1V1 nor PV-Cre::APP/PS1 + C1V1 mice showed a significantly different discrimination index (DI) than the respective Sham-treated controls (**Fig. 3.6.2 c**; PV-Cre::WT + Sham: 60.23 ±10.43%, n=8; PV-Cre::WT + C1V1 44.88 ±7.31%, n=6; PV-Cre::APP/PS1 + Sham: 59.52 ±8.48%, n=7; PV-Cre::APP/PS1 + C1V1: 65.11 ±8.16%, n=7). Furthermore, no significant difference in DI was observed between Sham-treated PV-Cre::WT and PV-Cre::APP/PS1 animals. In addition, total exploration time was not significantly different between the groups (**Fig. 3.6.2 d;** PV-Cre::WT

+ Sham: 13.19 ±4.16 sec; PV-Cre::WT + C1V1: 16.39 ±3.98 sec; PV-Cre::APP/PS1 + Sham: 21.31 ± 6.69 sec; PV-Cre::APP/PS1 + C1V1: 15.63 ±6.01 sec). Finally, travelled distance (**Fig. 3.6.2 e**; PV-Cre::WT + Sham: 862.3 ± 93.87 cm; PV-Cre::WT + C1V1: 1209 ±118.2 cm; PV-Cre::APP/PS1 + Sham: 1244 ±164.5 cm; PV-Cre::APP/PS1 + C1V1:1196 ±174.2 cm) and mean velocity during the test phase (**Fig. 3.6.2 f;** PV-Cre::WT + Sham: 3.12 ±0.26 cm/sec; PV-Cre::WT + C1V1: 4.13 ±0.42 cm/sec; PV-Cre::APP/PS1 + Sham: 4.4 ±0.42 cm/sec; PV-Cre::APP/PS1 + C1V1: 4.19 ±0.5 cm/sec) were not significantly different between the groups. Furthermore, testing against chance level (50%) by means of a two-tailed one sample t-test revealed that none of the groups showed a DI significantly higher than chance (PV-Cre::WT + Sham: $p(7)= 0.35$; PV-Cre::WT + C1V1: $p(5)= 0.51$; PV-Cre::APP/PS1 + Sham: $p(6)=0.3$; PV-Cre::APP/PS1 + C1V1: $p(6)=0.11$).

To summarize, DI of 19-20 month old PV-Cre::APP/PS1 mice in a NOR task was not significantly different compared to PV-Cre::WT mice. Furthermore, none of the groups showed a DI higher than chance level, which indicates that long-term recognition memory processes were impaired in this cohort of mice. Finally, increasing inhibitory tone via arrhythmic stimulation of hippocampal PV^+ interneurons was not sufficient to rescue the cognitive deficits displayed by both PV-Cre::WT and PV-Cre::APP/PS1 mice.

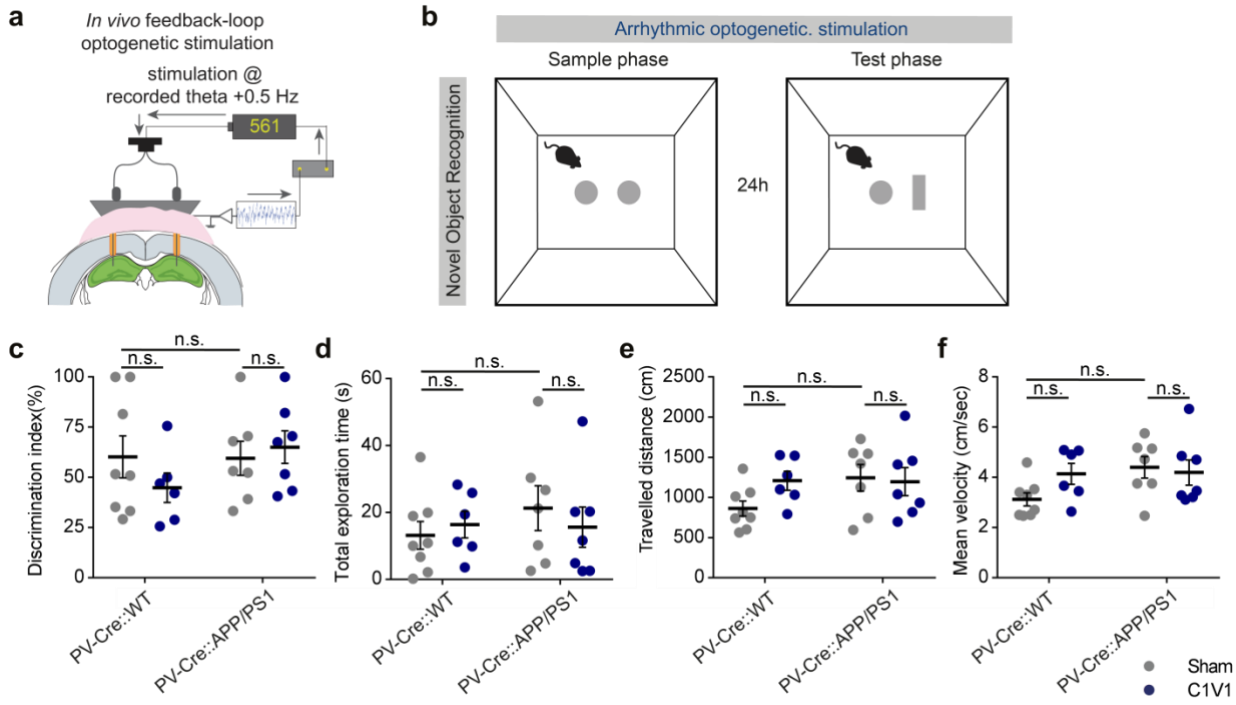

Figure 3.6.2 Closed-loop arrhythmic feedback optogenetic stimulation does not ameliorate recognition memory of 19-20 month old mice. a) Schematic of the feedback stimulation protocol and optic fiber implantation onto the hippocampi of PV-Cre::WT and PV-Cre::APP/PS1 mice. **b)**

Schematics of the behavioral test protocol. **c)** Discrimination index. PV-Cre::WT+Sham vs PV-Cre::APP/PS1+Sham, p=0.95; WT-Sham vs WT+C1V1 (n=6), p=0.56; PV-Cre::APP/PS1 + Sham vs PV-Cre::APP/PS1 + C1V1, p=0.86. **d)** Time spent exploring both old and novel objects. PV-Cre::WT + Sham vs PV-Cre::APP/PS1 + Sham, p=0.62; PV-Cre::WT + Sham vs PV-Cre::WT + C1V1, p=0.71; PV-Cre::APP/PS1 + Sham vs PV-Cre::APP/PS1 + C1V1, p= 0.71 **e)** Total travelled distance during the test phase. PV-Cre::WT + Sham vs PV-Cre::APP/PS1+Sham, p=0.16; PV-Cre::WT + Sham vs PV-Cre::WT + C1V1, p=0.18; PV-Cre::APP/PS1 + Sham vs PV-Cre::APP/PS1 + C1V1, p= 0.81 **f)** Mean velocity during the test phase. PV-Cre::WT-Sham vs APP/PS1-Sham, p=0.0.8; PV-Cre::WT + Sham vs PV-Cre::WT + C1V1, p=0.17; PV-Cre::APP/PS1 + Sham vs PV-Cre::APP/PS1 + C1V1, p= 0.72.
Statistics: two-way ANOVA with Holm-Sidak's correction for multiple comparisons; PV-Cre::WT+Sham n=8, PV-Cre::APP/PS1+Sham n=7, PV-Cre::WT + C1V1 n= 6, PV-Cre::APP/PS1 + C1V1, n= 7. All graphs represent individual values (mice), bars represent mean ±SEM.

3.7 Rhythmic optogenetic stimulation of hippocampal PV$^+$ interneurons during the Y-Maze test

Recognition memory is a process that involves hippocampal and other neocortical structures that are part of the medial temporal lobe. It is still debated whether the novel object recognition test optimally investigates hippocampal function (Cohen & Stackman, 2015). Thus, the 19-20 month old cohort of PV-Cre::WT and PV-Cre::APP/PS1 animals was additionally tested in the Y-Maze task for spontaneous alternations, which is typically considered hippocampus-dependent as it tests spatial working memory (Albani, McHail, & Dumas, 2014). Additionally, it has been shown that PV$^+$ neurons promote spatial working memory in the hippocampus (Murray et al., 2011). As we had previously observed that rhythmic, but not arrhythmic inhibition in the hippocampus lead to an increase in recognition memory in animals aged on average 13 months (Ambrad Giovannetti, 2018), here it was investigated whether spatial working memory of PV-Cre::WT and PV-Cre::APP/PS1 mice would benefit from the rhythmic optogenetic stimulation of PV$^+$ interneurons described in Fig. 3.5 (**Fig. 3.7 a**). For the Y-Maze test, mice were introduced in the center of the maze and let explore the arms for the next 10 minutes. Each of the three arms was equipped with a different set of black and white patterns. Then, the number of spontaneous alterations was calculated for 5 minutes (**Fig. 3.7 b**). A percentage of alterations higher than 50%, given that re-entry into an immediately exited arm is rare (Albani et al., 2014), indicates correct working memory processes. Here, there was no significant difference in percentage of alterations between groups (**Fig. 3.7 c;** PV-Cre::WT + Sham: 50.9 ±4.2, n= 9; PV-Cre::APP/PS1+Sham: 41.6 ±6.7%, n= 9; PV-Cre::WT + C1V1: 54.78 ±5.3%, n= 8; PV-Cre::APP/PS1 + C1V1: 48.7 ±9.1%, n= 7). Measures of spontaneous alterations were not biased by differences in exploration, as shown by a comparable number of total arm entries (**Fig. 3.7 d**; PV-Cre::WT + Sham: 16.11 ±1.98; PV-Cre::APP/PS1+Sham: 15.44 ±2.65; PV-Cre::WT + C1V1: 18.75 ±2.11; PV-Cre::APP/PS1 + C1V1: 13.14 ±1.84). Furthermore, testing against chance level by means of a a two-tailed one-sample t-test did not reveal significant differences in the percentage of spontaneous alternations for any of the groups (PV-Cre::WT + Sham: $p(8)=0.83$; PV-Cre::WT + C1V1: $p(7)=0.39$; PV-Cre::APP/PS1 + Sham: $p(8)=0.24$; PV-Cre::APP/PS1 + C1V1: $p(6)=0.89$).

Overall, the results indicated that the percentage of spontaneous alternations in the Y-Maze test was not significantly different between 19-20 month old PV-Cre::APP/PS1 mice and PV-Cre::WT mice. Furthermore, none of the groups tested showed a percentage of alterations higher than chance levels, which indicates that spatial working memory is impaired in all the treatment groups. Finally, entrainment of theta oscillations via optogenetic stimulation of

hippocampal PV^+ neurons was not sufficient to restore spatial working memory defects in neither PV-Cre::WT nor PV-Cre::APP/PS1 mice.

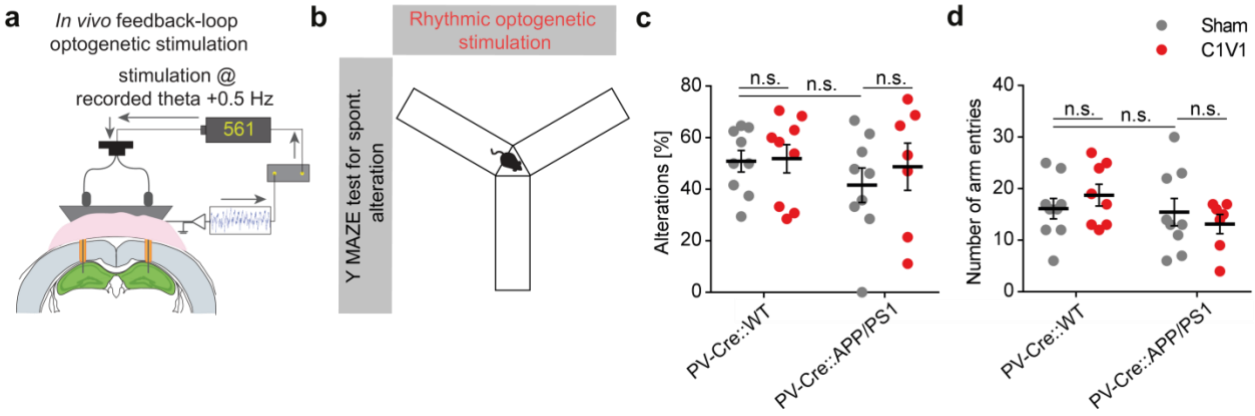

Figure 3.7 Closed-loop rhythmic feedback optogenetic stimulation does not ameliorate working memory of 19-20 month old mice. a) Schematic of the feedback stimulation protocol and optic fiber implantation onto the hippocampi of PV-Cre::WT and PV-Cre::APP/PS1 mice. **b)** Schematics of the behavioral test protocol. **c)** Percentage of arm alternations. PV-Cre::WT + Sham vs PV-Cre::APP/PS1 + Sham, p=0.63; PV-Cre::WT + Sham vs PV-Cre::WT + C1V1, p=0.68; PV-Cre::APP/PS1 + Sham vs PV-Cre::APP/PS1 + C1V1, p=0.68. **d)** Total number of arm entries. PV-Cre::WT + Sham vs APP/PS1 + Sham, p= 0.82; PV-Cre::WT + Sham vs PV-Cre::WT + C1V1, p=0.78; PV-Cre::APP/PS1 + Sham vs PV-Cre::APP/PS1 + C1V1, p=0.78.
Statistics: two-way ANOVA with Holm Sidak's correction for multiple comparisons. PV-Cre::WT + Sham n= 9, PV-Cre::APP/PS1 + Sham n= 9, PV-Cre::WT + C1V1 n= 8, PV-Cre::APP/PS1 + C1V1 n= 7. Graphs show individual values (mice) and bars represent mean ±SEM.

3.8 Rhythmic optogenetic stimulation of hippocampal PV$^+$ interneurons during the NOL test

With the Y-Maze, we assessed the effect of rhythmic optogenetic stimulation of PV$^+$ interneurons on spatial working memory. Impairments in long-term spatial memory have been described in aged rodents (Lester et al., 2017; Verbitsky et al., 2004), and in the APP/PS1 mouse model (Hijazi, Heistek, Scheltens, et al., 2020; Roy et al., 2016). To test whether the long-term spatial memory of 19-20 month old PV-Cre::WT and PV-Cre::APP/PS1 mice would benefit from a rhythmic increase in inhibitory tone and a concomitant amplification of endogenous theta oscillations, this cohort of animals was tested in the novel object location test (NOL). In this test, similar to the NOR test, a discrimination index higher than 50% is indicative of correct spatial memory processes. Furthermore, this test also relies on the innate exploratory activity of the animals to investigate a displaced object compared to one that has been left in the same position compared to a previous exposure. The optogenetic feedback stimulation protocol described in section 3.5 was employed throughout both learning and retrieval phase of the NOL test (**Fig. 3.8.1 a, b**). Mice were exposed to two identical objects placed adjacent to one of the walls of the open field (**Fig.3.8.1 b**, Sample phase). Mice were inserted in the open field from the same corner of the arena for three times, for a total duration of 6 minutes each time, at an interval of 20 minutes. Insertion from the same corner promotes the formation of a spatial map in the hippocampus, thus enabling to form consistent relationships between local objects in the arena. Corner of entry was pseudo-randomized between genotypes to exclude a spatial bias in the preference of one object over the other. After 24 hours (**Fig. 3.8.1 b**, Test phase), mice were inserted in the same open field arena where one of the objects had been displaced to the corner on the opposite wall. The behavior of the mice was analyzed for 5 minutes during the test phase. As a result, no significant difference between the DIs of each group was observed (**Fig. 3.8.1 c;** PV-Cre::WT + Sham: 52.3 ±11, n= 10; PV-Cre::APP/PS1 + Sham: 49.9 ±4.6%, n=10; PV-Cre::WT + C1V1: 52.4 ±9.8%, n= 8; PV-Cre::APP/PS1 + C1V1: 48.1 ±8.1%, n= 9). In addition, total exploration time of both objects was comparable between groups (**Fig. 3.8.1 d**; PV-Cre::WT + Sham median: 14.6 sec [8.54 sec, 23.32 sec]; PV-Cre::APP/PS1 + Sham median: 11.24 sec [4.76 sec, 15.54 sec]; PV-Cre::WT + C1V1 median: 4.84 sec [2.46 sec, 8.9 sec]; PV-Cre::APP/PS1 + C1V1 median: 5.92 sec [3.96 sec, 24.88 sec]). A significant genotype effect in the two-way ANOVA revealed that PV-Cre::APP/PS1 mice travelled more (**Fig.3.8.1 e**; PV-Cre::WT + Sham: 770.5 cm ±80.24%; PV-Cre::APP/PS1 + Sham: 1014 ±98.81 cm; PV-Cre::WT + C1V1: 638.6 ±142.3 cm; PV-Cre::APP/PS1 + C1V1: 1021 ± 153.8 cm) and faster than PV-Cre::WT animals (**Fig. 3.8.1 f**; PV-Cre::WT + Sham: 2.57 ±0.26 cm/sec; PV-

Cre::APP/PS1 + Sham: 3.38 ±0.32 cm/sec; PV-Cre::WT + C1V1: 2.19 ±0.47 cm/sec; PV-Cre::APP/PS1 + C1V1: 3.4 ±0.51 cm/sec). Furthermore, testing against chance level (50%) by means of a two-tailed one-sample t-test revealed that none of the groups showed a DI higher than chance (PV-Cre::WT + Sham: $p(9)=0.89$; PV-Cre::WT + C1V1: $p(7)=0.81$; PV-Cre::APP/PS1 + Sham: $p(9)=0.97$; PV- Cre::APP/PS1 + C1V1: $p(8)= 0.82$).

These results showed that the DI of 19-20 month old PV-Cre::WT and PV-Cre::APP/PS1 during the NOL test was not significantly different. Additionally, none of the groups tested displayed a DI higher than chance levels, indicating that long-term spatial memory is impaired in all groups. Furthermore, rhythmic stimulation of PV^+ neurons at theta frequency was not sufficient to restore the long-term spatial memory defects of neither C1V1-expressing PV-Cre::WT nor PV-Cre::APP/PS1 mice.

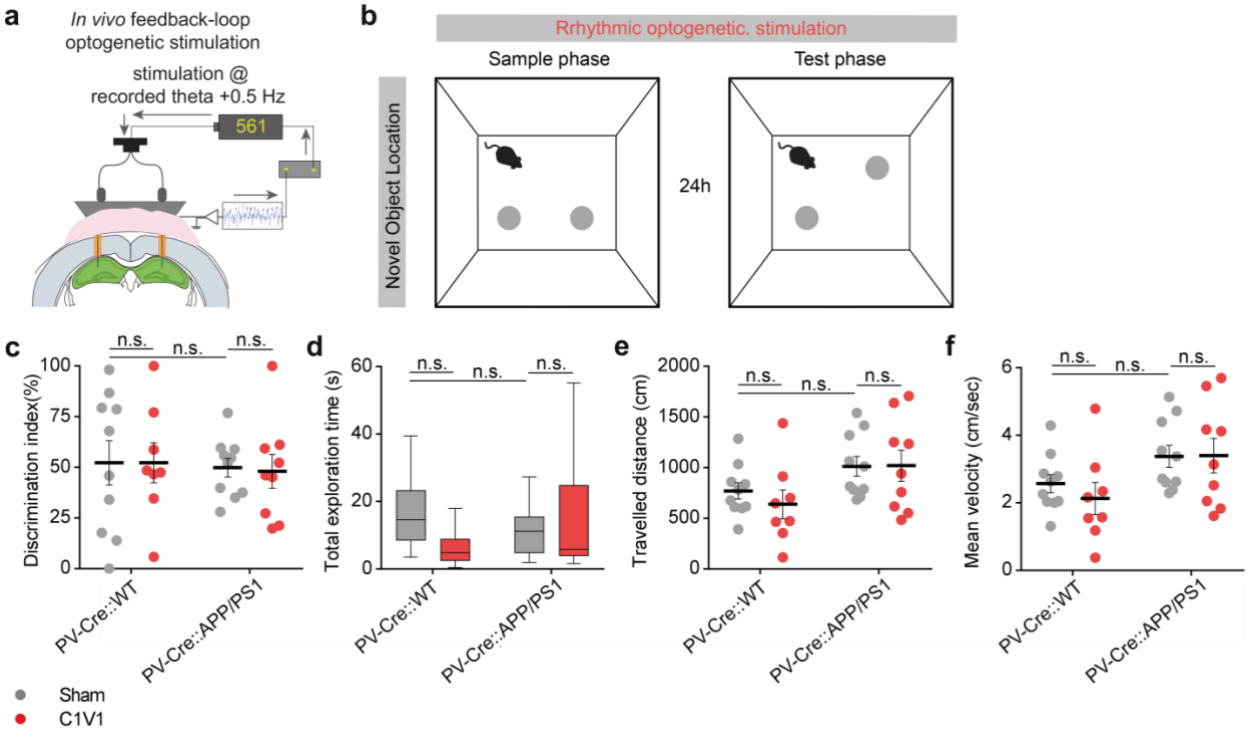

Figure 3.8.1 Closed-loop rhythmic feedback optogenetic stimulation does not ameliorate spatial memory of 19-20 month old mice. a) Schematic of the feedback stimulation protocol and optic fiber implantation onto the hippocampi of PV-Cre::WT and PV-Cre::APP/PS1 mice. **b)** Schematics of the behavioral test protocol. **c)** Discrimination index. PV-Cre::WT + Sham vs PV-Cre::APP/PS1 + Sham, p= 0.99; PV-Cre::WT + Sham vs PV-Cre::WT + C1V1, p= 0.99; PV-Cre::APP/PS1 + Sham vs PV-Cre::APP/PS1 + C1V1, p= 0.99. **d)** Time spent exploring both objects. PV-Cre::WT + Sham vs PV-Cre::APP/PS1 + Sham, p= 0.82; PV-Cre::WT + Sham vs PV-Cre::WT + C1V1, p=0.06; PV-Cre::APP/PS1 + Sham vs PV-Cre::APP/PS1 + C1V1, p>0.99. **e)** Total travelled distance during the test phase. PV-Cre::WT + Sham vs PV-Cre::APP/PS1 + Sham, p= 0.36; PV-Cre::WT + Sham vs PV-Cre::WT + C1V1, p= 0.69; PV-Cre::APP/PS1 + Sham vs PV-Cre::APP/PS1 + C1V1, p= 0.96. **f)** Mean velocity during the test phase. PV-Cre::WT + Sham vs PV-Cre::APP/PS1 + Sham, p=0.36; PV-Cre::WT + Sham vs PV-Cre::WT + C1V1, p= 0.69; PV-Cre::APP/PS1 + Sham vs PV-Cre::APP/PS1 + C1V1, p= 0.97.

Statistics for **c**, **e**, **f**: two-way ANOVA with Holm-Sidak's correction for multiple comparisons; for **d**: Kruskal-Wallis test with Dunn's correction for multiple comparisons. PV-Cre::WT + Sham n= 10; PV-Cre::APP/PS1 + Sham n= 10, PV-Cre::WT + C1V1 n= 8, PV-Cre::APP/PS1 + C1V1 n= 9. Graphs show individual values (mice) and bars represent mean ±SEM. Box plots show interquartile ranges and median, whiskers show minimum and maximum values.

To determine whether the age of the mice tested and/or the behavioral protocol were contributing factors for the results observed in experiment described in section 3.8, the novel object location test (NOL) was repeated in an additional independent cohort of younger mice (**Fig. 3.8 a, b**). For this experiment, mice were aged on average 15.4 ±2.02 months [mean ±SD]. These mice will be referred to as 15 month old mice for the rest of the manuscript. First, to maximize the formation of a hippocampal cognitive map, visual cues were added to the walls of the open field (stripes and dots, **Fig. 3.8.2 b**). Second, the sample phase was modified so that mice would explore the arena with the objects placed in the familiar locations for two consecutive days, each day for 12 minutes. The test phase (in which one object was displaced to the opposite wall of the arena, as in 3.8) was carried out for 12 minutes and the behavior was analyzed for 5 minutes (**Fig. 3.8.2 b**). Here, PV-Cre::APP/PS1 + Sham mice performed worse than PV-Cre::WT + Sham and PV-Cre::APP/PS1 + C1V1 animals, as shown by a significantly lower discrimination index of these mice compared to the latter two groups (**Fig. 3.8.2 c;** PV-Cre::WT + Sham: 58.27 ±10.14%, n= 11; PV-Cre::APP/PS1 + Sham: 28.66 ±5.73%, n= 9; PV-Cre-Cre::WT + C1V1: 47 ±10%, n= 8; PV-Cre::APP/PS1 + C1V1: 71.73 ±9.71%, n= 7). Furthermore, the total time spent exploring both objects (**Fig.3.8.2 d;** PV-Cre::WT + Sham: 9.65 ±2.01 sec; PV-Cre::APP/PS1 + Sham: 15.88 ±4.86 sec; PV-Cre-Cre::WT + C1V1: 12.1 ±3.06 sec; PV-Cre::APP/PS1 + C1V1: 20.06 ±12.09 sec), the total travelled distance (**Fig.3.8.2 e;** PV-Cre::WT + Sham: 765.2 ±112.6 cm; PV-Cre::APP/PS1 + Sham: 928 ±136.2 cm; PV-Cre-Cre::WT + C1V1: 754.2 ±152.8 cm; PV-Cre::APP/PS1 + C1V1: 742 ±127.9 cm) and mean velocity during the test phase (**Fig. 3.8.2 f**; PV-Cre::WT + Sham: 2.67 ±0.33 cm/sec; PV-Cre::APP/PS1 + Sham: 3.11 ±0.45 cm/sec; PV-Cre-Cre::WT + C1V1: 2.51 ±0.5 cm/sec; PV-Cre::APP/PS1 + C1V1: 2.51 ±0.42 cm/sec) were not significantly different between the groups. In addition, during the test phase, the number of stimulation intervals triggered by the feedback stimulation protocol (**Fig. 3.8.2 g;** PV-Cre::WT + Sham: 21.55 ±5.88; PV-Cre::APP/PS1 + Sham: 17.44 ±3.73; PV-Cre-Cre::WT + C1V1: 16.5 ±2.66; PV-Cre::APP/PS1 + C1V1: 25.29 ±3.46) was not significantly different between the groups.

Overall, these results indicate that PV-Cre::APP/PS1 mice perform worse than PV-Cre::WT mice in the NOL test at the age of 15 months on average. Furthermore, the long-term spatial memory of PV-Cre::APP/PS1 animals benefited from the rhythmic entrainment of inhibitory PV^+ neurons in the hippocampus, as C1V1-expressing PV-Cre::APP/PS1 mice showed a higher DI compared to Sham-treated mice.

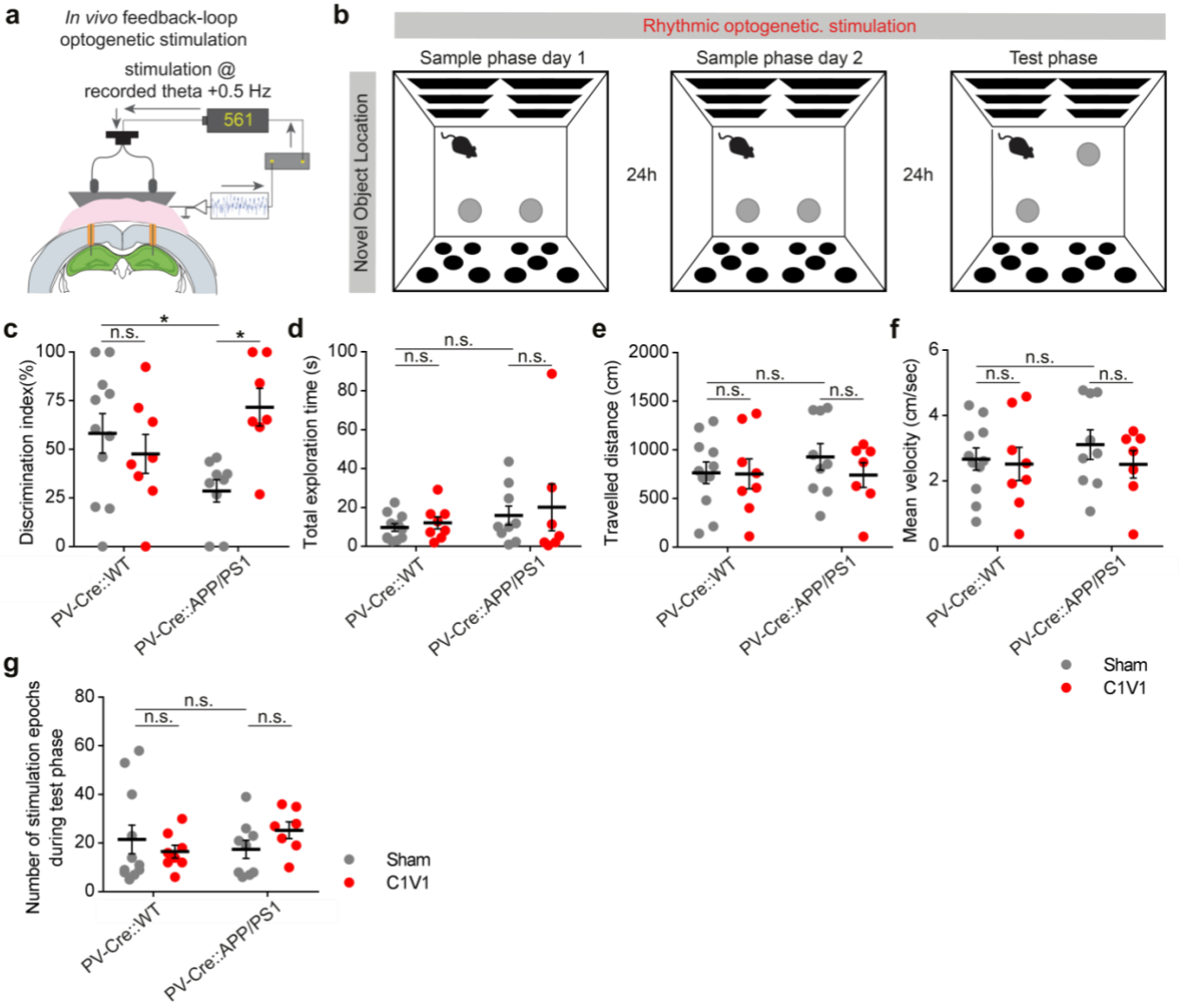

Figure 3.8.2 Closed-loop rhythmic feedback optogenetic stimulation ameliorates spatial memory of 15 month old mice. **a)** Schematic of the feedback stimulation protocol and optic fiber implantation onto the hippocampi of PV-Cre::WT and PV-Cre::APP/PS1 mice. **b)** Schematics of the behavioral test protocol. **c)** Discrimination index. PV-Cre::WT + Sham (n=11) vs PV-Cre::APP/PS1 + Sham, *p=0.04; PV-Cre::WT + Sham vs PV-Cre::WT + C1V1 (n=8), p=0.41; PV-Cre::APP/PS1 + Sham vs PV-Cre::APP/PS1 + C1V1, *p=0.01. **d)** Time spent exploring both objects. PV-Cre::WT + Sham vs PV-Cre::APP/PS1 + Sham, p>0.99; PV-Cre::WT + Sham vs PV-Cre::WT + C1V1, p>0.99; PV-Cre::APP/PS1 + Sham vs PV-Cre::APP/PS1 + C1V1, p>0.99. **e)** Total travelled distance during the test phase. PV-Cre::WT + Sham vs PV-Cre::APP/PS1 + Sham, p=0.72; PV-Cre::WT + Sham vs PV-Cre::WT + C1V1, p=0.95; PV-Cre::APP/PS1 + Sham vs PV-Cre::APP/PS1 + C1V1, p= 0.72. **f)** Mean velocity during the test phase. PV-Cre::WT + Sham vs PV-Cre::APP/PS1 + Sham, p=0.82; PV-Cre::WT + Sham vs PV-Cre::WT + C1V1, p=0.99; PV-Cre::APP/PS1 + Sham vs PV-Cre::APP/PS1 + C1V1, p=0.72.

Statistics: two-way ANOVA with Holm-Sidak's correction for multiple comparisons. PV-Cre::WT + Sham n= 11, PV-Cre::APP/PS1 + Sham n= 9, PV-Cre::WT + C1V1 n= 8, PV-Cre::APP/PS1 + C1V1 n= 7. Graphs show individual values (mice) and bars represent mean ±SEM.

3.9 Simultaneous two-photon calcium imaging and laminar LFP recordings

In this study, mice were implanted with single tungsten wire electrodes targeted at the SLM area of CA1. Chronic LFP recordings using a single tungsten wire are not suitable to record single unit activity, hence to correlate action potentials (representing neuronal output) to the activity of the input measured with the LFP. Furthermore, whether age and/or the AD pathology affects the phase coding properties of a large population of hippocampal neurons (i.e., whether single cell firing along the underlying LFP phase) has been poorly investigated. A way to circumvent this would be by making use of population wide calcium imaging techniques with fast calcium indicators, which serve as a proxy for neural activity, and combine them with laminar LFP recordings that span all layers of CA1. Indeed, it is possible to infer spiking from somatic calcium transients (Friedrich, Zhou, & Paninski, 2017), and because the rise time of GCaMP6f is faster than 50 ms (T. W. Chen et al., 2013), it is possible to correlate action potential burst to the theta cycle in the 8-10 Hz range (1 theta cycle=125-100 ms; (Li et al., 2019)). Thus, I implanted a chronical hippocampal window onto the right hemisphere of a Thy1-GCaMP6f animal, and a 16 channel silicon probe spanning the dorsal hippocampus on the left hemisphere (**Fig. 3.9 a, b, c**). This configuration enables to correlate the activity of pyramidal neurons recorded by means of fluorescence changes in GCaMP6f signal (**Fig. 3.9 d**) that fire during ongoing theta field activity with LFP recordings from *stratum pyramidale* (**Fig. 3.9 e**), which instead reflects sub-threshold events occurring in the broader population(Li et al., 2019). Additionally, it is possible to measure activity of place cells by two-photon calcium imaging (Dombeck, Harvey, Tian, Looger, & Tank, 2010); **Fig. 3.9 g, h**). Thus, this approach would enable to correlate place cell activity with LFP recordings and to evaluate whether age and/or AD pathology affects place cell coding along the theta cycle. Furthermore, laminar recordings enable input-specific analysis in each compartment of CA1.

Here, I was able to successfully carry out simultaneous laminar LFP recordings and two-photon calcium imaging in an animal that was head fixed on the linear treadmill, which paves the way for future experiments employing this setup.

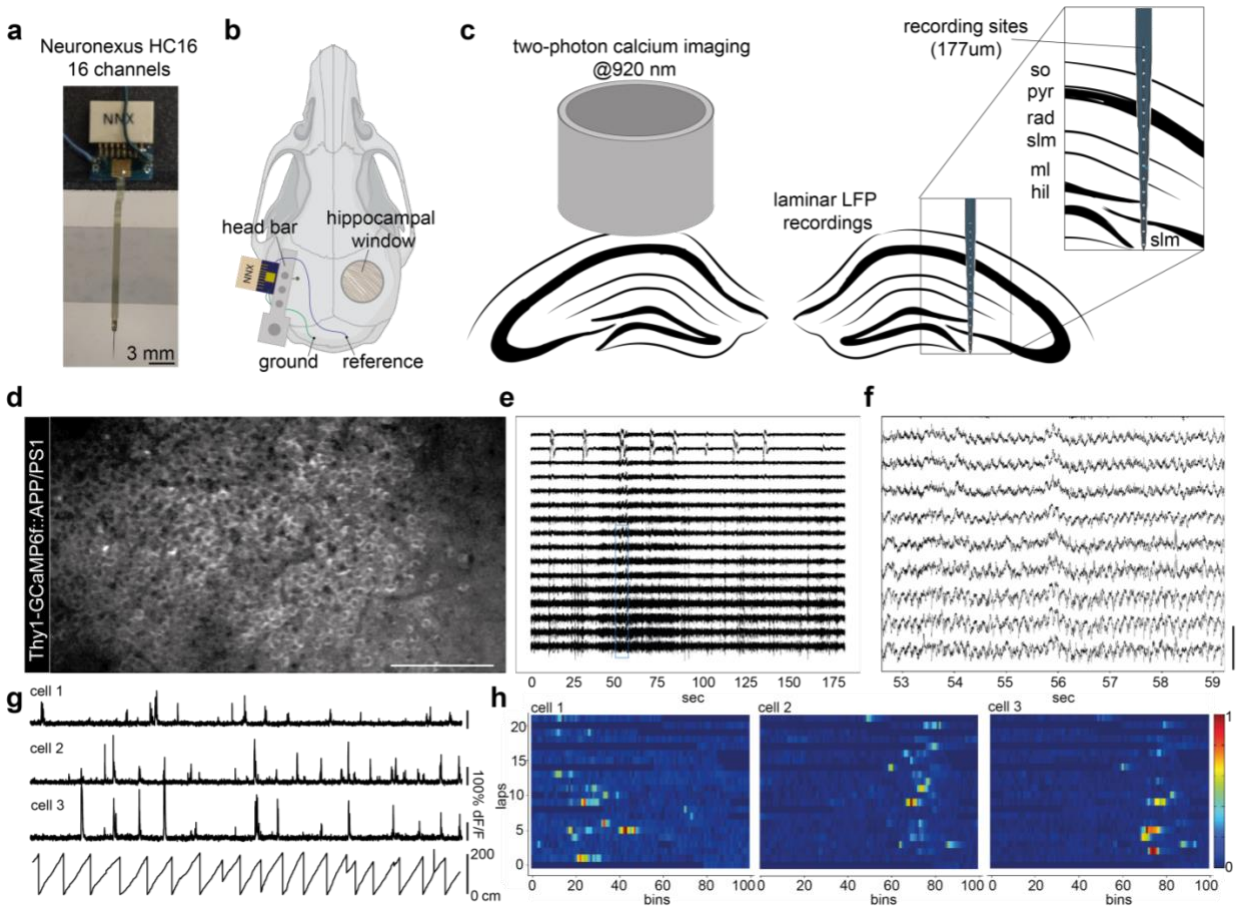

Fig. 3.9 Two-photon calcium imaging and laminar LFP recordings in the hippocampus. a) Picture of the laminar probe employed for the laminar LFP recordings in the hippocampus. The silicon probe consisted of 16 channels and was implanted on the left hemisphere, as shown in b. **b)** Schematic of the implantation sites of hippocampal window and silicon probe on the contralateral hemisphere. Ground and reference electrodes of the laminar probe were inserted in the cerebellum. A metal bar used as holder (head bar) was fixed on top of the flexible part of the laminar probe and served as a way to fix the head of the mouse while it was running on a linear treadmill. [*Skull illustration exported from BioRender*]. **c)** Schematic depicting the recording site of the silicon probe spanning CA1 and DG-CA3 and representative placement of the hippocampal window on the contralateral hemisphere. **d)** Average intensity projection image of a 50 second time interval during two-photon calcium imaging of a Thy1-GCaMP6f::APP/PS1 animal. **e)** LFP recording acquired using the laminar probe during two-photon calcium imaging. **f)** Exemplary calcium traces of 3 cells in the field of view shown in d, aligned to the animal's position along the linear treadmill, shown below. **g)** Heatmap of normalized ΔF/F values along the treadmill for the cells shown in f.

3.10 Layer-specific analysis of Aβ deposition in the MEC of APP/PS1 mice

The results presented in the previous sections showed that the hippocampal system undergoes remodeling in age and AD-like pathology, observed at the level of hippocampal LFPs and behavioral phenotypes. Particularly, alterations in theta-gamma modulation of PV-Cre::APP/PS1 animals are indicative of an aberrant hippocampo-entorhinal feedback communication. Interestingly, in the APP/PS1 mouse model, the MEC and LEC are affected by Aβ pathology prior to the hippocampus proper (Whitesell et al., 2019). Because the activity of the majority of neurons in layer II of the MEC is strongly modulated by locomotion and navigation, neurons in this region have been proposed to represent a neural code for navigation (Hafting et al., 2005; Schmidt-Hieber & Hausser, 2013). Direct MEC-layer III input onto CA1 is crucial for replay of place cell sequences along the theta cycle during awake immobility (Chenani et al., 2019; Yamamoto & Tonegawa, 2017). Besides, theta rhythmicity in the MEC is thought to originate in layer V and that this is ultimately the source of the current observed in CA1 SLM (Deshmukh et al., 2010). Distribution of Aβ plaques across layers, and over the course of the pathology, could therefore potentially reveal which components of the circuit are affected over time. To characterize in detail how Aβ deposits are distributed in the MEC at advanced stages of the pathology, when Aβ plaque burden is already substantial in the hippocampus (Schmid et al., 2016), brains of 7.5 and 11.5 month old heterozygote APP/PS1 mice were stained with the compound methoxy-X04 (Klunk et al., 2002), which has a high affinity for Aβ plaques in post-mortem brain sections **(Fig. 3.10 a)**. In 7.5 month old mice, the percentage area covered by Aβ plaques in each layer was not higher than 1.5% for MEC layers I, III and IV, and slightly but not significantly lower for layers II and V **(Fig. 3.10 b)**. With the progression of the disease, these proportions were broadly maintained, and the Aβ plaque burden was by trend increased **(Fig. 3.10 c, d)**. Specifically, in the MEC of 11.5 month old APP/PS1 mice, Aβ plaque burden was highest in LI (median 1.81% [1.38%, 2.45%]) and significantly higher compared to LII (median 0.78 % [0.66%, 1.24%]) and LV (median 0.88 % [0.6%, 3.5%]). On average, across the MEC areas examined, the percentage area covered by Aβ plaques had a median value of 0.86% [0.34%, 2.22%] in 7.5 month old mice, and a median value of 1.39% [1.04%, 1.87%] in 11.5 month old mice **(Fig. 3.10 d)**.

These results indicate that Aβ plaques are distributed across all layers of the MEC in both 7.5 and 11.5 month old animals, and that plaque deposition does not increase significantly over this time period. Additionally, the layer specific analysis revealed that LI is primarily affected in 11.5 month old animals.

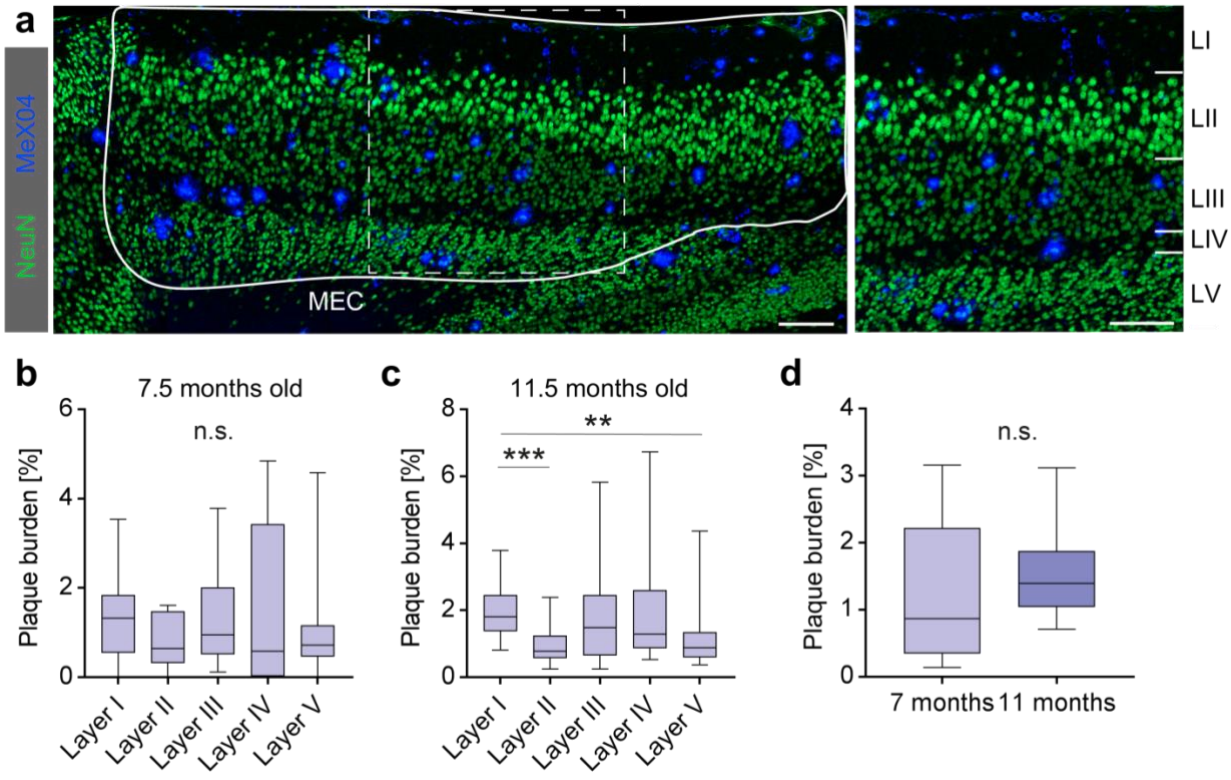

Figure 3.10 Aβ plaque burden profile in the MEC of APP/PS1 mice. a) Exemplary confocal microscopy picture showing Aβ plaques in the MEC of an APP/PS1 mouse. An anti-NeuN antibody was used as a pan-neuronal marker for cell bodies (green). White dashed box indicates zoom in on the right panel. Layers (LI to LV) were manually identified according to the distribution of the NeuN staining. **b)** Plaque burden expressed as percentage of area covered by plaques for each layer in 7.5 month old animals; n= 14 slices (3-5 slices per mouse, 3 mice in total). **c)** Same as b, but for 11.5 months old mice. LI vs LII, ***p=0.0008; LI vs LV **p=0.006; n= 22 slices (3-5 slices per mouse, 6 mice in total). **d)** Comparison of plaque burden across overall MEC between 7.5 and 11.5 month old mice; n= 14 slices from 3 mice (7.5 months old) and 22 slices from 6 animals (11.5 months old).
Statistics for **b**, **c**: Kruskal-Wallis test with Dunn's correction for multiple comparisons, for **d**: Mann-Whitney test. Scale bar: 100 µm Box plots represent interquartile ranges and median, whiskers represent minimum and maximum values.

3.11 Reduced SOM-immunoreactivity in the MEC of APP/PS1 mice

The vulnerability of inhibitory neurons to amyloidosis has been extensively researched (Ambrad G. & Fuhrmann, 2019). Inhibitory neurons play a pivotal role in the instatement and maintenance of oscillatory activity in the hippocampal system (Roux & Buzsaki, 2015; Unal et al., 2018). Thus, gaining knowledge on which inhibitory neuron type is affected over time is crucial for understanding the mechanisms behind the emergence of aberrant LFP and single unit activity that occurs with age and AD-like pathology. In spite of the numerous studies carried out in diverse mouse models, data from the APP/PS1 mouse model is scarce. To assess the potential impact of beta-amyloidosis on the function of inhibitory and/or excitatory neurons in the MEC of WT and APP/PS1 transgenic mice, fluorescent immunohistochemical stainings were performed on brains of aged-matched WT and APP/PS1 mice. The antibodies targeted the two most abundant inhibitory neuron populations in the MEC (somatostatin (*SOM*) and parvalbumin (*PV*)), and a category of principal neurons that are Wolframin Syndrome 1-positive neurons (*WFS1*)). Neuronal densities were quantified in a layer specific manner and compared between genotypes. This analysis revealed a reduction of SOM-immunoreactivity in cell bodies of MEC layer IV of 7.5 month old APP/PS1 transgenic mice compared to WT age-matched controls **(Fig. 3.11 a, b**; WT-LIV: 225.5 ±27.83 cells/mm^2; APP/PS1-LIV: 150.1 ±41.35 cells/mm^2). When considering the full area of MEC analyzed, no significant reduction in SOM$^+$ immunoreactivity was detected in APP/PS1 mice (**Fig. 3.11 c**; WT: 87.06 ±6.88 cells/mm^2; APP/PS1 mice: 69.92 ±16.69 cells/mm^2). In 11.5 month old APP/PS1, SOM-immunoreactivity was further decreased, and cell densities were lower not only in MEC layer IV, but also in layer II and layer V compared to WT controls (**Fig. 3.11, d**; WT-LII: 86.9 ±14.96 cells/mm^2 vs APP/PS1-LII: 49.9 ±3.78 cells/mm^2; WT-LIV: 217.4 ±19.6 cells/mm^2 vs APP/PS1-LIV: 134 ±10.86 cells/mm^2; WT-LV: 110.1 ±11.38 cells/mm^2 vs APP/PS1-LV: 70.55 ±1.79 cells/mm^2). Additionally, SOM-immunoreactivity of APP/PS1 mice was significantly reduced compared to WT mice over the whole MEC area (**Fig. 3.11 e**; WT: 100.6 ±9.79 cells/mm^2; APP/PS1: 61.8 ±2.65 cells/mm^2). In contrast, PV-immunoreactivity within each layer was not significantly altered in 7.5 month old APP/PS1 transgenic animals **(Fig. 3.11 f, g)**, although a significant effect for genotype was detected in the two-way ANOVA. Average numbers of PV-immunoreactive cells within the full area of the MEC analyzed were not significantly different between WT and AP/PS1 mice (**Fig. 3.11 h**; WT: 342 ±15.88 cells/mm^2; APP/PS1: 274.5 ±32.55 cells/mm^2). Similarly, the percentage of excitatory WFS1$^+$ neurons, which form the cell clusters named "Islands" in MEC-LII, over the whole NeuN populations was not significantly altered in APP/PS1 animals compared to WT controls (**Fig. 3.11 i, j**; WT:

67.35 ±2.1%; APP/PS1: 68.62 ±1.64%), nor was the total number of WFS^+Island clusters in MEC-LII in the area analyzed **(Fig. 3.11 k**; WT 8.8 ±1.59; APP/PS1 8.5 ±1.23). Besides, total numbers of $NeuN^+$ cells within the island clusers analyzed was not significantly different between WT and APP/PS1 mice (**Fig. 3.11 l**; WT: 229 ±49.58; APP/PS1: 191.3 ±30.34).

In conclusion, we have observed that SOM-immunoreactivity, but not PV-immunoreactivtiy is reduced, in a layer-specific manner, in the MEC of APP/PS1 transgenic animals when compared to age-matched WT controls. In contrast, WFS1-immunoreactivity was not altered, indicating that SOM^+ inhibitory neurons, but not pyramidal $WFS1^+$ neurons are susceptible to amyloidosis at the age of 11.5 months.

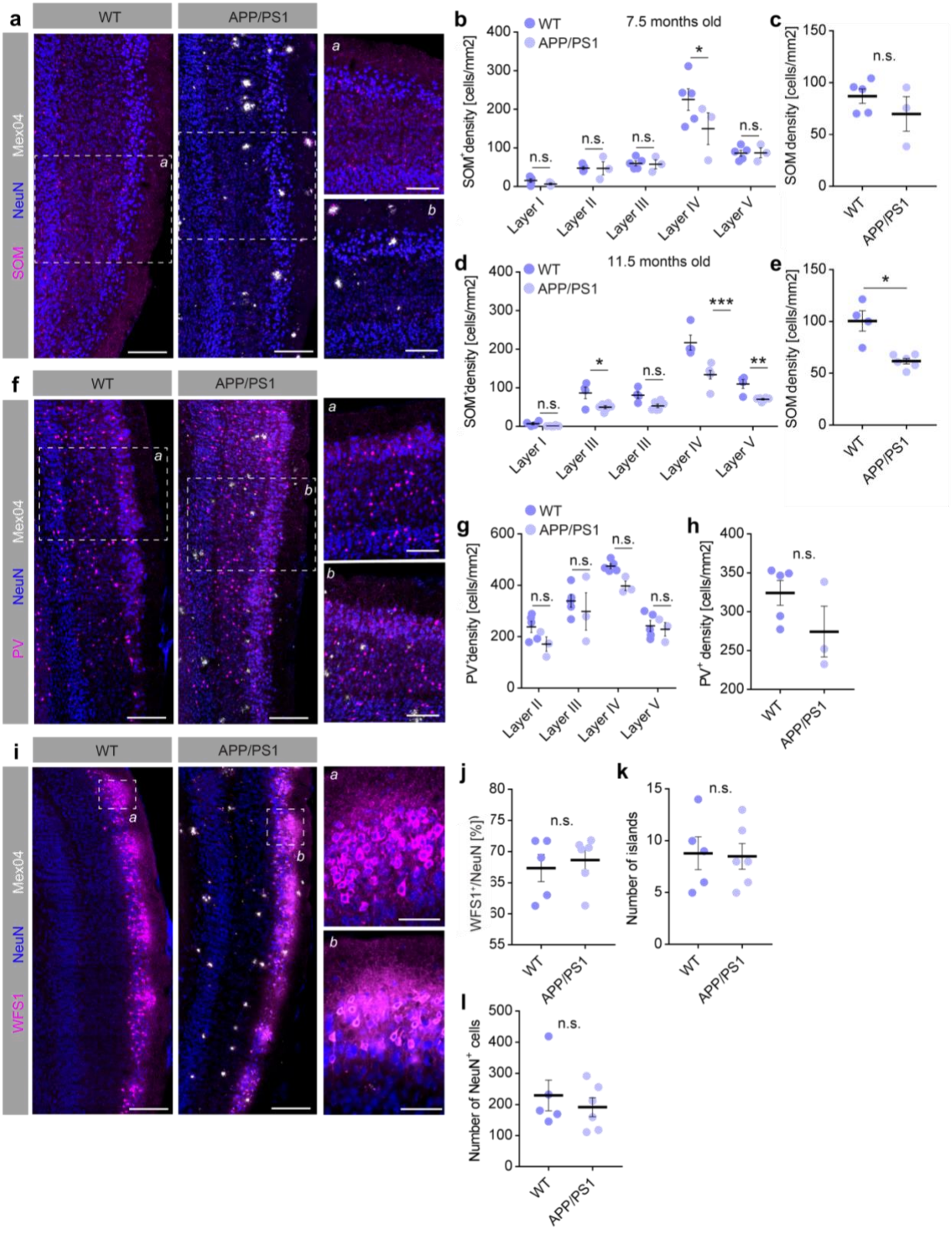

Figure 3.11 Reduction of SOM-immunoreactivity in the MEC of APP/PS1 mice. a) Exemplary confocal microscopy picture of anti-SOM immunofluorescent stainings (magenta) in 7.5 month old WT and APP/PS1 transgenic mice. Boxes *a* and *b* are expanded in the corresponding panels on the right side of the picture. An anti-NeuN antibody was used as a pan-neuronal marker for cell bodies (blue). Aβ plaques were stained using the MeX04 compound (white). **b)** Density of SOM^+ cells per mm^2 in the MEC of 7.5 month old animals. WT-LIV vs APP/PS1-LIV *p=0.017; n= 5 WT and 3 APP/PS1 mice

(4-7 slices per animal). **c)** Density of SOM^+ cells over the total MEC area, in 7.5 month old mice. Two-tailed unpaired student's t-test: t(6)= 1.12, p= 0.3. **d)** Density of SOM^+ cells per mm^2 in the MEC of 11.5 month old animals. WT-LII vs APP/PS1-LII *p=0.013, WT-LIV vs APP/PS1 LIV ****p<0.0001, WT-LV vs APP/PS1-LV *p=0.015; n=4 WT and 6 APP/PS1 mice (3-5 slices per animal). **e)** Density of SOM^+ cells over the total MEC area, in 11.5 month old mice. Two-tailed unpaired student's t-test with Wlelch's correction: t(3.45)= 3.84, p= 0.02. **f)** Exemplary confocal microscopy picture of anti- PV immunofluorescent stainings (magenta) in 7.5 month old WT and APP/PS1 transgenic mice. NeuN (blue) and MeX04 (white), same as in **a. g)** Density of PV^+ cells per mm^2 in the MEC of 7.5 month old animals. n= 5 WT and n= 3 APP/PS1 mice (3 slices per mouse). **h)** Density of PV^+ cells per mm^2 over the total MEC area of 7.5 month old mice. Two-tailed unpaired student's t-test: t(6)= 1.56, p= 0.16. **i)** Exemplary confocal microscopy picture of anti-WFS1 immunofluorescent stainings (magenta) in 11.5 month old WT and APP/PS1 transgenic mice. NeuN (blue) and MeX04 (gray). **j)** Percentage of $WFS1^+$ neurons over total NeuN in WT vs APP/PS1 mice. Two-tailed unpaired student's t-test: t(9)= 0.47, p= 0.64. **k)** Number of islands in WT and APP/PS1 animals. Two-tailed unpaired student's t-test: t(9)= 0.15, p= 0.88 **l)** Number of $NeuN^+$ cells in the counted islands. Two-tailed unpaired student's t-test: t(9)= 0.67, p= 0.51. For **g**, **h**, **i**; n= 6-14 Islands (defined as $WFS1^+$NeuN patches) from 5 WT and 6 APP/PS1 mice.

Scale bars: 200 µm for overview panels, 100 µm for zoom in panels. All graphs represent individual values (mice, averaged over slices) and bars represent mean ± SEM.

3.12 Dysfunction of hippocampal SOM$^+$ long-range inhibitory projections

Long-range inhibitory connectivity between the hippocampus and the MEC has been poorly investigated. Melzer et al. (Melzer et al., 2012) have, for the first time, reported the existence of hippocampal SOM$^+$ long-range inhibitory projections (LRIPs) in the hippocampus whose afferents predominantly innervate local inhibitory neurons in layer I of the MEC. Furthermore, the authors described PV$^+$ LRIPs in the MEC whose post-synaptic targets are local CCK$^+$ inhibitory interneurons in CA1 (Melzer et al., 2012). Here, I was able to reproduce this findings by stereotactic intracranial injection of an AAV encoding a Cre-dependent fluorescent tracer (*rAAV.tdTomato.flex Allen 864*) in SST-Cre::WT (**Fig. 3.12.1 a-b**) and PV-Cre::WT mice (**Fig. 3.12.1 c-d**), respectively. Note that the distribution of the PV$^+$ LRIPs was predominantly localized to lateral portions of the hippocampus (**Fig. 3.12.1 b**).

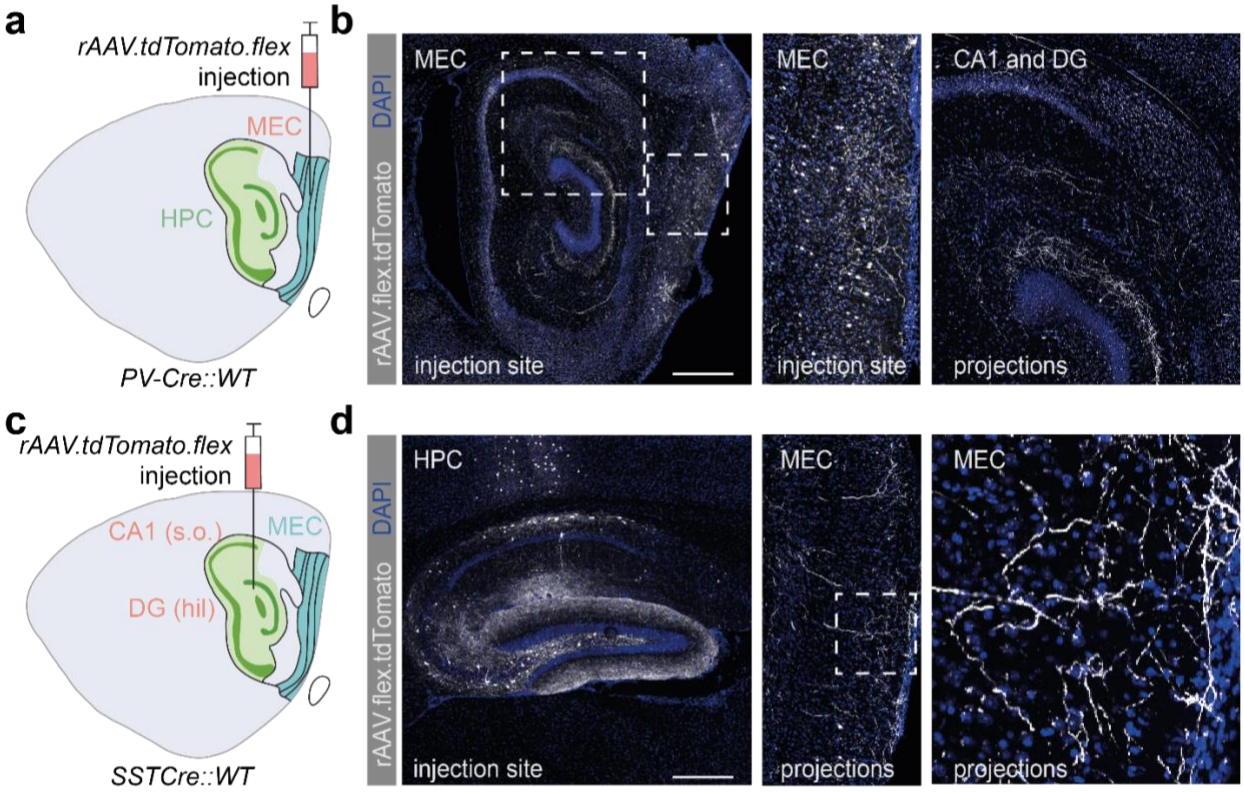

Figure 3.12.1 Long-range inhibitory projections (LRIPs) between the hippocampus and the MEC. **a)** Schematic of a sagittal section of a mouse brain illustrating stereotaxic injection of *rAAV.flex.tdTomato Allen 864* as anterograde tracer in the MEC of PV-Cre::APP/PS1 mice, labeling hippocampal-targeting LRIPs. **b)** Overview image of injection site in the MEC and projection sites in the HPC. Dashed boxes indicate zoomed-in regions. Note that MEC-PV$^+$LRIPs target both the SR-SLM border in CA1 and the ML of DG. **c)** Injection of *rAAV.flex.tdTomato Allen 864* as anterograde tracer in CA1-SO and hilus of SST-Cre::WT mice DG, labeling entorhinal-targeting LRIPs. **d)** Overview images of injection sites in the HPC and projections sites in the MEC. Dashed boxes indicates zoomed-in region. Note that HPC-SOM$^+$LRIPs target MEC-LI. Scale bars: 500 µm.

LRIPs may be critical for the emergence of hippocampo-entorhinal oscillatory coupling, and thereby support memory processes (Melzer & Monyer, 2020). Furthermore, we have previously reported that SOM^+ OLM interneurons in CA1 lose axonal segments over the course of the pathology (Schmid et al., 2016). Finally, immunofluorescent staining of SOM^+ neurons in the MEC confirmed that this population is vulnerable to beta-amyloidosis (Fig. 3.11). Thus, to assess whether and how SOM^+ long-range inhibitory neurons (LRIPs) of APP/PS1 transgenic mice also showed signs of degeneration, *rAAV.tdTomato.flex* was stereotactically injected in the hippocampus of SST-Cre::WT and SST-Cre::APP/PS1 mice. Because it was shown by retrograde studies that the majority of MEC-projecting SST^+LRIPs reside in the SO of CA1 and in the hilus of DG (Melzer et al., 2012), the intracranial injection targeted these two compartments of the hippocampus **(Fig. 3.12.2 a-b)**. Animals were aged on average 11 months at the time of injection. After 4 weeks of expression, SOM^+ axonal projections were readily visible in the MEC of both genotypes (**Fig. 3.12.2 c**). Post-mortem histological quantifications revealed a significant reduction of total area covered by tdTomato-positive axonal segments in the MEC of SST-Cre::APP/PS1 mice (**Fig. 3.12.2, d-f**; SST-Cre::WT: 26.92 ±2.1 mm/area vs SST-Cre::APP/PS1: 18.17 ±1.8 mm/area; two-tailed unpaired t-test, **p=0.002).

To summarize, a reduction of SOM^+ axonal segments was observed in the MEC of 12 month old SST-Cre::APP/PS1 animals compared to age matched controls. These results indicate that not only SOM^+ local inhibitory neurons in the MEC, but also long-range projecting neurons are affected by beta-amyloidosis in the hippocampal system.

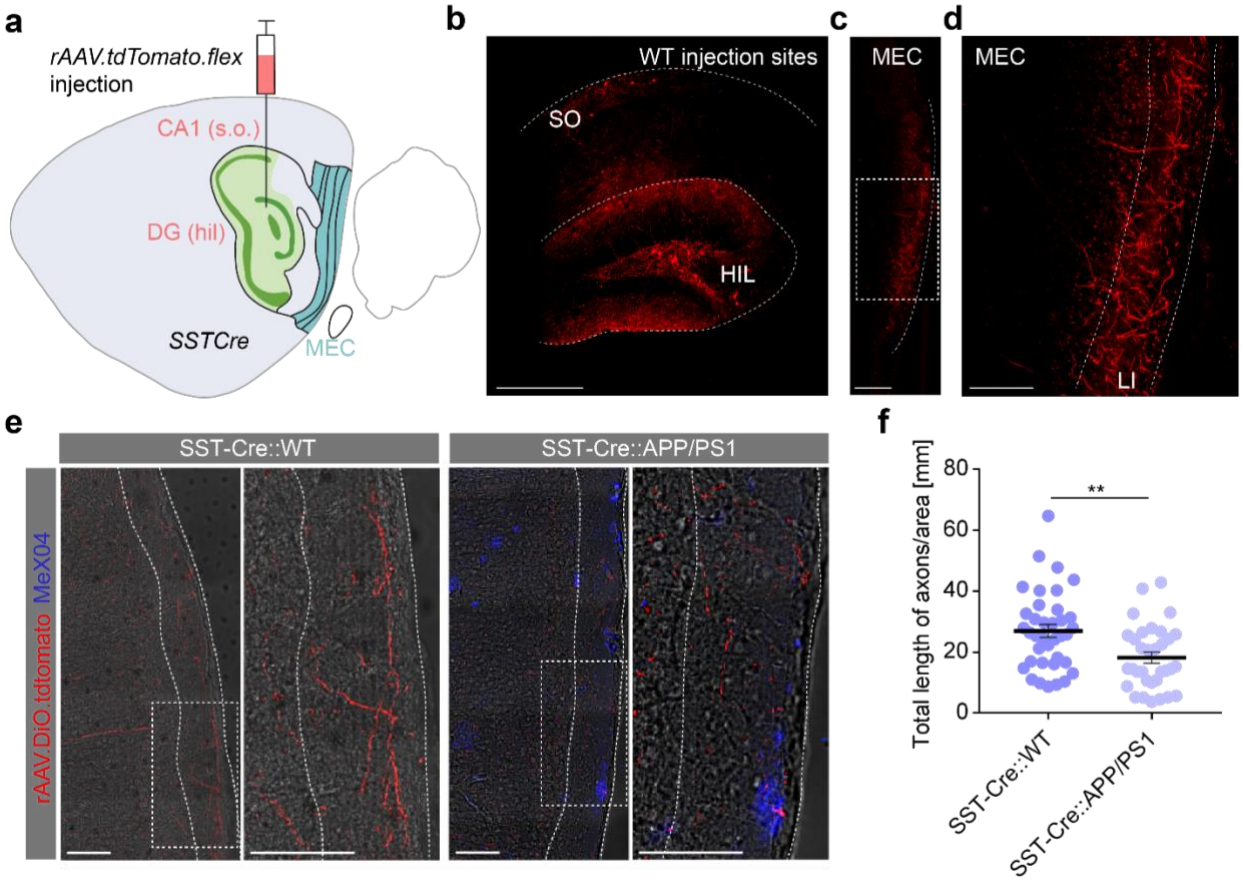

Figure 3.12.2 Area covered by SOM$^+$LRIP axons is reduced in the MEC of 12 month old SST-Cre::APP/PS1 mice. a) Schematics of stereotactic intracranial injections of the *rAAV.flox.tdTomato*. The viral construct was unilaterally injected in the right hippocampus (CA1 and DG) of SST-Cre::WT and APP/PS1 animals and used as a fluorescent anterograde tracer. **b)** Exemplary histological section of a mouse expressing tdTomato 4 weeks after injection at the level of the injection site, and exemplary images of SOM$^+$ LRIPs axons in the MEC of the same animal **(c-d)** MeX04 (blue) was used to stain Aβ plaques. **e)** Exemplary histological sections of SST-Cre::WT and SST-Cre::APP/PS1 animals, showing a deficiency in axonal segments in the MEC of the latter. Boxes indicate magnifications shown in the adjacent panels. **f)** Quantification of total length of axonal segments in the MEC of both genotypes. Two-tailed unpaired t-test: t(68)= 3.11,**p=0.002; SST-Cre::WT n=37 slices in 8 mice, SST-Cre::APP/PS1 n=33 slices in 7 mice (2-6 slices per mouse). Scale bars: **b)** 300µm; **c-f)** 100µm. Graphs represent individual values (slices) and bars represent means ±SEM.

3.13 Two-photon calcium imaging in the EC

Functionally, LRIPs reaching the layer I of the MEC have been poorly characterized (Melzer et al. 2012). Thus, I sought to investigate how their activity correlates with behavioral readout in both healthy and AD-like conditions by means of two-photon calcium imaging. Two-photon imaging in the MEC is particularly difficult due to the depth of the brain region. Previous methods described the assembly and implantation of a microprism in the fissure between the MEC and cerebellum (Low, Gu, & Tank, 2014). This enables imaging at a depth of 1.5 mm, which is sufficient to reach the dorsal portion of the MEC (Low et al., 2014). Here, I was able to successfully implant the microprism assembly facing the MEC, thereby gaining optical access to this region that I had previously stereotactically injected with a pan-neuronal calcium indicator (**Fig. 3.13 a-c**). Mice were head-fixed on the treadmill, and an angled objective was employed to direct the laser beam perpendicularly to the microprism (**Fig. 3.13 d**). Calcium transients were readily visible through the microprism (**Fig. 3.13 e, f**), and cells were active as the animal ran on the linear treadmill (**Fig. 3.13 g**).

Overall, the establishment of this approach paves the way for future experiments that involve monitoring of cellular activity in the MEC upon, for example, manipulation of hippocampal afferents by chemogenetic or optogenetic approaches.

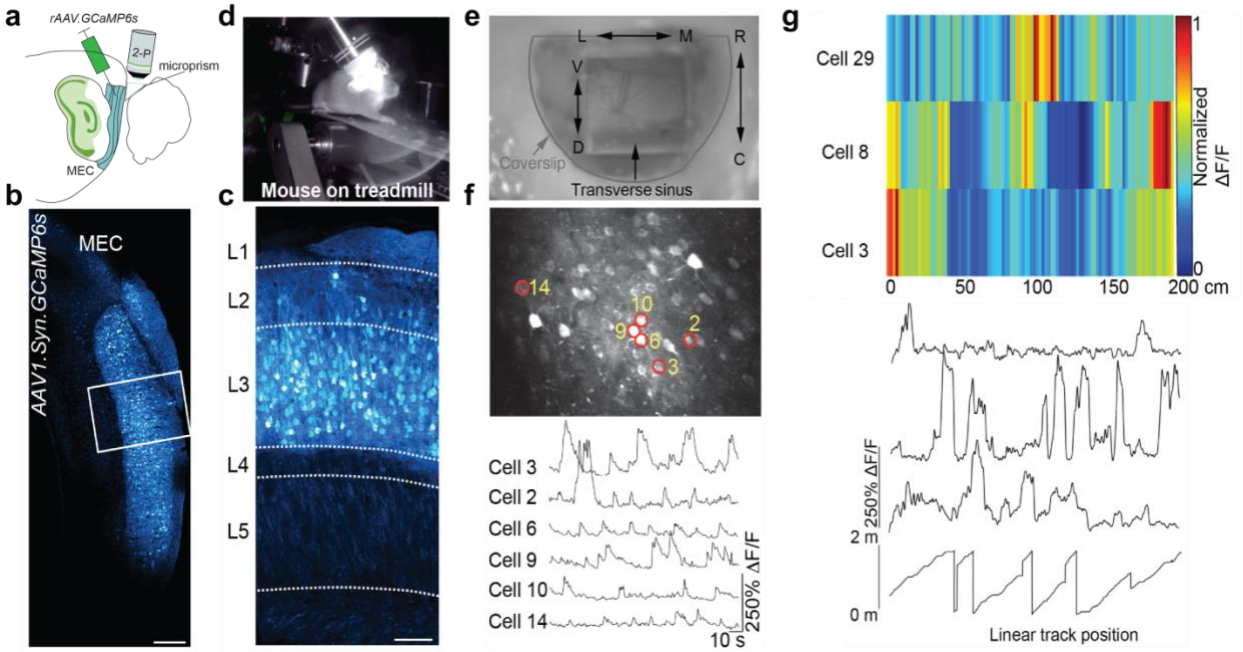

Fig. 3.13 Two-photon calcium imaging in the EC. a) Schematics of rAAV.Syn.GcaMP6s intracranial injection in the MEC and microprism implantation. b) Exemplary injection of the AAV expressing the calcium indicator in the MEC. **c)** Expression of GCaMP6s across MEC layers 1 to 3. **d)** Head-fixed mouse on the linear treadmill and angled objective used for two-photon excitation of the calcium indicator. **e)** Dorsal view of the microprism. The imaging planes are indicated along the microprism (r→c: rostro-caudal; d→v: dorso-ventral; l→m; lateral-medial). **f)** Field of view showing cells in the MEC acquired through the microprism. ROIs indicate cells whose exemplary calcium transients are shown in the section below. **g)** Normalized ΔF/F of three putatively spatially tuned cells as function of position on the linear treadmill, shown in the section below (linear track position).

4 Discussion

Peak frequency of theta oscillations decreases with age

Hippocampal oscillations in the theta range have been linked to various cognitive functions such as active exploration, spatial navigation and spatial memory (Korotkova et al., 2018). Cognitive decline is a hallmark of both human healthy aging and AD, and this correlates with reduced theta power in humans (Cummins & Finnigan, 2007; Toth et al., 2014) and rats exploring a novel environment (Jacobson et al., 2013). A comprehensive study on how age affects WT and an AD mouse model (PLB1Triple) was carried out by Jyoti et al. (Jyoti, Plano, Riedel, & Platt, 2015). The authors showed that power of hippocampal theta oscillations was significantly increased in transgenic animals, a phenomenon often reported in literature. At the age of 21 months, WT animals showed a generalized decrease in oscillation power of all the major frequency bands. In our study, we could not draw conclusions about how the spectral power of hippocampal CA1 changes with age, given the recording condition employed. Indeed, single wire configurations do not enable the required degree of precision to target the same compartment of CA1 in all animals, which is crucial when quantifying power of theta oscillations. Theta oscillations in CA1 display the highest power in SLM and in the hippocampal fissure (Buzsaki, 2002), and displacing the electrodes by only 50 µm would result in entirely different oscillatory amplitudes. Nonetheless, frequency of theta oscillations is conserved across layers (Buzsaki, 2002). Here, although no difference between PV-Cre::WT and PV-Cre::APP/PS1 mice could be detected as the animals performed an open field test (**Fig. 3.1 c**), I observed that peak theta frequency decreased linearly with age (**Fig. 3.2 a**). Interestingly, the velocity of WT mice was also inversely correlated to age (**Fig. 3.2 d**), which could be a potential explanation to the reduction in peak theta frequency. Peak theta frequency, in fact, has been shown to directly correlate with speed during exploratory, voluntary movement (Bender et al., 2015; Vanderwolf, 1969), and also during running epochs when animals are head-fixed on a linear treadmill (Fuhrmann et al., 2015). In the animals tested in this thesis we could not reproduce the relationship between running speed and linear increase in peak theta frequency. Interestingly, it was shown that lack of correlation between peak theta frequency and velocity correlates with poor learning abilities of rats (Richard et al., 2013). Thus, it is possible that the missing correlation between peak theta frequency and running speed underlies the decline in cognitive abilities of PV-Cre::WT animals that I observed in this study (**Fig. 3.6.2, 3.7, 3.8.1**). Alternatively, this lack of direct relationship could be explained by the exploratory patterns displayed by the animals. As seen by the positive correlation of the

duration of theta oscillations and mean velocity (**Fig. 3.2 g** and **Fig. 3.2 k**) in both genotypes, theta oscillations are more prominent when the animals move in a sustained way. It is therefore possible that a linear correlation between peak theta frequency in the range of 7-12 Hz will be observed in a different behavioral paradigm that requires the animals to move linearly along a track or linear treadmill, as observed by Cayzac et al. (Cayzac et al., 2015) and Fuhrmann et al. (Fuhrmann et al., 2015).

Interestingly, though, neither peak theta frequency nor running speed correlated with age in PV-Cre::APP/PS1 animals (**Fig. 3.2 h-n**). We have previously observed a reduced peak theta frequency in the same mouse model, which was concomitant with increased velocity of the animals in the open field (Ambrad Giovannetti, 2018). This hyperactive motility phenotype, which did not correspond to linear increase in peak theta frequency, has been observed by others in the same mouse model (Cayzac et al., 2015), *in vivo. In vitro*, a reduction of peak theta frequency was observed in a different model, but in this case the theta oscillations were in the range of 4-6 Hz as expected by measuring theta oscillations in an ex vivo setup (Goutagny et al., 2013). In this thesis, in which older mice were investigated, peak frequency of PV-Cre::WT and PV-Cre::APP/PS1 animals was not significantly different (**Fig. 3.1 c**), and PV-Cre::APP/PS1 animals did not travel significantly faster than PV-Cre::WT animals at any age (**Fig. 3.1**).

Overall, these and previously acquired data in a younger cohort of animals suggest that a) peak frequency of theta oscillations decrease linearly with age in PV-Cre::WT animals; b) PV-Cre::APP/PS1 animals showed a hyperactive motility phenotype at a younger age, which was unexpectedly correlated with a lower peak frequency of theta oscillations. As peak theta frequency was correlated neither to age nor to velocity in the PV-Cre::APP/PS1 animals measured in this study, one could speculate that theta oscillations are affected at earlier early stages of the pathology and then do not worsen significantly with age. Indeed, aging had a stronger effect on hippocampal LFPs of PV-Cre::WT than on that of PV-Cre::APP/PS1 animals, and this potentially underlies behavioral deficits observed in aged PV-Cre::WT rodents that were observed in behavioral experiments.

A reduction in peak theta frequency in rodents has been observed not only with age (Abe & Toyosawa, 1999; Wimmer et al., 2013), but also when foraging rats were exposed to a novel environment; this phenomenon gradually disappeared upon gaining familiarity with the context (Jeewajee, Lever, Burton, O'Keefe, & Burgess, 2008). Importantly, this was not due to decrease in median running speed, calculated during intervals of movement higher than 5 cm/sec

(Jeewajee et al., 2008). Novelty detection is one of the hypothesized functions of the CA1 compartment, which is thought to function as a comparator between acquired and current experiences (Duncan, Ketz, Inati, & Davachi, 2012). We have recently demonstrated that the hippocampus of APP/PS1 animals broadcasts an improper novelty signal seen at the level of immediate early gene (IEG) expression when exposed to a familiar environment (Poll et al., 2020). Therefore, it would be interesting to correlate peak theta frequency in the LFP with the evolution of CA1 population activity at the level of immediate early gene expression. Indeed, recent evidence showed that IEGs expressing cells recruit stronger PV^+ perisomatic inhibition onto themselves, which could function as a strategy to regulte the recruitment and excitability of engram cells (Yap et al., 2021). A locomotion-independent reduction in peak theta frequency has been also reported by Montgomery and Petersen et al. (Petersen & Buzsaki, 2020) upon slowing down the activity of the MS. Noteworthy, reduced peak theta, but not reduced running speed correlated with increased errors in a working memory task (Petersen & Buzsaki, 2020). These findings support the notion that theta oscillations are multi-faceted and controlled by distinct circuits in a brain-state dependent manner (Korotkova et al., 2018). However, the question whether experience-dependent reduction of peak theta frequency is supported by the same structures and mechanisms that cause a reduction of peak theta frequency with age remains open.

Locomotion, theta oscillations and arousal are governed by partially overlapping, but functionally dissociable brain structures, in particular by hypothalamic nuclei (Bender et al., 2015; Fuhrmann et al., 2015; Lu et al., 2020). Reductions in both locomotor activity and cognitive functions with age have been extensively reported in literature (Bordner et al., 2011; Shoji et al., 2016; Szentes et al., 2019). Among the hypothesized causes behind the age-dependent motoric and cognitive decline are reduced levels of arousal and dysfunction of neurotransmitter systems linked to motor initiation, like the monoaminergic system (Darbin, 2012), and the simultaneous alterations in GABA and GABA receptor composition that occur with age (Rissman, De Blas, & Armstrong, 2007). In fact, while a reduction of inhibitory input may account for alterations in oscillatory frequencies observed with aging, this alone is not likely to be the cause of the reduced velocity of the animals observed in this and in other studies performed in aged rodents. Indeed, optogenetic stimulation of septal PV^+ long range projection neurons was not sufficient to induce movement in PV-Cre animals (Bender et al., 2015). On the other hand, the observed reduction of peak theta frequency speaks for alterations in GABAergic signaling that occur with aging (Rozycka & Liguz-Lecznar, 2017). In fact, a similar slowing down of peak theta frequency was observed in rodent models where PV^+ neurons were

lacking a subunit of the GABA receptor, thus removing fast synaptic inhibition onto them (Wulff et al., 2009). Besides, it was shown that medial septal GABAergic inputs control frequency, but not amplitude of hippocampal theta, which remains subjected to endogenous locomotor activity of the animal (Zuschi 2018).

Finally, further experiments need to be performed to formulate a cohesive view of how hippocampal field and single cell activity evolve longitudinally (i.e. in the same individual) with age in healthy and APP/PS1 transgenic mice. In particular, the use of laminar LFP recordings established in this thesis (**Fig. 3.9**) would be required to observe alterations in different compartments of the CA1 area with age, hence enabling a higher temporal (i.e. across age) and spatial (i.e. layer-specific) resolution. A reduction of theta power in the SLM, for example, would support the lack of insufficient excitatory (via temporo-ammonic synaptic activation) or disinhibitory (via LRIPs) input from the EC.

To summarize, it was shown here that peak frequency of theta oscillations negatively correlates with age in PV-Cre::WT, but not in PV-Cre::APP/PS1 animals aged between 10 and 21 months. Furthermore, exploratory activity of PV-Cre::WT and PV-Cre::APP/PS1 animals was affected by age. These observations support the hypothesis that oscillatory rhythmicity and behavior are altered due to malfunction of the excitatory/inhibitory balance, possibly because of a lack of inhibitory control.

Altered theta-gamma phase-amplitude coupling in PV-Cre::WT and PV-Cre::APP/PS1 animals

In this study, LFP recordings of theta oscillations were carried out in the SLM of CA1. Here, amplitude of theta oscillations is the highest compared to other hippocampal layers (Buzsaki, 2002). Coherent with an increase in amplitude of theta oscillations, LFP recordings in CA1 SLM reveal also the strongest amplitude of oscillations in the mid-gamma (60-80 Hz) and fast gamma range (80-130 Hz; (Colgin, 2016; Fernandez-Ruiz et al., 2017; Lisman & Jensen, 2013; Scheffer-Teixeira et al., 2012; Schomburg et al., 2014). Here, we observed a significant reduction in modulation index (MI) of mid-gamma oscillations by theta oscillations in the SLM of PV-Cre::APP/PS1 animals (**Fig. 3.3 c**). Alterations in the theta, gamma, and theta-gamma frequency range are a hallmark of AD dementia in mouse models and patients (Goodman et al., 2018; Nakazono, Jun, Blurton-Jones, Green, & Igarashi, 2018). Alterations in MI have been observed in pre-plaque hippocampi extracted from 1 month old TgCRND8 transgenic mice (Goutagny et al., 2013), in the MEC of APP-KI mice (Nakazono et al., 2017), and in the parietal cortex of an APP-KO mouse model (X. Zhang et al., 2016). Furthermore, reduced theta-gamma

coupling in absence of alterations in gamma power was also observed in the hippocampus of adult animals in which PV^+ interneurons lacked fast synaptic inhibition onto them (Wulff et al., 2009). In this thesis, the MI was calculated for the mid-gamma range (60-80 Hz) in animals in which single tungsten wire electrodes targeted the SLM. Therefore, the mechanisms behind the observed reduction in MI may be rather driven by a distal dysfunction of EC input than to a local GABAergic phenotype, which would instead probably be observed in case of a disturbance in the slow gamma range in *stratum pyramidale* (SP) or in *stratum radiatum* (SR). Nonetheless, studies on theta, gamma, or theta-gamma coupling in the EC of mouse models of AD are not abundant, and whether theta-gamma coupling impairments are due to an upstream and earlier dysfunction of entorhinal circuits has not been elucidated yet (Nakazono et al., 2018). Interestingly, it has been shown that gamma power of the LEC is altered in 5 month old animals, in *in vivo*, in the APP/PS1 mouse model (Klein, Donoso, Kempter, Schmitz, & Beed, 2016). In the future, laminar LFP recordings, as shown in Fig. 3.9, are needed to elucidate whether alterations of MI are observed in other CA1 layers like the SP or SR. In SR, the input of CA3 Schaffer collaterals is the strongest, and so is the amplitude of low-gamma oscillations (Fernandez-Ruiz et al., 2017; Schomburg et al., 2014). If a reduced low-gamma MI in SR, and a concomitant reduction of MI in SLM are simultaneously recorded, it would indicate that both micro- (i.e. occurring within the hippocampus proper) and macro-circuits are affected in PV-Cre::APP/PS1 animals.

Next to the significant reduction of mid-gamma MI in PV-Cre::APP/PS1 animals, we have observed an age-dependent increase in MI in PV-Cre::WT animals, which was not detected in PV-Cre::APP/PS1 animals (**Fig. 3.3 d, e**). Similar to the results presented in Fig. 3.2, in PV-Cre::APP/PS1 mice, oscillatory activity of hippocampal circuit function did not undergo significant change between the age of 13 and 24 months. In addition, the strong reduction in MI observed between PV-Cre::WT and PV-Cre::APP/PS1 animals seems to be largely due to the lack of age-dependent increase of theta-mid gamma MI in transgenic animals (i.e. the difference is higher at an older age). Interestingly, the higher degree of theta-mid gamma MI in SLM has been correlated with increased strength of MEC layer III input (Fernandez-Ruiz et al., 2017). The method used here to calculate MI is a noise insensitive and gamma amplitude-independent method. As shown in **Fig. 3.3 b**, the increase we observed is likely not due to increased amplitude of gamma oscillations with age (Tort et al., 2010). Speed is also not a likely factor causing the increase in MI, as the average velocity of the animals investigated decreased with age. Strikingly, increase in theta-gamma coupling has been observed upon learning and at the decision making time point during a working memory task (Tamura, Spellman, Rosen,

Gogos, & Gordon, 2017; Tort et al., 2009) Hence, the age-dependent linear increase of MI in SLM is possibly the result of compensatory mechanisms occurring in the MEC of aged PV-Cre::WT animals, which fail to manifest in PV-Cre::APP/PS1 animals.

Because gamma rhythmogenesis is tightly linked to inhibitory neuron function, and it is also correlated to learning processes, it would be highly relevant to investigate the role of the recently described long-range inhibitory projections (LRIPs) originating in the MEC, whose post-synaptic targets are local CCK^+ interneurons located at the SR-SLM border in the hippocampus (Basu et al., 2016; Melzer et al., 2012). In particular, the questions whether LRIPs contribute to the locking of mid-gamma to the theta phase in SLM, and whether these inhibitory neurons undergo an age-dependent remodeling in healthy aging and disease-like conditions need to be addressed. Indeed, LRIPs are required to promote precisely timed disinhibition of pyramidal cells in CA1, so that inputs from the CA3 elicit a strong depolarizing response in the distal dendrites (Basu et al., 2016). Thus, MEC LRIPs would be ideal in promoting redirection of information flow, and increase coupling of distinct gamma bands onto different phases of theta (Akam & Kullmann, 2014). Possibly, an exaggerate "baseline" degree of phase locking in absence of learning is undesirable, as it may result in the rigidity of the network when switching between encoding and retrieval states is required (Lisman & Jensen, 2013). In this regard, it would be insightful to quantify whether and how the MI of slow gamma in SR changes by age in PV-Cre::WT animals, especially because it is known that excitatory connections of the perforant pathway undergo degeneration in humans and rodents (Yassa, Mattfeld, Stark, & Stark, 2011).

In conclusion the presented findings indicate that modulation of gamma oscillations by underlying theta undergoes remodeling in the hippocampus of PV-Cre::WT animals but not in PV-Cre::APP/PS1 animals between 10 and 24 months of age.

Entrainment of theta oscillations via optogenetic stimulation of PV^+ interneurons

To test whether stimulation on local inhibitory neurons would result in an increase of amplitude in frequencies within and outside the theta band in aged PV-Cre::WT and PV-Cre::APP/PS1 transgenic mice, an AAV encoding a Cre-dependent excitatory opsin (C1V1) was injected in the hippocampus of PV-Cre::APP/PS1 animals. As a control, animals were intracranially injected with PBS. LFP recording tungsten wires targeting the SR/SLM were implanted together with bilateral optic fibers on top of both hippocampi. Optogenetic stimulation at 5, 8, 10 and 15 Hz was carried out in an open field where the mice were able to freely explore (**Fig. 3.4 g-j**). Stimulation at the different frequency bands resulted in an increase of amplitude of the

stimulation frequency compared to the baseline interval for all frequencies in PV-Cre::APP/PS1 mice (**Fig. 3.4 k-n**) and for all frequencies except 8 Hz in PV-Cre::WT animals (**Fig. 3.4 h**). Additionally, frequency modulation was observed in C1V1-expressing animals but not in Sham-injected animals. This proves that the laser intensity employed does not cause photovoltaic artifacts in the LFP (Mikulovic et al., 2016). This result confirms previous reports indicating that local PV^+ interneuron stimulation is sufficient to generate oscillations in an organotypic slice culture preparation, in absence of medial septal input (Amilhon et al., 2015), and *in vivo* (Ognjanovski et al., 2017). Here, I showed that this is also reproducible in PV-Cre::APP/PS1 animals used to model the AD pathology.

The stimulation frequency that elicited the strongest and most reliable response in both genotypes was the 10 Hz stimulation (**Fig. 3.4 i, m**). The reason why stimulation at 8 Hz did not suffice to modulate this frequency in PV-Cre::WT mice might be caused by the inability of the hippocampal system to resonate and in turn generate a sustained 8 Hz oscillation in aged PV-Cre::WT animals. Resonance is a phenomenon that depends on not only global circuit factors, but also on local constrains of the microcircuit imposed by, for example, the passive membrane properties of the cells that participate in the networks (Hutcheon & Yarom, 2000). Interestingly, not only learning and memory processes (McKay, Oh, & Disterhoft, 2013), but also age impacts cell excitability in the hippocampus (Oh, Oliveira, Waters, & Disterhoft, 2013; Oh, Simkin, & Disterhoft, 2016). For example, it was shown that CA1 pyramidal cells of aged rats show a higher Ca^{2+} buffer capacity, i.e. they accumulate more internal calcium when firing a train of action potentials (Oh et al., 2013). Furthermore, effects of aging on the CA1 synaptic compartment and on the intrinsic excitability of pyramidal cells are well documented, and they suggest that these neurons become less excitable with age (Murphy et al., 2004). The observation that the same type of stimulation was sufficient to elicit an increase of the 8 Hz frequency amplitude in PV-Cre::APP/PS1 animals suggests that the mechanisms behind the decline of peak theta frequency with age in PV-Cre::WT animals (Fig. 3.2) may differ between healthy aging and AD-like pathology. In fact, clusters of hyperexcitable hippocampal pyramidal neurons were observed near Aβ plaques in rodent models of amyloidosis (Busche et al., 2008; Kerrigan, Brown, & Randall, 2014; Siskova et al., 2014; Sosulina, 2020), opposite to what is documented for healthy aged rodents. A second hypothesis to explain the lack of increase in amplitude of the 8 Hz frequency band in PV-Cre::WT mice may be the difficulty of "overwriting" the most prominent theta oscillatory frequency observed when animals are freely moving. In the future, it will be necessary to control for movement intervals when evaluating the effect of the stimulation, to exclude that entrainment fidelity is not biased by the behavior

of the animal. Nonetheless, the results shown in Fig. 3.1 showed that the peak theta frequency of the PV-Cre::WT animals tested in this study was not higher than 7.5 Hz. This supports the hypothesis that the "slowing down" of theta frequency is caused by mechanisms that also prevent the entrainment of the most prominent theta peak frequency observed in younger freely behaving animals. Future investigations with narrower age groups, and possibly performed in a longitudinal fashion, will elucidate whether and how the overall excitability and feedback response of the network deteriorate with age and disease.

To determine how optogenetic stimulation of PV^+ neurons may reorganize single cell firing in both PV-Cre::WT and PV-Cre::APP/PS1 animals, single unit recordings via tetrodes, silicon probes, or multi-unit activity recordings would be required in the future. Insights on how PV^+ interneuron stimulation may coordinate hippocampal cell assemblies were provided by Ogjanovski et al. (Ognjanovski et al., 2017), who showed that rhythmic optogenetic stimulation of PV^+ CA1 interneurons at theta frequencies is able to increase synchronization of pyramidal cell firing in non-anesthesized animals. Furthermore, Stark et al. (Stark et al., 2013) demonstrated that PV^+ optogenetic activation induced theta resonance in pyramidal cells, as a result of post-inhibitory spiking of PV^+ interneurons, in freely behaving animals. Optogenetic stimulation of PV^+ interneurons in rodent models of AD has been performed predominantly at gamma frequencies (Etter et al., 2019; Iaccarino et al., 2016). However, evidence on whether and how the rate and phase coding of single neurons change upon this intervention, *in vivo*, is lacking. As briefly mentioned, clusters of hippocampal hyperactive neurons emerge before plaque onset in a mouse model of AD (Busche et al., 2012). Pyramidal cell hyperactivity has been linked to alterations in dendritic morphology, leading to higher likelihood of supralinear integration of EPSPs and thus increasing probability of burst firing (Siskova et al., 2014). Similarly, increased hippocampal activation is observed in human subjects that are at risk of developing AD (Bakker et al., 2012). At the level of inhibitory interneurons, Hijazi et al. (Hijazi, Heistek, Scheltens, et al., 2020) recently demonstrated that PV^+ interneurons in CA1 are hyperactive, *in vitro*, in the APP/PS1 mouse model when the animals were approximately 16 weeks of age, and that this is not the case for glutamatergic cells. Subsequently, PV^+ interneuron function becomes hypoactive at the age of 6 months, the point in time when plaque burden is substantial in the hippocampus (Hijazi, Heistek, Scheltens, et al., 2020). Furthermore, hyperexcitable PV^+ neurons were shown to render the circuit susceptible to neurotoxic effects of Aβ, indicating that familial AD may indeed be the result of an early dysfunction of inhibitory neurons (Hijazi, Heistek, van der Loo, et al., 2020). Indeed, inhibitory neuron hyper- or hypo-activity has been observed in multiple mouse models of AD (Ambrad G. & Fuhrmann, 2019;

Martinez-Losa et al., 2018; Palop et al., 2007; Palop & Mucke, 2010, 2016; Verret et al., 2012), and its intensity or direction are strictly dependent on the genetic background of the animals, but also on the time of investigation. Thus, it would be relevant to study whether and how PV^+ interneuron stimulation counteracts the hyperexcitability of CA1 pyramidal cells in PV-Cre::APP/PS1 animals. We have shown that pulsed stimulation of PV^+ interneurons, *in vitro*, induces somatic IPSPs in pyramidal cells, as expected when stimulating PVBCs, but it was not sufficient to elicit post-inhibitory rebound spiking in brain slices extracted from PV-Cre::WT animals (Ambrad Giovannetti, 2018). Yet, it is not known how this applies to PV-Cre::APP/PS1 animals, *in vivo*. Possibly, entraining the network at theta oscillations in both PV-Cre::WT and PV-Cre::APP/PS1 animals would result in the activation of entorhinal inputs, which would then contribute to the amplitude increase in the SLM. Nonetheless, it is not easy to exclude that the increase in amplitude of the stimulation frequency is the result of back-propagating action potentials.

In summary, it was shown that it is possible to increase theta power and drive theta frequency of interest by stimulating local PV^+ interneurons in the hippocampus, without relying onto a septal stimulation as done previously (Bender et al., 2015; Fuhrmann et al., 2015; Zutshi et al., 2018). This eliminates the network effects that would otherwise arise upon stimulation of local cell bodies in the septum, and is a more effective strategy than stimulating axonal terminations. Furthermore, we have elucidated that optogenetic stimulation of PV^+ interneurons elicits different responses in the network of PV-Cre::WT and PV-Cre::APP/PS1 animals, further corroborating the hypothesis that the hippocampal system may be subjected to different remodeling in age and disease.

Increasing inhibitory tone is not sufficient to restore recognition memory

Impaired recognition memory is a hallmark of several mouse models of AD (R. Zhang et al., 2012). We have previously demonstrated that rhythmic optogenetic stimulation of PV^+ hippocampal interneurons during a NOR test is sufficient to improve the recognition memory of PV-Cre::APP/PS1 transgenic mice compared to Sham-treated controls (Ambrad Giovannetti, 2018) in a cohort of mice aged on average 13 months. The optogenetic stimulation was designed as a closed-loop feedback protocol based on the endogenous theta oscillations recorded in the SLM of CA1. Briefly, if an increase of the theta band amplitude (between 4 and 12 Hz) was detected in the LFP within a 4 second window, optogenetic stimulation would be initiated for the following 5 seconds at a frequency equal to the peak detected, with an additional 0.5 Hz added to it (**Fig. 3.5**). To discern whether this effect was due to an increase in inhibitory

tone alone, or whether an entrainment of theta rhythmicity in the hippocampal network is also necessary to observe the rescue of cognitive defects, we designed a stimulation protocol in which laser pulses were delivered in an "arrhythmic" way, as a jitter of ±30ms was included between each laser pulse. This resulted in an enhancement of inhibitory tone on pyramidal cells, measured as somatic IPSPs, but in the disruption of the theta rhythmic firing of PV^+ interneurons (Ambrad Giovannetti, 2018).

First, the NOR test coupled with the closed-loop arrythmic optogenetic stimulation was performed on a cohort of 14 month old PV-Cre::APP/PS1 animals (**Fig. 3.6.1 a, b)**. As a result, the discrimination index (DI) of PV-Cre::APP/PS1 expressing the excitatory opsin C1V1 in PV^+ interneurons was not significantly different than that of Sham-treated PV-Cre::APP/PS1 mice (**Fig. 3.6.1 c)**. Long-term recognition memory relies on the function of hippocampus and neocortical regions, provided that a sufficient delay is introduced between sample and test phases (Cohen et al., 2013; Cohen & Stackman, 2015). Also, it was shown that recognition memory becomes independent of the hippocampus only upon a very long-term retrieval, in rats with bilateral hippocampal lesion (8 weeks, (Broadbent & Clark, 2013)). This is consistent with the hypothesized irrelevance of the hippocampus for retrieval of memories that have been stored already in prefrontal cortical circuits (Sivakumaran, Mackenzie, Callan, Ainge, & O'Connor, 2018; Wiltgen & Silva, 2007). In this thesis, the delay of 24 hours was short enough to hypothetically require hippocampal activity during the test phase, excluding the possibility that the stimulation, or the increase on inhibition, did not act upon the correct memory circuit. Hence, it is possible that lack of memory improvement in PV-Cre::APP/PS1 transgenic mice is due to the necessity for rhythmic inhibitory pulses to increase network synchrony, thereby guaranteeing network-efficient communication by PV^+ mediated theta-rhythmic control of pyramidal neuron excitability.

Subsequently, to test whether the optogenetic entrainment of inhibitory tone alone would be beneficial for PV-Cre::WT and PV-Cre::APP/PS1 animals at an older age, when the decrease of peak theta oscillations is most evident, arrhythmic feedback optogenetic stimulation was applied to on an older independent cohort of mice aged 19-20 months (**Fig. 3.6.2**). Here, no significant difference in DI could be detected between Sham-treated PV-Cre::WT and PV-Cre::APP/PS1 mice, in contrast to what was observed previously (Ambrad Giovannetti, 2018). This is an indication that PV-Cre::APP/PS1 animals did not show memory impairment. Nevertheless, neither the DI of Sham-treated PV-Cre::APP/PS1 animals, nor the DI of Sham-treated PV-Cre::WT animals were different than chance levels (50%). This indicates that neither PV-Cre::WT, nor PV-Cre::APP/PS1 mice displayed proper recognition memory.

Indeed, none of the groups tested showed a DI which was higher than chance levels, indicating that learning and memory was impaired in all conditions. The advanced age of the animals may partially explain why PV-Cre::WT mice did not perform the test significantly better than PV-Cre::APP/PS1 mice, as it is known that aging can strongly affect hippocampus-dependent recollection memory in humans and mice (Robitsek, Fortin, Koh, Gallagher, & Eichenbaum, 2008; Yang, Zhou, & Ma, 2019). Interestingly, degradation of learning and memory with age is paralleled by defective perforant path transmission at the EC-dentate gyrus synapse, in aged humans (Geinisman, deToledo-Morrell, Morrell, Persina, & Rossi, 1992; Lippa, Hamos, Pulaski-Salo, DeGennaro, & Drachman, 1992; Rogalski et al., 2012; Yassa, Muftuler, & Stark, 2010). Loss of neurons, instead, is not a typical marker of ageing (Rapp, Deroche, Mao, & Burwell, 2002), thus substantiating the observation that ageing affects predominantly the axonal and synaptic compartment. Direct information transmission between the hippocampus proper and the EC was shown to be relevant for appropriate novelty detection, performed by the CA1 compartment (Knight, 1996; Lisman & Otmakhova, 2001; Poll et al., 2020; Vago & Kesner, 2008; Vinogradova, 2001). In particular, the lateral entorhinal cortex (LEC) is responsible for the association of local (e.g. objects in the open field) to global landmarks. For example, it was shown that rats with LEC lesions did not perform the NOR test correctly (Kuruvilla & Ainge, 2017). In addition, input from long-range inhibitory connections (LRIPs) in the LEC was necessary to sustain NOR memory in mice (Basu et al., 2016). Thus, it would be relevant to investigate whether and how the entorhinal afferents into the hippocampus proper are affected in the animals that underwent the behavioral test by performing immunohistochemical and electrophysiological investigations. Finally, a deficit of recognition memory in APP/PS1 mice was previously demonstrated by us and others (Ambrad Giovannetti, 2018; R. Zhang et al., 2012). Here, 20 month old PV-Cre::APP/PS1 also showed memory impairment, as their DIs were not different than chance levels. Similarly to aged PV-Cre::WT animals, an early perforant pathway degeneration at the synaptic and dendritic level has been observed in mouse models of AD and humans (Harris et al., 2010; Hyman, Van Hoesen, Kromer, & Damasio, 1986; Roy et al., 2016). Thus, these are also possibly among the mechanisms that underlie the observed decline in recognition memory which occurs in PV-Cre::APP/PS1 animals, albeit at an earlier age and concomitant with degeneration of cholinergic and glutamatergic transmission. This, potentially, hinders the rescue of the cognitive impairment by increasing GABAergic transmission alone, as shown by lack of memory improvement in either C1V1-expressing PV-Cre::WT (**Fig. 3.6.2 c**) and PV-Cre::APP/PS1 animals (**Fig. 3.6.1 c** and **Fig. 3.6.2 c**). Lastly, it was shown that the total exploration time, total travelled distance and mean velocity of 19-20

month old PV-Cre animals (**Fig. 3.6.2 d, e**) were comparable to those of the 14 month old cohort (**Fig. 3.6.1 d, e).** This is in contrast to what was observed in the open field test, in which an age-dependent decrease in mean velocity was observed. Nonetheless, this suggests that the cognitive decline observed in 20 month old animals is independent of locomotion parameters, which corroborates the hypothesis that the decline in peak theta frequency correlates with cognitive decline.

In conclusion, these results indicate that 19-20 month old PV-Cre::WT animals mice perform indistinguishably than age matched PV-Cre::APP/PS1 transgenic mice in a NOR test. Additionally, increasing inhibitory tone in the hippocampus via optogenetic stimulation of PV^+ interneurons was not sufficient to influence the behavioral performance of either PV-Cre::WT or PV-Cre::APP/PS1 transgenic mice during the NOR test. This indicates that proper recognition memory processes rely on precisely timed excitation/inhibition balance in age and disease.

Rhythmic optogenetic stimulation of hippocampal PV^+ interneurons during the Y-Maze test

To test whether optogenetic stimulation of PV^+ interneurons in the hippocampus of PV-Cre::APP/PS1 and PV-Cre::WT mice would lead to the amelioration of spatial working memory in either or both genotypes, the feedback stimulation protocol was applied throughout the Y-Maze test for spontaneous alterations. Here, we tested the effect of theta-rhythmic stimulation of PV^+ interneurons on the spatial working memory of the 19-20 month old cohort of animals (**Fig. 3.7**). Unlike long-term memory, working memory encompasses processes that require consolidation and rapid manipulation of memory, in absence of previously occurred storage (Baddeley, 1992a, 1992b). Spatial working memory relies on both the hippocampus and neocortical areas, in humans, as shown by lesion studies (Baddeley, 2010; Chai, Abd Hamid, & Abdullah, 2018) and as seen in neurological disorders like schizophrenia (Forbes 2018). The spontaneous alteration in the Y-Maze has been used as a useful tool to assess hippocampal function in rodents, as it can rely on both egocentric (self-centered representation of a space) and allocentric (world-based, object to object based representation of a space) navigation strategies (Vorhees & Williams, 2014). Furthermore, the spontaneous alternation test is performed in absence of prior training, hence relying on the innate exploratory drive of the animals. Here, we performed the Y-Maze in presence of both local cues and distal cues. Here, the Y-Maze test did not reveal significant differences between any of the groups tested (**Fig. 3.7 c**). This, on the one hand, could signify that PV-Cre::APP/PS1 animals do not show a

working memory impairment in the spontaneous alternation test. On the other hand, it could indicate that PV-Cre::WT animals do not show proper working memory processes, and are indeed cognitively impaired in a way similar to PV-Cre::APP/PS1 animals. Interestingly, none of the groups tested displayed a spontaneous alternation percentage higher than chance level (50%). This indicates that aged PV-Cre::WT animals did not show proper working memory mechanisms, and in fact their performance did not differ from the one of PV-Cre::APP/PS1 animals. Furthermore, optogenetic entrainment of theta oscillations via hippocampal PV^+ neurons did not rescue the cognitive defects observed in PV-Cre::WT and PV-Cre::APP/PS1 mice (**Fig. 3.7 c**), similarly to the results of the NOR test (Fig. 3.6.2). Efficacy of the Y-Maze test may depend on the different ways the environment is cued, or on the time allowed for the animals to explore. In this study, the walls of the arms were cued with four different black and white pattern cues. In addition, the curtain walls surrounding the arena were equipped with colored cues. Presence of distal cues (external to the maze) is supposed to facilitate spatial navigation of a maze with the formation of the so called "spatial map", as proposed by O'Keefe et al. (Knierim & McNaughton, 2001), as distal cues are providing exclusively visual input and cannot influence the behavior of the rodent via other sensory stimuli like touch or smell. It is known, though, that humans and aged rats perform worse in navigational tests that require allocentric navigation strategies compared to egocentric ones (Colombo et al., 2017), a phenomenon attributed to loss of hippocampal function with age (Colombo et al., 2017). Thus, the observed cognitive deficits of PV-Cre::WT animals are unlikely to be attributed to an improperly cued environment and are likely caused by a progressive decline in cognitive abilities due to age. Regarding the time of the test analyzed, the behavior of the animals was quantified for 5 minutes. Traditionally, the Y-Maze test for spontaneous alterations is quantified for times ranging from 2 to 10 minutes, so our analysis was performed according to what is reported in the literature.

Lack of proper working memory mechanisms is a hallmark of both healthy aging (Reinhart & Nguyen, 2019; Yang et al., 2019) and AD, in humans (Goodman et al., 2018) and mouse models. Even though reports of behavioral deficits in the Y-Maze for the mouse model employed in this thesis (APP/PS1) are contradictory (Hsiao et al., 1995; Huang et al., 2016; Jura, Macrez, Meyrand, & Bem, 2019; Reiserer, Harrison, Syverud, & McDonald, 2007), defects in spontaneous alteration percentage have been observed in mice overexpressing Aβ and plaques compared to age-matched controls. Assuming that PV^+ stimulation would result in an improvement of working memory was legitimated by the finding that PV^+ neuron function is necessary for hippocampal spatial working- and long-term memory (Korotkova et al., 2010).

Indeed, lack of PV^+ interneuron function and concomitant loss of theta oscillations caused alterations in frequency and power of theta oscillations (Korotkova et al., 2010; Wulff et al., 2009). In addition, it was shown that CA1 PV^+ interneurons, specifically, are required for spatial working memory (Murray et al., 2011). In humans (Alekseichuk, Turi, Amador de Lara, Antal, & Paulus, 2016) and rodents theta oscillations are prominent during working memory (M. W. Jones & Wilson, 2005; Tamura et al., 2017), and they are affected by aging (Toth et al., 2014). In the future, it would be relevant to investigate how theta oscillations are altered during episodes of arm choice in both PV-Cre::WT and PV-Cre::APP/PS1 animals that perform the spontaneous alternation task (Belchior, Lopes-Dos-Santos, Tort, & Ribeiro, 2014).

Thus, 19-20 month old PV-Cre::WT mice showed impaired navigational and/or spatial working memory tasks, and they perform indistinguishably from PV-Cre::APP/PS1 mice. Additionally, optogenetic stimulation at theta frequencies was not able to influence the behavior of either PV-Cre::WT or PV-Cre::APP/PS1 mice in the Y-Maze test for spontaneous alterations.

Rhythmic optogenetic stimulation of hippocampal PV^+ interneurons during the NOL test

To test whether long-term spatial memory of aged mice would benefit from rhythmic entrainment of theta oscillations via stimulation of hippocampal PV^+ interneurons, the 19-20 month old cohort of PV-Cre::WT and age-matched PV-Cre::APP/PS1 animals was tested in the novel object location test (NOL; **Fig. 3.8.1**). For this test, the walls of the open field were not cued, and the behavioral protocol was designed in a similar way as the one employed for the NOR test. The protocol consisted of a repeated exposure to the familiar objects during the sample phase and a 24h interval between sample and test phase. As a result, no significant differences in DI could be detected between genotypes or treatment groups (**Fig. 3.8.1 c**). This suggested that, on the one hand PV-Cre::APP/PS1 animals did not show impaired long-term spatial memory processes; on the other, though, none of the groups tested showed a discrimination index (DI) higher than chance level. Thus, PV-Cre::WT animals displayed cognitive deficits and their performance was comparable to that of PV-Cre::APP/PS1 animals at the age of approximately 20 months, corroborating the results acquired during the NOR and Y-Maze test. Furthermore, optogenetic stimulation was not sufficient to ameliorate cognitive dysfunction in either genotype (**Fig. 3.8.1 c**). Only a significant difference in the two-way ANOVA test performed on the mean velocity and total travelled distance parameters was detected, indicating that PV-Cre::APP/PS1 mice travelled at a higher velocity compared to WT animals (**Fig. 3.8.1 e and f**, see figure legend for ANOVA results). This is in line with the results presented in Fig. 3.2, as the velocity of PV-Cre::WT animals, but not PV-Cre.::APP/PS1

animals linearly decreased with age. Defective long-term spatial memory processes in the NOL test were described in the literature for the APP/PS1 mouse model (Sierksma et al., 2014). However, the interval between sample and test phase employed by Sierksma et al. was of only 4 hours (Sierksma et al., 2014). Another study reported a difference in time spent at the displaced object after only 30 min of interval (Viana da Silva et al., 2016). In both cases, effects were small and mice tested were relatively young (approximately 6 months of age). The reason behind the PV-Cre::WT's groups lack of spatial reference memory and lack of effect of the optogenetic stimulation in both PV-Cre::WT and PV-Cre::APP/PS1 mice may be the advanced age of the animals tested. Defects in spatial memory with age have been described for rodents and humans, and they are in accordance with the higher susceptibility of the hippocampus to aging (Lester et al., 2017). Nonetheless, one cannot exclude that lack of local cues may have hindered proper formation of a spatial map in 20 month old animals.

Recent studies *in vitro* have shown that optogenetic activation of PV^+ interneurons in the hippocampus is able to restore theta-gamma coupling and also long-term potentiation (LTP) in slices incubated with the Aβ42 oligomers (Park et al., 2020). LTP has been proposed as a synaptic mechanism required for consolidation and storage of spatial memory in the hippocampus (Pastalkova et al., 2006). LTP is just one of the synaptic plasticity events that need to occur upon learning and memory. Among others is the synaptic turnover, i.e. the formation and elimination of new dendritic spines. We have previously shown that this phenomenon in particular is impaired in the mouse model employed in this study (L. Gu et al., 2014; Schmid et al., 2016). The reason why the optogenetic feedback stimulation protocol has failed to increase long term spatial memory in PV-Cre::WT and PV-Cre::APP/PS1 mice may be that the synaptic plasticity deficits in the hippocampal circuit of these animals were far too advanced at the age of approximately 20 months to be recovered by the rhythmic stimulation. An alternative explanation would be that spatial memory becomes reliant on cortical structures rather than on hippocampal function, as shown by decrease in allocentric navigation strategies that occurs in older humans (Colombo et al., 2017). Thus, stimulating the hippocampus alone would not be sufficient to elicit a behavioral response. Furthermore, it is known that oscillatory activity during sleep supports long-term memory storage and consolidation (Watson & Buzsaki, 2015), and that sleep disturbances are predictors for the development of MCI and AD. Interestingly, these disturbances are different from those that occur in healthy aging (Pak et al., 2020). It would therefore be insightful to record and possibly manipulate oscillations during different sleep stages and observe potential rescue in memory retrieval and cognition at this

advanced age, an approach that has been already tested in humans (Grimaldi, Papalambros, Zee, & Malkani, 2020).

Thus, these results showed that the NOL test did not disclose differences in behavior of 19-20 month old PV-Cre::WT compared to age-matched PV-Cre::APP/PS1 transgenic mice. Because PV-Cre::WT animals did not show a DI higher than chance levels, this supports the hypothesis that PV-Cre::WT animals display cognitive deficits that are comparable to those of PV-Cre::APP/PS1 animals at the age of 19-20 months. Furthermore, the spatial long-term memory of age-matched PV-Cre::WT nor PV-Cre::APP/PS1 mice was not rescued by rhythmic optogenetic stimulation at theta frequencies. This possibly indicates that, at the age of 20 months on average, the hippocampal circuit probed with the optogenetic stimulation fails to support long-term spatial memory processes.

We had previously observed that recognition memory is preserved in 13 months old PV-Cre::WT animals. The question whether spatial memory was preserved at a comparable age was not answered by the experiments described in Fig. 3.8, as animals were aged on average 19-20 months. Thus, to discern whether the spatial reference memory was preserved in younger PV-Cre::WT animals compared to age-matched controls, and to validate whether and how optogenetic stimulation of PV^+ interneurons would promote spatial memory processes, an independent cohort of 15 month old animals was tested in the NOL. (**Fig. 3.8.2 a, b**). As a result, we observed that PV-Cre::APP/PS1-Sham treated mice performed significantly worse than PV-Cre::WT Sham-treated animals. Furthermore, PV-Cre::APP/PS1 animals expressing the excitatory opsin C1V1 in PV^+ interneurons performed significantly better than their Sham-treated controls (**Fig. 3.8.2 c**). This effect was not due to differences in exploration times or motility parameters (**Fig. 3.8.2, d-f**). It is possible that the significant difference observed between PV-Cre::WT and PV-Cre::APP/PS1 Sham-treated animals is due to PV-Cre::APP/PS1-Sham injected animals' preference for the exploration of the object in the familiar location (approximately 30% DI). However, C1V1-expressing PV-Cre::APP/PS1 animals performed similarly to PV-Cre::WT Sham-treated animals. These results indicate that rhythmic optogenetic stimulation of PV^+ interneurons during a spatial memory test ameliorated cognitive deficits of the APP/PS1 mouse model. In contrast, the same optogenetic stimulation paradigm did not have an effect on the behavior of C1V1-expressing PV-Cre::WT mice. This could be caused, on the one hand, by the difficulty of the optogenetic stimulation to recruit the network of 15-19 month old PV-Cre::WT animals, as shown in Fig. 3.4. On the other hand, this could be explained by the insufficient role of the hippocampus in a healthy aged organism to sustain long-term spatial memory processes due to dysfunction or compensation by other brain

regions participating in the circuit, as hypothesized before. It is tempting to speculate that the memory circuits of PV-Cre::APP/PS1 animals are affected not only earlier in life compared to healthy aged animals, but also in a different anatomical and temporal sequence (Toepper, 2017), hence resulting in a different effect of the optogenetic stimulation in these individuals.

As the optogenetic stimulation was applied throughout both sample and test phases, it is not possible to discern whether our effect is due to an increase in encoding capacities of the network or to increased memory retrieval. Recently, though, we have shown that APP/PS1 mice are able to form a memory trace, as it is possible to detect an engram ensemble in the CA1 area of these animals upon exposure to a contextual fear conditioning task (Poll et al., 2020). It is tempting to speculate that the optogenetic feedback stimulation employed in this study was able to restore micro- and macro-circuit computations required to suppress interference of competing memory traces during retrieval of a long-term memory, which is dependent on not only hippocampal, but also neocortical function (de Sousa et al., 2019; Eichenbaum, 2017a). Additionally, we have not yet investigated the effect of the optogenetic stimulation on theta-gamma coupling. It was shown here that theta-gamma coupling is impaired in PV-Cre::APP/PS1 animals (**Fig. 3.3**), so it would be highly relevant to measure whether the MI of mid-gamma and theta is increased upon optogenetic stimulation in PV-Cre::APP/PS1 animals, and whether this, and not merely increase in theta frequency, results in the increased performance of PV-Cre::APP/PS1 animals expressing C1V1. Even though dissociating these mechanisms might be challenging, a possible way to discern this would be by temporally inactivating the entorhinal cortex during memory retrieval and simultaneous optogenetic stimulation, hence preserving septal driven theta-rhythmicity, but abolishing theta-gamma coupling at the *stratum lacunosum moleculare*.

The results presented in **Fig. 3.8.2** are in line with recent findings elucidating the possibility to restore spatial memory deficits in mouse models of AD by targeting hippocampal PV^+ interneurons (Etter et al., 2019; Hijazi, Heistek, Scheltens, et al., 2020; Iaccarino et al., 2016; Martinez-Losa et al., 2018; Verret et al., 2012). PV^+ basket cells (PVBCs), in particular, were proved crucial for hippocampal function, as their lack of recruitment by actively spiking excitatory networks resulted in behavioral impairments in both spatial reference and working memory (Fuchs et al., 2007; Korotkova et al., 2010; Murray et al., 2011). Hippocampal PV^+ interneurons are affected early in the APP/PS1 mouse model, as they show a hyperactive phenotype which reverses with age to a hypoactive profile (Hijazi, Heistek, Scheltens, et al., 2020). Etter et al. (Etter et al., 2019), (Iaccarino et al., 2016), and Verret et al.(Verret et al., 2012) have demonstrated that entraining gamma oscillations is sufficient to restore cognitive

deficits in the APPJ20 mouse model. However, none of these studies was performed in animals aged more than 12 months, and the behavioral paradigms used were different than what we have tested. Furthermore, a mechanistic insight of the single-cell or network processes mediating the rescue of spatial memory processes in PV-Cre::APP/PS1 mice is missing. It is tempting to speculate that the concomitant increase in inhibition and the theta-driven subthreshold oscillations driven onto pyramidal cells promote efficient information coding and flow within the hippocampus and between the hippocampal system and prefrontal cortex, for example. In particular, it would be crucial to investigate if theta phase coding of pyramidal neurons is impaired in APP/PS1 animals, and whether low-frequency PV^+ interneuron activation (Stark et al., 2013) would be sufficient to shift this to more physiological levels.

In conclusion, the findings presented in this section contribute to the already existing evidence that restoring aberrant network functionality by recruiting inhibitory neurons is a viable therapeutic strategy to counteract the mnemonic deficits displayed by AD mouse models and, eventually, patients. Nonetheless, we showed that age is a crucial factor to determine the success of this strategy. Furthermore, here it was shown for the first time that the phase locking of gamma oscillations to the underlying theta is significantly reduced in the late stage of the beta-amyloid pathology in APP/PS1 mice (Fig. 3.3). Because slow-wave oscillations reflect the synchrony between distal brain regions, entraining theta rather than gamma oscillations represents the optimal way to increase information flow between distal brain regions participating in the circuit; this, in turn, could potentially lead to the generation of local, fast oscillatory events that are modulated by the underlying phase of theta, thus potentially resulting in the normalization of both distal and local computations. In the future, this paradigm should be employed in different behavioral tasks requiring prior training and decision making, as it was shown that theta oscillations are most prominent in humans and rodents during this type of memory processes (Belchior et al., 2014).

Aβ plaques show a layer-specific deposition in the MEC of APP/PS1 mice

Here, we observed an age-dependent decrease of peak theta frequency in PV-Cre::WT animals and a reduction in theta-gamma coupling in PV-Cre::APP/PS1 animals and (**Fig. 3.10**). Because theta and theta-gamma coupling are processes that depend on the mono- and poly-synaptic input from the MEC to CA1 (Mizuseki et al., 2009), we investigated whether a layer-specific distribution of Aβ pathology in the MEC would reveal which component of the upstream circuit is mostly affected at a stage when hippocampal amyloidosis is already substantial. Aβ plaque deposition pattern and temporal distribution course has been described in the APP/PS1 mouse

model. It was shown that, at the age of approximately 6 months, neocortical structures have a slightly higher Aβ plaque burden than the hippocampal formation (Whitesell et al., 2019). Subsequently, Aβ plaques form first in the MEC and LEC, and ultimately appear in the hippocampus proper (Whitesell et al., 2019). This is in line with what is reported in most cases of human AD, and with the most commonly used pathology staging systems aimed at describing the topographic distribution of neuritic plaques across disease progression (Braak, Alafuzoff, Arzberger, Kretzschmar, & Del Tredici, 2006; Braak & Braak, 1991b; Braak, Braak, & Bohl, 1993; Thal, Rub, Orantes, & Braak, 2002). Compared to other mouse models like the hAPP/J20, the APP/PS1 mouse model shows an Aβ plaque distribution profile that recapitulates better the human condition in terms of temporal distribution patterns (Whitesell et al., 2019). Here, MeXO4 labeling of plaques in the MEC (**Fig. 3.10**) revealed an average Aβ plaque burden of less than 1% in 7.5 month old animals, and of 1.4% in 11.5 months old animals. The distribution of Aβ plaques at later stages was also more uniform across animals, as shown by a lower value distribution in this age group compared to 7.5 month old animals (**Fig. 3.10, d**). The values reported in this study are in line with those reported in the literature for this mouse model (Whitesell et al., 2019). Interestingly, in 11.5 month old mice, the layer of MEC mostly covered by Aβ plaques was layer I (**Fig. 3.10 c**). In this layer reside the inhibitory neurons contacted by SOM^+ hippocampal LRIPs, whose molecular identity is not yet known (Melzer et al., 2012). To reveal what molecular markers are expressed by these local interneurons it would be valuable to investigate it by, for example, single cell RNA sequencing techniques. Furthermore, revealing whether and how these interneurons in particular are affected by amyloidosis would give new important insights into the pathological mechanisms behind inhibitory dysfunction in AD.

Because Aβ plaque deposition shows an anatomically progressive course, it was proposed that misfolded amyloid peptides propagate due to “spreading” from upstream brain regions that are anatomically and functionally connected, with a prion like mechanism (Braak et al., 2006; Braak & Braak, 1991a).Harris et al. (Harris et al., 2010) showed that APP/Aβ overproduction in the EC LII-III caused disinhibition and hyperactivity in the EEG recordings of 4 month old animals. Additionally, they identified higher Aβ plaque burden in the DG of transgenic animals. We have previously shown that larger amyloid deposits are visible trhough a hippocampal window beginning at 5-6 months in SLM compared to SO (Schmid et al., 2016). This suggests a similar amyloid propagation as the one described by Harris et al. (Harris et al., 2010), as SLM is the site where synaptic terminals of the temporoammonic pathway are located.

To conclude, the mouse model employed in this study shows patterns of amyloid deposition in the MEC that are consistent with what is reported in the literature. Interestingly, layer I of the MEC resulted to be the most affected at the age of 11.5 months.

Reduction of SOM-immunoreactivity in the MEC of APP/PS1 mice

Mid-gamma and fast gamma rhythms are thought to be generated by inhibitory neurons in the MEC. Therefore, we investigated if inhibitory neurons in the MEC are altered in a layer-specific manner in the MEC. Quantification of immunohistochemical stainings against the two most common inhibitory neuron markers (*PV* and *SOM*) in the MEC revealed a selective loss of SOM^+ immunoreactivity in the brains of APP/PS1 transgenic mice aged 7.5 and 11.5 months, compared to age-matched controls (**Fig. 3.11**). These results are consistent with previously described studies, despite the mouse models investigated were different from the one employed in this study. In particular, Sanchez et al. (Saiz-Sanchez, Ubeda-Banon, De la Rosa-Prieto, & Martinez-Marcos, 2012) reported a deficit of SOM^+ interneurons in the LEC of 2, 4, 6 and 8 month old transgenic animals compared to healthy aged matched controls. The almost complete reduction of SOM^+ immunoreactivity observed by the authors in 8 month old transgenic animals is more profound compared to what we observed (approximately 23% in LIV, **Fig. 3.11 a-e**). This may be due to the homozygosity of the transgene in the APPβPS1 model investigated by the authors. On average, though, SOM^+ cell density in the MEC was higher compared to the one observed by Sanchez et al. (Saiz-Sanchez et al., 2012) in the LEC. Possibly, this results from the use of different antibodies or different image acquisition parameters. Our results showed that SOM^+ cell density is higher in layer IV of the MEC, which is in line with the findings presented by Sanchez-Mejia et al. (Sanchez-Mejias et al., 2020), who reported a loss of SOM^+ immunoreactivity in the perirhinal cortex of 4 and 6 month old APP751Swe/Lond/PS1M14L mice. Moreover, we observed that in 11-12 month old animals the reduction in SOM^+ immunoreactivity is more pronounced. Nonetheless, average cell densities in WT mice are also higher by trend, in LII and LV, which could be the source of the detected significant difference in SOM^+ cell densities in transgenic mice. Age was shown to cause a reduction of SOM^+, but not PV^+ immunoreactivity in the hippocampus of rats (Stanley, Fadel, & Mott, 2012). An increase in SOM^+ immunoreactivity with age may signify that compensatory mechanisms are taking place to in WT animals, although further experiments with a higher sample size are required to substantiate this finding and hypothesis.

SOM^+ interneurons in the hippocampus and MEC are of particular interest in the context of AD. In humans, density of SOM^+ interneurons is among the most consistently affected

neuropathological hallmarks (Davies, Katzman, & Terry, 1980; Davies & Terry, 1981; Rossor, 1982; Rossor et al., 1982), and SOM receptor subtypes are similarly altered in expression (Kumar, 2005). SOM^+ interneurons express cholinergic receptors in the SO, indicating that they are post synaptic sites of the ascending septal cholinergic pathways that are strongly deteriorated in AD (Muir, 1997; Schmid et al., 2016). Loss of SOM immunoreactivtiy has been reported in a plethora of mouse models and is also a hallmark of human AD brains (Davies et al., 1980; Epelbaum et al., 2009; Saiz-Sanchez et al., 2012; Sanchez-Mejias et al., 2020), as well as in this study. Furthermore, loss of somatostatin caused a reduction in activity of the enzyme neprilysin, *in vitro*, which is responsible for the degradation of Aβ42 (Saito et al., 2005). In murine models, though, loss of SOM^+ inhibitory neuron function would instate a vicious circle that leads to an increase of Aβ deposition, together with the exacerbation of cognitive defects linked to SOM^+ interneuron dysfunction. SOM^+ interneurons in the MEC are responsible for regulating the activity of spatially tuned cells (Fuchs et al., 2016; Miao, Cao, Moser, & Moser, 2017). Indeed, loss of function of SOM^+ interneurons in the MEC may and exacerbate the typical spatial memory impairments observed in AD patients at early stages of the disease. We have previously shown that applying a cholinergic agonist on the hippocampus O-LM interneurons was sufficient to ameliorate cognitive deficits of the APP/PS1 mouse model (Schmid et al., 2016), a process that is mediated by O-LM interneurons as they express acetylcholine receptors. Thus, it would be insightful to manipulate SOM^+ interneurons in the MEC in a similar fashion and observe whether navigational or mnemonic processes are restored in APP/PS1 animals.

Finally, SOM^+ inhibitory neuron reduction is observed in other neurodegenerative disorders like Parkinson's and Hungtington's chorea. Nevertheless, it is relevant to study the mechanisms and the consequences behind SOM^+ interneuron loss of function in the context of AD and AD-related rhythmopathies, as SOM^+ neurons are key regulators of information flow and cognition by promoting disinhibition in the neocortex and hippocampal system (Artinian & Lacaille, 2018; M. Lovett-Barron et al., 2014; Schmid et al., 2016; Stefanelli, Bertollini, Luscher, Muller, & Mendez, 2016), a process that correlates and is potentially regulated by oscillatory activity.

PV^+ immunoreactivity in the MEC of 7.5 month old WT and APP/PS1 mice was not significantly different between the groups (**Fig. 11 f, g, h**). This is a similar result to what is reported by Sanchez-Mejia et al. (Sanchez-Mejias et al., 2020), who showed that PV^+ neurons are not affected in the perirhinal cortex of the APPβPS1 model. In a previous study, the authors had showed that aged transgenic mice also suffered from a loss of PV immunoreactivity, albeit

to a lesser extent compared to the SOM immunoreactivity. It is possible that a deficiency in PV^+ immunoreactivity would be observed at later stages of the pathology in our mouse model.

Interestingly, the only excitatory population investigated in this context (**Fig. 11 i-l**, namely $WFS1^+$ neurons, was not altered in transgenic animals compared to WT controls. This finding supports the previously formulated hypothesis that amyloid pathology in our mouse model affects primarily inhibitory neurons, as already stated by Verdaguer et al. (Verdaguer et al., 2015) regarding the hippocampus. Nonetheless, loss of immunoreactivity does not necessarily imply loss of neural cell bodies, but most likely a loss of function of the neural population that expresses it.

In summary, we showed that inhibitory immunoreactivity of SOM^+ interneurons was reduced with age in APP/PS1 animals, but not in WT animals. In contrast, excitatory $WFS1^+$ neurons were not affected in 11-12 month old APP/PS1 animals. These result support the hypothesis that inhibitory neurons are highly susceptible to AD-like pathology.

Dysfunction of hippocampal SOM^+ LRIPs in SST-Cre::APP/PS1 mice

As previously mentioned, SOM^+ inhibitory neurons are important in the context of AD, as their dysfunction within the hippocampal circuit results in cognitive deficits typically observed in humans and mouse models (Artinian & Lacaille, 2018; Schmid et al., 2016). Long-range inhibitory motifs have been appointed as important coordinators of brain activity and cognition via oscillatory coupling (Caputi et al., 2013; Letzkus et al., 2015; Melzer et al., 2012; Melzer & Monyer, 2020). The hippocampus is not only the post-synaptic target of septal inhibition (Unal et al., 2018), but it also is the source of afferent feedback projections to other regions in the circuit like the MEC (Melzer et al., 2012). SOM^+ LRIPs residing in the SO and hilus of DG have been only recently discovered and characterized, *in vitro* (Melzer et al., 2012). Because we had previously observed a reduction in axonal segments of local O-LM interneurons in CA1 (Schmid et al., 2016), we asked whether SOM^+LRIPs would also degrade in late stages of the pathology. Upon transfecting hippocampal SOM^+ inhibitory neurons in the SO of CA1 and hilus of the DG with a fluorescent reporter encoded by an AAV (*rAAV.tdTomato.flex*), it was possible to label their axons projecting to the MEC (**Fig. 3.12**). In this study, total axonal length in the MEC was calculated and compared between SST-Cre::WT and SST-Cre::APP/PS1 transgenic mice at the age of 12 months on average. This revealed a significant reduction in fluorescence in the MEC of SST-Cre::APP/PS1 transgenic mice (**Fig. 3.12 c, d**). Expression of rAAV constructs has been characterized for this mouse line, and it was shown that the localization of the expressed fluorophores was highly specific to SOM^+ cells identified with an anti-SOM

antibody (Müller-Komorowska et al., 2020). To explain this, various hypotheses can be advanced. First, it is possible that the axonal localization of the viral construct is impaired in SOM^+ neurons in SST-Cre::APP/PS1 mice due to reduced expression of proteins that mediate this process. Second, it is possible that the loss of fluorescence was caused by a loss of axonal fragments of the LRIPs transfected by the viral construct. We have previously shown that SOM^+ O-LM interneurons in the hippocampus lose entire axons between 6 and 11 months of age (Schmid et al., 2016), hence strengthening this hypothesis. In the future, it will be crucial to quantify transfection rates of the cell bodies at the injection site to completely rule out the hypothesis that a decreased transfection lies behind loss of fluorescence in SST-Cre::APP/PS1 animals. However, this is an unlikely explanation because of the high number of animals employed in the experiment. Finally, even though the mechanism behind the reduction of *tdTomato* labeled axonal fragments in 12 month old SST-Cre::APP/PS1 animals has not been elucidated yet, this implies a loss of function of SOM^+ LRIPs.

Disinhibition is a key circuit motif promoting the emergence of higher cognitive functions in the cortex (Letzkus et al., 2015). Indeed, inhibitory interneurons support the generation of cortical oscillatory activity, and long distance disinhibition may be a potent generator of synchronous currents between distal brain areas (Melzer & Monyer, 2020). Strikingly, hippocampal SOM^+ LRIPs have been poorly investigated, with only one study reporting that optogenetic stimulation of axon terminals *in vitro* generates subthreshold theta oscillations in monosynaptically connected interneurons the MEC (Melzer et al., 2012). LRIPs originating in the MEC and LEC have been functionally characterized *in vivo* by Basu et al. (Basu et al., 2016). The authors showed that inactivation of LRIPs originating from the LEC was sufficient to impair associative memory in a contextual fear conditioning test and in the novel object recognition test (Basu et al., 2016). Most importantly, entorhinal LRIPs were required for CA1 pyramidal neurons to show a form of synaptic plasticity referred to as “ITDP” (input timing dependent plasticity) (Basu et al., 2016). Specifically, within the hippocampal system, LRIPs originating from the LEC and targeting the SR-SLM border are needed to redirect the information flow between CA3 and MEC onto pyramidal neurons in presence of a relevant, emotionally salient stimulus (Alexander & Soltesz, 2016; Basu et al., 2016). Entorhinal LRIPs, in fact, guarantee that excitatory entorhinal afferents excite SLM synapses 20ms after the input from CA3 has evoked post-synaptic potentials at the SR synapses (Basu et al., 2016). Hence, is tempting to speculate that the population of hippocampal LRIPs targeting local inhibitory neurons in layer I of MEC (i.e. the neurons targeted by this study) serves as a precisely timed feedback loop that gates and promotes integration of contextual and spatial information between

the two brain regions, operating in conjunction with the perforant pathway (Alexander & Soltesz, 2016,Chamberland, 2012 #12366). Whether the activity of these neurons is relevant for processing navigational or mnemonic information is not yet known. Besides, SOM^+ LRIPs likely target various types of superficial local inhibitory neurons in the MEC (Martinez, Rahsepar, & White, 2017). In turn, and their postsynaptic targets comprise various typologies of principal cells with distinct functions (Fuchs et al., 2016). Nonetheless, dysfunction of hippocampo-entorhinal LRIPs in AD may be partly responsible for the poor associative capabilities of APP/PS1 mice, who have well described deficits in contextual memory retrieval (Kilgore et al., 2010; Poll et al., 2020; Schmid et al., 2016). Additionally, it was shown that grid cells require excitatory input from the hippocampus (Bonnevie et al., 2013), and degradation of disinhibitory circuits may contribute to increased hyperpolarization states in spatially modulated cells, provided that this would happen before, or in absence of local interneuron remodeling. It was shown that grid cells are impaired in mouse models of AD (Cacucci, Yi, Wills, Chapman, & O'Keefe, 2008; Fu et al., 2017; Jun et al., 2020) and in humans (Kunz et al., 2015), but there is yet no indication that this may be caused by loss of hippocampal afferents. Furthermore, Kitamura et al. (Kitamura et al., 2015) have shown that WFS^+ Island cells in the MEC are responsible for the emergence of trace fear conditioning, and they speculate that their activity is sustained by the presence of disinhibitory input from the MEC. Thus, applying the same behavioral paradigm and probing the function of hippocampal SOM^+LRIPs may reveal valuable insights on the function of these inhibitory neurons.

In the future, the role of SOM^+LRIPs for the generation of oscillatory synchrony and their relevance for the emergence of cognitive functions in the hippocampo-entorhinal circuit needs to be evaluated *in vivo*. Interestingly, it was shown that SOM^+ O-LM interneurons are phase locked to the descending phase/trough of theta cycle measured in *stratum pyramidale* (Klausberger et al., 2003; Klausberger & Somogyi, 2008). In fact, the firing rate of SOM^+O-LMs increases when pyramidal cells are most excitable (Klausberger & Somogyi, 2008; M. Lovett-Barron et al., 2014), guaranteeing a balance in the excitation/inhibition of the CA1 microcircuit. Indeed, SOM^+ O-LM interneurons are essential for goal-directed (Geiller et al., 2020) and contextual learning (Matthew Lovett-Barron et al., 2014; Stefanelli et al., 2016), as they either facilitate - by disinhibiting local SR-SLM interneurons (Fuhrmann et al., 2015; Geiller et al., 2020) - or inhibiting pyramidal cell input integration at distal dendrites, in particular entorhinal input (Geiller et al., 2020; M. Lovett-Barron et al., 2014) during learning of an aversive fear conditioning task. Thus, investigating whether this mechanism occurs in the MEC by means of single cell and population recordings, and whether the loss of axonal

segments in the AD mouse model causes disruption of theta and gamma oscillations in the MEC, would yield valuable insights on inhibitory neuron control of theta-driven communication between brain regions. Furthermore, future experiments are required to describe how structure and function of LRIPs are affected by healthy aging. We have previously shown that axons of local SOM^+ inhibitory neurons in the SO of CA1 are also slightly, but not significantly reduced between 6 and 11 months of age (Schmid et al., 2016). Possibly, this decrease is exacerbated with increasing age. Additionally, it would be crucial to investigate how local and long-range inhibitory circuits are affected over time and whether their alterations show similar or divergent directions between healthy aging and disease-like conditions.

To conclude, these results confirmed that defects in inhibitory neurons, whether in function or structural connectivity, are a hallmark of AD patients and mouse models, and it opens the question as to whether restoring their function would be beneficial for rescuing rhythmopathy-associated cognitive defects observed in both humans and animal models.

5 Conclusions and future directions

Overall, the data presented in this thesis support the hypothesis that hippocampal oscillatory alterations are a hallmark of healthy aging and of AD mouse models. In particular, the changes observed in the hippocampal network activity, measured at the level of local field potentials, correlated with inhibitory neuron dysfunction in APP/PS1 transgenic animals. Lack of inhibitory control could indeed result in the observed dysregulated oscillatory activity, which is in turn linked to improper encoding and retrieval of memory. Even though a strict causal relationship between inhibitory neuron dysfunction, oscillatory alterations and decline in cognitive capabilities is lacking in this study, substantial evidence from the literature suggests that hypo/hyperactivity of inhibitory neurons partially underlies spectral alterations observed in EEG and LFP recordings in age and disease. Indeed, it was shown here that optogenetic stimulation of PV^+ interneurons in the hippocampus was sufficient to improve spatial memory processes in PV-Cre::APP/PS1 animals. Nonetheless, the success of this strategy was crucially dependent on the age of the animals tested.

Neural network properties of APP/PS1 animals and other models of AD are highly influenced by age, as revealed by seemingly opposite pathophysiological processes observed at different stages of the disease. Interestingly, in this study, the hippocampal field activity of PV-Cre::APP/PS1 animals was not as profoundly altered with age as that of PV-Cre::WT animals. In fact, peak theta frequency linearly decreased between 9 and 24 months of age in PV-Cre::WT animals but not in age-matched PV-Cre::APP/PS1 animals. At the time of investigation, the CA1 network of PV-Cre::APP/PS1 animals was indeed at a highly advanced pathological stage with respect to the β-amyloid deposition. Possibly, within this time frame, oscillatory activity of PV-Cre::APP/PS1 animals would be subject to minor alterations that are not easily detected in LFP recordings, as most remodeling had been taking place earlier. Furthermore, decline in peak frequency of theta oscillations was paralleled by an age-dependent decline in mean velocity of the PV-Cre::WT but not in PV-Cre::APP/PS1 animals. This suggests that hippocampal network activity, reflected by LFPs, may be “dissociated” from the rest of the brain in PV-Cre::APP/PS1 mice, as hinted by the observed dysfunction of hippocampal LRIPs. Local dysfunction of inhibitory neurons in the MEC, which was revealed here by fluorescent immunohistochemistry, would in turn result in alterations of spatially modulated cells and also on the function of temporo-ammonic pathway terminals. This may substantially contribute to the modulation of phase and amplitude of theta oscillations and theta-modulation of gamma activity, measured with a theta-gamma modulation index (MI). Indeed, in this study, the theta-

gamma MI was significantly reduced in PV-Cre::APP/PS1 animals. Furthermore, the MI showed a linear increase with age in PV-Cre::WT but not in PV-Cre::APP/PS1 animals. This further corroborates the hypothesis that feedback interactions within the hippocampal system, and possibly between the hippocampal system and other brain regions responsible for the generation of cognitive related rhythmogenesis, are impaired in PV-Cre::APP/PS1 animals and in healthy aging. Crucially, lack of theta-gamma remodeling with age in PV-Cre::APP/PS1 mice suggests that cognitive decline and concomitant oscillatory alterations are possibly governed by distinct mechanisms in healthy aging and rodent models of genetic β-amyloidosis. Finally, whether oscillatory aberrations constitute a causal link to explain why 19-20-month old PV-Cre::WT animals showed impaired recognition and spatial memory processes, as revealed by the behavioral experiments performed in this thesis, is not yet possible to know. Finally, and most importantly, it was shown here that PV^+ interneuron-driven rhythmogenesis by means of a closed-loop optogenetic stimulation improved spatial memory of 15 month old PV-Cre::APP/PS1 mice, but not in 19-20 month old PV-Cre::APP/PS1 mice. This confirms that interventional strategies are highly sensitive to age.

Here, distinct oscillatory and behavioral correlates emerged during exploratory activity and in response to optogenetic stimulation of hippocampal PV^+ interneurons, in aged PV-Cre::WT and PV-Cre::APP/PS1 mice, respectively. Because it is known that oscillatory function strongly relies on inhibitory neuron function, further research is needed to elucidate the mechanisms that affect the hippocampo-entorhinal GABAergic system. In the future, a closer inspection at the functional role of hippocampal and entorhinal LRIPs for the emergence of neural oscillatory coherence between these two brain regions is required *in vivo*. This could be achieved by monitoring the neural activity of axonal projections by means of calcium imaging while the animals are performing a behavioral task that requires the integration of novel context and retrieval of previously stored information. Simultaneous LFP recordings in MEC and HPC would enable to measure oscillatory coupling of these brain areas. Potentially, optogenetic stimulation of hippocampal and entorhinal LRIPs would lead to a rescue of the cognitive deficits observed in age and disease. Besides, as oscillatory function during sleep is thought to support mnemonic and cognitive function, investigating the sleep patterns of aged and diseased mice may reveal the time point at which an interventional strategy is effective for both conditions. Additionally, while lack or dysfunction of inhibitory neurons may be a very plausible reason of hippocampal hyperactivity in animal models of AD, it is not yet known whether this might be due to upstream impairments in, for example, medial septal, entorhinal, or subcortical afferents. Finally, a longitudinal investigation of hippocampal GABAergic and

pyramidal neuron activity, coupled with LFP recording from the different layers of the hippocampus, *in vivo*, would provide insight into the dynamics of circuit remodeling that correlate with spectral and cognitive changes observed in age and AD-like pathology.

6 Appendix

6.1 Abbreviations

AAV	Adeno-associated virus
Aβ	Amyloid beta
Ach	Acetylcholine
AD	Alzheimer's disease
AICD	Amyloid precursor intracellular domain
AMPA	α-amino-3-hydroxy-5-methyl-4-isoxazolepropionic acid
AP	Antero-posterior
APP	Amyloid precursor protein
AUD	Auditory
BACE	Beta site of APP cleaving enzyme
BP	Bandpass filter
BSA	Bovine serum albumin
CA	Cornu ammonis
CCK	Cholecystokinin
CamKII	Calcium/calmodulin-dependent protein kinase II
CTFβ	Beta-carboxyl-terminal fragment
DBS	Deep brain stimulation
DG	Dentate gyrus
DV	Dorso-ventral
EC	Entorhinal cortex
EEG	Electroencephalogram
EPSP	Excitatory post synaptic potential
i.p.	Intraperitoneal
ITDP	Input timing dependent plasticity
GABA	Gamma amino butyric acid
HPC	Hippocampus
IEG	Immediate early gene
IPSP	Inhibitory post synaptic potential
LEC	Lateral entorhinal cortex
LRP	Low-density lipoprotein receptor related protein

LRIP	Long-range inhibitory projection
LP	Long pass dichroic mirror
LTD	Long term depression
LTP	Long term potentiation
LFP	Local field potential
MEC	Medial entorhinal cortex
MCI	Mild cognitive impairment
MI	Modulation index
ML	Medio-lateral
MS	Medial septum
MTL	Medial temporal lobe
NA	Numeric aperture
n.s.	Not significant
NMDA	N-methyl-D-aspartate
NOR	Novel object recognition
NOL	Novel object location
OLF	Olfactory
O-LM	Oriens-lacunosum-moleculare
PBS	Phosphate buffer saline
PFA	Paraformaldehyde
PHC	Parahippocampal cortex
PMT	Photomultiplier
PP	Perforant pathway
PRC	Perirhinal cortex
PS1	Presenilin 1
PV	Parvalbumin
PVBC	Parvalbumin basket cell
RAGE	Receptor for advanced glycation end products
ROI	Region of interest
Rpm	Rounds per minute
RT	Room temperature
SO	*Stratum oriens*
SOM	Somatostatin
SP	*Stratum pyramidale*
SR	*Stratum radiatum*

SLM	*Stratum lacunosum moleculare*
STDP	Spike timing dependent plasticity
SWR	Sharp wave ripple
TA	Temporo ammonic pathway
tDCS	Transcranial direct current stimulation
TMS	Transcranial magnetic stimulation
VIS	visual
WFS1	Wolframin syndrome 1
WT	Wild type

6.2 Consumables

6.2.1 Anesthesia and medication

Designation	Product no.	Company
Dexamethasone 21-phosphate disodium salt	D1159-500MG	Sigma Aldrich (Taufkirchen, Germany)
Ketavet® (Ketaminhydrochlorid) 100 mg/ml	D3821-07	Pfizer (New York, USA)
Rompun® (Xylazinhydrochloride) 2%	KP09X0L	Bayer (Leverkusen, Germany)
Temgesic® (Buprenorphinhydrochloride) 0.3 mg/ml	n.a.	RB Pharmaceuticals Limited (Mumbai, India)
Metapyrin® 500 mg/ml		Pharma-Partner-Vertriebs GmbH (Hamburg, Germany)

6.2.2 Commons for surgical procedures

Designation	Product no.	Company
Bepanthen® Augen- und Nasensalbe (ointment)	n.a.	Bayer (Leverkusen, Germany)
Cyano Fast	152261	Hager Werken (Duisburg, Germany)
Cyano Veneer® Anmischblock	152270	Hager Werken (Duisburg, Germany)
Cyano Veneer® Pulver	152255	Hager Werken (Duisburg, Germany)
Disposable scalpels, sterile	0505	Swann-Morton (Sheffield, England)
Drill head	H71.104.004 or 003	Gebr. Basseler (Lemgo, Germany)
EUROTUBO®, sterile collection swabs	300202	DeltaLab (Barcelona, Spain)
GRADIA® DIRECT FloBW	2358	GC (Leuven, Belgium)
Norland Optical Adhesive 81	NOA 81	Norland Products (Cranbury, New Jersey)
OptiBond™ FL, two-component bonding agent	26684 E	Kerr (Salerno, Italy)
Pasteur-pipette, disposable	211C	COPAN (Brescia, Italy)
Pattex, instant adhesive, liquid	n/a	Henkel (Düsseldorf, Germany)

Standard Biopsy Punch, 3 mm	48301	pfm medical (Cologne, Germany)
Sterican® cannula, BL/LB, 27G x 3/4"	4657705	B Braun (Melsungen, Germany)
Sterican® cannula, blunt, 21G x 7/8"	9180109	B Braun (Melsungen, Germany)
Sterican® cannula, blunt, 27G x 1"	9180117	B Braun (Melsungen, Germany)
Sugi®Eyespear	30601	Kettenbach (Eschenburg, Germany)
Suture, coated VICRYL®	MPV490H	Ethicon (New Jersey, USA)
TERUMO® Tuberculin Syringes	SS-01T1	Terumo (Tokyo)

6.2.3 Adeno-associated viruses used for stereotactic injections

Designation	**Product no.**	**Company**
AAV1/2.CAG.flex.tdTomato. WPRE.SV40	5328A2	UNC Vector core
AAV2/1.CAG.flex.tdTomato. WPRE.bGH (AllenInstitute864)	CS0917	Penn Vector core
AAV2.EF1a.C1V1(E122T/E162T)-TS-mCherry	AV4859d	UNC Vector core
AAV9.CamKII0.4Cre	105558	Addgene (Watertown, MA USA)

6.2.4 Local field potential recordings

Designation	**Product no.**	**Company**
Tungsten insulated wire	W5584	ADVENT Research Materials (Oxford, England)
Goldpin connector	10120832	Conrad Electronic SE (Hirschau, Germany) Electronic (Bonn, Germany)
Soldering wire	518649	Stannol (Wuppertal, Germany)
Shrinking tube	various	Conrad Electronic SE (Hirschau, Germany) Electronic (Bonn, Germany)
16 channel silicon probes	A1x16-3mm-100-177-H16_21	Neuronexus (Ann Arbor, Michigan, USA)
16 channel headstage	RHD-16-2132	Intan Technologies (Los Angeles, California, USA
Recording cable for 16 channel headstage	SPI-RHD 6ft, part #C3216	Intan Technologies (Los Angeles, California, USA

6.2.5 Immunohistochemistry

Designation	**Product no.**	**Company**
10% normal goat serum	50062Z	Life technologies (Carlsbad, USA)
Fluorescence mounting medium	S3023	Dako/Agilent Technologies (Santa Clara, USA)
Triton-X100	A1388	Sigma-Aldrich (St. Louis, USA)
Bovine serum albumine	0163	Roth (Karlsruhe, Germany)
Phosphate buffered saline	A0964	AppliChem (Darmstadt, Germany)
Dako fluorescent mounting medium	S3023	Dako Denmark (Glostrup, Denmark)
Coverslips	H878.2	Carl Roth GmbH + Co. KG (Karlsruhe, Germany)
Glass slides	H870.1	Carl Roth GmbH + Co. KG (Karlsruhe, Germany)

6.3 Equipment

6.3.1 Surgery equipment

Designation	**Product no.**	**Company**
Micro4 Micro Syringe Pump Controller	SYS-MICRO4	World Precision Instruments (Sarasota, USA)
UMP3 Ultra Micro Pump	UMP3	World Precision Instruments (Sarasota, USA)
NanoFil Syringe 10 µL	NANOFIL	World Precision Instruments (Sarasota, USA)
Remote Control SM-7	200-100 900 9050	Luigs and Neumann (Ratingen, Germany)
Control system SM7	200-100 900 7411	Luigs and Neumann (Ratingen, Germany)
LN Junior RE/LE (3 axes)	210-1000000070-RE/LE	Luigs and Neumann (Ratingen, Germany)
Dentalbohrer	A755983	Schick (Schemmerhofen, Germany)
Stereomicroscope SZ 51	19320	Olympus (Tokyo, Japan)
Sterilizer, Steri 250	031100	Keller (Burgdorf, Switzerland)
Pipette holder	UPN-1	Narishige (Tokyo, Japan)
Pipette holder	UPN-2	Narishige (Tokyo, Japan)
Peri-Star Pro, peristaltic pump	PERIPRO-4LS	World Precision Instruments (Sarasota, USA)
Light-curing device, LED smart (420nm-480nm, 1000 W/cm^2)	14012119	Kohlschein-Dental GmbH & Co. KG (Altenberge, Germany)
Surgical tools	various	Fine Science Tools (Foster City, CA USA)
Stereotactic base plate for mice	SR-A	Narishige (Tokyo, Japan)
Auxiliary ear bars for mice	EB-3B	Narishige (Tokyo, Japan)
Auxiliary ear bars for mice	EB-5N	Narishige (Tokyo, Japan)
Head holding device for mice	MA-6N	Narishige (Tokyo, Japan)

6.3.2 Local field potential recordings

Designation	**Product no.**	**Company**
Amplifier	EXT-02F	NPI Electronic GmbH (Hamm, Germany)
Analog/digital converter	ITC-18/USB	InstruTech (Port Washington, NY USA)
Custom made headstage	n.a.	NPI Electronic GmbH (Hamm, Germany)
Faraday cage	n.a.	Custom built
Humbug noise eliminator (50/60Hz)	n.a.	Quest Scientifica (North Vancouver, BC Canada)
Cables: single conductor wire, insulated (LifY 0.05 mm^2)	1180269	Conrad Electronic SE (Hirschau, Germany) Electronic SE (Hirschau, Germany)
OpenEphys acquisition board	-	OpenEphys (open-ephys.org/store)

6.3.3 Behavior and optogenetics

Designation	**Product no.**	**Company**
CCTV camera		Sygonix GmbH (Nürenberg, Germany)
Open field box	n.a.	Custom built
OBIS 561nm laser	1253300	Coherent Inc. (Santa Clara, CA USA)
Double optic ferrules	TFC_300/370 0.22_2.5_TM 3_FLT	Doric Lenses (Ville de Québec, Canada)
Mono Fiberoptic Patchchords	MFP_300/330 /900- 0.22_1.5m_C M3-RMC	Doric Lenses (Ville de Québec, Canada)
Fiberoptic Rotary Joint	FRJ_1x2i_FC -2M3	Doric Lenses (Ville de Québec, Canada)

6.3.4 Two-photon microscopy

Designation	**Product no.**	**Company**
Thorlabs resonant setup	n.a.	Thorlabs Inc. (USA)
GaSP photomultiplier (detector)	n.a.	Thorlabs Inc. (USA)

Ti:Sa Laser	Chameleon Ultra II	Coherent Inc. (USA)
Resonant scanner (7.9 kHz)	n.a.	Thorlabs Inc. (USA)
Filter BP 525/50	ET Bandpass	Chroma Technology Corp. (USA)
Objective 16x (Water)	CFI75 LWD 16XW	Nikon Corp. (Japan)

6.3.5 Immunohistochemistry

Designation	**Product no.**	**Company**
Automated Vibatome	VT1200 S	Leica (Nussloch, Germany)
Titramax 100, shaker	544-11200-00	Heidolph (Schwabach, Germany)
Confocal microscope LSM700	n.a.	Carl Zeiss GmbH (Oberkochen, Germany)

6.4 Software

Designation	**Company**
Adobe Illustrator CS5, Version 15.0.1	Adobe Systems Inc. (Mountain View, CA USA)
EthoVision XT11.5 and XT13	Noldus (Wahningen, Netherlands)
Fiji/ImageJ 2.0.0	Wayne Rasband (NIH, USA)
GraphPad Prism 5 and 6	GraphPad Software, Inc. (San Diego, CA USA)
IgorPro 6.22A	WaveMetrics (Portland, OR USA)
MATLAB R2015 and R2016b	MathWorks (Natick, MA USA)
ZEN 2010	Carl Zeiss AG (Jena, Germany)

6.5 Statistical tests

Fig. 3.1, panel	Statistical test	Test results
c	Two-tailed unpaired student's t-test	t(64)=0.78, p=0.43
d	Two-tailed unpaired student's t-test	t(64)=0.43, p=0.66
e	Two-tailed Mann-Whitney test	Mann-Whitney U= 484.5, p=0.54
f	Two-tailed Mann-Whitney test	Mann-Whitney U= 482, p=0.52
g	Two-tailed Mann Whitney test	Mann-Whitney U= 511, p=0.79
h	Two-tailed student's t-test	t(63)=1.98, p=0.06
Fig. 3.2, panel	**Statistical test**	**Test results (best fit values ± SE)**
a	Linear regression analysis	slope= -0.07 ±0.01, Y-intercept: 8.08 ±0.25 Hz, Sy.x=0.31, r^2= 0.12, p= 0.03
b		slope= -0.008 ± 0.025, Y-intercept= -10.25 ± 0.37 (a.u.) Sy.x= 0.46, r^2=0.002, p=0.75
c		slope= -0.91 ± 1.81 Y-intercept= 132,1 ± 26,83 sec Sy.x= 33.01, r^2= 0,007, p= 0.61
d		slope= -0.15 ± 0.067 Y-intercept= 11,76 ± 1 cm/sec Sy.x= 1.234, r^2= 0.12, p= 0.03
e		slope= 0.024 ± 0.04 Y-intercept= 7.28± 0.41 Hz Sy.x= 0.33 , r^2= 0.008 , p= 0.57
f		slope= 0.05 ± 0.05 Y-intercept= -10.88 ± 0.56 (a.u.) Sy.x= 0.46, r^2= 0.02 , p= 0.35
g		slope= 15.06 ± 3.35 Y-intercept= -25.01 ± 32.3 sec Sy.x= 26.52 , r^2= 0.35, p <0,0001
h		slope= 0.02 ± 0.02 Y-intercept= 7.82 ± 0.36 Hz Sy.x= 0.43 , r^2= 0.042, p=0.29
i		slope= 0.006 ± 0.02 Y-intercept= -10.41 ± 0.42 (a.u.) Sy.x= 0.5 , r^2= 0.002, p=0.29
j		slope= -0.69 ± 1.62 Y-intercept= 134.7 ± 25.6 sec Sy.x= 30.6 , r^2= 0.006, p=0.67
k		slope= -0.1 ± 0.09 Y-intercept= 11.79 ± 1.57 cm/sec Sy.x= 1.88 , r^2= 0.04 , p= 0.28
l		slope= -0.07 ± 0.04 Y-intercept= 8.1 ± 0.4 Hz Sy.x= 0.42 , r^2= 0.09 , p= 0.1
m		slope= -0.03 ± 0.05 Y-intercept= -10.01 ± 0.52 Sy.x= 0.54, r^2= 0.01 , p= 0.55
n		slope= 10.93 ± 2.27 Y-intercept= 13.62 ± 23.43 sec Sy.x= 22.43, r^2= 0.46 , p<0.0001
Fig. 3.3, panel	**Statistical test**	**Test results (best fit values ± SE)**
b	Two-tailed unpaired t-test	t(43)= 2.79, p=0.0078
c	Linear regression analysis	slope= 0.0005 ± 0.0001 , Y-intercept= -0.0004 ± 0.002 (a.u.) Sy.x= 0.002, r^2=0.24, p=0.01
d		slope= 4.94e-005 ± 0.0001

		Y-intercept= 0.004 ± 0.002 (a.u.) Sy.x= 0.002, r^2=0.007, p=0.71
Fig. 3.4, panel	**Statistical test**	**Test results**
g	Two-way repeated measures ANOVA Treatment: Sham vs C1V1 Time: baseline vs stimulation	Interaction, F(1, 55)= 1.63, 0.85% of total variation, p=0.25 treatment, F(1, 55)= 2.79e-005, p=0.99; 4.42% of tot.var.; time, F(1, 55)= 8.42, 4.42% of tot. var., p=0.005 matching, F(55,55): 66% of tot. var., p=0.001 Holm-Sidak's correction for multiple comparisons: Baseline vs Stimulation: Sham, p= 0.24; C1V1, p=0.01
h		Interaction, F(1, 44)= 0.29, 0.25% of total variation, p=0.59 treatment, F(1, 44)= 1.31; 1.74% of tot.var. p= 0.25 time, F(1, 44)= 1.76, 1.53% of tot. var., p=0.19 matching, F(44,44)=1.52, 58% of tot. var., p= 0.08 Holm-Sidak's correction for multiple comparisons: Baseline vs Stimulation: Sham, p= 0.53; C1V1, p=0.41
i		Interaction, F(1, 44)= 18.45, 10.93% of total variation, p<0.0001 treatment, F(1, 44)= 3.05; 3.68% of tot.var. p= 0.08 time, F(1, 44)= 13.19, 7.81% of tot. var., p= 0.0007 matching, F(44,44)=2.03, 52.97% of tot. var., p= 0.01 Holm-Sidak's correction for multiple comparisons: Baseline vs Stimulation: Sham, p= 0.62; C1V1, p<0.0001
j		Interaction, F(1, 44)= 1.55, 1.27% of total variation, p=0.21 treatment, F(1, 44)= 3.86; 4.44% of tot.var. p= 0.055 time, F(1, 44)= 9.57, 7.81% of tot. var., p= 0.003 matching, F(44,44)=1.41, 50.47% of tot. var., p= 0.13 Holm-Sidak's correction for multiple comparisons: Baseline vs Stimulation: Sham, p= 0.2; C1V1, p= 0.007
k		Interaction, F(1, 55)= 6.91, 4.72% of total variation, p=0.01 treatment, F(1, 55)= 0.13; 0.13% of tot.var. p= 0.71 time, F(1, 55)= 2.12, 1.45% of tot. var., p= 0.15 matching, F(55,55)=1.46, 50.47% of tot. var., p= 0.07 Holm-Sidak's correction for multiple comparisons: Baseline vs Stimulation: Sham, p= 0.44; C1V1, p= 0.005
l		Interaction, F(1, 66)= 14.83, 5.77% of total variation, p=0.0003 treatment, F(1, 66)= 10.88; 8.37% of tot.var. p= 0.016 time, F(1, 66)= 31.23, 12.17% of tot. var., p<0.0001 matching, F(66,66)= 1.97, 50.78% of tot. var., p= 0.03 Holm-Sidak's correction for multiple comparisons: Baseline vs Stimulation: Sham, p= 0.17; C1V1, p<0.0001
m		Interaction, F(1, 64)= 20.71, 8.68% of total variation, p<0.0001 treatment, F(1, 64)= 11.78; 7.12% of tot.var. p= 0.001 time, F(1, 64)= 42.61, 17.86% of tot. var., p<0.0001 matching, F(66,64)=1.44, 38.72% of tot. var., p= 0.07 Holm-Sidak's correction for multiple comparisons: Baseline vs Stimulation: Sham, p= 0.17; C1V1, p<0.0001
n		Interaction, F(1, 56)= 19.04, 9.69% of total variation, p<0.0001 treatment, F(1, 56)= 11.71; 6.21% of tot.var. p= 0.001 time, F(1, 56)= , 17.86% of tot. var., p<0.0001 matching, F(56,56)=1.02, 38.72% of tot. var., p= 0.43 Holm-Sidak's correction for multiple comparisons: Baseline vs Stimulation: Sham, p= 0.27; C1V1, p<0.0001
Fig. 3.5, panel	**Statistical test**	**Test results**
g	Two-way ANOVA	Interaction, F(1,37)= 15.41, 29.37% of tot. var., p=0.0004 genotype, F(1, 37)= 0.09, 0.18% of tot. var., p= 0.75 treatment, F(1, 37)= 0.33, 0.64% of tot. var., p= 0.56 Holm-Sidak's correction for multiple comparisons: PV-Cre::WT + Sham vs PV-Cre::APP/PS1 + Sham, p=0.0132 PV-Cre::WT + Sham vs PV-Cre::WT + C1V1, p= 0.012 PV-Cre::APP/P1 + Sham vs PV-Cre::APP/PS1 + C1V1, p= 0.01
i	Two-tailed unpaired student's t-test	t(34), 2.51, p= 0.01
Fig. 3.6.1, panel	**Statistical test**	**Test results**
c	Two-tailed unpaired student's t-test	t(8)= 0.87, p=0.4
d	Two-tailed unpaired student's t-test	t(8)= 0.13, p=0.89

e	Two-tailed unpaired student's t-test with Welch's correction	t(4.7)= 0.54, p=0.60
f	Two-tailed unpaired student's t-test with Welch's correction	t(4.7)= 0.54, p=0.61
Fig. 3.6.2, panel	**Statistical test**	**Test results**
c	Two-way ANOVA	Interaction, F(1, 24)= 1.39, 5.08% of total variation, p= 0.25 genotype, F(1, 24)= 1.17, 4.41% of tot.var., p= 0.28 treatment, F(1, 24)= 0.29, 1.1% of tot.var., p= 0.59 Holm-Sidak's correction for multiple comparisons: PV-Cre::WT+Sham vs PV-Cre::APP/PS1 + Sham, p= 0.95 PV-Cre::WT+Sham vs PV-Cre::WT+C1V1, p= 0.56 PV-Cre::APP/PS1+Sham vs PV-Cre::APP/PS1+C1V1, p= 0.88
d		Interaction, F(1, 24)= 0.67, 2.67% of total variation, p=0.41 genotype, F(1, 24)= 0.46, 1.84% of tot.var., p= 0.5 treatment, F(1, 24)= 0.05, 0.82% of tot.var., p= 0.82 Holm-Sidak's correction for multiple comparisons: PV-Cre::WT+Sham vs PV-Cre::APP/PS1 + Sham, p=0.62 PV-Cre::WT+Sham vs PV-Cre::WT+C1V1, p= 0.71 PV-Cre::APP/PS1+Sham vs PV-Cre::APP/PS1+C1V1, p= 0.71
e		Interaction, F(1, 24)= 1.94, 6.66% of total variation, p=0.17 genotype, F(1, 24)= 1.7, 5.83% of tot.var., p=0.2 treatment, F(1, 24)= 1.11, 3.81% of tot.var., p= 0.3 Holm-Sidak's correction for multiple comparisons: PV-Cre::WT+Sham vs PV-Cre::APP/PS1 + Sham, p=0.16 PV-Cre::WT+Sham vs PV-Cre::WT+C1V1, p= 0.18; PV-Cre::APP/PS1+Sham vs PV-Cre::APP/PS1+C1V1, p= 0.81
f		Interaction, F(1, 24)= 2.24, 7.36% of total variation, p=0.14 genotype, F(1, 24)= 2.69, 8.81% of tot.var., p= 0.11 treatment, F(1, 24)= 0.98, 3.22% of tot.var., p= 0.3 Holm-Sidak's correction for multiple comparisons: PV-Cre::WT+Sham vs PV-Cre::APP/PS1 + Sham, p=0.08 PV-Cre::WT+Sham vs PV-Cre::WT+C1V1, p= 0.17; PV-Cre::APP/PS1+Sham vs PV-Cre::APP/PS1+C1V1, p= 0.72
Fig. 3.7, panel	**Statistical test**	**Test results**
c	Two-way ANOVA	Interaction, F(1, 24)= 0.23, 0.74% of total variation, p=0.63; genotype, F(1, 24)= 0.94, 2.98% of tot.var., p=0.3 treatment, F(1, 24)= 0.4, 1.28% of tot.var., p= 0.52 Holm-Sidak's correction for multiple comparisons: PV-Cre::WT+Sham vs PV-Cre::APP/PS1 + Sham, p=0.63 PV-Cre::WT+Sham vs PV-Cre::WT+C1V1, p= 0.68; PV-Cre::APP/PS1+Sham vs PV-Cre::APP/PS1+C1V1, p= 0.68
d		Interaction, F(1, 29)= 1.22, 3.83% of total variation, p=0.27 genotype, F(1, 29)= 1.98, 6.18% of tot.var., p=0.17 treatment, F(1, 29)= 0.005, 0.01% of tot.var., p= 0.94 Holm-Sidak's correction for multiple comparisons: PV-Cre::WT+Sham vs PV-Cre::APP/PS1 + Sham, p=0.82 PV-Cre::WT+Sham vs PV-Cre::WT+C1V1, p= 0.78; PV-Cre::APP/PS1+Sham vs PV-Cre::APP/PS1+C1V1, p= 0.78
Fig. 3.8.1, panel	**Statistical test**	**Test results**
c	Two-way ANOVA	Interaction, F(1, 33)= 0.01, 0.33% of total variation, p=0.91 genotype, F(1, 33)= 0.14, 0.44% of tot.var., p=0.7 treatment, F(1, 33)= 0.08, 0.02% of tot.var., p= 0.92 Holm-Sidak's correction for multiple comparisons: PV-Cre::WT+Sham vs PV-Cre::APP/PS1 + Sham, p=0.99; PV-Cre::WT+Sham vs PV-Cre::WT+C1V1, p= 0.99; PV-Cre::APP/PS1+Sham vs PV-Cre::APP/PS1+C1V1, p= 0.99
d	Kruskal-Wallis test	Kruskal-Wallis statistic= 5.21, p= 0.15 Dunn's correction for multiple comparisons: PV-Cre::WT+Sham vs PV-Cre::APP/PS1 + Sham, p=0.82 PV-Cre::WT+Sham vs PV-Cre::WT+C1V1, p= 0.06 PV-Cre::APP/PS1+Sham vs PV-Cre::APP/PS1+C1V1, p>0.99
e	Two-way ANOVA	Interaction, F(1, 33)= 0.33, 0.84% of total variation, p=0.56 genotype, F(1, 33)= 6.89, 0.17.15% of tot.var., p=0.01 treatment, F(1, 33)= 0.27, 0.6% of tot.var., p= 0.6

		Holm-Sidak's correction for multiple comparisons: PV-Cre::WT+Sham vs PV-Cre::APP/PS1 + Sham, p=0.36 PV-Cre::WT+Sham vs PV-Cre::WT+C1V1, p= 0.69; PV-Cre::APP/PS1+Sham vs PV-Cre::APP/PS1+C1V1, p=0.96
f		Interaction, F(1, 33)= 0.34, 0.84% of total variation, p=0.56 genotype, F(1, 33)= , 6.88,17.12% of tot.var., p=0.01 treatment, F(1, 33)= 0.28, 0.7% of tot.var., p= 0.59 Holm-Sidak's correction for multiple comparisons: PV-Cre::WT+Sham vs PV-Cre::APP/PS1 + Sham, p=0.36 PV-Cre::WT+Sham vs PV-Cre::WT+C1V1, p= 0.69; PV-Cre::APP/PS1+Sham vs PV-Cre::APP/PS1+C1V1, p=0.97
Fig. 3.8.2, panel	**Statistical test**	**Test results**
c	Two-way ANOVA	Interaction, F(1, 31)= 8.17, 19.52% of total variation, p=0.0075 genotype, F(1, 31)= , 0.08,0.2% of tot.var., p=0.77 treatment, F(1, 31)= 2.98, 7.12% of tot.var., p= 0.09 Holm-Sidak's correction for multiple comparisons: PV-Cre::WT+Sham vs PV-Cre::APP/PS1 + Sham, p=0.04; PV-Cre::WT+Sham vs PV-Cre::WT+C1V1, p= 0.41; PV-Cre::APP/PS1+Sham vs PV-Cre::APP/PS1+C1V1, p=0.01
d		Interaction, F(1, 31)= 0.02, 0.06% of total variation, p=0.88 genotype, F(1, 31)= 1.5, 4.58% of tot.var., p=0.22 treatment, F(1, 31)= 0.32, 1% of tot.var., p= 0.57 Holm-Sidak's correction for multiple comparisons: PV-Cre::WT+Sham vs PV-Cre::APP/PS1 + Sham, p=0.8 PV-Cre::WT+Sham vs PV-Cre::WT+C1V1, p= 0.86 PV-Cre::APP/PS1+Sham vs PV-Cre::APP/PS1+C1V1, p=0.86
e		Interaction, F(1, 31)= 0.43, 1.33% of total variation, p=0.51 genotype, F(1, 31)= 0.32, 0.99% of tot.var., p= 0.57 treatment, F(1, 31)= 0.54, 1.69% of tot.var., p= 0.46 Holm-Sidak's correction for multiple comparisons: PV-Cre::WT+Sham vs PV-Cre::APP/PS1 + Sham, p= 0.72 PV-Cre::WT+Sham vs PV-Cre::WT+C1V1, p= 0.95 PV-Cre::APP/PS1+Sham vs PV-Cre::APP/PS1+C1V1, p=0.72
f		Interaction, F(1, 31)= 0.26, 0.82% of total variation, p= 0.6 genotype, F(1, 31)= 0.24, 0.76% of tot.var., p= 0.62 treatment, F(1, 31)= 0.75, 2.33% of tot.var., p= 0.39 Holm-Sidak's correction for multiple comparisons: PV-Cre::WT+Sham vs PV-Cre::APP/PS1 + Sham, p= 0.72 PV-Cre::WT+Sham vs PV-Cre::WT+C1V1, p= 0.79 PV-Cre::APP/PS1+Sham vs PV-Cre::APP/PS1+C1V1, p=0.72
g		Interaction, F(1, 31)= 1.91, 5.79% of total variation, p= 0.17 genotype, F(1, 31)= 0.25, 0.76% of tot.var., p= 0.61 treatment, F(1, 31)= 0.09, 27% of tot.var., p= 0.76 Holm-Sidak's correction for multiple comparisons: PV-Cre::WT+Sham vs PV-Cre::APP/PS1 + Sham, p= 0.67 PV-Cre::WT+Sham vs PV-Cre::WT+C1V1, p= 0.67 PV-Cre::APP/PS1+Sham vs PV-Cre::APP/PS1+C1V1, p=0.52
Fig. 3.10	**Statistical test**	**Test results**
b	Kruskal-Wallis test	Kruskal-Wallis statistic= 3.57, p= 0.47 Dunn's correction for multiple comparisons: n.s.
c	Kruskal-Wallis test	Kruskal-Wallis statistic= 20.97, p=0.0003 Dunn's correction for multiple comparisons: Layer I vs Layer II, p= 0.0008 Layer I vs Layer V, p= 0.0069 Rest of mult. comparison, n.s.
d	Two-tailed unpaired Mann-Whitney test	Mann-Whitney U=103; p= 0.18
Fig. 3.11	**Statistical test**	**Test results**
b	Two-way ANOVA	Interaction, F(4, 30)= 1.88, 3.98% of total variation, p= 0.13 layer, F(4, 30)= 31.48, 66.5% of tot.var., p< 0.0001 genotype, F(4, 30)= 2.58, 1.36% of tot.var., p= 0.11 Holm-Sidak's correction for multiple comparisons: WT-LI vs APP/PS1-LI, p= 0.99 WT-LII vs APP/PS1-LII, p= 0.99 WT-LIII vs APP/PS1-LIII, p= 0.99

		WT-LIV vs APP/PS1-LIV, p= 0.01 WT-LV vs APP/PS1-LV, p=0.99
c	Two-tailed unpaired student's t-test	t(6)= 1.12, p= 0.3
d	Two-way ANOVA	Interaction, F(4, 40)= 5.24, 4.25% of total variation, p= 0.0017 layer, F(4, 40)= 100.7, 81.7% of tot.var., p<0.0001 genotype, F(4, 40)= 49.47, 10.04% of tot.var., p<0.0001 Holm-Sidak's correction for multiple comparisons: WT-LI vs APP/PS1-LI, p= 0.62 WT-LII vs APP/PS1-LII, p= 0.01 WT-LIII vs APP/PS1-LIII, p= 0.057 WT-LIV vs APP/PS1-LIV, p<0.0001 WT-LV vs APP/PS1-LV, p= 0.01
e	Two-tailed unpaired student's t-test	t(3.45)= 3.84, p= 0.02
g	Two-way ANOVA	Interaction, F(3, 24)= 0.47, 1.24% of total variation, p= 0.7 layer, F(3, 24)=25.4, 66.11% of tot.var., p< 0.0001 genotype, F(3, 24)= 5.78, 5.02% of tot.var., p= 0.02 Holm-Sidak's correction for multiple comparisons: WT-LII vs APP/PS1-LII, p= 0.31 WT-LIII vs APP/PS1-LIII, p= 0.55 WT-LIV vs APP/PS1-LIV, p= 0.26 WT-LV vs APP/PS1-LV, p= 0.74
h	Two-tailed unpaired student's t-test	t(6)= 1.56, p= 0.16
j		t(9)= 0.47, p= 0.64
k		t(9)= 0.15, p= 0.88
l		t(9)= 0.67, p= 0.51
Fig. 3.12.2	**Statistical test**	**Test results**
f	Two-tailed unpaired student's t-test	t(68)= 3.11, p= 0.002

7 References

Abe, Y., & Toyosawa, K. (1999). Age-related changes in rat hippocampal theta rhythms: a difference between type 1 and type 2 theta. *J Vet Med Sci, 61*(5), 543-548. doi:10.1292/jvms.61.543

Adaikkan, C., Middleton, S. J., Marco, A., Pao, P. C., Mathys, H., Kim, D. N., . . . Tsai, L. H. (2019). Gamma Entrainment Binds Higher-Order Brain Regions and Offers Neuroprotection. *Neuron, 102*(5), 929-943 e928. doi:10.1016/j.neuron.2019.04.011

Adaikkan, C., & Tsai, L. H. (2020). Gamma Entrainment: Impact on Neurocircuits, Glia, and Therapeutic Opportunities. *Trends Neurosci, 43*(1), 24-41. doi:10.1016/j.tins.2019.11.001

Adrian, E. D., & Matthews, B. H. (1934). The interpretation of potential waves in the cortex. *J Physiol, 81*(4), 440-471. doi:10.1113/jphysiol.1934.sp003147

Akam, T., & Kullmann, D. M. (2014). Oscillatory multiplexing of population codes for selective communication in the mammalian brain. *Nat Rev Neurosci, 15*(2), 111-122. doi:10.1038/nrn3668

Albani, S. H., McHail, D. G., & Dumas, T. C. (2014). Developmental studies of the hippocampus and hippocampal-dependent behaviors: insights from interdisciplinary studies and tips for new investigators. *Neurosci Biobehav Rev, 43*, 183-190. doi:10.1016/j.neubiorev.2014.04.009

Alekseichuk, I., Diers, K., Paulus, W., & Antal, A. (2016). Transcranial electrical stimulation of the occipital cortex during visual perception modifies the magnitude of BOLD activity: A combined tES-fMRI approach. *Neuroimage, 140*, 110-117. doi:10.1016/j.neuroimage.2015.11.034

Alekseichuk, I., Turi, Z., Amador de Lara, G., Antal, A., & Paulus, W. (2016). Spatial Working Memory in Humans Depends on Theta and High Gamma Synchronization in the Prefrontal Cortex. *Curr Biol, 26*(12), 1513-1521. doi:10.1016/j.cub.2016.04.035

Alexander, A., & Soltesz, I. (2016). Hippogate: a break-in from entorhinal cortex. *Nat Neurosci, 19*(4), 530-532. doi:10.1038/nn.4253

Alonso, A., & Llinas, R. R. (1989). Subthreshold Na+-dependent theta-like rhythmicity in stellate cells of entorhinal cortex layer II. *Nature, 342*(6246), 175-177. doi:10.1038/342175a0

Ambrad G., E., & Fuhrmann, M. (2019). Unsupervised excitation: GABAergic dysfunctions in Alzheimer's disease. *Brain Res, 1707*, 216-226. doi:10.1016/j.brainres.2018.11.042

Ambrad Giovannetti, E. P., S.; Justus, D.; Kaneko, H.; Fuhrmann, F.; Steffen, J.; Remy, S.; Fuhrmann, M. (2018). Restoring memory by optogenetic synchronization of hippocampal oscillations in an Alzheimer's disease mouse model. *bioRxiv*. doi:https://doi.org/10.1101/363820

Amemiya, S., & Redish, A. D. (2018). Hippocampal Theta-Gamma Coupling Reflects State-Dependent Information Processing in Decision Making. *Cell Rep, 22*(12), 3328-3338. doi:10.1016/j.celrep.2018.02.091

Amilhon, B., Huh, C. Y., Manseau, F., Ducharme, G., Nichol, H., Adamantidis, A., & Williams, S. (2015). Parvalbumin Interneurons of Hippocampus Tune Population Activity at Theta Frequency. *Neuron, 86*(5), 1277-1289. doi:10.1016/j.neuron.2015.05.027

Andersen, P., Holmqvist, B., & Voorhoeve, P. E. (1966). Excitatory synapses on hippocampal apical dendrites activated by entorhinal stimulation. *Acta Physiol Scand, 66*(4), 461-472. doi:10.1111/j.1748-1716.1966.tb03224.x

Artinian, J., & Lacaille, J. C. (2018). Disinhibition in learning and memory circuits: New vistas for somatostatin interneurons and long-term synaptic plasticity. *Brain Res Bull, 141*, 20-26. doi:10.1016/j.brainresbull.2017.11.012

Augustinack, J. C., Huber, K. E., Postelnicu, G. M., Kakunoori, S., Wang, R., van der Kouwe, A. J., . . . Fischl, B. (2012). Entorhinal verrucae geometry is coincident and correlates with Alzheimer's lesions: a combined neuropathology and high-resolution ex vivo MRI analysis. *Acta Neuropathol, 123*(1), 85-96. doi:10.1007/s00401-011-0929-5

Baddeley, A. (1992a). Working memory. *Science, 255*(5044), 556-559. doi:10.1126/science.1736359

Baddeley, A. (1992b). Working Memory: The Interface between Memory and Cognition. *J Cogn Neurosci, 4*(3), 281-288. doi:10.1162/jocn.1992.4.3.281

Baddeley, A. (2010). Working memory. *Curr Biol, 20*(4), R136-140. doi:10.1016/j.cub.2009.12.014

Bakker, A., Krauss, G. L., Albert, M. S., Speck, C. L., Jones, L. R., Stark, C. E., . . . Gallagher, M. (2012). Reduction of hippocampal hyperactivity improves cognition in amnestic mild cognitive impairment. *Neuron, 74*(3), 467-474. doi:10.1016/j.neuron.2012.03.023

Basu, J., Srinivas, K. V., Cheung, S. K., Taniguchi, H., Huang, Z. J., & Siegelbaum, S. A. (2013). A cortico-hippocampal learning rule shapes inhibitory microcircuit activity to enhance hippocampal information flow. *Neuron, 79*(6), 1208-1221. doi:10.1016/j.neuron.2013.07.001

Basu, J., Zaremba, J. D., Cheung, S. K., Hitti, F. L., Zemelman, B. V., Losonczy, A., & Siegelbaum, S. A. (2016). Gating of hippocampal activity, plasticity, and memory by entorhinal cortex long-range inhibition. *Science, 351*(6269), aaa5694. doi:10.1126/science.aaa5694

Bedard, C., Gomes, J. M., Bal, T., & Destexhe, A. (2017). A framework to reconcile frequency scaling measurements, from intracellular recordings, local-field potentials, up to EEG and MEG signals. *J Integr Neurosci, 16*(1), 3-18. doi:10.3233/JIN-160001

Belchior, H., Lopes-Dos-Santos, V., Tort, A. B., & Ribeiro, S. (2014). Increase in hippocampal theta oscillations during spatial decision making. *Hippocampus, 24*(6), 693-702. doi:10.1002/hipo.22260

Bellenguez, C., Grenier-Boley, B., & Lambert, J. C. (2020). Genetics of Alzheimer's disease: where we are, and where we are going. *Curr Opin Neurobiol, 61*, 40-48. doi:10.1016/j.conb.2019.11.024

Belluscio, M. A., Mizuseki, K., Schmidt, R., Kempter, R., & Buzsaki, G. (2012). Cross-frequency phase-phase coupling between theta and gamma oscillations in the hippocampus. *J Neurosci, 32*(2), 423-435. doi:10.1523/JNEUROSCI.4122-11.2012

Bender, F., Gorbati, M., Cadavieco, M. C., Denisova, N., Gao, X., Holman, C., . . . Ponomarenko, A. (2015). Theta oscillations regulate the speed of locomotion via a hippocampus to lateral septum pathway. *Nat Commun, 6*, 8521. doi:10.1038/ncomms9521

Biasucci, A. F., B; Murray, M.M. (2019). Electroencephalograpy. *Current Biology, 29(3)*, R80-R85. doi:doi: 10.1016/j.cub.2018.11.052

Bieri, K. W., Bobbitt, K. N., & Colgin, L. L. (2014). Slow and fast gamma rhythms coordinate different spatial coding modes in hippocampal place cells. *Neuron, 82*(3), 670-681. doi:10.1016/j.neuron.2014.03.013

Binder, S., Molle, M., Lippert, M., Bruder, R., Aksamaz, S., Ohl, F., . . . Marshall, L. (2019). Monosynaptic Hippocampal-Prefrontal Projections Contribute to Spatial Memory Consolidation in Mice. *J Neurosci, 39*(35), 6978-6991. doi:10.1523/JNEUROSCI.2158-18.2019

Bird, C. M., & Burgess, N. (2008). The hippocampus and memory: insights from spatial processing. *Nat Rev Neurosci, 9*(3), 182-194. doi:10.1038/nrn2335

Bolding, K. A., Ferbinteanu, J., Fox, S. E., & Muller, R. U. (2020). Place cell firing cannot support navigation without intact septal circuits. *Hippocampus, 30*(3), 175-191. doi:10.1002/hipo.23136

Bonnevie, T., Dunn, B., Fyhn, M., Hafting, T., Derdikman, D., Kubie, J. L., . . . Moser, M. B. (2013). Grid cells require excitatory drive from the hippocampus. *Nat Neurosci, 16*(3), 309-317. doi:10.1038/nn.3311

Bordner, K. A., Kitchen, R. R., Carlyle, B., George, E. D., Mahajan, M. C., Mane, S. M., . . . Simen, A. A. (2011). Parallel declines in cognition, motivation, and locomotion in aging mice: association with immune gene upregulation in the medial prefrontal cortex. *Exp Gerontol, 46*(8), 643-659. doi:10.1016/j.exger.2011.03.003

Braak, H., Alafuzoff, I., Arzberger, T., Kretzschmar, H., & Del Tredici, K. (2006). Staging of Alzheimer disease-associated neurofibrillary pathology using paraffin sections and immunocytochemistry. *Acta Neuropathol, 112*(4), 389-404. doi:10.1007/s00401-006-0127-z

Braak, H., & Braak, E. (1991a). Neuropathological stageing of Alzheimer-related changes. *Acta Neuropathol, 82*(4), 239-259.

Braak, H., & Braak, E. (1991b). Neuropathological stageing of Alzheimer-related changes. *Acta Neuropathol, 82*(4), 239-259. Retrieved from http://www.ncbi.nlm.nih.gov/pubmed/1759558

Braak, H., Braak, E., & Bohl, J. (1993). Staging of Alzheimer-related cortical destruction. *European neurology, 33*(6), 403-408. Retrieved from http://www.ncbi.nlm.nih.gov/pubmed/8307060

Bragin, A., Jando, G., Nadasdy, Z., van Landeghem, M., & Buzsaki, G. (1995). Dentate EEG spikes and associated interneuronal population bursts in the hippocampal hilar region of the rat. *J Neurophysiol, 73*(4), 1691-1705. doi:10.1152/jn.1995.73.4.1691

Brioni, J. D., Decker, M. W., Gamboa, L. P., Izquierdo, I., & McGaugh, J. L. (1990). Muscimol injections in the medial septum impair spatial learning. *Brain Res, 522*(2), 227-234. doi:10.1016/0006-8993(90)91465-s

Broadbent, N. J., & Clark, R. E. (2013). Remote context fear conditioning remains hippocampus-dependent irrespective of training protocol, training-surgery interval, lesion size, and lesion method. *Neurobiol Learn Mem, 106*, 300-308. doi:10.1016/j.nlm.2013.08.008

Buhl, E. H., Halasy, K., & Somogyi, P. (1994). Diverse sources of hippocampal unitary inhibitory postsynaptic potentials and the number of synaptic release sites. *Nature, 368*(6474), 823-828. doi:10.1038/368823a0

Burgos-Ramos, E., Hervas-Aguilar, A., Aguado-Llera, D., Puebla-Jimenez, L., Hernandez-Pinto, A. M., Barrios, V., & Arilla-Ferreiro, E. (2008). Somatostatin and Alzheimer's disease. *Mol Cell Endocrinol, 286*(1-2), 104-111. doi:10.1016/j.mce.2008.01.014

Busche, M. A., Chen, X., Henning, H. A., Reichwald, J., Staufenbiel, M., Sakmann, B., & Konnerth, A. (2012). Critical role of soluble amyloid-beta for early hippocampal hyperactivity in a mouse model of Alzheimer's disease. *Proc Natl Acad Sci U S A, 109*(22), 8740-8745. doi:1206171109 [pii]

10.1073/pnas.1206171109

Busche, M. A., Eichhoff, G., Adelsberger, H., Abramowski, D., Wiederhold, K. H., Haass, C., . . . Garaschuk, O. (2008). Clusters of hyperactive neurons near amyloid plaques in a mouse model of Alzheimer's disease. *Science, 321*(5896), 1686-1689. doi:321/5896/1686 [pii]

10.1126/science.1162844

Butler, J. L., Mendonca, P. R., Robinson, H. P., & Paulsen, O. (2016). Intrinsic Cornu Ammonis Area 1 Theta-Nested Gamma Oscillations Induced by Optogenetic Theta Frequency Stimulation. *J Neurosci, 36*(15), 4155-4169. doi:10.1523/JNEUROSCI.3150-15.2016

Buzsaki, G. (2002). Theta oscillations in the hippocampus. *Neuron, 33*(3), 325-340. Retrieved from https://www.ncbi.nlm.nih.gov/pubmed/11832222

Buzsaki, G. (2004). Large-scale recording of neuronal ensembles. *Nat Neurosci, 7*(5), 446-451. doi:10.1038/nn1233

Buzsaki, G. (2005). Theta rhythm of navigation: link between path integration and landmark navigation, episodic and semantic memory. *Hippocampus, 15*(7), 827-840. doi:10.1002/hipo.20113

Buzsaki, G. (2010). Neural syntax: cell assemblies, synapsembles, and readers. *Neuron, 68*(3), 362-385. doi:10.1016/j.neuron.2010.09.023

Buzsaki, G. (2015). Hippocampal sharp wave-ripple: A cognitive biomarker for episodic memory and planning. *Hippocampus, 25*(10), 1073-1188. doi:10.1002/hipo.22488

Buzsaki, G., Anastassiou, C. A., & Koch, C. (2012). The origin of extracellular fields and currents--EEG, ECoG, LFP and spikes. *Nat Rev Neurosci, 13*(6), 407-420. doi:10.1038/nrn3241

Buzsaki, G., & Chrobak, J. J. (1995). Temporal structure in spatially organized neuronal ensembles: a role for interneuronal networks. *Curr Opin Neurobiol, 5*(4), 504-510. doi:10.1016/0959-4388(95)80012-3

Buzsaki, G., Czopf, J., Kondakor, I., & Kellenyi, L. (1986). Laminar distribution of hippocampal rhythmic slow activity (RSA) in the behaving rat: current-source density analysis, effects of urethane and atropine. *Brain Res, 365*(1), 125-137. doi:10.1016/0006-8993(86)90729-8

Buzsaki, G., & Draguhn, A. (2004). Neuronal oscillations in cortical networks. *Science, 304*(5679), 1926-1929. doi:10.1126/science.1099745

Buzsaki, G., & Freeman, W. (2015). Editorial overview: brain rhythms and dynamic coordination. *Curr Opin Neurobiol, 31*, v-ix. doi:10.1016/j.conb.2015.01.016

Buzsaki, G., Logothetis, N., & Singer, W. (2013). Scaling brain size, keeping timing: evolutionary preservation of brain rhythms. *Neuron, 80*(3), 751-764. doi:10.1016/j.neuron.2013.10.002

Buzsaki, G., & Moser, E. I. (2013). Memory, navigation and theta rhythm in the hippocampal-entorhinal system. *Nat Neurosci, 16*(2), 130-138. doi:10.1038/nn.3304

Buzsaki, G., & Wang, X. J. (2012). Mechanisms of gamma oscillations. *Annu Rev Neurosci, 35*, 203-225. doi:10.1146/annurev-neuro-062111-150444

Buzsaki, G., & Watson, B. O. (2012). Brain rhythms and neural syntax: implications for efficient coding of cognitive content and neuropsychiatric disease. *Dialogues Clin Neurosci, 14*(4), 345-367. Retrieved from https://www.ncbi.nlm.nih.gov/pubmed/23393413

Cacucci, F., Yi, M., Wills, T. J., Chapman, P., & O'Keefe, J. (2008). Place cell firing correlates with memory deficits and amyloid plaque burden in Tg2576 Alzheimer mouse model. *Proc Natl Acad Sci U S A, 105*(22), 7863-7868. doi:10.1073/pnas.0802908105

Canolty, R. T., & Knight, R. T. (2010). The functional role of cross-frequency coupling. *Trends Cogn Sci, 14*(11), 506-515. doi:10.1016/j.tics.2010.09.001

Caputi, A., Melzer, S., Michael, M., & Monyer, H. (2013). The long and short of GABAergic neurons. *Curr Opin Neurobiol, 23*(2), 179-186. doi:10.1016/j.conb.2013.01.021

Caspers, H., Speckmann, E. J., & Lehmenkuhler, A. (1980). Electrogenesis of cortical DC potentials. *Prog Brain Res, 54*, 3-15. doi:10.1016/S0079-6123(08)61603-9

Cayzac, S., Mons, N., Ginguay, A., Allinquant, B., Jeantet, Y., & Cho, Y. H. (2015). Altered hippocampal information coding and network synchrony in APP-PS1 mice. *Neurobiol Aging, 36*(12), 3200-3213. doi:10.1016/j.neurobiolaging.2015.08.023

Chai, W. J., Abd Hamid, A. I., & Abdullah, J. M. (2018). Working Memory From the Psychological and Neurosciences Perspectives: A Review. *Front Psychol, 9*, 401. doi:10.3389/fpsyg.2018.00401

Chang, C. H., Lane, H. Y., & Lin, C. H. (2018). Brain Stimulation in Alzheimer's Disease. *Front Psychiatry, 9*, 201. doi:10.3389/fpsyt.2018.00201

Chen, G. F., Xu, T. H., Yan, Y., Zhou, Y. R., Jiang, Y., Melcher, K., & Xu, H. E. (2017). Amyloid beta: structure, biology and structure-based therapeutic development. *Acta Pharmacol Sin, 38*(9), 1205-1235. doi:10.1038/aps.2017.28

Chen, T. W., Wardill, T. J., Sun, Y., Pulver, S. R., Renninger, S. L., Baohan, A., . . . Kim, D. S. (2013). Ultrasensitive fluorescent proteins for imaging neuronal activity. *Nature, 499*(7458), 295-300. doi:10.1038/nature12354

Chenani, A., Sabariego, M., Schlesiger, M. I., Leutgeb, J. K., Leutgeb, S., & Leibold, C. (2019). Hippocampal CA1 replay becomes less prominent but more rigid without inputs from medial entorhinal cortex. *Nat Commun, 10*(1), 1341. doi:10.1038/s41467-019-09280-0

Chung, H., Park, K., Jang, H. J., Kohl, M. M., & Kwag, J. (2020). Dissociation of somatostatin and parvalbumin interneurons circuit dysfunctions underlying hippocampal theta and gamma oscillations impaired by amyloid beta oligomers in vivo. *Brain Struct Funct, 225*(3), 935-954. doi:10.1007/s00429-020-02044-3

Cohen, S. J., Munchow, A. H., Rios, L. M., Zhang, G., Asgeirsdottir, H. N., & Stackman, R. W., Jr. (2013). The rodent hippocampus is essential for nonspatial object memory. *Curr Biol, 23*(17), 1685-1690. doi:10.1016/j.cub.2013.07.002

Cohen, S. J., & Stackman, R. W., Jr. (2015). Assessing rodent hippocampal involvement in the novel object recognition task. A review. *Behav Brain Res, 285*, 105-117. doi:10.1016/j.bbr.2014.08.002

Cole, K. S., & Hodgkin, A. L. (1939). Membrane and Protoplasm Resistance in the Squid Giant Axon. *J Gen Physiol, 22*(5), 671-687. doi:10.1085/jgp.22.5.671

Colgin, L. L. (2015). Do slow and fast gamma rhythms correspond to distinct functional states in the hippocampal network? *Brain Res, 1621*, 309-315. doi:10.1016/j.brainres.2015.01.005

Colgin, L. L. (2016). Rhythms of the hippocampal network. *Nat Rev Neurosci, 17*(4), 239-249. doi:10.1038/nrn.2016.21

Colombo, D., Serino, S., Tuena, C., Pedroli, E., Dakanalis, A., Cipresso, P., & Riva, G. (2017). Egocentric and allocentric spatial reference frames in aging: A systematic review. *Neurosci Biobehav Rev, 80*, 605-621. doi:10.1016/j.neubiorev.2017.07.012

Corder, E. H., Saunders, A. M., Strittmatter, W. J., Schmechel, D. E., Gaskell, P. C., Small, G. W., . . . Pericak-Vance, M. A. (1993). Gene dose of apolipoprotein E type 4 allele and the risk of Alzheimer's disease in late onset families. *Science, 261*(5123), 921-923. doi:10.1126/science.8346443

Cummins, T. D., & Finnigan, S. (2007). Theta power is reduced in healthy cognitive aging. *Int J Psychophysiol, 66*(1), 10-17. doi:10.1016/j.ijpsycho.2007.05.008

Dana, H., Chen, T. W., Hu, A., Shields, B. C., Guo, C., Looger, L. L., . . . Svoboda, K. (2014). Thy1-GCaMP6 transgenic mice for neuronal population imaging in vivo. *PLoS One, 9*(9), e108697. doi:10.1371/journal.pone.0108697

Darbin, O. (2012). The aging striatal dopamine function. *Parkinsonism Relat Disord, 18*(5), 426-432. doi:10.1016/j.parkreldis.2011.11.025

Davies, P., Katzman, R., & Terry, R. D. (1980). Reduced somatostatin-like immunoreactivity in cerebral cortex from cases of Alzheimer disease and Alzheimer senile dementa. *Nature, 288*(5788), 279-280.

Davies, P., & Terry, R. D. (1981). Cortical somatostatin-like immunoreactivity in cases of Alzheimer's disease and senile dementia of the Alzheimer type. *Neurobiol Aging, 2*(1), 9-14. doi:10.1016/0197-4580(81)90053-1

de la Prida, L. M. (2019). The Theta Stone: 3 to 10 Hz Oscillations to Decipher the Human Brain Code. *Epilepsy Curr, 19*(2), 126-128. doi:10.1177/1535759719835662

de Sousa, A. F., Cowansage, K. K., Zutshi, I., Cardozo, L. M., Yoo, E. J., Leutgeb, S., & Mayford, M. (2019). Optogenetic reactivation of memory ensembles in the retrosplenial cortex induces systems consolidation. *Proc Natl Acad Sci U S A, 116*(17), 8576-8581. doi:10.1073/pnas.1818432116

Deshmukh, S. S., Yoganarasimha, D., Voicu, H., & Knierim, J. J. (2010). Theta modulation in the medial and the lateral entorhinal cortices. *J Neurophysiol, 104*(2), 994-1006. doi:10.1152/jn.01141.2009

Diba, K., & Buzsaki, G. (2007). Forward and reverse hippocampal place-cell sequences during ripples. *Nat Neurosci, 10*(10), 1241-1242. doi:10.1038/nn1961

Doan, T. P., Lagartos-Donate, M. J., Nilssen, E. S., Ohara, S., & Witter, M. P. (2019). Convergent Projections from Perirhinal and Postrhinal Cortices Suggest a Multisensory Nature of Lateral, but Not Medial, Entorhinal Cortex. *Cell Rep, 29*(3), 617-627 e617. doi:10.1016/j.celrep.2019.09.005

Dombeck, D. A., Harvey, C. D., Tian, L., Looger, L. L., & Tank, D. W. (2010). Functional imaging of hippocampal place cells at cellular resolution during virtual navigation. *Nat Neurosci, 13*(11), 1433-1440. doi:nn.2648 [pii]

10.1038/nn.2648

Drieu, C., Todorova, R., & Zugaro, M. (2018). Nested sequences of hippocampal assemblies during behavior support subsequent sleep replay. *Science, 362*(6415), 675-679. doi:10.1126/science.aat2952

Dubois, B., Feldman, H. H., Jacova, C., Dekosky, S. T., Barberger-Gateau, P., Cummings, J., . . . Scheltens, P. (2007). Research criteria for the diagnosis of Alzheimer's disease: revising the NINCDS-ADRDA criteria. *Lancet Neurol, 6*(8), 734-746. doi:10.1016/S1474-4422(07)70178-3

Dudman, J. T., Tsay, D., & Siegelbaum, S. A. (2007). A role for synaptic inputs at distal dendrites: instructive signals for hippocampal long-term plasticity. *Neuron, 56*(5), 866-879. doi:10.1016/j.neuron.2007.10.020

Duncan, K., Ketz, N., Inati, S. J., & Davachi, L. (2012). Evidence for area CA1 as a match/mismatch detector: a high-resolution fMRI study of the human hippocampus. *Hippocampus, 22*(3), 389-398. doi:10.1002/hipo.20933

Duzel, E., Penny, W. D., & Burgess, N. (2010). Brain oscillations and memory. *Curr Opin Neurobiol, 20*(2), 143-149. doi:10.1016/j.conb.2010.01.004

Eichenbaum, H. (2017a). Prefrontal-hippocampal interactions in episodic memory. *Nat Rev Neurosci, 18*(9), 547-558. doi:10.1038/nrn.2017.74

Eichenbaum, H. (2017b). Time (and space) in the hippocampus. *Curr Opin Behav Sci, 17*, 65-70. doi:10.1016/j.cobeha.2017.06.010

Eichenbaum, H., Yonelinas, A. P., & Ranganath, C. (2007). The medial temporal lobe and recognition memory. *Annu Rev Neurosci, 30*, 123-152. doi:10.1146/annurev.neuro.30.051606.094328

Einevoll, G. T., Kayser, C., Logothetis, N. K., & Panzeri, S. (2013). Modelling and analysis of local field potentials for studying the function of cortical circuits. *Nat Rev Neurosci, 14*(11), 770-785. doi:10.1038/nrn3599

English, D. F., McKenzie, S., Evans, T., Kim, K., Yoon, E., & Buzsaki, G. (2017). Pyramidal Cell-Interneuron Circuit Architecture and Dynamics in Hippocampal Networks. *Neuron, 96*(2), 505-520 e507. doi:10.1016/j.neuron.2017.09.033

Epelbaum, J., Guillou, J. L., Gastambide, F., Hoyer, D., Duron, E., & Viollet, C. (2009). Somatostatin, Alzheimer's disease and cognition: an old story coming of age? *Prog Neurobiol, 89*(2), 153-161. doi:10.1016/j.pneurobio.2009.07.002

Erten-Lyons, D., Woltjer, R. L., Dodge, H., Nixon, R., Vorobik, R., Calvert, J. F., . . . Kaye, J. (2009). Factors associated with resistance to dementia despite high Alzheimer disease pathology. *Neurology, 72*(4), 354-360. doi:10.1212/01.wnl.0000341273.18141.64

Etter, G., van der Veldt, S., Manseau, F., Zarrinkoub, I., Trillaud-Doppia, E., & Williams, S. (2019). Optogenetic gamma stimulation rescues memory impairments in an Alzheimer's disease mouse model. *Nature Communications, 10*(1), 5322. doi:10.1038/s41467-019-13260-9

Fernandez-Ruiz, A., & Herreras, O. (2013). Identifying the synaptic origin of ongoing neuronal oscillations through spatial discrimination of electric fields. *Front Comput Neurosci, 7*, 5. doi:10.3389/fncom.2013.00005

Fernandez-Ruiz, A., Oliva, A., Nagy, G. A., Maurer, A. P., Berenyi, A., & Buzsaki, G. (2017). Entorhinal-CA3 Dual-Input Control of Spike Timing in the Hippocampus by Theta-Gamma Coupling. *Neuron, 93*(5), 1213-1226 e1215. doi:10.1016/j.neuron.2017.02.017

Freund, T. F., & Antal, M. (1988). GABA-containing neurons in the septum control inhibitory interneurons in the hippocampus. *Nature, 336*(6195), 170-173. doi:10.1038/336170a0

Freund, T. F., & Buzsaki, G. (1996). Interneurons of the hippocampus. *Hippocampus, 6*(4), 347-470. doi:10.1002/(SICI)1098-1063(1996)6:4<347::AID-HIPO1>3.0.CO;2-I

Freund, T. F., & Katona, I. (2007). Perisomatic inhibition. *Neuron, 56*(1), 33-42. doi:S0896-6273(07)00710-6 [pii]

10.1016/j.neuron.2007.09.012

Friedrich, J., Zhou, P., & Paninski, L. (2017). Fast online deconvolution of calcium imaging data. *PLOS Computational Biology, 13*(3), e1005423. doi:10.1371/journal.pcbi.1005423

Fu, H., Rodriguez, G. A., Herman, M., Emrani, S., Nahmani, E., Barrett, G., . . . Duff, K. E. (2017). Tau Pathology Induces Excitatory Neuron Loss, Grid Cell Dysfunction, and Spatial Memory Deficits Reminiscent of Early Alzheimer's Disease. *Neuron, 93*(3), 533-541 e535. doi:10.1016/j.neuron.2016.12.023

Fuchs, E. C., Neitz, A., Pinna, R., Melzer, S., Caputi, A., & Monyer, H. (2016). Local and Distant Input Controlling Excitation in Layer II of the Medial Entorhinal Cortex. *Neuron, 89*(1), 194-208. doi:10.1016/j.neuron.2015.11.029

Fuchs, E. C., Zivkovic, A. R., Cunningham, M. O., Middleton, S., Lebeau, F. E., Bannerman, D. M., . . . Monyer, H. (2007). Recruitment of parvalbumin-positive interneurons determines hippocampal function and associated behavior. *Neuron, 53*(4), 591-604. doi:10.1016/j.neuron.2007.01.031

Fuhrmann, F., Justus, D., Sosulina, L., Kaneko, H., Beutel, T., Friedrichs, D., . . . Remy, S. (2015). Locomotion, Theta Oscillations, and the Speed-Correlated Firing of Hippocampal Neurons Are Controlled by a Medial Septal Glutamatergic Circuit. *Neuron, 86*(5), 1253-1264. doi:10.1016/j.neuron.2015.05.001

Fyhn, M., Molden, S., Witter, M. P., Moser, E. I., & Moser, M. B. (2004). Spatial representation in the entorhinal cortex. *Science, 305*(5688), 1258-1264. doi:10.1126/science.1099901

Gahete, M. D., Rubio, A., Duran-Prado, M., Avila, J., Luque, R. M., & Castano, J. P. (2010). Expression of Somatostatin, cortistatin, and their receptors, as well as dopamine receptors, but not of neprilysin, are reduced in the temporal lobe of Alzheimer's disease patients. *J Alzheimers Dis, 20*(2), 465-475. doi:10.3233/JAD-2010-1385

Galarreta, M., & Hestrin, S. (2002). Electrical and chemical synapses among parvalbumin fast-spiking GABAergic interneurons in adult mouse neocortex. *Proc Natl Acad Sci U S A, 99*(19), 12438-12443. doi:10.1073/pnas.192159599

Gandy, S. (2010). Testing the amyloid hypothesis of Alzheimer's disease in vivo. *Lancet Neurol, 9*(4), 333-335. doi:10.1016/S1474-4422(10)70055-7

Geiller, T., Vancura, B., Terada, S., Troullinou, E., Chavlis, S., Tsagkatakis, G., . . . Losonczy, A. (2020). Large-Scale 3D Two-Photon Imaging of Molecularly Identified CA1 Interneuron Dynamics in Behaving Mice. *Neuron, 108*(5), 968-983 e969. doi:10.1016/j.neuron.2020.09.013

Geinisman, Y., deToledo-Morrell, L., Morrell, F., Persina, I. S., & Rossi, M. (1992). Age-related loss of axospinous synapses formed by two afferent systems in the rat dentate gyrus as revealed by the unbiased stereological dissector technique. *Hippocampus, 2*(4), 437-444. doi:10.1002/hipo.450020411

Goodman, M. S., Kumar, S., Zomorrodi, R., Ghazala, Z., Cheam, A. S. M., Barr, M. S., . . . Rajji, T. K. (2018). Theta-Gamma Coupling and Working Memory in Alzheimer's Dementia and Mild Cognitive Impairment. *Front Aging Neurosci, 10*, 101. doi:10.3389/fnagi.2018.00101

Goutagny, R., Gu, N., Cavanagh, C., Jackson, J., Chabot, J. G., Quirion, R., . . . Williams, S. (2013). Alterations in hippocampal network oscillations and theta-gamma coupling arise before Abeta overproduction in a mouse model of Alzheimer's disease. *Eur J Neurosci, 37*(12), 1896-1902. doi:10.1111/ejn.12233

Goyal, A., Miller, J., Qasim, S. E., Watrous, A. J., Zhang, H., Stein, J. M., . . . Jacobs, J. (2020). Functionally distinct high and low theta oscillations in the human hippocampus. *Nat Commun, 11*(1), 2469. doi:10.1038/s41467-020-15670-6

Green, J. D., & Arduini, A. A. (1954). Hippocampal electrical activity in arousal. *J Neurophysiol, 17*(6), 533-557. doi:10.1152/jn.1954.17.6.533

Grimaldi, D., Papalambros, N. A., Zee, P. C., & Malkani, R. G. (2020). Neurostimulation techniques to enhance sleep and improve cognition in aging. *Neurobiol Dis, 141*, 104865. doi:10.1016/j.nbd.2020.104865

Gu, L., Kleiber, S., Schmid, L., Nebeling, F., Chamoun, M., Steffen, J., . . . Fuhrmann, M. (2014). Long-term in vivo imaging of dendritic spines in the hippocampus reveals structural plasticity. *J Neurosci, 34*(42), 13948-13953. doi:10.1523/JNEUROSCI.1464-14.2014

Gu, Z., Alexander, G. M., Dudek, S. M., & Yakel, J. L. (2017). Hippocampus and Entorhinal Cortex Recruit Cholinergic and NMDA Receptors Separately to Generate Hippocampal Theta Oscillations. *Cell Rep, 21*(12), 3585-3595. doi:10.1016/j.celrep.2017.11.080

Gu, Z., & Yakel, J. L. (2017). Inducing theta oscillations in the entorhinal hippocampal network in vitro. *Brain Struct Funct, 222*(2), 943-955. doi:10.1007/s00429-016-1256-3

Gulyas, A. I., Szabo, G. G., Ulbert, I., Holderith, N., Monyer, H., Erdelyi, F., . . . Hajos, N. (2010). Parvalbumin-containing fast-spiking basket cells generate the field potential oscillations induced by cholinergic receptor activation in the hippocampus. *J Neurosci, 30*(45), 15134-15145. doi:10.1523/JNEUROSCI.4104-10.2010

Haas, L. F. (2003). Hans Berger (1873-1941), Richard Caton (1842-1926), and electroencephalography. *J Neurol Neurosurg Psychiatry, 74*(1), 9. doi:10.1136/jnnp.74.1.9

Haass, C., & Selkoe, D. J. (2007). Soluble protein oligomers in neurodegeneration: lessons from the Alzheimer's amyloid beta-peptide. *Nat Rev Mol Cell Biol, 8*(2), 101-112. doi:nrm2101 [pii]

10.1038/nrm2101

Hafting, T., Fyhn, M., Molden, S., Moser, M. B., & Moser, E. I. (2005). Microstructure of a spatial map in the entorhinal cortex. *Nature, 436*(7052), 801-806. doi:10.1038/nature03721

Hall, A. M., & Roberson, E. D. (2012). Mouse models of Alzheimer's disease. *Brain Res Bull, 88*(1), 3-12. doi:10.1016/j.brainresbull.2011.11.017

Hamm, V., Heraud, C., Bott, J. B., Herbeaux, K., Strittmatter, C., Mathis, C., & Goutagny, R. (2017). Differential contribution of APP metabolites to early cognitive deficits in a TgCRND8 mouse model of Alzheimer's disease. *Sci Adv, 3*(2), e1601068. doi:10.1126/sciadv.1601068

Hardy, J. (1997). Amyloid, the presenilins and Alzheimer's disease. *Trends Neurosci, 20*(4), 154-159. doi:10.1016/s0166-2236(96)01030-2

Harris, J. A., Devidze, N., Verret, L., Ho, K., Halabisky, B., Thwin, M. T., . . . Mucke, L. (2010). Transsynaptic progression of amyloid-beta-induced neuronal dysfunction within the entorhinal-hippocampal network. *Neuron, 68*(3), 428-441. doi:10.1016/j.neuron.2010.10.020

Hasselmo, M. E. (2005a). The role of hippocampal regions CA3 and CA1 in matching entorhinal input with retrieval of associations between objects and context: theoretical comment on Lee et al. (2005). *Behav Neurosci, 119*(1), 342-345. doi:10.1037/0735-7044.119.1.342

Hasselmo, M. E. (2005b). What is the function of hippocampal theta rhythm?--Linking behavioral data to phasic properties of field potential and unit recording data. *Hippocampus, 15*(7), 936-949. doi:10.1002/hipo.20116

Hasselmo, M. E., & Eichenbaum, H. (2005). Hippocampal mechanisms for the context-dependent retrieval of episodes. *Neural Netw, 18*(9), 1172-1190. doi:10.1016/j.neunet.2005.08.007

Heneka, M. T., O'Banion, M. K., Terwel, D., & Kummer, M. P. (2010). Neuroinflammatory processes in Alzheimer's disease. *J Neural Transm (Vienna), 117*(8), 919-947. doi:10.1007/s00702-010-0438-z

Herreras, O. (2016). Local Field Potentials: Myths and Misunderstandings. *Front Neural Circuits, 10*, 101. doi:10.3389/fncir.2016.00101

Herrup, K. (2015). The case for rejecting the amyloid cascade hypothesis. *Nat Neurosci, 18*(6), 794-799. doi:10.1038/nn.4017

Herweg, N. A., Solomon, E. A., & Kahana, M. J. (2020). Theta Oscillations in Human Memory. *Trends Cogn Sci, 24*(3), 208-227. doi:10.1016/j.tics.2019.12.006

Hijazi, S., Heistek, T. S., Scheltens, P., Neumann, U., Shimshek, D. R., Mansvelder, H. D., . . . van Kesteren, R. E. (2020). Early restoration of parvalbumin interneuron activity prevents memory loss and network hyperexcitability in a mouse model of Alzheimer's disease. *Mol Psychiatry, 25*(12), 3380-3398. doi:10.1038/s41380-019-0483-4

Hijazi, S., Heistek, T. S., van der Loo, R., Mansvelder, H. D., Smit, A. B., & van Kesteren, R. E. (2020). Hyperexcitable Parvalbumin Interneurons Render Hippocampal Circuitry Vulnerable to Amyloid Beta. *iScience, 23*(7), 101271. doi:10.1016/j.isci.2020.101271

Hippenmeyer, S., Vrieseling, E., Sigrist, M., Portmann, T., Laengle, C., Ladle, D. R., & Arber, S. (2005). A developmental switch in the response of DRG neurons to ETS transcription factor signaling. *PLoS Biol, 3*(5), e159. doi:10.1371/journal.pbio.0030159

Hodgkin, A. L. (1937). Evidence for electrical transmission in nerve: Part II. *J Physiol, 90*(2), 211-232. doi:10.1113/jphysiol.1937.sp003508

Hodgkin, A. L. (1939). The relation between conduction velocity and the electrical resistance outside a nerve fibre. *J Physiol, 94*(4), 560-570. doi:10.1113/jphysiol.1939.sp003702

Hsiao, K. K., Borchelt, D. R., Olson, K., Johannsdottir, R., Kitt, C., Yunis, W., . . . et al. (1995). Age-related CNS disorder and early death in transgenic FVB/N mice overexpressing Alzheimer amyloid precursor proteins. *Neuron, 15*(5), 1203-1218. doi:10.1016/0896-6273(95)90107-8

Huang, H., Nie, S., Cao, M., Marshall, C., Gao, J., Xiao, N., . . . Xiao, M. (2016). Characterization of AD-like phenotype in aged APPSwe/PS1dE9 mice. *Age (Dordr), 38*(4), 303-322. doi:10.1007/s11357-016-9929-7

Hutcheon, B., & Yarom, Y. (2000). Resonance, oscillation and the intrinsic frequency preferences of neurons. *Trends Neurosci, 23*(5), 216-222. doi:10.1016/s0166-2236(00)01547-2

Huxter, J., Burgess, N., & O'Keefe, J. (2003). Independent rate and temporal coding in hippocampal pyramidal cells. *Nature, 425*(6960), 828-832. doi:10.1038/nature02058

Hyman, B. T., Van Hoesen, G. W., Kromer, L. J., & Damasio, A. R. (1986). Perforant pathway changes and the memory impairment of Alzheimer's disease. *Ann Neurol, 20*(4), 472-481. doi:10.1002/ana.410200406

Iaccarino, H. F., Singer, A. C., Martorell, A. J., Rudenko, A., Gao, F., Gillingham, T. Z., . . . Tsai, L. H. (2016). Gamma frequency entrainment attenuates amyloid load and modifies microglia. *Nature, 540*(7632), 230-235. doi:10.1038/nature20587

Isaacson, J. S., & Scanziani, M. (2011). How inhibition shapes cortical activity. *Neuron, 72*(2), 231-243. doi:10.1016/j.neuron.2011.09.027

Itskov, V., Pastalkova, E., Mizuseki, K., Buzsaki, G., & Harris, K. D. (2008). Theta-mediated dynamics of spatial information in hippocampus. *J Neurosci, 28*(23), 5959-5964. doi:10.1523/JNEUROSCI.5262-07.2008

Iwata, N., Tsubuki, S., Takaki, Y., Watanabe, K., Sekiguchi, M., Hosoki, E., . . . Saido, T. C. (2000). Identification of the major Abeta1-42-degrading catabolic pathway in brain parenchyma: suppression leads to biochemical and pathological deposition. *Nat Med, 6*(2), 143-150. doi:10.1038/72237

Jacobson, T. K., Howe, M. D., Schmidt, B., Hinman, J. R., Escabi, M. A., & Markus, E. J. (2013). Hippocampal theta, gamma, and theta-gamma coupling: effects of aging, environmental change, and cholinergic activation. *J Neurophysiol, 109*(7), 1852-1865. doi:10.1152/jn.00409.2012

Jankowsky, J. L., Fadale, D. J., Anderson, J., Xu, G. M., Gonzales, V., Jenkins, N. A., . . . Borchelt, D. R. (2004). Mutant presenilins specifically elevate the levels of the 42 residue beta-amyloid peptide in vivo: evidence for augmentation of a 42-specific gamma secretase. *Hum Mol Genet, 13*(2), 159-170. doi:10.1093/hmg/ddh019

ddh019 [pii]

Jeewajee, A., Lever, C., Burton, S., O'Keefe, J., & Burgess, N. (2008). Environmental novelty is signaled by reduction of the hippocampal theta frequency. *Hippocampus, 18*(4), 340-348. doi:10.1002/hipo.20394

Jiao, S. S., Bu, X. L., Liu, Y. H., Zhu, C., Wang, Q. H., Shen, L. L., . . . Wang, Y. J. (2016). Sex Dimorphism Profile of Alzheimer's Disease-Type Pathologies in an APP/PS1 Mouse Model. *Neurotox Res, 29*(2), 256-266. doi:10.1007/s12640-015-9589-x

Johnson, E. L., Adams, J. N., Solbakk, A. K., Endestad, T., Larsson, P. G., Ivanovic, J., . . . Knight, R. T. (2018). Dynamic frontotemporal systems process space and time in working memory. *PLoS Biol, 16*(3), e2004274. doi:10.1371/journal.pbio.2004274

Jones, D. T., Graff-Radford, J., Lowe, V. J., Wiste, H. J., Gunter, J. L., Senjem, M. L., . . . Jack, C. R., Jr. (2017). Tau, amyloid, and cascading network failure across the Alzheimer's disease spectrum. *Cortex, 97*, 143-159. doi:10.1016/j.cortex.2017.09.018

Jones, M. W., & Wilson, M. A. (2005). Theta rhythms coordinate hippocampal-prefrontal interactions in a spatial memory task. *PLoS Biol, 3*(12), e402. doi:10.1371/journal.pbio.0030402

Joshi, A., Salib, M., Viney, T. J., Dupret, D., & Somogyi, P. (2017). Behavior-Dependent Activity and Synaptic Organization of Septo-hippocampal GABAergic Neurons Selectively Targeting the Hippocampal CA3 Area. *Neuron, 96*(6), 1342-1357 e1345. doi:10.1016/j.neuron.2017.10.033

Jucker, M., & Walker, L. C. (2011). Pathogenic protein seeding in Alzheimer disease and other neurodegenerative disorders. *Ann Neurol, 70*(4), 532-540. doi:10.1002/ana.22615

Julian, J. B., Keinath, A. T., Marchette, S. A., & Epstein, R. A. (2018). The Neurocognitive Basis of Spatial Reorientation. *Curr Biol, 28*(17), R1059-R1073. doi:10.1016/j.cub.2018.04.057

Jun, H., Bramian, A., Soma, S., Saito, T., Saido, T. C., & Igarashi, K. M. (2020). Disrupted Place Cell Remapping and Impaired Grid Cells in a Knockin Model of Alzheimer's Disease. *Neuron, 107*(6), 1095-1112 e1096. doi:10.1016/j.neuron.2020.06.023

Jura, B., Macrez, N., Meyrand, P., & Bem, T. (2019). Deficit in hippocampal ripples does not preclude spatial memory formation in APP/PS1 mice. *Sci Rep, 9*(1), 20129. doi:10.1038/s41598-019-56582-w

Jyoti, A., Plano, A., Riedel, G., & Platt, B. (2015). Progressive age-related changes in sleep and EEG profiles in the PLB1Triple mouse model of Alzheimer's disease. *Neurobiol Aging, 36*(10), 2768-2784. doi:10.1016/j.neurobiolaging.2015.07.001

Kayed, R., & Lasagna-Reeves, C. A. (2013). Molecular mechanisms of amyloid oligomers toxicity. *J Alzheimers Dis, 33 Suppl 1*, S67-78. doi:10.3233/JAD-2012-129001

Kerrigan, T. L., Brown, J. T., & Randall, A. D. (2014). Characterization of altered intrinsic excitability in hippocampal CA1 pyramidal cells of the Abeta-overproducing PDAPP mouse. *Neuropharmacology, 79*, 515-524. doi:10.1016/j.neuropharm.2013.09.004

Khodagholy, D., Gelinas, J. N., & Buzsaki, G. (2017). Learning-enhanced coupling between ripple oscillations in association cortices and hippocampus. *Science, 358*(6361), 369-372. doi:10.1126/science.aan6203

Kilgore, M., Miller, C. A., Fass, D. M., Hennig, K. M., Haggarty, S. J., Sweatt, J. D., & Rumbaugh, G. (2010). Inhibitors of class 1 histone deacetylases reverse contextual memory deficits in a mouse model of Alzheimer's disease. *Neuropsychopharmacology, 35*(4), 870-880. doi:10.1038/npp.2009.197

Kitamura, T., Sun, C., Martin, J., Kitch, L. J., Schnitzer, M. J., & Tonegawa, S. (2015). Entorhinal Cortical Ocean Cells Encode Specific Contexts and Drive Context-Specific Fear Memory. *Neuron, 87*(6), 1317-1331. doi:10.1016/j.neuron.2015.08.036

Klausberger, T., Magill, P. J., Marton, L. F., Roberts, J. D., Cobden, P. M., Buzsaki, G., & Somogyi, P. (2003). Brain-state- and cell-type-specific firing of hippocampal interneurons in vivo. *Nature, 421*(6925), 844-848. doi:10.1038/nature01374

Klausberger, T., & Somogyi, P. (2008). Neuronal diversity and temporal dynamics: the unity of hippocampal circuit operations. *Science, 321*(5885), 53-57. doi:10.1126/science.1149381

Klein, A. S., Donoso, J. R., Kempter, R., Schmitz, D., & Beed, P. (2016). Early Cortical Changes in Gamma Oscillations in Alzheimer's Disease. *Front Syst Neurosci, 10*, 83. doi:10.3389/fnsys.2016.00083

Klunk, W. E., Bacskai, B. J., Mathis, C. A., Kajdasz, S. T., McLellan, M. E., Frosch, M. P., . . . Hyman, B. T. (2002). Imaging Abeta plaques in living transgenic mice with multiphoton microscopy

and methoxy-X04, a systemically administered Congo red derivative. *J Neuropathol Exp Neurol, 61*(9), 797-805. doi:10.1093/jnen/61.9.797

Knierim, J. J., & McNaughton, B. L. (2001). Hippocampal place-cell firing during movement in three-dimensional space. *J Neurophysiol, 85*(1), 105-116. doi:10.1152/jn.2001.85.1.105

Knight, R. (1996). Contribution of human hippocampal region to novelty detection. *Nature, 383*(6597), 256-259. doi:10.1038/383256a0

Koenig, J., Linder, A. N., Leutgeb, J. K., & Leutgeb, S. (2011). The spatial periodicity of grid cells is not sustained during reduced theta oscillations. *Science, 332*(6029), 592-595. doi:10.1126/science.1201685

Korotkova, T., Fuchs, E. C., Ponomarenko, A., von Engelhardt, J., & Monyer, H. (2010). NMDA receptor ablation on parvalbumin-positive interneurons impairs hippocampal synchrony, spatial representations, and working memory. *Neuron, 68*(3), 557-569. doi:10.1016/j.neuron.2010.09.017

Korotkova, T., Ponomarenko, A., Monaghan, C. K., Poulter, S. L., Cacucci, F., Wills, T., . . . Lever, C. (2018). Reconciling the different faces of hippocampal theta: The role of theta oscillations in cognitive, emotional and innate behaviors. *Neurosci Biobehav Rev, 85*, 65-80. doi:10.1016/j.neubiorev.2017.09.004

Kramis, R., Vanderwolf, C. H., & Bland, B. H. (1975). Two types of hippocampal rhythmical slow activity in both the rabbit and the rat: relations to behavior and effects of atropine, diethyl ether, urethane, and pentobarbital. *Exp Neurol, 49*(1 Pt 1), 58-85. doi:10.1016/0014-4886(75)90195-8

Kriener, B., Helias, M., Rotter, S., Diesmann, M., & Einevoll, G. T. (2013). How pattern formation in ring networks of excitatory and inhibitory spiking neurons depends on the input current regime. *Front Comput Neurosci, 7*, 187. doi:10.3389/fncom.2013.00187

Kullmann, D. M. (2011). Interneuron networks in the hippocampus. *Curr Opin Neurobiol, 21*(5), 709-716. doi:10.1016/j.conb.2011.05.006

Kumar, U. (2005). Expression of somatostatin receptor subtypes (SSTR1-5) in Alzheimer's disease brain: an immunohistochemical analysis. *Neuroscience, 134*(2), 525-538. doi:10.1016/j.neuroscience.2005.04.001

Kunz, L., Schroder, T. N., Lee, H., Montag, C., Lachmann, B., Sariyska, R., . . . Axmacher, N. (2015). Reduced grid-cell-like representations in adults at genetic risk for Alzheimer's disease. *Science, 350*(6259), 430-433. doi:10.1126/science.aac8128

Kuruvilla, M. V., & Ainge, J. A. (2017). Lateral Entorhinal Cortex Lesions Impair Local Spatial Frameworks. *Front Syst Neurosci, 11*, 30. doi:10.3389/fnsys.2017.00030

Lasztoczi, B., & Klausberger, T. (2014). Layer-specific GABAergic control of distinct gamma oscillations in the CA1 hippocampus. *Neuron, 81*(5), 1126-1139. doi:10.1016/j.neuron.2014.01.021

Lee, S. H., Urbano, F. J., & Garcia-Rill, E. (2018). The Critical Role of Intrinsic Membrane Oscillations. *Neurosignals, 26*(1), 66-76. doi:10.1159/000493900

Lester, A. W., Moffat, S. D., Wiener, J. M., Barnes, C. A., & Wolbers, T. (2017). The Aging Navigational System. *Neuron, 95*(5), 1019-1035. doi:10.1016/j.neuron.2017.06.037

Letzkus, J. J., Wolff, S. B., & Luthi, A. (2015). Disinhibition, a Circuit Mechanism for Associative Learning and Memory. *Neuron, 88*(2), 264-276. doi:10.1016/j.neuron.2015.09.024

Leung, L. S. (1984). Theta rhythm during REM sleep and waking: correlations between power, phase and frequency. *Electroencephalogr Clin Neurophysiol, 58*(6), 553-564. doi:10.1016/0013-4694(84)90045-2

Li, P., Geng, X., Jiang, H., Caccavano, A., Vicini, S., & Wu, J. Y. (2019). Measuring Sharp Waves and Oscillatory Population Activity With the Genetically Encoded Calcium Indicator GCaMP6f. *Front Cell Neurosci, 13*, 274. doi:10.3389/fncel.2019.00274

Linden, H., Tetzlaff, T., Potjans, T. C., Pettersen, K. H., Grun, S., Diesmann, M., & Einevoll, G. T. (2011). Modeling the spatial reach of the LFP. *Neuron, 72*(5), 859-872. doi:10.1016/j.neuron.2011.11.006

Lippa, C. F., Hamos, J. E., Pulaski-Salo, D., DeGennaro, L. J., & Drachman, D. A. (1992). Alzheimer's disease and aging: effects on perforant pathway perikarya and synapses. *Neurobiol Aging, 13*(3), 405-411. doi:10.1016/0197-4580(92)90115-e

Lisman, J. E., & Jensen, O. (2013). The theta-gamma neural code. *Neuron, 77*(6), 1002-1016. doi:10.1016/j.neuron.2013.03.007

Lisman, J. E., & Otmakhova, N. A. (2001). Storage, recall, and novelty detection of sequences by the hippocampus: elaborating on the SOCRATIC model to account for normal and aberrant effects of dopamine. *Hippocampus, 11*(5), 551-568. doi:10.1002/hipo.1071

Liu, C. C., Liu, C. C., Kanekiyo, T., Xu, H., & Bu, G. (2013). Apolipoprotein E and Alzheimer disease: risk, mechanisms and therapy. *Nat Rev Neurol, 9*(2), 106-118. doi:10.1038/nrneurol.2012.263

Llinas, R., & Yarom, Y. (1986). Oscillatory properties of guinea-pig inferior olivary neurones and their pharmacological modulation: an in vitro study. *J Physiol, 376*, 163-182. doi:10.1113/jphysiol.1986.sp016147

Lloret, M. A., Cervera-Ferri, A., Nepomuceno, M., Monllor, P., Esteve, D., & Lloret, A. (2020). Is Sleep Disruption a Cause or Consequence of Alzheimer's Disease? Reviewing Its Possible Role as a Biomarker. *Int J Mol Sci, 21*(3). doi:10.3390/ijms21031168

Lopez-Madrona, V. J., Perez-Montoyo, E., Alvarez-Salvado, E., Moratal, D., Herreras, O., Pereda, E., . . . Canals, S. (2020). Different theta frameworks coexist in the rat hippocampus and are coordinated during memory-guided and novelty tasks. *Elife, 9*. doi:10.7554/eLife.57313

Lovett-Barron, M., Kaifosh, P., Kheirbek, M. A., Danielson, N., Zaremba, J. D., Reardon, T. R., . . . Losonczy, A. (2014). Dendritic inhibition in the hippocampus supports fear learning. *Science, 343*(6173), 857-863. doi:10.1126/science.1247485

Lovett-Barron, M., Kaifosh, P., Kheirbek, M. A., Danielson, N., Zaremba, J. D., Reardon, T. R., . . . Losonczy, A. (2014). Dendritic inhibition in the hippocampus supports fear learning. *Science (New York, N.Y.), 343*(6173), 857-863. doi:10.1126/science.1247485

Low, R. J., Gu, Y., & Tank, D. W. (2014). Cellular resolution optical access to brain regions in fissures: imaging medial prefrontal cortex and grid cells in entorhinal cortex. *Proc Natl Acad Sci U S A, 111*(52), 18739-18744. doi:10.1073/pnas.1421753111

Lu, L., Ren, Y., Yu, T., Liu, Z., Wang, S., Tan, L., . . . Luo, M. (2020). Control of locomotor speed, arousal, and hippocampal theta rhythms by the nucleus incertus. *Nat Commun, 11*(1), 262. doi:10.1038/s41467-019-14116-y

Lucey, B. P., McCullough, A., Landsness, E. C., Toedebusch, C. D., McLeland, J. S., Zaza, A. M., . . . Holtzman, D. M. (2019). Reduced non-rapid eye movement sleep is associated with tau pathology in early Alzheimer's disease. *Sci Transl Med, 11*(474). doi:10.1126/scitranslmed.aau6550

Mably, A. J., & Colgin, L. L. (2018). Gamma oscillations in cognitive disorders. *Curr Opin Neurobiol, 52*, 182-187. doi:10.1016/j.conb.2018.07.009

Maccaferri, G., Roberts, J. D., Szucs, P., Cottingham, C. A., & Somogyi, P. (2000). Cell surface domain specific postsynaptic currents evoked by identified GABAergic neurones in rat hippocampus in vitro. *J Physiol, 524 Pt 1*, 91-116. doi:10.1111/j.1469-7793.2000.t01-3-00091.x

Martinez-Losa, M., Tracy, T. E., Ma, K., Verret, L., Clemente-Perez, A., Khan, A. S., . . . Palop, J. J. (2018). Nav1.1-Overexpressing Interneuron Transplants Restore Brain Rhythms and Cognition in a Mouse Model of Alzheimer's Disease. *Neuron, 98*(1), 75-89 e75. doi:10.1016/j.neuron.2018.02.029

Martinez, J. J., Rahsepar, B., & White, J. A. (2017). Anatomical and Electrophysiological Clustering of Superficial Medial Entorhinal Cortex Interneurons. *eNeuro, 4*(5). doi:10.1523/ENEURO.0263-16.2017

Martorell, A. J., Paulson, A. L., Suk, H. J., Abdurrob, F., Drummond, G. T., Guan, W., . . . Tsai, L. H. (2019). Multi-sensory Gamma Stimulation Ameliorates Alzheimer's-Associated Pathology and Improves Cognition. *Cell, 177*(2), 256-271 e222. doi:10.1016/j.cell.2019.02.014

Mazzoni, A., Linden, H., Cuntz, H., Lansner, A., Panzeri, S., & Einevoll, G. T. (2015). Computing the Local Field Potential (LFP) from Integrate-and-Fire Network Models. *PLoS Comput Biol, 11*(12), e1004584. doi:10.1371/journal.pcbi.1004584

McFarland, W. L., Teitelbaum, H., & Hedges, E. K. (1975). Relationship between hippocampal theta activity and running speed in the rat. *J Comp Physiol Psychol, 88*(1), 324-328. doi:10.1037/h0076177

McKay, B. M., Oh, M. M., & Disterhoft, J. F. (2013). Learning increases intrinsic excitability of hippocampal interneurons. *J Neurosci, 33*(13), 5499-5506. doi:10.1523/JNEUROSCI.4068-12.2013

Melamed, O., Gerstner, W., Maass, W., Tsodyks, M., & Markram, H. (2004). Coding and learning of behavioral sequences. *Trends Neurosci, 27*(1), 11-14; discussion 14-15. doi:10.1016/j.tins.2003.10.014

Melzer, S., Gil, M., Koser, D. E., Michael, M., Huang, K. W., & Monyer, H. (2017). Distinct Corticostriatal GABAergic Neurons Modulate Striatal Output Neurons and Motor Activity. *Cell Rep, 19*(5), 1045-1055. doi:10.1016/j.celrep.2017.04.024

Melzer, S., Michael, M., Caputi, A., Eliava, M., Fuchs, E. C., Whittington, M. A., & Monyer, H. (2012). Long-range-projecting GABAergic neurons modulate inhibition in hippocampus and entorhinal cortex. *Science, 335*(6075), 1506-1510. doi:10.1126/science.1217139

Melzer, S., & Monyer, H. (2020). Diversity and function of corticopetal and corticofugal GABAergic projection neurons. *Nat Rev Neurosci, 21*(9), 499-515. doi:10.1038/s41583-020-0344-9

Meyer, G., Carponcy, J., Salin, P. A., & Comte, J. C. (2018). Differential recordings of local field potential: A genuine tool to quantify functional connectivity. *PLoS One, 13*(12), e0209001. doi:10.1371/journal.pone.0209001

Miao, C., Cao, Q., Moser, M. B., & Moser, E. I. (2017). Parvalbumin and Somatostatin Interneurons Control Different Space-Coding Networks in the Medial Entorhinal Cortex. *Cell, 171*(3), 507-521 e517. doi:10.1016/j.cell.2017.08.050

Mikulovic, S., Pupe, S., Peixoto, H. M., Do Nascimento, G. C., Kullander, K., Tort, A. B., & Leao, R. N. (2016). On the photovoltaic effect in local field potential recordings. *Neurophotonics, 3*(1), 015002. doi:10.1117/1.NPh.3.1.015002

Miller, J., Watrous, A. J., Tsitsiklis, M., Lee, S. A., Sheth, S. A., Schevon, C. A., . . . Jacobs, J. (2018). Lateralized hippocampal oscillations underlie distinct aspects of human spatial memory and navigation. *Nat Commun, 9*(1), 2423. doi:10.1038/s41467-018-04847-9

Mitchell, S. J., Rawlins, J. N., Steward, O., & Olton, D. S. (1982). Medial septal area lesions disrupt theta rhythm and cholinergic staining in medial entorhinal cortex and produce impaired radial arm maze behavior in rats. *J Neurosci, 2*(3), 292-302. Retrieved from https://www.ncbi.nlm.nih.gov/pubmed/7062110

Mizuseki, K., Sirota, A., Pastalkova, E., & Buzsaki, G. (2009). Theta oscillations provide temporal windows for local circuit computation in the entorhinal-hippocampal loop. *Neuron, 64*(2), 267-280. doi:10.1016/j.neuron.2009.08.037

Morris, R. (1984). Developments of a water-maze procedure for studying spatial learning in the rat. *J Neurosci Methods, 11*(1), 47-60. doi:10.1016/0165-0270(84)90007-4

Morris, R. G., Garrud, P., Rawlins, J. N., & O'Keefe, J. (1982). Place navigation impaired in rats with hippocampal lesions. *Nature, 297*(5868), 681-683. doi:10.1038/297681a0

Moscovitch, M., Cabeza, R., Winocur, G., & Nadel, L. (2016). Episodic Memory and Beyond: The Hippocampus and Neocortex in Transformation. *Annu Rev Psychol, 67*, 105-134. doi:10.1146/annurev-psych-113011-143733

Mueller, P., & Rudin, D. O. (1963). Induced excitability in reconstituted cell membrane structure. *J Theor Biol, 4*(3), 268-280. doi:10.1016/0022-5193(63)90006-7

Muir, J. L. (1997). Acetylcholine, aging, and Alzheimer's disease. *Pharmacol Biochem Behav, 56*(4), 687-696. doi:10.1016/s0091-3057(96)00431-5

Müller-Komorowska, D., Opitz, T., Elzoheiry, S., Schweizer, M., Ambrad Giovannetti, E., & Beck, H. (2020). Nonspecific Expression in Limited Excitatory Cell Populations in Interneuron-Targeting Cre-driver Lines Can Have Large Functional Effects. *Front Neural Circuits, 14*(16). doi:10.3389/fncir.2020.00016

Murphy, G. G., Fedorov, N. B., Giese, K. P., Ohno, M., Friedman, E., Chen, R., & Silva, A. J. (2004). Increased neuronal excitability, synaptic plasticity, and learning in aged Kvbeta1.1 knockout mice. *Curr Biol, 14*(21), 1907-1915. doi:10.1016/j.cub.2004.10.021

Murray, A. J., Sauer, J. F., Riedel, G., McClure, C., Ansel, L., Cheyne, L., . . . Wulff, P. (2011). Parvalbumin-positive CA1 interneurons are required for spatial working but not for reference memory. *Nat Neurosci, 14*(3), 297-299. doi:10.1038/nn.2751

Nakazono, T., Jun, H., Blurton-Jones, M., Green, K. N., & Igarashi, K. M. (2018). Gamma oscillations in the entorhinal-hippocampal circuit underlying memory and dementia. *Neurosci Res, 129*, 40-46. doi:10.1016/j.neures.2018.02.002

Nakazono, T., Lam, T. N., Patel, A. Y., Kitazawa, M., Saito, T., Saido, T. C., & Igarashi, K. M. (2017). Impaired In Vivo Gamma Oscillations in the Medial Entorhinal Cortex of Knock-in Alzheimer Model. *Front Syst Neurosci, 11*, 48. doi:10.3389/fnsys.2017.00048

Neher, E., & Sakmann, B. (1992). The patch clamp technique. *Sci Am, 266*(3), 44-51. doi:10.1038/scientificamerican0392-44

Neher, E., Sakmann, B., & Steinbach, J. H. (1978). The extracellular patch clamp: a method for resolving currents through individual open channels in biological membranes. *Pflugers Arch, 375*(2), 219-228. doi:10.1007/BF00584247

Nilsson, X. Q. K. D. H. T. H. D. N. A. B. M.-M. N. S. J. H.-L. M. (2018). A spatial atlas of inhibitory cell types in mouse hippocampus. *bioRxiv*. doi:https://doi.org/10.1101/431957

Numata, K., & Kaplan, D. L. (2010). Mechanisms of enzymatic degradation of amyloid Beta microfibrils generating nanofilaments and nanospheres related to cytotoxicity. *Biochemistry, 49*(15), 3254-3260. doi:10.1021/bi902134p

Nyhus, E., & Curran, T. (2010). Functional role of gamma and theta oscillations in episodic memory. *Neurosci Biobehav Rev, 34*(7), 1023-1035. doi:10.1016/j.neubiorev.2009.12.014

O'Keefe, J. (1976). Place units in the hippocampus of the freely moving rat. *Exp Neurol, 51*(1), 78-109. Retrieved from https://www.ncbi.nlm.nih.gov/pubmed/1261644

O'Keefe, J., & Dostrovsky, J. (1971). The hippocampus as a spatial map. Preliminary evidence from unit activity in the freely-moving rat. *Brain Res, 34*(1), 171-175.

O'Keefe, J., & Recce, M. L. (1993). Phase relationship between hippocampal place units and the EEG theta rhythm. *Hippocampus, 3*(3), 317-330. doi:10.1002/hipo.450030307

O'Mara, S. M., & Aggleton, J. P. (2019). Space and Memory (Far) Beyond the Hippocampus: Many Subcortical Structures Also Support Cognitive Mapping and Mnemonic Processing. *Front Neural Circuits, 13*, 52. doi:10.3389/fncir.2019.00052

Ognjanovski, N., Schaeffer, S., Wu, J., Mofakham, S., Maruyama, D., Zochowski, M., & Aton, S. J. (2017). Parvalbumin-expressing interneurons coordinate hippocampal network dynamics required for memory consolidation. *Nat Commun, 8*, 15039. doi:10.1038/ncomms15039

Oh, M. M., Oliveira, F. A., Waters, J., & Disterhoft, J. F. (2013). Altered calcium metabolism in aging CA1 hippocampal pyramidal neurons. *J Neurosci, 33*(18), 7905-7911. doi:10.1523/JNEUROSCI.5457-12.2013

Oh, M. M., Simkin, D., & Disterhoft, J. F. (2016). Intrinsic Hippocampal Excitability Changes of Opposite Signs and Different Origins in CA1 and CA3 Pyramidal Neurons Underlie Aging-Related Cognitive Deficits. *Front Syst Neurosci, 10*, 52. doi:10.3389/fnsys.2016.00052

Ooms, S., Overeem, S., Besse, K., Rikkert, M. O., Verbeek, M., & Claassen, J. A. (2014). Effect of 1 night of total sleep deprivation on cerebrospinal fluid beta-amyloid 42 in healthy middle-aged men: a randomized clinical trial. *JAMA Neurol, 71*(8), 971-977. doi:10.1001/jamaneurol.2014.1173

Pak, V. M., Onen, S. H., Bliwise, D. L., Kutner, N. G., Russell, K. L., & Onen, F. (2020). Sleep Disturbances in MCI and AD: Neuroinflammation as a Possible Mediating Pathway. *Front Aging Neurosci, 12*, 69. doi:10.3389/fnagi.2020.00069

Palop, J. J., Chin, J., & Mucke, L. (2006). A network dysfunction perspective on neurodegenerative diseases. *Nature, 443*(7113), 768-773. doi:10.1038/nature05289

Palop, J. J., Chin, J., Roberson, E. D., Wang, J., Thwin, M. T., Bien-Ly, N., . . . Mucke, L. (2007). Aberrant excitatory neuronal activity and compensatory remodeling of inhibitory hippocampal circuits in mouse models of Alzheimer's disease. *Neuron, 55*(5), 697-711. doi:10.1016/j.neuron.2007.07.025

Palop, J. J., & Mucke, L. (2010). Amyloid-beta-induced neuronal dysfunction in Alzheimer's disease: from synapses toward neural networks. *Nat Neurosci, 13*(7), 812-818. doi:nn.2583 [pii]

10.1038/nn.2583

Palop, J. J., & Mucke, L. (2016). Network abnormalities and interneuron dysfunction in Alzheimer disease. *Nat Rev Neurosci, 17*(12), 777-792. doi:10.1038/nrn.2016.141

Pandis, D., & Scarmeas, N. (2012). Seizures in Alzheimer disease: clinical and epidemiological data. *Epilepsy Curr, 12*(5), 184-187. doi:10.5698/1535-7511-12.5.184

Park, K., Lee, J., Jang, H. J., Richards, B. A., Kohl, M. M., & Kwag, J. (2020). Optogenetic activation of parvalbumin and somatostatin interneurons selectively restores theta-nested gamma

oscillations and oscillation-induced spike timing-dependent long-term potentiation impaired by amyloid beta oligomers. *BMC Biol, 18*(1), 7. doi:10.1186/s12915-019-0732-7

Pastalkova, E., Itskov, V., Amarasingham, A., & Buzsaki, G. (2008). Internally generated cell assembly sequences in the rat hippocampus. *Science, 321*(5894), 1322-1327. doi:10.1126/science.1159775

Pastalkova, E., Serrano, P., Pinkhasova, D., Wallace, E., Fenton, A. A., & Sacktor, T. C. (2006). Storage of spatial information by the maintenance mechanism of LTP. *Science, 313*(5790), 1141-1144. doi:10.1126/science.1128657

Pelkey, K. A., Chittajallu, R., Craig, M. T., Tricoire, L., Wester, J. C., & McBain, C. J. (2017). Hippocampal GABAergic Inhibitory Interneurons. *Physiol Rev, 97*(4), 1619-1747. doi:10.1152/physrev.00007.2017

Petersen, P. C., & Buzsaki, G. (2020). Cooling of Medial Septum Reveals Theta Phase Lag Coordination of Hippocampal Cell Assemblies. *Neuron, 107*(4), 731-744 e733. doi:10.1016/j.neuron.2020.05.023

Petsche, H., Pockberger, H., & Rappelsberger, P. (1984). On the search for the sources of the electroencephalogram. *Neuroscience, 11*(1), 1-27. doi:10.1016/0306-4522(84)90212-4

Pfeiffer, B. E., & Foster, D. J. (2013). Hippocampal place-cell sequences depict future paths to remembered goals. *Nature, 497*(7447), 74-79. doi:10.1038/nature12112

Poll, S., Mittag, M., Musacchio, F., Justus, L. C., Giovannetti, E. A., Steffen, J., . . . Fuhrmann, M. (2020). Memory trace interference impairs recall in a mouse model of Alzheimer's disease. *Nat Neurosci, 23*(8), 952-958. doi:10.1038/s41593-020-0652-4

Rak, M., Del Bigio, M. R., Mai, S., Westaway, D., & Gough, K. (2007). Dense-core and diffuse Abeta plaques in TgCRND8 mice studied with synchrotron FTIR microspectroscopy. *Biopolymers, 87*(4), 207-217. doi:10.1002/bip.20820

Rapp, P. R., Deroche, P. S., Mao, Y., & Burwell, R. D. (2002). Neuron number in the parahippocampal region is preserved in aged rats with spatial learning deficits. *Cereb Cortex, 12*(11), 1171-1179. doi:10.1093/cercor/12.11.1171

Reinhart, R. M. G., & Nguyen, J. A. (2019). Working memory revived in older adults by synchronizing rhythmic brain circuits. *Nat Neurosci, 22*(5), 820-827. doi:10.1038/s41593-019-0371-x

Reiserer, R. S., Harrison, F. E., Syverud, D. C., & McDonald, M. P. (2007). Impaired spatial learning in the APPSwe + PSEN1DeltaE9 bigenic mouse model of Alzheimer's disease. *Genes Brain Behav, 6*(1), 54-65. doi:10.1111/j.1601-183X.2006.00221.x

Richard, G. R., Titiz, A., Tyler, A., Holmes, G. L., Scott, R. C., & Lenck-Santini, P. P. (2013). Speed modulation of hippocampal theta frequency correlates with spatial memory performance. *Hippocampus, 23*(12), 1269-1279. doi:10.1002/hipo.22164

Rissman, R. A., De Blas, A. L., & Armstrong, D. M. (2007). GABA(A) receptors in aging and Alzheimer's disease. *J Neurochem, 103*(4), 1285-1292. doi:10.1111/j.1471-4159.2007.04832.x

Robitsek, R. J., Fortin, N. J., Koh, M. T., Gallagher, M., & Eichenbaum, H. (2008). Cognitive aging: a common decline of episodic recollection and spatial memory in rats. *J Neurosci, 28*(36), 8945-8954. doi:10.1523/JNEUROSCI.1893-08.2008

Rogalski, E., Stebbins, G. T., Barnes, C. A., Murphy, C. M., Stoub, T. R., George, S., . . . deToledo-Morrell, L. (2012). Age-related changes in parahippocampal white matter integrity: a diffusion tensor imaging study. *Neuropsychologia, 50*(8), 1759-1765. doi:10.1016/j.neuropsychologia.2012.03.033

Rossor, M. N. (1982). Neurotransmitters and CNS disease. Dementia. *Lancet, 2*(8309), 1200-1204. doi:10.1016/s0140-6736(82)91212-0

Rossor, M. N., Emson, P. C., Mountjoy, C. Q., Roth, M., & Iversen, L. L. (1980). Reduced amounts of immunoreactive somatostatin in the temporal cortex in senile dementia of Alzheimer type. *Neurosci Lett, 20*(3), 373-377. doi:10.1016/0304-3940(80)90177-9

Rossor, M. N., Garrett, N. J., Johnson, A. L., Mountjoy, C. Q., Roth, M., & Iversen, L. L. (1982). A post-mortem study of the cholinergic and GABA systems in senile dementia. *Brain, 105*(Pt 2), 313-330. doi:10.1093/brain/105.2.313

Roux, L., & Buzsaki, G. (2015). Tasks for inhibitory interneurons in intact brain circuits. *Neuropharmacology, 88*, 10-23. doi:10.1016/j.neuropharm.2014.09.011

Roy, D. S., Arons, A., Mitchell, T. I., Pignatelli, M., Ryan, T. J., & Tonegawa, S. (2016). Memory retrieval by activating engram cells in mouse models of early Alzheimer's disease. *Nature, 531*(7595), 508-512. doi:10.1038/nature17172

Rozycka, A., & Liguz-Lecznar, M. (2017). The space where aging acts: focus on the GABAergic synapse. *Aging Cell, 16*(4), 634-643. doi:10.1111/acel.12605

Saito, T., Iwata, N., Tsubuki, S., Takaki, Y., Takano, J., Huang, S. M., . . . Saido, T. C. (2005). Somatostatin regulates brain amyloid beta peptide Abeta42 through modulation of proteolytic degradation. *Nat Med, 11*(4), 434-439. doi:10.1038/nm1206

Saiz-Sanchez, D., Ubeda-Banon, I., De la Rosa-Prieto, C., & Martinez-Marcos, A. (2012). Differential expression of interneuron populations and correlation with amyloid-beta deposition in the olfactory cortex of an AbetaPP/PS1 transgenic mouse model of Alzheimer's disease. *J Alzheimers Dis, 31*(1), 113-129. doi:10.3233/JAD-2012-111889

Sanchez-Mejias, E., Nunez-Diaz, C., Sanchez-Varo, R., Gomez-Arboledas, A., Garcia-Leon, J. A., Fernandez-Valenzuela, J. J., . . . Gutierrez, A. (2020). Distinct disease-sensitive GABAergic neurons in the perirhinal cortex of Alzheimer's mice and patients. *Brain Pathol, 30*(2), 345-363. doi:10.1111/bpa.12785

Sanchez, P. E., Zhu, L., Verret, L., Vossel, K. A., Orr, A. G., Cirrito, J. R., . . . Mucke, L. (2012). Levetiracetam suppresses neuronal network dysfunction and reverses synaptic and cognitive deficits in an Alzheimer's disease model. *Proc Natl Acad Sci U S A, 109*(42), E2895-2903. doi:10.1073/pnas.1121081109

Sasaki, T., Leutgeb, S., & Leutgeb, J. K. (2015). Spatial and memory circuits in the medial entorhinal cortex. *Curr Opin Neurobiol, 32*, 16-23. doi:10.1016/j.conb.2014.10.008

Scheffer-Teixeira, R., Belchior, H., Caixeta, F. V., Souza, B. C., Ribeiro, S., & Tort, A. B. (2012). Theta phase modulates multiple layer-specific oscillations in the CA1 region. *Cereb Cortex, 22*(10), 2404-2414. doi:10.1093/cercor/bhr319

Schmid, L. C., Mittag, M., Poll, S., Steffen, J., Wagner, J., Geis, H. R., . . . Fuhrmann, M. (2016). Dysfunction of Somatostatin-Positive Interneurons Associated with Memory Deficits in an Alzheimer's Disease Model. *Neuron, 92*(1), 114-125. doi:10.1016/j.neuron.2016.08.034

Schmidt-Hieber, C., & Hausser, M. (2013). Cellular mechanisms of spatial navigation in the medial entorhinal cortex. *Nat Neurosci, 16*(3), 325-331. doi:10.1038/nn.3340

Schomburg, E. W., Fernandez-Ruiz, A., Mizuseki, K., Berenyi, A., Anastassiou, C. A., Koch, C., & Buzsaki, G. (2014). Theta phase segregation of input-specific gamma patterns in entorhinal-hippocampal networks. *Neuron, 84*(2), 470-485. doi:10.1016/j.neuron.2014.08.051

Scoville, W. B., & Milner, B. (2000). Loss of recent memory after bilateral hippocampal lesions. 1957. *J Neuropsychiatry Clin Neurosci, 12*(1), 103-113. doi:10.1176/jnp.12.1.103

Selkoe, D. J. (2002). Alzheimer's disease is a synaptic failure. *Science, 298*(5594), 789-791. doi:10.1126/science.1074069

Serrano-Pozo, A., Frosch, M. P., Masliah, E., & Hyman, B. T. (2011). Neuropathological alterations in Alzheimer disease. *Cold Spring Harb Perspect Med, 1*(1), a006189-a006189. doi:10.1101/cshperspect.a006189

Sheremet, A., Kennedy, J. P., Qin, Y., Zhou, Y., Lovett, S. D., Burke, S. N., & Maurer, A. P. (2019). Theta-gamma cascades and running speed. *J Neurophysiol, 121*(2), 444-458. doi:10.1152/jn.00636.2018

Shim, Y., Philippides, A., Staras, K., & Husbands, P. (2016). Unsupervised Learning in an Ensemble of Spiking Neural Networks Mediated by ITDP. *PLoS Comput Biol, 12*(10), e1005137. doi:10.1371/journal.pcbi.1005137

Shoji, H., Takao, K., Hattori, S., & Miyakawa, T. (2016). Age-related changes in behavior in C57BL/6J mice from young adulthood to middle age. *Mol Brain, 9*, 11. doi:10.1186/s13041-016-0191-9

Sierksma, A. S., van den Hove, D. L., Pfau, F., Philippens, M., Bruno, O., Fedele, E., . . . Prickaerts, J. (2014). Improvement of spatial memory function in APPswe/PS1dE9 mice after chronic inhibition of phosphodiesterase type 4D. *Neuropharmacology, 77*, 120-130. doi:10.1016/j.neuropharm.2013.09.015

Sirota, A., Montgomery, S., Fujisawa, S., Isomura, Y., Zugaro, M., & Buzsaki, G. (2008). Entrainment of neocortical neurons and gamma oscillations by the hippocampal theta rhythm. *Neuron, 60*(4), 683-697. doi:10.1016/j.neuron.2008.09.014

Siskova, Z., Justus, D., Kaneko, H., Friedrichs, D., Henneberg, N., Beutel, T., . . . Remy, S. (2014). Dendritic structural degeneration is functionally linked to cellular hyperexcitability in a mouse model of Alzheimer's disease. *Neuron, 84*(5), 1023-1033. doi:10.1016/j.neuron.2014.10.024

Sitaram, R., Ros, T., Stoeckel, L., Haller, S., Scharnowski, F., Lewis-Peacock, J., . . . Sulzer, J. (2017). Closed-loop brain training: the science of neurofeedback. *Nat Rev Neurosci, 18*(2), 86-100. doi:10.1038/nrn.2016.164

Sivakumaran, M. H., Mackenzie, A. K., Callan, I. R., Ainge, J. A., & O'Connor, A. R. (2018). The Discrimination Ratio derived from Novel Object Recognition tasks as a Measure of Recognition Memory Sensitivity, not Bias. *Sci Rep, 8*(1), 11579. doi:10.1038/s41598-018-30030-7

Small, S. A., & Duff, K. (2008). Linking Abeta and tau in late-onset Alzheimer's disease: a dual pathway hypothesis. *Neuron, 60*(4), 534-542. doi:10.1016/j.neuron.2008.11.007

Somogyi, P., & Klausberger, T. (2005). Defined types of cortical interneurone structure space and spike timing in the hippocampus. *J Physiol, 562*(Pt 1), 9-26. doi:jphysiol.2004.078915 [pii]

10.1113/jphysiol.2004.078915

Sosulina, L. M., M.; Geis, H.R.; Hoffmann, K.; Klyubin, I.; Qi, Y.; Steffen, J.; Friedrichs, D.; Henneberg, N.; Fuhrmann, F.; Justus, D.; Keppler, K.; Cuello, C.; Rowan, M.J.; Fuhrmann, M.; Remy S. (2020). Hippocampal hyperactivity in a rat model of Alzheimer's disease. *bioRxiv*. doi:10.1101/2020.06.09.141598

Squire, L. R., & Wixted, J. T. (2011). The cognitive neuroscience of human memory since H.M. *Annual Review of Neuroscience, 34*, 259-288. doi:10.1146/annurev-neuro-061010-113720

Stanley, E. M., Fadel, J. R., & Mott, D. D. (2012). Interneuron loss reduces dendritic inhibition and GABA release in hippocampus of aged rats. *Neurobiol Aging, 33*(2), 431 e431-413. doi:10.1016/j.neurobiolaging.2010.12.014

Stark, E., Eichler, R., Roux, L., Fujisawa, S., Rotstein, H. G., & Buzsaki, G. (2013). Inhibition-induced theta resonance in cortical circuits. *Neuron, 80*(5), 1263-1276. doi:10.1016/j.neuron.2013.09.033

Stefanelli, T., Bertollini, C., Luscher, C., Muller, D., & Mendez, P. (2016). Hippocampal Somatostatin Interneurons Control the Size of Neuronal Memory Ensembles. *Neuron, 89*(5), 1074-1085. doi:10.1016/j.neuron.2016.01.024

Stoub, T. R., deToledo-Morrell, L., Stebbins, G. T., Leurgans, S., Bennett, D. A., & Shah, R. C. (2006). Hippocampal disconnection contributes to memory dysfunction in individuals at risk for Alzheimer's disease. *Proc Natl Acad Sci U S A, 103*(26), 10041-10045. doi:10.1073/pnas.0603414103

Strange, B. A., Witter, M. P., Lein, E. S., & Moser, E. I. (2014). Functional organization of the hippocampal longitudinal axis. *Nat Rev Neurosci, 15*(10), 655-669. doi:10.1038/nrn3785

Szentes, N., Tekus, V., Mohos, V., Borbely, E., & Helyes, Z. (2019). Exploratory and locomotor activity, learning and memory functions in somatostatin receptor subtype 4 gene-deficient mice in relation to aging and sex. *Geroscience, 41*(5), 631-641. doi:10.1007/s11357-019-00059-1

Tamura, M., Spellman, T. J., Rosen, A. M., Gogos, J. A., & Gordon, J. A. (2017). Hippocampal-prefrontal theta-gamma coupling during performance of a spatial working memory task. *Nat Commun, 8*(1), 2182. doi:10.1038/s41467-017-02108-9

Taniguchi, H., He, M., Wu, P., Kim, S., Paik, R., Sugino, K., . . . Huang, Z. J. (2011). A resource of Cre driver lines for genetic targeting of GABAergic neurons in cerebral cortex. *Neuron, 71*(6), 995-1013. doi:10.1016/j.neuron.2011.07.026

Tejera, D., & Heneka, M. T. (2016). Microglia in Alzheimer's disease: the good, the bad and the ugly. *Current Alzheimer research, 13*(4), 370-380. Retrieved from http://www.ncbi.nlm.nih.gov/pubmed/26567746

Thal, D. R., Rub, U., Orantes, M., & Braak, H. (2002). Phases of A beta-deposition in the human brain and its relevance for the development of AD. *Neurology, 58*(12), 1791-1800. doi:10.1212/wnl.58.12.1791

Toepper, M. (2017). Dissociating Normal Aging from Alzheimer's Disease: A View from Cognitive Neuroscience. *J Alzheimers Dis, 57*(2), 331-352. doi:10.3233/JAD-161099

Tong, L. M., Djukic, B., Arnold, C., Gillespie, A. K., Yoon, S. Y., Wang, M. M., . . . Huang, Y. (2014). Inhibitory interneuron progenitor transplantation restores normal learning and memory in

ApoE4 knock-in mice without or with Abeta accumulation. *J Neurosci, 34*(29), 9506-9515. doi:10.1523/JNEUROSCI.0693-14.2014

Tort, A. B., Komorowski, R., Eichenbaum, H., & Kopell, N. (2010). Measuring phase-amplitude coupling between neuronal oscillations of different frequencies. *J Neurophysiol, 104*(2), 1195-1210. doi:10.1152/jn.00106.2010

Tort, A. B., Komorowski, R. W., Manns, J. R., Kopell, N. J., & Eichenbaum, H. (2009). Theta-gamma coupling increases during the learning of item-context associations. *Proc Natl Acad Sci U S A, 106*(49), 20942-20947. doi:10.1073/pnas.0911331106

Toth, B., Kardos, Z., File, B., Boha, R., Stam, C. J., & Molnar, M. (2014). Frontal midline theta connectivity is related to efficiency of WM maintenance and is affected by aging. *Neurobiol Learn Mem, 114*, 58-69. doi:10.1016/j.nlm.2014.04.009

Tukker, J. J., Beed, P., Schmitz, D., Larkum, M. E., & Sachdev, R. N. S. (2020). Up and Down States and Memory Consolidation Across Somatosensory, Entorhinal, and Hippocampal Cortices. *Front Syst Neurosci, 14*, 22. doi:10.3389/fnsys.2020.00022

Uhlhaas, P. J., & Singer, W. (2012). Neuronal dynamics and neuropsychiatric disorders: toward a translational paradigm for dysfunctional large-scale networks. *Neuron, 75*(6), 963-980. doi:10.1016/j.neuron.2012.09.004

Uhlhaas, P. J., & Singer, W. (2015). Oscillations and neuronal dynamics in schizophrenia: the search for basic symptoms and translational opportunities. *Biol Psychiatry, 77*(12), 1001-1009. doi:10.1016/j.biopsych.2014.11.019

Unal, G., Crump, M. G., Viney, T. J., Eltes, T., Katona, L., Klausberger, T., & Somogyi, P. (2018). Spatio-temporal specialization of GABAergic septo-hippocampal neurons for rhythmic network activity. *Brain Struct Funct, 223*(5), 2409-2432. doi:10.1007/s00429-018-1626-0

Unal, G., Joshi, A., Viney, T. J., Kis, V., & Somogyi, P. (2015). Synaptic Targets of Medial Septal Projections in the Hippocampus and Extrahippocampal Cortices of the Mouse. *J Neurosci, 35*(48), 15812-15826. doi:10.1523/JNEUROSCI.2639-15.2015

Vago, D. R., & Kesner, R. P. (2008). Disruption of the direct perforant path input to the CA1 subregion of the dorsal hippocampus interferes with spatial working memory and novelty detection. *Behav Brain Res, 189*(2), 273-283. doi:10.1016/j.bbr.2008.01.002

Valero, M., & de la Prida, L. M. (2018). The hippocampus in depth: a sublayer-specific perspective of entorhinal-hippocampal function. *Curr Opin Neurobiol, 52*, 107-114. doi:10.1016/j.conb.2018.04.013

van Deursen, J. A., Vuurman, E. F., Verhey, F. R., van Kranen-Mastenbroek, V. H., & Riedel, W. J. (2008). Increased EEG gamma band activity in Alzheimer's disease and mild cognitive impairment. *J Neural Transm (Vienna), 115*(9), 1301-1311. doi:10.1007/s00702-008-0083-y

van Strien, N. M., Cappaert, N. L. M., & Witter, M. P. (2009). The anatomy of memory: an interactive overview of the parahippocampal?hippocampal network. *Nature Reviews Neuroscience, 10*(4), 272-282. doi:10.1038/nrn2614

Vandecasteele, M., Varga, V., Berenyi, A., Papp, E., Bartho, P., Venance, L., . . . Buzsaki, G. (2014). Optogenetic activation of septal cholinergic neurons suppresses sharp wave ripples and enhances theta oscillations in the hippocampus. *Proc Natl Acad Sci U S A, 111*(37), 13535-13540. doi:10.1073/pnas.1411233111

Vanderwolf, C. H. (1969). Hippocampal electrical activity and voluntary movement in the rat. *Electroencephalogr Clin Neurophysiol, 26*(4), 407-418. doi:10.1016/0013-4694(69)90092-3

Varga, C., Golshani, P., & Soltesz, I. (2012). Frequency-invariant temporal ordering of interneuronal discharges during hippocampal oscillations in awake mice. *Proc Natl Acad Sci U S A, 109*(40), E2726-2734. doi:10.1073/pnas.1210929109

Vassar, R., Bennett, B. D., Babu-Khan, S., Kahn, S., Mendiaz, E. A., Denis, P., . . . Citron, M. (1999). Beta-secretase cleavage of Alzheimer's amyloid precursor protein by the transmembrane aspartic protease BACE. *Science, 286*(5440), 735-741. Retrieved from https://www.ncbi.nlm.nih.gov/pubmed/10531052

Vaz, A. P., Wittig, J. H., Jr., Inati, S. K., & Zaghloul, K. A. (2020). Replay of cortical spiking sequences during human memory retrieval. *Science, 367*(6482), 1131-1134. doi:10.1126/science.aba0672

Verbitsky, M., Yonan, A. L., Malleret, G., Kandel, E. R., Gilliam, T. C., & Pavlidis, P. (2004). Altered hippocampal transcript profile accompanies an age-related spatial memory deficit in mice. *Learn Mem, 11*(3), 253-260. doi:10.1101/lm.68204

Verdaguer, E., Brox, S., Petrov, D., Olloquequi, J., Romero, R., de Lemos, M. L., . . . Auladell, C. (2015). Vulnerability of calbindin, calretinin and parvalbumin in a transgenic/knock-in APPswe/PS1dE9 mouse model of Alzheimer disease together with disruption of hippocampal neurogenesis. *Exp Gerontol, 69*, 176-188. doi:10.1016/j.exger.2015.06.013

Verkhratsky, A., & Parpura, V. (2014). History of electrophysiology and the patch clamp. *Methods Mol Biol, 1183*, 1-19. doi:10.1007/978-1-4939-1096-0_1

Verret, L., Mann, E. O., Hang, G. B., Barth, A. M., Cobos, I., Ho, K., . . . Palop, J. J. (2012). Inhibitory interneuron deficit links altered network activity and cognitive dysfunction in Alzheimer model. *Cell, 149*(3), 708-721. doi:10.1016/j.cell.2012.02.046

Viana da Silva, S., Haberl, M. G., Zhang, P., Bethge, P., Lemos, C., Goncalves, N., . . . Mulle, C. (2016). Early synaptic deficits in the APP/PS1 mouse model of Alzheimer's disease involve neuronal adenosine A2A receptors. *Nat Commun, 7*, 11915. doi:10.1038/ncomms11915

Villette, V., Poindessous-Jazat, F., Simon, A., Lena, C., Roullot, E., Bellessort, B., . . . Stephan, A. (2010). Decreased rhythmic GABAergic septal activity and memory-associated theta oscillations after hippocampal amyloid-beta pathology in the rat. *J Neurosci, 30*(33), 10991-11003. doi:10.1523/JNEUROSCI.6284-09.2010

Vinogradova, O. S. (2001). Hippocampus as comparator: role of the two input and two output systems of the hippocampus in selection and registration of information. *Hippocampus, 11*(5), 578-598. doi:10.1002/hipo.1073

Vorhees, C. V., & Williams, M. T. (2014). Assessing spatial learning and memory in rodents. *ILAR J, 55*(2), 310-332. doi:10.1093/ilar/ilu013

Vossel, K. A., Ranasinghe, K. G., Beagle, A. J., Mizuiri, D., Honma, S. M., Dowling, A. F., . . . Nagarajan, S. S. (2016). Incidence and impact of subclinical epileptiform activity in Alzheimer's disease. *Ann Neurol, 80*(6), 858-870. doi:10.1002/ana.24794

Waldert, S., Lemon, R. N., & Kraskov, A. (2013). Influence of spiking activity on cortical local field potentials. *J Physiol, 591*(21), 5291-5303. doi:10.1113/jphysiol.2013.258228

Walter, J., Capell, A., Grunberg, J., Pesold, B., Schindzielorz, A., Prior, R., . . . Haass, C. (1996). The Alzheimer's disease-associated presenilins are differentially phosphorylated proteins located predominantly within the endoplasmic reticulum. *Mol Med, 2*(6), 673-691. Retrieved from https://www.ncbi.nlm.nih.gov/pubmed/8972483

Wang, S., Li, K., Zhao, S., Zhang, X., Yang, Z., Zhang, J., & Zhang, T. (2020). Early-stage dysfunction of hippocampal theta and gamma oscillations and its modulation of neural network in a transgenic 5xFAD mouse model. *Neurobiol Aging, 94*, 121-129. doi:10.1016/j.neurobiolaging.2020.05.002

Watson, B. O., & Buzsaki, G. (2015). Sleep, Memory & Brain Rhythms. *Daedalus, 144*(1), 67-82. doi:10.1162/DAED_a_00318

Webster, S. J., Bachstetter, A. D., Nelson, P. T., Schmitt, F. A., & Van Eldik, L. J. (2014). Using mice to model Alzheimer's dementia: an overview of the clinical disease and the preclinical behavioral changes in 10 mouse models. *Front Genet, 5*, 88. doi:10.3389/fgene.2014.00088

Weidemann, A., Konig, G., Bunke, D., Fischer, P., Salbaum, J. M., Masters, C. L., & Beyreuther, K. (1989). Identification, biogenesis, and localization of precursors of Alzheimer's disease A4 amyloid protein. *Cell, 57*(1), 115-126. doi:10.1016/0092-8674(89)90177-3

Whitesell, J. D., Buckley, A. R., Knox, J. E., Kuan, L., Graddis, N., Pelos, A., . . . Harris, J. A. (2019). Whole brain imaging reveals distinct spatial patterns of amyloid beta deposition in three mouse models of Alzheimer's disease. *J Comp Neurol, 527*(13), 2122-2145. doi:10.1002/cne.24555

Wiltgen, B. J., & Silva, A. J. (2007). Memory for context becomes less specific with time. *Learn Mem, 14*(4), 313-317. doi:10.1101/lm.430907

Wimmer, M. E., Rising, J., Galante, R. J., Wyner, A., Pack, A. I., & Abel, T. (2013). Aging in mice reduces the ability to sustain sleep/wake states. *PLoS One, 8*(12), e81880. doi:10.1371/journal.pone.0081880

Winson, J. (1978). Loss of hippocampal theta rhythm results in spatial memory deficit in the rat. *Science, 201*(4351), 160-163. doi:10.1126/science.663646

Witter, M. P., Wouterlood, F. G., Naber, P. A., & Van Haeften, T. (2000). Anatomical organization of the parahippocampal-hippocampal network. *Ann N Y Acad Sci, 911*, 1-24. doi:10.1111/j.1749-6632.2000.tb06716.x

Wulff, P., Ponomarenko, A. A., Bartos, M., Korotkova, T. M., Fuchs, E. C., Bahner, F., . . . Monyer, H. (2009). Hippocampal theta rhythm and its coupling with gamma oscillations require fast inhibition onto parvalbumin-positive interneurons. *Proc Natl Acad Sci U S A, 106*(9), 3561-3566. doi:10.1073/pnas.0813176106

Xia, F., Richards, B. A., Tran, M. M., Josselyn, S. A., Takehara-Nishiuchi, K., & Frankland, P. W. (2017). Parvalbumin-positive interneurons mediate neocortical-hippocampal interactions that are necessary for memory consolidation. *Elife, 6*. doi:10.7554/eLife.27868

Xiao, M. F., Xu, D., Craig, M. T., Pelkey, K. A., Chien, C. C., Shi, Y., . . . Worley, P. F. (2017). NPTX2 and cognitive dysfunction in Alzheimer's Disease. *Elife, 6*. doi:10.7554/eLife.23798

Xu, Y., Zhao, M., Han, Y., & Zhang, H. (2020). GABAergic Inhibitory Interneuron Deficits in Alzheimer's Disease: Implications for Treatment. *Front Neurosci, 14*, 660. doi:10.3389/fnins.2020.00660

Yamamoto, J., & Tonegawa, S. (2017). Direct Medial Entorhinal Cortex Input to Hippocampal CA1 Is Crucial for Extended Quiet Awake Replay. *Neuron, 96*(1), 217-227 e214. doi:10.1016/j.neuron.2017.09.017

Yang, W., Zhou, X., & Ma, T. (2019). Memory Decline and Behavioral Inflexibility in Aged Mice Are Correlated With Dysregulation of Protein Synthesis Capacity. *Front Aging Neurosci, 11*, 246. doi:10.3389/fnagi.2019.00246

Yap, E. L., Pettit, N. L., Davis, C. P., Nagy, M. A., Harmin, D. A., Golden, E., . . . Greenberg, M. E. (2021). Bidirectional perisomatic inhibitory plasticity of a Fos neuronal network. *Nature, 590*(7844), 115-121. doi:10.1038/s41586-020-3031-0

Yassa, M. A., Mattfeld, A. T., Stark, S. M., & Stark, C. E. (2011). Age-related memory deficits linked to circuit-specific disruptions in the hippocampus. *Proc Natl Acad Sci U S A, 108*(21), 8873-8878. doi:10.1073/pnas.1101567108

Yassa, M. A., Muftuler, L. T., & Stark, C. E. (2010). Ultrahigh-resolution microstructural diffusion tensor imaging reveals perforant path degradation in aged humans in vivo. *Proc Natl Acad Sci U S A, 107*(28), 12687-12691. doi:10.1073/pnas.1002113107

Ylinen, A., Bragin, A., Nadasdy, Z., Jando, G., Szabo, I., Sik, A., & Buzsaki, G. (1995). Sharp wave-associated high-frequency oscillation (200 Hz) in the intact hippocampus: network and intracellular mechanisms. *J Neurosci, 15*(1 Pt 1), 30-46. Retrieved from https://www.ncbi.nlm.nih.gov/pubmed/7823136

Zanos, S., Zanos, T. P., Marmarelis, V. Z., Ojemann, G. A., & Fetz, E. E. (2012). Relationships between spike-free local field potentials and spike timing in human temporal cortex. *J Neurophysiol, 107*(7), 1808-1821. doi:10.1152/jn.00663.2011

Zemla, R., & Basu, J. (2017). Hippocampal function in rodents. *Curr Opin Neurobiol, 43*, 187-197. doi:10.1016/j.conb.2017.04.005

Zhang, R., Xue, G., Wang, S., Zhang, L., Shi, C., & Xie, X. (2012). Novel object recognition as a facile behavior test for evaluating drug effects in AbetaPP/PS1 Alzheimer's disease mouse model. *J Alzheimers Dis, 31*(4), 801-812. doi:10.3233/JAD-2012-120151

Zhang, X., Zhong, W., Brankack, J., Weyer, S. W., Muller, U. C., Tort, A. B., & Draguhn, A. (2016). Impaired theta-gamma coupling in APP-deficient mice. *Sci Rep, 6*, 21948. doi:10.1038/srep21948

Zhou, S., & Yu, Y. (2018). Synaptic E-I Balance Underlies Efficient Neural Coding. *Front Neurosci, 12*, 46. doi:10.3389/fnins.2018.00046

Zola-Morgan, S., Squire, L. R., & Amaral, D. G. (1986). Human amnesia and the medial temporal region: enduring memory impairment following a bilateral lesion limited to field CA1 of the hippocampus. *J Neurosci, 6*(10), 2950-2967.

Zott, B., Busche, M. A., Sperling, R. A., & Konnerth, A. (2018). What Happens with the Circuit in Alzheimer's Disease in Mice and Humans? *Annu Rev Neurosci, 41*, 277-297. doi:10.1146/annurev-neuro-080317-061725

Zutshi, I., Brandon, M. P., Fu, M. L., Donegan, M. L., Leutgeb, J. K., & Leutgeb, S. (2018). Hippocampal Neural Circuits Respond to Optogenetic Pacing of Theta Frequencies by Generating Accelerated Oscillation Frequencies. *Curr Biol, 28*(8), 1179-1188 e1173. doi:10.1016/j.cub.2018.02.061

8 Contributions

Julia Steffen, Andrea Baral and Olga Sharma performed genotyping of the mice employed in this thesis. Julia Steffen performed immunohistochemistry and counting of PV^+ and SOM^+ neurons in the MEC and provided help with perfusions of the animals. Stefanie Poll partially performed surgeries of the 19-20 month animal cohort and partially performed the Y-Maze experiment. Manuel Mittag performed analysis of calcium imaging experiments. Ricardo Neves Melo performed theta-gamma modulation analyses. Fabrizio Musacchio wrote parts of the code used for LFP data analysis. Daniel Justus (former member of AG Remy) wrote other parts of the custom MATLAB code.

List of figures

Figure 1.1 Cortical afferents into the dorsal hippocampus and hippocampal microcircuit 13

Figure 1.2 Theta generation in CA1 20

Figure 1.3 Exemplary recording of hippocampal local field potentials during active exploration in CA1-SLM 25

Figure 1.4 Generation of Aβ plaques and amyloid cascade hypothesis 28

Figure 1.5 The "GABAergic cascade hypothesis" of Alzheimer's disease 34

Figure 2.2 Experimental setup 42

Figure 3.1 Theta oscillations and locomotor activity of 15 month old PV-Cre::WT and PV-Cre::APP/PS1 mice 55

Figure 3.2 Peak frequency, but not amplitude of theta oscillations negatively correlates with age in PV-Cre::WT mice 59

Figure 3.3 Reduced theta-gamma modulation index in PV-Cre::APP/PS1 animals 62

Figure 3.4 Optogenetic stimulation of PV^+ hippocampal interneurons entrains oscillatory activity in CA1 65

Figure 3.5 Closed-loop rhythmic feedback optogenetic stimulation ameliorates recognition memory of 13 month old mice 68

Figure 3.6.1 Closed-loop arrhythmic feedback optogenetic stimulation does not ameliorate recognition memory of 14 month old mice 70

Figure 3.6.2 Closed-loop rhythmic feedback optogenetic stimulation does not ameliorate recognition memory of 19-20 month old mice 71

Figure 3.7 Closed-loop rhythmic feedback optogenetic stimulation does not ameliorate working memory of 19 month old mice 74

Figure 3.8.1 Closed-loop rhythmic feedback optogenetic stimulation does not ameliorate spatial memory of 19-20 month old mice 77

Figure 3.8.2 Closed-loop rhythmic feedback optogenetic stimulation ameliorates spatial memory of 15 month old mice 79

Fig. 3.9 Two-photon calcium imaging and laminar LFP recordings in the hippocampus 81

Figure 3.10 Aβ plaque burden profile in the MEC of APP/PS1 mice 83

Figure 3.11 Reduction of SOM^+ immunoreactivity in the MEC of APP/PS1 mice 86

Figure 3.12.1 Long-range inhibitory projections (LRIPs) between the hippocampus and the MEC 88

Figure 3.12.2 Area covered by SOM^+LRIP axons is reduced in the MEC of 11 month old SST-Cre::APP/PS1 mice 90

Fig. 3.13 Two-photon calcium imaging in the EC 92

Acknowledgements

Writing a thesis is an exciting process, let alone the performance of experiments. I therefore want to thank my supervisor Prof. Dr. Martin Fuhrmann for giving me this wonderful and humbling opportunity, for his continuous support and input, and for valuing my work throughout the years.

My gratitude goes also to the members of the committee, Prof. Dr. M. Hofmann, Prof. Dr. D. Isbrandt, Prof. Dr. E. Mass, for the time they spent reading and evaluating this thesis, and for the discussion that will take place during the defense day.

I want to thank the Studienstiftung des deutschen Volkes for the financial support and the highly valuable cultural stimuli provided during three of my PhD years. I am very grateful to Prof. Dr. Kinzig for the organizations of our "Stipendiatentreffen", during which many interesting worlds collided.

This thesis would have not been the same without Prof. Isbrandt, Ricardo and Stephane, whom I want to thank for their discussions and contributions on ephys matters. Thank you to Prof. Remy for the insightful discussions on the project and for the time spent preparing the manuscript. I want to thank Andrea, Julia and Olga for their priceless work in the lab and for bringing organization where chaos would otherwise easily develop. Thank you also to Fabrizio for the support in the data analysis.

My PhD's years were rich in interactions, amazing scientific exchanges, and emotions.
I cannot begin to describe how grateful I am for everything that I shared with the current and former members of my work group: from unforgettable bursts of uncontrolled laughter to overt manifestations of frustration, my colleagues and friends were there throughout this whole time. Thank you all for being so real, so open and so incredibly supportive – and for all the cookies. In particular: Steffi, thank you for being *always* there, with your ears open, ready for the next experimental challenge, the next laugh, the next highly valuable scientific (and not) discussion. Thank you for reading and commenting this thesis and for the great perspectives! Moni (Pilsmädchen!): thank you for helping me putting things into perspective in hard times, for being my friend and always pointing at the right shutter. Manule: thank you for being so patient and for the cool outdoor experiences; I will never trust you in hikes again, but you have my full trust in scientific – and friendship – matters. Felix N. (Lettuce boy): thank you for helping me develop the ability to work under unfavorable conditions, such as lack of a chair; I took it all as a sign of friendship, which I am very grateful for. Julia: thank you for being *so* yourself, for checking in on me in difficult times, and for the experimental support. Andrea: thank you for all your work and for putting up with me in tricky situations. Sophie (Lemongirl!): thank you for your kindness, scientific insights on this thesis, and irreplaceable enthusiasm over the last year. Fabrizio: thank you for the fun times in the office, and for the effort you put into teaching me the MATLAB ways. Falko: thanks for the technical and scientific support and for not getting too mad about me working in the Werkstatt. I also want to thank Lena, for the fun lab and out-of lab times and for her support.

I also want to thank all current and former members of our "neighbor" working group AG Remy for their help throughout the years and for the collaborative and friendly atmosphere. In

particular, Petra (Pizzagirl!): your invaluable positivity and friendship, literally all the times we chatted at my desk over cookies at 15 pm, and all the trips and runs to see the otters at the Rheinaue. Kevin (Oatlyboy): thanks for all the fun times, the jam sessions and the crazy gaming evenings. Hiroshi: thank you for always finding a solution with me and for the work you did for the manuscript. Rüdiger: thank you for your wise words, helping at the microscope in the eary days and in general fun unexpected chats. Felix L.: thank you for all the coffee and beer chats! Daniel: thank you for your help, kindness and support in analytical and mood matters.

I want to sincerely thank the LMF and ARF facilities and all animal caretakers, whose work is irreplaceable.

My gratitude goes also to my friends Telma, Tomke, Babbi, Giovanni, Gio, Stephanie, for all the amazing evenings full of laughter and ridiculously good food. Thank you to my friends Hana for the great and fun “quatschen” sessions, Nelli and Stephanie from AG Petzold for the great atmosphere in the Dokuzone. Joanna and Daniel: thank you for the game evenings and your constant affection! Dennis: thank you for the creative energy and chats that kept me sane in trying times!

I want to thank my friends and family in Rome and Colombia, for showing me constant affection. In particular Roberto, Alessandro, Jackie – whose support during the writing process was invaluable, Arianna, Cecilia, Marta, Bianca: thank you for making me smile in tough times. Thank you Basti, for your support during the first years. Patrick: thank you for being next to me this last year, which was probably the hardest of all, and for being strong when I wasn’t.

Lastly, I want to thank my mother and my father. Your infinite support and dedication brought me where I am today. Thank you for being my inspiration.

List of publications

1) Stefanie Poll, Manuel Mittag, Fabrizio Musacchio, Lena C. Justus, **Eleonora Ambrad Giovannetti**, Julia Steffen, Jens Wagner, Lioba Zohren, Susanne Schoch, Boris Schmidt, Walker S. Jackson, Dan Ehninger, Martin Fuhrmann (2020). **Memory trace interference impairs recall in a mouse model of Alzheimer's disease.** Nat Neurosci, 23(8), 952-958. doi:10.1038/s41593-020-0652-4

2) Daniel Müller-Komorowska, Thoralf Opitz, Shehabeldin Elzoheiry, Michaela Schweizer, **Eleonora Ambrad Giovannetti**, Heinz Beck (2020). **Nonspecific Expression in Limited Excitatory Cell Populations in Interneuron-Targeting Cre-driver Lines Can Have Large Functional Effects**. *Front Neural Circuits*, *14*(16). doi:10.3389/fncir.2020.00016

3) **Eleonora Ambrad Giovannetti**, Martin Fuhrmann (2019). **Unsupervised excitation: GABAergic dysfunctions in Alzheimer's disease**. *Brain Res,1707*, 216-26.doi:10.1016/j.brainres.2018.11.042

4) **Eleonora Ambrad Giovannetti**, Stefanie Poll, Daniel Justus, Hiroshi Kaneko, Falko Fuhrmann, Julia Steffen, Stefan Remy, Martin Fuhrmann (2018). **Restoring memory by optogenetic synchronization of hippocampal oscillations in an Alzheimer's disease mouse model.** bioRxiv, 9.11.2018; doi: 10.1101/363820